Photodisintegration of the Deuteron at 18 MeV using Linearly Polarized Photons

A Thesis Submitted to the

College of Graduate Studies and Research

in Partial Fulfillment of the Requirements

for the degree of Master of Science

in the Department of Physics and Engineering Physics

University of Saskatchewan

Saskatoon

By

Glen Anthony Pridham

Permission to Use

In presenting this thesis in partial fulfilment of the requirements for a Postgraduate degree from the University of Saskatchewan, I agree that the Libraries of this University may make it freely available for inspection. I further agree that permission for copying of this thesis in any manner, in whole or in part, for scholarly purposes may be granted by the professor or professors who supervised my thesis work or, in their absence, by the Head of the Department or the Dean of the College in which my thesis work was done. It is understood that any copying or publication or use of this thesis or parts thereof for financial gain shall not be allowed without my written permission. It is also understood that due recognition shall be given to me and to the University of Saskatchewan in any scholarly use which may be made of any material in my thesis.

Requests for permission to copy or to make other use of material in this thesis in whole or part should be addressed to:

Head of the Department of Physics and Engineering Physics
116 Science Place
University of Saskatchewan
Saskatoon, Saskatchewan
Canada
S7N 5C9

Abstract

This thesis reports the: cross section, parameterized differential cross section, and analyzing power (a.k.a. the photon asymmetry), for neutron production via the photodisintegration of the unpolarized deuteron at 18 MeV using linearly polarized photons: $d(\vec{\gamma},n)p$.

The data were collected in October 2010 using the High Intensity Gamma Source (HI$\vec{\gamma}$S) at the Duke Free-Electron Laser Laboratory (DFELL) located at Duke University in Durham, North Carolina. The ejectile neutrons from the photodisintegration reaction were measured using the Blowfish detector array: a spherical array of 88 BC-505 liquid organic scintillator cells which cover approximately π steradians.

The initial goal of our experiment was to perform tests on the detector characteristics and check a few potential sources of systematic error, and so uncontaminated experimental runs were only taken with the remaining beam-time. Our data are therefore not optimized for precision, and so presented a number of data analysis challenges. This thesis delineates the challenges and respective solutions.

Contrary to earlier results near deuteron binding energy threshold, we see reasonable agreement with a theoretical calculation based on retarded one meson exchange with empirical cutoffs in the propagators, including: off-shell corrections, relativistic corrections and the Δ isobar degree-of-freedom. Our results show similar agreement to theory as previous experiments at 14 and 16 MeV, although we see no target length dependence: such has been observed at 20 MeV.

Acknowledgements

Much of my life has been dedicated to uncovering new, more difficult methods (also known as "my way") for achieving the same success as more mundane approaches; my master's project has continued the trend nicely. Thankfully, a few people imposed upon me a bounty of good sense which I must acknowledge.

First, I'd like to thank my supervisor, Dr. Robert Pywell, for his guidance in navigating the stormy waters of this project. I'd also like to thank Dr. Blain Norum, who provided me with the theoretical calculations, and was readily available to discuss (with great enthusiasm) the eccentricities of my results. Of course, I must thank the previous Blowfish researchers who laid out and smoothed the path before me; in particular, Dr. Ward Wurtz for his extensive code, and for his extensive records: his thesis proved an invaluable resource. Dr. Brad Sawatzky also left a useful record of his work: if only I had read his thesis closely the first time, I might have saved months of agonizing personal errors.

Second, I offer a warm blanket thanks to my family and friends for their support. I'll add a special, begrudging thanks to Lindsay Goodwin for convincing me to write this thesis in LaTeX.

Finally, I must thank Dr. Jason Donev, he both sparked my interest in nuclear science and put me into contact with people whom actively research the subject, one of whom (Cody Crewson) would eventually lead me to my supervisor.

Dedicated to Florence M. Pridham, who's reverence for the written word has inspired me to write as a compression inspires an ideal spring to oscillate: tirelessly and assuredly.

Contents

Permission to Use i

Abstract ii

Acknowledgements iii

Contents v

List of Tables ix

List of Figures xi

List of Abbreviations xv

List of Nomenclature xvi

1 Introduction 1
- 1.1 Background . . . 1
- 1.2 Experiment . . . 2
- 1.3 Motivation . . . 2
- 1.4 Relevance . . . 3
- 1.5 Observables . . . 4
  - 1.5.1 Total Cross Section . . . 4
  - 1.5.2 Spatial Distribution . . . 5
  - 1.5.3 Theoretical Calculation . . . 12
  - 1.5.4 Outline . . . 12

2 Background 14
- 2.1 The Deuteron . . . 14
- 2.2 Photodisintegration of The Deuteron . . . 15
- 2.3 Kinematics . . . 23
- 2.4 Interactions of Particles with Matter . . . 25
- 2.5 Theoretical Calculations . . . 28
  - 2.5.1 The Nucleon-Nucleon Interaction . . . 28
  - 2.5.2 Meson Exchange Potentials . . . 31
  - 2.5.3 The Schwamb and Arenhövel Model . . . 34
    - The Elster and Bonn-OPEBR Potentials . . . 34
    - Retarded Meson Exchange Currents . . . 37
    - Δ Baryon Degree-of-Freedom Corrections . . . 38
    - Off-Shell Corrections . . . 40
    - Relativistic Corrections . . . 43
  - 2.5.4 Deuteron Photodisintegration: the S and T Matrices . . . 44

2.5.5 Legendre Expansion of the Cross Section . . . 47

3 Experimental Apparatus 51
3.1 Introduction . . . 51
3.2 Run Summary . . . 51
3.3 The High Intensity Gamma Source (HI$\vec{\gamma}$S) . . . 53
3.3.1 Synchrotrons . . . 58
3.4 Experimental Layout . . . 60
3.5 Targets . . . 61
3.6 Blowfish . . . 63
3.6.1 Detector Coordinates . . . 65
3.7 Detector Structure . . . 70
3.7.1 Photomultiplier Tubes (PMTs) . . . 71
3.8 Principles of Detection . . . 73
3.8.1 Organic Scintillators . . . 74
BC-505 Liquid Organic Scintillator . . . 78
3.8.2 Scintillator Light Output . . . 80
3.9 The Five Paddle Flux Monitor . . . 85
3.10 Data Acquisition System . . . 88
3.10.1 Circuit Logic . . . 88
The Data Acquisition Windows . . . 89
The Detector Circuits . . . 91
The Master Trigger System . . . 94
3.10.2 Gain . . . 96
3.10.3 The Gain Monitoring System . . . 97
3.10.4 Analogue-to-Digital Converters (ADCs) . . . 100
3.10.5 Time-to-Digital Converters (TDCs) . . . 101
3.10.6 Lucid . . . 102

4 Simulation 104
4.1 Introduction . . . 104
4.2 GEANT4 . . . 105
4.2.1 Physics Lists . . . 107
4.2.2 Using GEANT4 . . . 108
4.2.3 The Monte Carlo Method . . . 109
4.2.4 Simulation Consistency Checks . . . 110
4.3 Simulation Implementation . . . 114
4.3.1 BlowfishX . . . 114
4.4 Probability Density Functions . . . 116
4.4.1 Target Attenuation . . . 118
4.4.2 Legendre Probability Density Functions . . . 119
4.4.3 Inverse Transform Sampling . . . 141
4.4.4 The Bisection Method . . . 143
4.4.5 Newton's Method . . . 144

5 Analysis **146**
5.1 Introduction . . . 146
5.2 ROOT . . . 146
5.2.1 BFROOT . . . 149
RLucid . . . 151
5.3 Calibration . . . 151
5.3.1 Beam Calibration . . . 151
Verifying the Beam Polarization . . . 151
Out-of-Time Photons . . . 152
5.3.2 ADC Calibration . . . 158
Pedestals . . . 158
Determining the ADC Gains . . . 159
Scaling the Light Output . . . 161
Gain Offset . . . 163
5.3.3 Gain Tracking . . . 165
5.3.4 Gain Monitoring Problems . . . 170
5.3.5 TDC Calibration . . . 172
Determining the TDC Gains . . . 172
Aligning the TDCs . . . 172
Time-of-Flight Uncertainty . . . 174
5.3.6 Decomposing the TDC Spectrum . . . 176
5.3.7 Upstream Scattering . . . 180
5.3.8 Time-to-Digital Converter (TDC) Drift . . . 182
5.3.9 Pulse-Shape Discrimination . . . 184
5.4 Analysis Cuts . . . 193
5.4.1 Multiplicity Cut . . . 195
5.4.2 Pulse-Shape Discrimination (PSD) Cut . . . 196
5.4.3 Light Cuts . . . 199
5.4.4 Time-of-Flight Cut . . . 204
5.4.5 Background Cut . . . 206
5.4.6 Water (H_2O) Target Correction . . . 208
5.4.7 Cell Exclusions . . . 209
5.4.8 Out-of-Time Photon Exclusions . . . 209
5.5 Total Cross Section . . . 211
5.5.1 Computing the Beam Flux . . . 211
5.5.2 Computing the Total Cross Section . . . 214
5.6 Differential Cross Section . . . 216
5.6.1 Analyzing Power . . . 217

6 Results and Discussion **218**
6.1 Introduction . . . 218
6.2 Total Cross Section . . . 218
6.2.1 Discussion of Cross Section Data . . . 223
6.3 Legendre Parameterization of the Differential Cross Section . . . 224
6.3.1 Observables . . . 235

6.3.2 Discussion of Parameterization and Descendant Observables 240
6.4 Beam 244

7 Conclusion **246**
7.1 Sources of Error 246
7.1.1 Estimating the Sources of Error 246
7.1.2 Breakdown of Quantified Sources of Error 248
7.1.3 Unaccounted Sources of Error 255
Incorrect Light Output 255
Efficiencies 256
Effect of Beam Attenuation in Neutron Yield 257
Imperfect Beam Polarization 258
Miscellaneous Sources of Error 259
7.2 Future Considerations 259
7.3 Conclusion 261

References **270**

A Photon Interactions with Matter **278**

B Neutron Interactions with Matter **282**

C Full Kinematics Calculation **284**
C.1 Lorentz Transformation between Frames 287

D The High Intensity Gamma Source (HI$\vec{\gamma}$S) Metrics **289**

E GEANT4 Example **291**

F Target Attenuation Probability Density Functions **293**

G Gain Tracking Principle **295**

H Light Scaling Factors **297**

I Cell Exclusions **298**

J Simulation Consistency Checks **302**
J.1 Discussion of Simulation Consistency 308

List of Tables

2.1 Nucleon-Nucleon Lagrangians and Effective Potentials 32

3.1 Run Summary 52
3.2 HI$\vec{\gamma}$S Contemporaries 54
3.3 Target Metrics 61
3.4 Blowfish Metrics 64
3.5 Blowfish Detector Arrangement 69
3.6 HadronsPhotonis XP2262/B PMT Metrics 71
3.7 BC-505 Metrics 79
3.8 BC-505 Comparison 80

4.1 `QGSP BERT HP` Physics List 107
4.2 `QGSP BERT HP` Libraries 108
4.3 Target Attenuation Functions 118
4.4 Analytical CDF Inverses for Invertible Legendre Probability Density Functions 125

5.1 Neutron Time-of-Flight Offsets 179
5.2 Multiplicity Cut Summary 195
5.3 PSD Cut Summary 196
5.4 Light Cut Summary 199
5.5 Time-of-Flight Cut Summary 204
5.6 Background Cut Summary 206
5.7 Water Target Correction Summary 208

6.1 Run-by-Run Total Cross Section Data 219
6.2 Averaged Total Cross Section Data 220
6.3 Total Cross Section with Varied Time-of-Flight Cut 223
6.4 Legendre Expansion Parameters 227
6.5 Correlation of Fit Parameters 231
6.6 Full Errors for Parameterization 232
6.7 Additional Parameters 232
6.8 Light Water Target Parameters 233
6.9 Ratio of Cross Section at Select Lab Polar Angles (θ) 236

7.1 Summary of Error Methodologies 248
7.2 Error Summary of Neutron Yield for Cell 27 and Run 142 250
7.3 Error Summary of Total Cross Section for Run 142 254
7.4 Legendre Expansion Parameters 264
7.5 Ratio of Cross Section at Select Lab Polar Angles (θ) 267

A.1 Photon Attenuation Coefficients for Elements in This Experiment 280
A.2 Photon Attenuation Coefficients for Materials in This Experiment 281

B.1 Neutron Cross Sections for Materials in Experiment 283

D.1 HI$\vec{\gamma}$S Metrics 289
D.2 HI$\vec{\gamma}$S FEL Metrics 290

E.1 GEANT4 Output Example 292

H.1 Cell-by-Cell Light Scaling Factors 297

I.1 Cell Exclusions for Runs 142-149 298
I.2 Cell Exclusions for Run 150-153 299
I.3 Cell Exclusions for Run 154 299
I.4 Cell Exclusions for Runs 155-157 300
I.5 Cell Exclusions for Runs 158-159 301

J.1 Particle Generation Consistency Check 303

List of Figures

1.1 Literature Review of the Total Cross Section 5
1.2 Unpolarized Differential Cross Section at 20 and 29 MeV 8
1.3 Unpolarized Differential Cross Section at 14 and 16 MeV 9
1.4 Analyzing Power at 14 and 16 MeV 10
1.5 Ratio of Cross Section at Selected Neutron Lab Angles for Energy in Range: 3-18 MeV 11

2.1 Unpolarized Differential Cross Section at 20 and 29 MeV 16
2.2 Comparison of Total Cross Section to Theory for Deuteron Photodisintegration from 0 to 75 MeV 17
2.3 The Total Cross Section for Deuteron Photodisintegration from 5 to 25 MeV 18
2.4 Ratio of Cross Section at Selected Neutron Lab Angles for Energy in Range: 3-12 MeV 20
2.5 Ratio of Cross Section at Selected Neutron Lab Angles for Energy in Range: 3-18 MeV 21
2.6 Unpolarized Differential Cross Section at 14 and 16 MeV 22
2.7 Neutron Kinetic Energy 25
2.8 Energy loss ($-\frac{dE}{dx}$) of Common Particles in Air 26
2.9 A Meson-Nucleon Vertex 33
2.10 Nucleon Self-Energy 36
2.11 Box Diagrams of Δ Baryon Intermediate State 37
2.12 The Δ Isobar Contribution to the Deuteron Photodisintegration Cross Section 39
2.13 On-shell Δ Baryon Contributions 40
2.14 Meson Radiation and Nucleon Self Energy 41
2.15 Off-shell Contributions to Nucleon Current 43

3.1 The HI$\vec{\gamma}$S Facility 53
3.2 Operation of the Free-Electron Laser at HI$\vec{\gamma}$S 57
3.3 Idealized Synchrotron Potential 59
3.4 Experimental Layout 60
3.5 Long Targets 61
3.6 A Target Suspended in Blowfish 62
3.7 The Blowfish Detector Array 63
3.8 Blowfish Coordinates 66
3.9 Blowfish Detector Numbering 67
3.10 A Blowfish Cell 70
3.11 A Photonis XP2262 Photomultiplier Tube (PMT) 71
3.12 Photomultiplier tube operation 72
3.13 Scintillator Excitation (Energy Levels) 77
3.14 Light Response of Stilbene 78
3.15 BC-505 Emission Spectrum 79

3.16 Stilbene Detector Response . . . 81
3.17 BC-505 Light Output Response . . . 82
3.18 The Five Paddle Flux Monitor . . . 85
3.19 Five Paddle Flux Monitor Acceptance . . . 87
3.20 Circuit Symbol Legend . . . 88
3.21 Logical Symbols Used for Circuit Diagrams . . . 89
3.22 Data Acquisition Windows . . . 90
3.23 Detector Circuit . . . 92
3.24 The Master Trigger System . . . 95
3.25 Gain Drift During the Experiment . . . 98
3.26 LED Flashers . . . 99
3.27 Conceptual Overview of Lucid Integrated with Blowfish . . . 103

4.1 Simulated BC-505 Light Output . . . 111
4.2 Simulated Flux Monitor Light Output . . . 113
4.3 BlowfishX Update . . . 116
4.4 Simulated Neutron Yields from the ρ_{00} PDF . . . 129
4.5 Simulated Neutron Yields from the ρ_{01} PDF . . . 130
4.6 Simulated Neutrons Yields from the ρ_{02} PDF . . . 131
4.7 Simulated Neutrons Yields from the ρ_{03} PDF . . . 132
4.8 Simulated Neutrons Yields from the ρ_{04} PDF . . . 133
4.9 Simulated Neutrons Yields from the ρ_{22} PDF . . . 134
4.10 Simulated Neutrons Yields from the ρ_{23} PDF . . . 135
4.11 Simulated Neutrons Yields from the ρ_{24} PDF . . . 136
4.12 Simulated Neutrons Yields from the ρ_{11} PDF . . . 137
4.13 Simulated Neutrons Yields from the ρ_{12} PDF . . . 138
4.14 Simulated Neutrons Yields from the ρ_{11}' PDF . . . 139
4.15 Simulated Neutrons Yields from the ρ_{12}' PDF . . . 140

5.1 ROOT Prompt . . . 148
5.2 BFROOT Main Menu . . . 150
5.3 Out-of-Time Beam Photons . . . 153
5.4 Out-of-Time Beam Photon Arrival Time Constancy . . . 155
5.5 Out-of-Time Beam Photon Time Evolution during Experiment . . . 156
5.6 Out-of-Time Beam Photons as a Function of Beam Flux . . . 157
5.7 Pedestal Determination and Subtraction . . . 159
5.8 Determining the Gain of the Blowfish Cells. . . . 161
5.9 Gain Linearity of Cell Average . . . 164
5.10 Gain Linearity of Arbitrary Cells . . . 165
5.11 Gain Tracking Principle . . . 166
5.12 Detector Response to The LED Flash . . . 167
5.13 LED Monitor Spectrum . . . 168
5.14 The Gain Monitoring System Electronics . . . 169
5.15 Discrepancy in the Gain Monitoring System . . . 171
5.16 TDC Alignment . . . 173

5.17 Time-of-Flight Uncertainty . . . 175
5.18 Simulated Effects in Neutron Time-of-Flight Spectrum . . . 177
5.19 Asymmetric Neutron Time-of-Flight Spectrum in Simulation . . . 178
5.20 Upstream Scattering of Beam . . . 181
5.21 Time-to-Digital Converter Drift . . . 183
5.22 An Idealized View of How PSD is Performed . . . 185
5.23 Raw PSD Plot . . . 186
5.24 PSD Slice Plot Example . . . 188
5.25 PSD Fit Plot . . . 189
5.26 Final PSD Plot . . . 190
5.27 PSD Parameters Change During the Experiment . . . 191
5.28 Aging Cell PSD . . . 193
5.29 Estimating the Uncertainty in the PSD Cut . . . 199
5.30 Final PSD Plot (2) . . . 201
5.31 Effect of the Light Cuts . . . 202
5.32 Effect of the Time-of-Flight Cut . . . 205
5.33 Typical Background Spectrum . . . 207
5.34 Typical Background Time-of-Flight Spectrum with Out-of-Time Photons Present 210
5.35 Calibrating the Five Paddle Flux Monitor . . . 212

6.1 Total Cross Section . . . 221
6.2 Total Cross Section with Varied Time-of-Flight Cut . . . 222
6.3 Parameterized Neutron Yield for Long Target Average . . . 226
6.4 Parameterized Theoretical Predictions . . . 228
6.5 Comparison of the Extracted a_k Parameters . . . 229
6.6 Comparison of the Extracted e_k Parameters . . . 230
6.7 Light Water Target Neutron Yield . . . 234
6.8 Differential Cross Section vs θ in the CM Frame . . . 235
6.9 Ratio of Cross Section at Selected Neutron Lab Angles for Energy in Range 3-18 MeV . . . 237
6.10 Differential Cross Section vs ϕ in the CM Frame . . . 238
6.11 Cross Section in 3 Dimensional Plot . . . 239
6.12 Analyzing Power . . . 240
6.13 Beam Asymmetry . . . 244
6.14 Analyzing Power with Imperfect Beam Polarization . . . 245

7.1 Breakdown of Uncertainty in Neutron Yield; Run 142 . . . 251
7.2 Breakdown of Uncertainty in Neutron Yield; Cell 27, Run 142 . . . 251
7.3 Asymmetry of the Pulse-Shape Discrimination Uncertainty . . . 253
7.4 Breakdown of Uncertainty in Total Cross Section for Run 142 . . . 254
7.5 Effect of Beam Attenuation in Simulated Neutron Yield . . . 258
7.6 Total Cross Section . . . 262
7.7 Parameterized Neutron Yield for Long Target Average . . . 263
7.8 Differential Cross Section vs θ in the CM Frame . . . 265
7.9 Differential Cross Section vs ϕ in the CM Frame . . . 266

7.10 Analyzing Power 267
7.11 Ratio of Cross Section at Selected Neutron Lab Angles for Energy in Range 3-18 MeV 268

A.1 Photon Interactions with Water 279

C.1 Deuteron Photodisintegration Kinematics 284
C.2 Center-of-Momentum Frame after Photodisintegration 285

E.1 GEANT4 Output Example 291

J.1 Particle Generation Consistency Check 303
J.2 Simulation Consistency Check for Neutron Distribution and Parameterization 305
J.3 Simulation Consistency Check for Neutron Distribution 306
J.4 Simulated vs Experimental Light Output 307
J.5 The Simulation Correctly Reacts to the Light Cut 308

List of Abbreviations

ADC	Analogue-to-Digital Converter
BC-505	Bicron-505 liquid organic scintillator.
CAMAC	Computer Automated Measurement And Control
CDF	Cumulative Distribution Function
CFD	Constant-Fraction Discriminator
CM	Center of Mass/Momentum (frame)
d	The deuteron: the nucleus of ^{2}H.
DAQ	Data Acquisition System
DC	Direct Current
FEL	Free-Electron Laser
GSO	Gadolinium-silicon-trioxide solid organic scintillator.
GUI	Graphic User Interace
HI$\vec{\gamma}$S	The High Intensity Gamma Source at Duke University
IG	Independent Gate
LED	Light-Emitting Diode
Linac	Linear Accelerator
OK	Optical Klystron
PDF	Probability Density Function
PMT	Photomultiplier Tube
PSD	Pulse-Shape Discrimination
QCD	Quantum Chromodynamics
RTEMS	Real-Time Executive for Multiprocessor Systems
TDC	Time-to-Digial Converter
UV	Ultraviolet
VME	Versa Module Eurocard

List of Nomenclature

A(B,C)D	A reaction wherein projectile B is incident on target A (in the lab frame), producing ejectile C (which is measured) and recoil D.
Barn	1 barn $\equiv 10^{-24}$ cm^2
Bucket	A potential energy minimum in a synchrotron where electrons are stored.
Bunches	Any number of electrons which share a mutual potential minimum in a synchrotron.
eVee	Electron-equivalent electronvolt: defined as the detector response to absorbing the kinetic energy of one 1 eV electron.
Five Paddle	The Five Paddle Flux Monitor.
Gamma Ray	Used as a synonym for a high energy photon.
God-given units	A unit system where by definition $c \equiv \hbar \equiv 1$.
Multipole	The order of a specific term in an expansion describing an electromagnetic transition.
Observable	A quantity which can be measured experimentally.
Phenomenological	A description of phenomenon which does no have a rigorous theoretical foundation.
We	The various collaborators whom at any point contributed to the work in this thesis.

Chapter 1

Introduction

Photodisintegration of the deuteron[1] using linearly polarized photons occurs when a linearly polarized photon causes a deuteron to break into its nuclear constituents: a neutron, and a proton (destroying both the photon and deuteron in the process). In this experiment, we measured the reaction: $d(\vec{\gamma},n)p$ i.e. we measured the ejectile neutron from the deuteron photodisintegration reaction and ignored the recoiling proton.

1.1 Background

Low energy deuteron photodisintegration of unpolarized deuterons has purportedly been well replicated by theory since the late 1980's, when realistic nucleon-nucleon potentials became available to perform accurate calculations, and, concurrently, Compton scattering based photon sources: capable of gathering high precision data, became widely available [Are91]. It was also during this time that inconsistencies in the spatial distribution of the cross section near threshold energies ($\lesssim$ 20 MeV) appeared [Ste87, Bir88], leading to a bifurcation of theoretical calculations: Arenhövel ignored the results [Sch91, Are91], while Hadjimichael *et al.* altered their theoretical calculation by fitting their higher order terms to the new experimental data [Had87].

Sawatzky [Saw05] returned to the subject in 2005, and his results verified that there was indeed a discrepancy with the then accepted theoretical calculations performed by Arenhövel [Are00]; specifically in the spatial distribution of the cross section.

Blackston [Bla07] continued the search at 14 and 16 MeV and his data agreed with the calculations by Schwamb and Arenhövel. Next, Kucuker [Kuc10] used unpolarized photons

[1]The deuteron is the nucleus of deuterium: ^{2}H.

to perform the photodisintegration at 20 MeV: her data agreed well with the same calculations, although she also found an unexplained short (2.0 cm) and long (10.7 cm) target discrepancy: possibly due to some unaccounted scattering process (this was conjectured to be spin-dependent scattering), or possibly due to an artifact of the analysis or experimental procedure.

1.2 Experiment

Our experiment was performed at the High Intensity Gamma Source (HI$\vec{\gamma}$S) facility at Duke University, Durham, NC in October 2010. The HI$\vec{\gamma}$S facility is a synchrotron with a free-electron laser which utilizes Compton backscattering within an optical cavity to produce highly polarized, nearly monochromatic photons at nuclear energies [Wel09].

We detected the ejectile neutrons using the Blowfish detector array: a spherical array of 88 organic scintillator detectors placed on an imaginary sphere of radius 40.64 ± 0.30 cm, covering a solid angle of approximately π steradians over the interval $\theta \in [22.5°, 157.5°]$ (polar angle) and $\phi \in [0°, 360°)$ (azimuthal angle).

The targets we used were composed of deuterated water: D_2O, in lengths of: 2.0 ± 0.1 cm (short) and 10.7 ± 0.1 cm (long). We accounted for neutrons from sources other than the deuteron; such as from ^{16}O and ^{13}C, by using a 10.7 ± 0.1 cm H_2O target to measure, and later subtract, the neutron cross section due to other reactions.

1.3 Motivation

Our ultimate goal is to provide accurate and precise data on the deuteron: to allow theoreticians to improve the quality of their theoretical calculations. In this work, this specifically means we will test the theoretical predictions for the: total cross section, analyzing power, and polar angle differential cross section.

The data in this thesis were initially collected in order to test for possible sources of error in the experimental configuration, and it was only when the author inherited these data in 2011 that it became clear that the data taken were sufficiently precise to compare

meaningfully to theoretical calculations. A secondary, pragmatic goal of this research is to continue in the spirit of the collection of these data: to take a careful look at potential sources of error using Blowfish at HI$\vec{\gamma}$S in order to maximize the precision of future experiments.

Previous experiments with Blowfish [Saw05, Bla07, Wur10c, Kuc10] found a few discrepancies which we would like to settle: old theoretical calculations showed discrepancies at low energies [Saw05], the neutron light output of the Blowfish cells differ from the simulated data [Bla07, Wur10c], and the short and long target produced inconsistent results [Kuc10]. We aim to verify these results, or uncover the reason for the discrepancies observed.

1.4 Relevance

The importance of deuteron photodisintegration derives from the fact that the deuteron is ostensibly the simplest nuclear system, and the photon is the "cleanest" (i.e. best understood) probe [Are91]. Understanding how the deuteron is disintegrated by photons will allow for more precise nucleon-nucleon potentials by directly improving the precision of the cutoff parameters used in phenomenological potentials. Enhanced accuracy in nucleon-nucleon potentials will improve calculations involving *any* nucleus.

The deuteron is also important on its own merit: it has by far the smallest binding energy per nucleon of any stable nucleus (1.11 $\frac{\text{MeV}}{\text{nucleon}}$ contrasted to 7.59 $\frac{\text{MeV}}{\text{nucleon}}$ for ^{235}U [Son13]) and therefore has the largest mass per nucleon available for conversion into energy, giving it the potential for use as an energy resource (or as a weapon), or as an energy carrier.[2] The future of deuteron-based technologies is limited only by engineering and the quality of quantitative scientific data available. By testing the theoretical calculations we can either increase confidence in nuclear predicative power, or provide evidence that theoreticians need to improve the way they perform their calculations.

[2]For example, a reversible conversion between ^{4}He and ^{2}H would carry 24 MeV [Son13] per ^{4}He nucleus; in contrast to the $\approx$ eV (per atom) stored in atomic chemical reactions.

1.5 Observables

The fundamental observable for unpolarized photodisintegration is the cross section, σ, and its spatial distribution, $\frac{d\sigma}{d\Omega}$ (i.e. the differential cross section). We therefore measured; and report here, the total cross section and the differential cross section. We also report the analyzing power (also known as the photon asymmetry) which is a function of the differential cross section at azimuthal angles $\phi = 0°$ and $90°$ relative to the photon polarization. Schwamb and Arenhövel [Sch01c, Sch01a, Sch01b] provided the theoretical calculations of: the ϕ-averaged differential cross section (i.e. the unpolarized photodisintegration differential cross section), the total cross section, and the analyzing power.

1.5.1 Total Cross Section

In order to deduce the total cross section, σ, we measured the total number of incident photons using the Five Paddle Flux Monitor, and the total neutron yield using the Blowfish detector array. Using a Monte Carlo simulation to replicate the experimental detector efficiency, we can calculate the total cross section:

$$\sigma = \frac{N^{sim}}{N_d^{sim}} \frac{N_d \mu}{\rho n N_0 (1 - e^{-\mu x})} \tag{1.1}$$

where: N_d is the neutron yield for detector, d, N_d^{sim} is the neutron yield for detector, d, *in the simulation*, N^{sim} is the total number of events simulated, x is the target length, N_0 is the number of incident photons, σ is the cross section (cm^2/atom), ρ is mass density of the target ($\mathrm{g/cm}^3$), μ is the linear mass attenuation coefficient for photon interactions in the target (cm^{-1}),[3] and n is the number density of the target (atoms/g).

The theoretical cross section agrees well with the interpolated data from earlier researchers (figure 1.1 on the next page),[4] but not very well with either of the direct measurements at 18 MeV, performed by: Skopik *et al.* [Sko74] (640 ± 31 μbarns) and De Graeve *et al.* [DGr91]

[3]The attenuation due to the photodisintegration process is small relative to μ allowing this equation to be approximately valid: since μ does technically include a contribution from σ.

[4]We performed a phenomenological fit in order to interpolate the cross section at 18 MeV for those researchers who did measured the cross section at nearby energies but not 18 MeV.

(716 ± 22 μbarns). Taking the weighted average [Tay97] of the previous experiments in figure 1.1, one finds that the theory (685.14 μbarns) agrees very well with past experimental results (690 ± 15 μbarns). The direct measurements agree with the theoretical prediction only at an error interval of 2σ, and do not agree with each other.

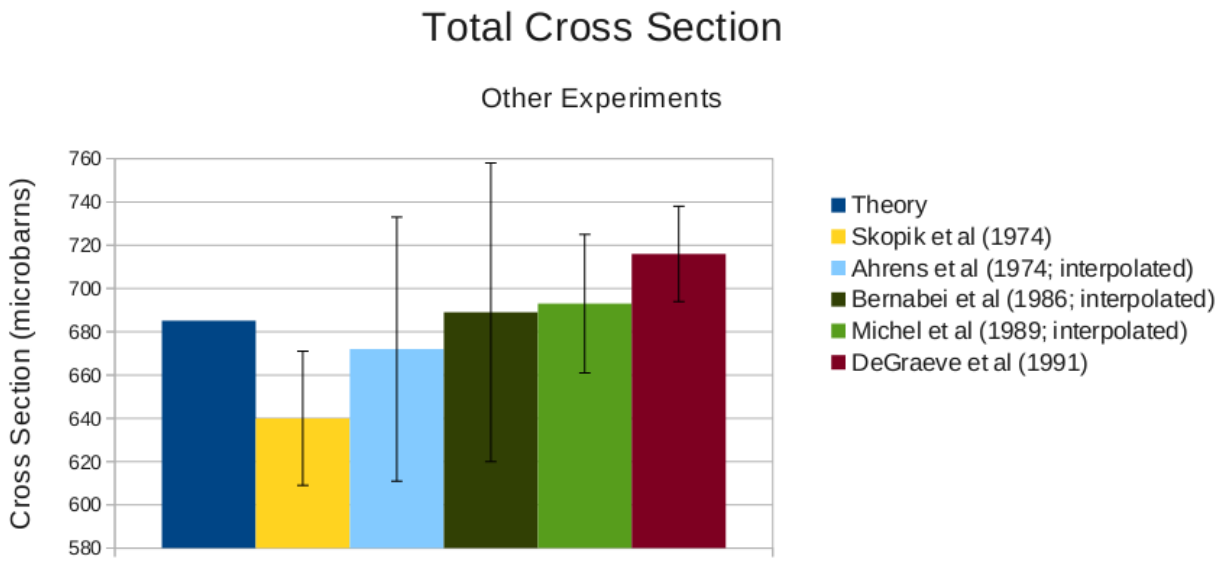

Figure 1.1: Literature Review of Total Cross Section, with contemporary theory.

In this work we compute the total cross section with the hope of elucidating the discrepancy between the two direct measurements, as well as testing the theoretical prediction.

1.5.2 Spatial Distribution

The spatial distribution of the cross section is described by the differential cross section: $\frac{d\sigma}{d\Omega}$, and a few other observables, namely the analyzing power (eq. (1.3) on the next page). The differential cross section can be represented as an expansion of the associated Legendre

polynomials, and so our key measurements are the values of the parameters in the expansion:

$$\begin{aligned}\frac{d\sigma}{d\Omega} \approx & \frac{\sigma}{4\pi}\left[1+\sum_{k=1}^{4} a_k P_k^0(\cos\theta)+\sum_{k=2}^{4} e_k P_k^2(\cos\theta)\cos 2\phi\right. \\ & \left.+\sum_{k=1}^{2} c_k P_k^1(\cos\theta)\cos\phi+\sum_{k=1}^{2} d_k P_k^1(\cos\theta)\sin\phi\right] \end{aligned} \tag{1.2}$$

where: P_k^i are the associated Legendre polynomials, a_k, e_k, c_k and d_k are fitting parameters, and σ is the total cross section. This expansion is given in Cambi *et al.* [Cam82], with the following changes: we absorbed the photon polarization factor into our e_k parameters, and we have added the c_k and d_k parameters to test target alignment (they are subsequently fixed to zero once target alignment has been verified).

Using the differential cross section, we can calculate the analyzing power:

$$\begin{aligned}\Sigma(\theta) \equiv & \frac{1}{\Sigma^l}\frac{\frac{d\sigma}{d\Omega}(\theta,\phi=0^\circ)-\frac{d\sigma}{d\Omega}(\theta,\phi=90^\circ)}{\frac{d\sigma}{d\Omega}(\theta,\phi=0^\circ)+\frac{d\sigma}{d\Omega}(\theta,\phi=90^\circ)} \\ = & \frac{1}{\Sigma^l}\frac{\sum_{k=2} e_k P_k^2(\cos\theta)}{\sum_{k=1} a_k P_k^0(\cos\theta)} \end{aligned} \tag{1.3}$$

where: $\frac{d\sigma}{d\Omega}$ is the differential cross section, Σ^l is the probability of an incident photon being horizontal polarized, the a_k and e_k are the extracted parameters from the Legendre expansion, and P_k^i are the associated Legendre polynomials.

The horizontal polarization fraction in eq. (1.3), Σ^l, depends on the photon source used; for our experimental setup at HI$\vec{\gamma}$S, we expect that this values is close to 1 (i.e. 100% polarization of incident photons).

In order to extract the parameters in eq. (1.2) we mapped each Legendre polynomial into a probability density function, then used a GEANT4 simulation to calculate an expected

yield for each term. This allowed us to fit directly to the neutron yield via:

$$\begin{aligned} N_d \approx & A[(1 - \sum_{k=1}^{4} a_k - 3e_2 - 6e_3 - 10e_4 - c_1 - \frac{3}{2}c_2 - d_1 - \frac{3}{2}d_2)N_{d,00}^{sim} \\ & + \sum_{k=1}^{4} a_k N_{d,0k}^{sim} + 3e_2 N_{d,22}^{sim} + 6e_3 N_{d,23}^{sim} + 10e_4 N_{d,24}^{sim} \\ & + c_1 N_{d,11}^{sim} + \frac{3}{2}c_2 N_{d,12}^{sim} + d_1 N_{d,11'}^{sim} + \frac{3}{2}d_2 N_{d,12'}^{sim}] \end{aligned} \tag{1.4}$$

where: N_{ki}^{sim} are the simulated neutron yields associated with their respective Legendre polynomial, a_k, e_k, c_k and d_k are fitting parameters, and A is a scaling parameter proportional to the: flux, target density, cross section, and efficiencies.

Previous researchers have found fairly good agreement with the theoretical calculations by Schwamb and Arenhövel; however, the theory appears to underestimate the probability of forward scattering in some experiments. For example, figure 1.2 on the next page at 20 and 29 MeV, and figure 1.3 on page 9 at 14 and 16 MeV.

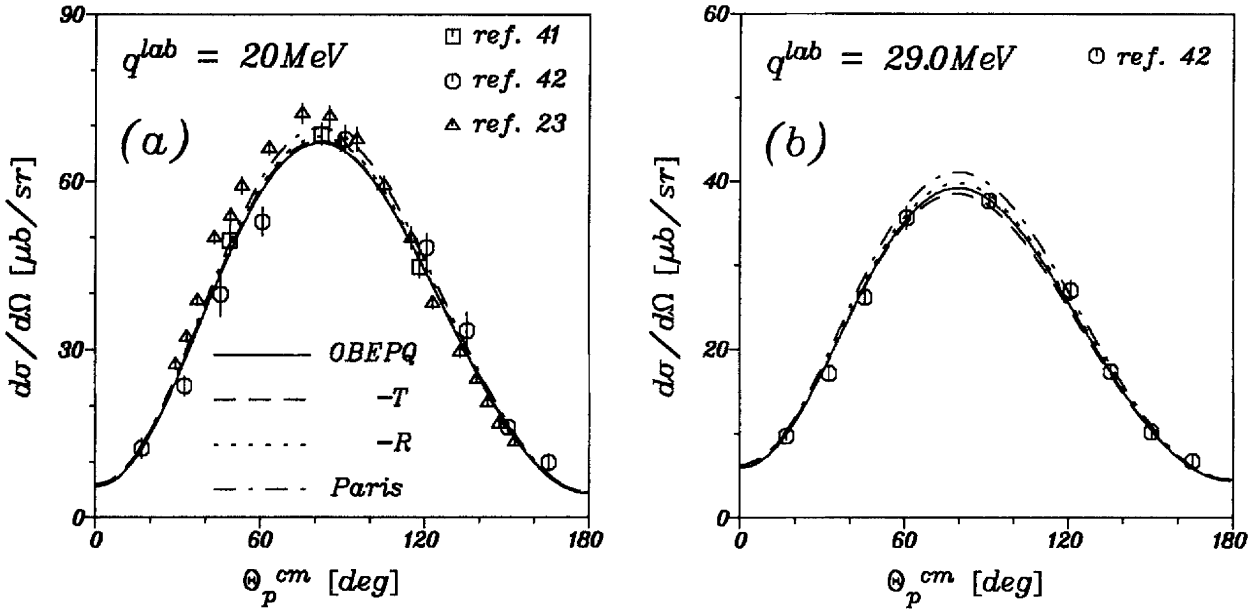

Figure 1.2: Unpolarized Differential Cross Section at 20 and 29 MeV. Where: q^{lab} is the lab energy (equal to the photon energy), and θ^{CM} is the center-of-mass/momentum polar angle. The different lines represent the potential used: OBEPQ, -T and -R are based on the Bonn potential [Mac87], and Paris is the Paris potential [Lac81]. The references are: 23: Skopik *et al.* [Sko74], 41: Fink *et al.* (1989), 42: De Pascale *et al.* (1985). Reference 23 is skewed in favour of small theta, and 42 is skewed in favour of large theta. No substantial discrepancy is observed. Image credit: Schmitt *et al.* [Sch91].

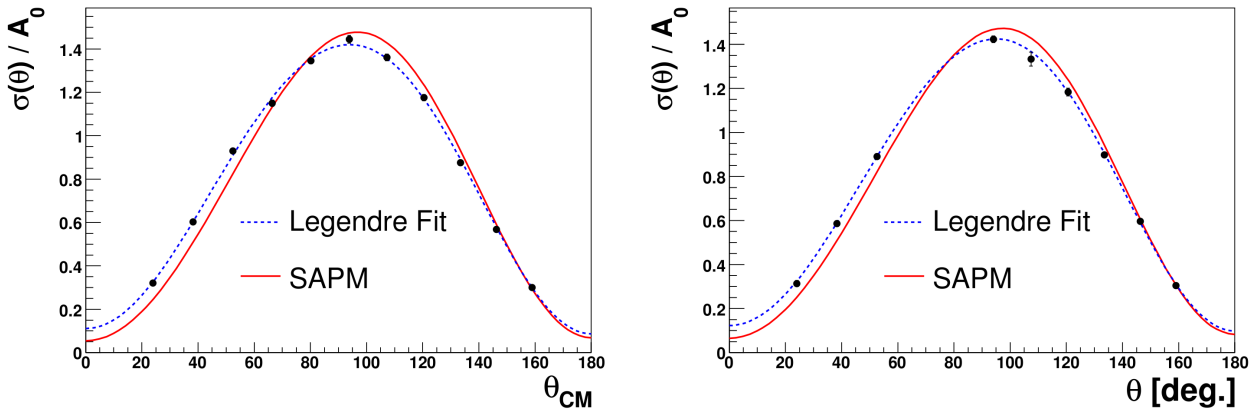

(a) 14 MeV Unpolarized Cross Section.

(b) 16 MeV Unpolarized Cross Section.

Figure 1.3: Unpolarized Differential Cross Section at 14 and 16 MeV. Notice that the experimental data (blue and black) disagrees with theory (red) at the forward scattering angles. SAPM: Schwamb-Arenhövel potential model. Image credit: Blackston *et al.* [Bla08].

The analyzing power was also computed by Blackston [Bla07]: he found good agreement with theory: figure 1.4 on the next page.

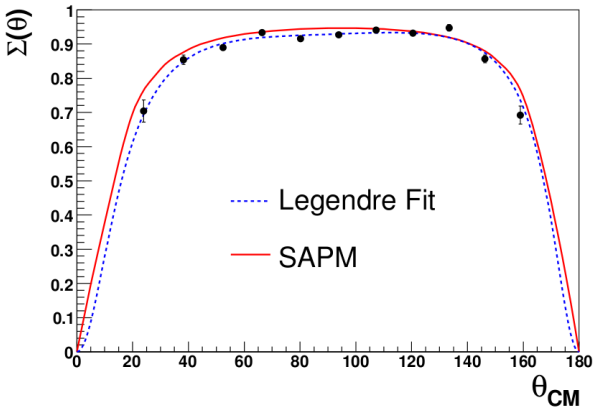

(c) 14 MeV Analyzing Power.

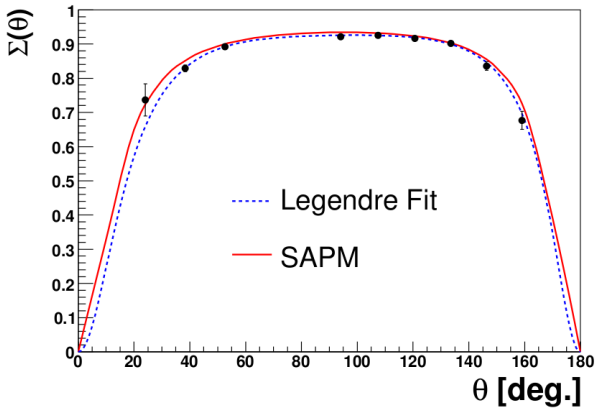

(d) 16 MeV Analyzing Power.

Figure 1.4: Analyzing Power at 14 and 16 MeV. The experimental data (blue and black) agrees well with the theoretical calculation performed by Schwamb and Arenhövel (red). SAPM: Schwamb-Arenhövel potential model. Image credit: Blackston *et al.* [Bla08].

The results of Stephenson *et al.* [Ste87] showed a discrepancy in the cross section at polar angles: $\theta = 45°, 135°$, and $155°$ when normalized to the cross section at $\theta = 90°$, Sawatzky [Saw05] also found a discrepancy with theory, but was unable to replicate Stephenson *et al.*'s results (figure 1.5 on the next page). It should be noted that it is believed that Stepheson *et al.* had an unknown photon polarization when collecting their data [Kuc10], and so it is therefore possible that their results are incorrect.[5]

[5]Stephenson *et al.* used the measured photon spectrum to calibrate their detectors, and so it is difficult (if not impossible) to determine which of their results are incorrect.

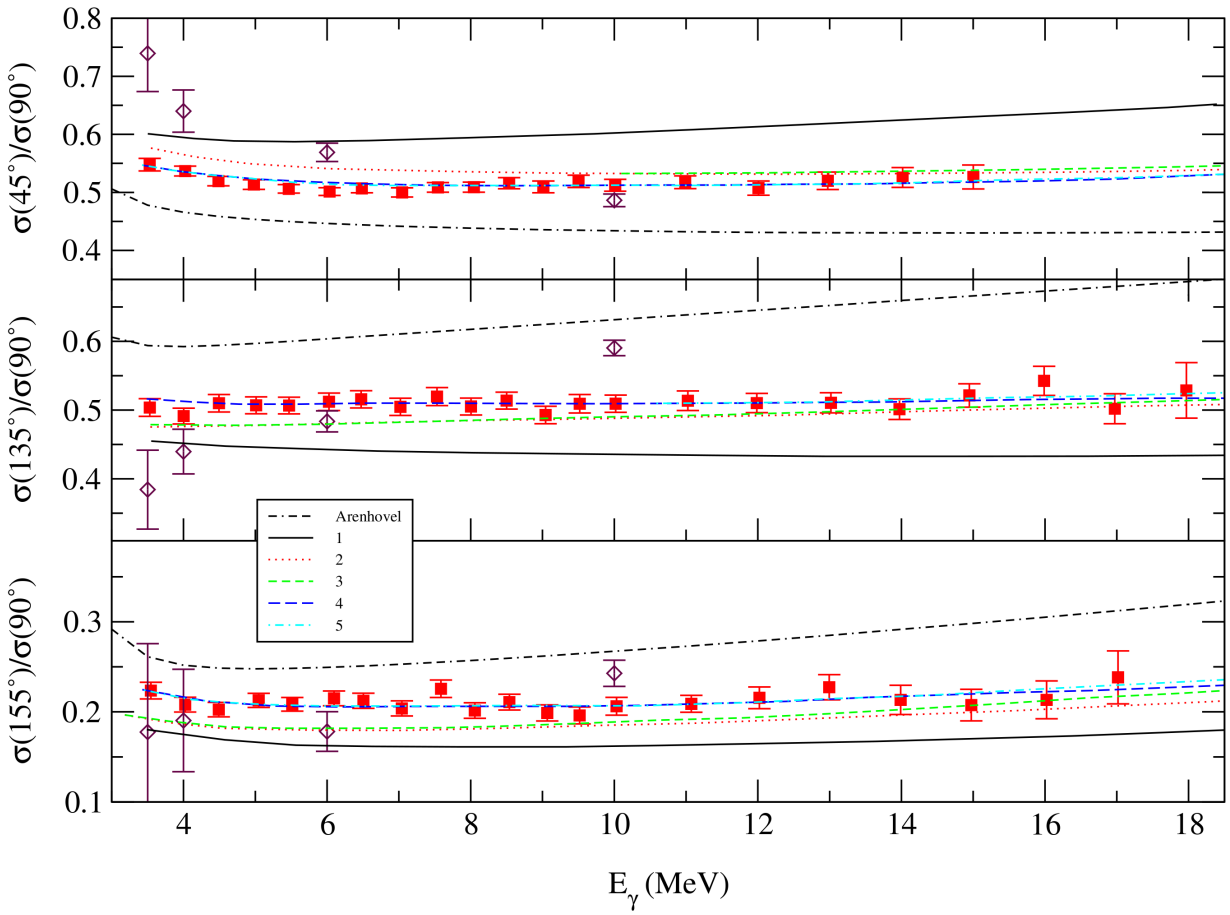

Figure 1.5: Ratio of Cross Section at Selected Neutron Lab Angles for Energy in Range: 3-18 MeV. Open diamonds: Sawatzky [Saw05], solid squares: Stephenson *et al.* [Ste87], the numbered lines are calculations performed by Hadjimichael *et al.* [Had87], and the dotted line labeled Arenhövel is an old calculation by Arenhövel *et al.* [Are00]. Arenhövel's calculations greatly overestimates the backward scattering cross section and underestimates the forward scattering cross section. Image credit: Sawatzky [Saw05].

Our results do not demonstrate the observed discrepancy with theory by Sawatzky, indicating that it may not extend to higher energies. We also failed to observe any significant discrepancy with the theoretical forward scattering probability such has been observed previously.

1.5.3 Theoretical Calculation

The theoretical calculations which we compare to were performed by Schwamb and Arenhövel [Sch01c, Sch01a, Sch01b] and include: the total cross section, the ϕ-averaged differential cross section (i.e. the unpolarized differential cross section), the analyzing power, and a number of polarized observables which we cannot make use of (because our target was not polarized). Schwamb and Arenhövel's full calculation is based on the non-relativistic Elster Potential [Sch01c]: the 1987 Bonn one-boson exchange parameterization in r-space (OPEBR) potential [Mac87] with: off-shell meson corrections, Δ baryon intermediate states, and meson retardation.

The Bonn-OPEBR potential [Mac87] is a phenomenological, non-relativistic potential which is based on single meson exchange, including the: $\pi, \omega, \delta/\mathrm{a}_0(980), \sigma, \eta$ and ρ mesons using the static limit for propagators. The mesons act as effective degrees of freedom for quantum chromodynamics at low (i.e. nuclear) energies and large ($\gtrsim$ fm) distances [Wal04]. Regulating functions of the cutoff parameters must be included in the meson exchange propagators to enable perturbation theory to be applied, these cutoffs are determined empirically by fitting to experimental data. Also derived from the experimental data are the coupling constants for each meson which represent the strength of the interaction.

The Elster Potential extends the Bonn-OPEBR above pion-threshold by including off-shell meson corrections, Δ baryon intermediate states, and meson retardation.

Schwamb and Arenhövel [Sch01c, Sch01a, Sch01b] used both the Bonn-OPEBR, and the Elster Potential to demonstrate the importance of the following contributions in deuteron photodisintegration: retarded meson exchange currents, Δ baryon intermediate states, off-shell corrections, and relativistic corrections. At 18 MeV these effects are small, and in the end we found that comparing them was impertinent given the precision of our final data: thus we compared our results only to the full calculation.

1.5.4 Outline

This thesis describes: the necessary background in chapter 2 on page 14, the experimental methodology in chapter 3 on page 51, the simulation methodology in chapter 4 on page 104,

the analysis methodology in chapter 5 on page 146, the results in chapter 6 on page 218, and ends with some concluding remarks, including a description of the sources of error, in chapter 7 on page 246. The author performed the simulation and analysis, including finalizing the results, but did not participate in the collection of the data, nor any of the background experiments.

Chapter 2

Background

2.1 The Deuteron

The deuteron is the nucleus of deuterium, it consists of a neutron and a proton together in a bound state. It is the only bound two nucleon state, and therefore it is reasonable to expect that it is the closest nucleus to a composite two-body state, and the most direct way of testing the nucleon-nucleon interaction.[1]

The deuteron has only one bound state: with a binding energy of approximately 2.226 MeV, and $l^{\pi} = 1^{+}$ (angular momentum of $l = 1$ and positive parity) [Han11]. It has also been surmised from nucleon-proton scattering experiments that the deuteron has a quasi-bound state at approximately 60 keV with angular momentum of 0. The presence of an electric quadrupole moment ($Q = 2.87500 \pm 0.00002 \cdot 10^{-27}\text{cm}^2$ [Han11]) is indicative of an $l = 2$ state, and therefore the deuteron is modeled non-relativistically as a superposition of $\approx 96\%$ ^{3}S ($l = 0$, $s = 1$) and $\approx 4\%$ ^{3}D ($l = 2$, $s = 1$) states [Han11].[2]

The bound state of the deuteron provides a good test case for nucleon-nucleon potentials [Sch89, Are91] and therefore high precision data on deuteron interactions; especially those involving the well-known electromagnetic interaction, are important for both extracting parameters for phenomenological models and testing their accuracy.

[1] In light of recent developments in nuclear condensed matter physics (e.g. Ebran *et al.*'s [Ebr12] work on ^{4}He clusters in the ^{20}Ne nucleus), one wonders if the deuteron: a collection of two weakly bound fermions, is the simplest testing ground for the nucleon-nucleon interaction, or if there is a larger nuclei which actually has fewer degrees of freedom.

[2] s: total spin quantum number.

2.2 Photodisintegration of The Deuteron

The photodisintegration of the unpolarized deuteron in the low energy region ($\lesssim$ 40 MeV) using unpolarized photons has been modeled to a high accuracy and precision for over two decades by simple one meson exchange potential models of the deuteron [Sch91, Are91], but with the important caveat that there are some conflicting experimental results near disintegration threshold ($\lesssim$ 20 MeV) [Ste87, Bir88, Saw05], which may be compensated for via the use of an *ad hoc* empirical fit of higher-order terms [Had87].

There were issues with the total cross section values up to the 1980s due to the nearly ubiquitous use of bremsstrahlung beams;[3] which are prone to systematic errors due to their dependence on theory to derive a total number of photons. These issues were smoothed out with the development of tagged bremsstrahlung,[4] and then verified by Laser Compton Scattering (LCS) beams [Ber86] and early free-electron lasers [Are91].

On the theoretical side, one pion exchange potentials were long considered an adequate description of the deuteron,[5] and it was only when calculations aspired to reach higher precision (and to describe new nuclei by incorporating multiple pions) that the need for more realistic nucleon-nucleon interactions were recognized as necessary [Mac11]. The picture circa 1990 is illustrated in the figures below: figure 2.1 on the next page for the differential cross section, and figure 2.2 on page 17 and figure 2.3 on page 18 for the total cross section.

[3]For example, Baglin *et al.* [Bag73], Whetstone and Halpern (1958) [Whe58], and Skopik *et al.* [Sko74] all underestimated the currently accepted total cross section at 18 MeV by $\approx$ 10-20% using bremsstrahlung beams.

[4]Ahrens *et al.* [Ahr74] were able to use an untagged bremsstrahlung beam to record cross sections at 15, 20, and 25 MeV which are consistent with contemporary results by comparing the relative photon attenuation of heavy water versus light water, thus eliminating their dependence on theory for photon flux.

[5]In hindsight, this is because the deuteron is a relatively large nucleus ($\approx$ 10% larger than the radius of a neutron plus a proton [Ber12]) and therefore the effective QCD field is dominated by a single exchange of the lightest mesons: the pions (because the potential is $\propto e^{-m_s r}$) [Won94].

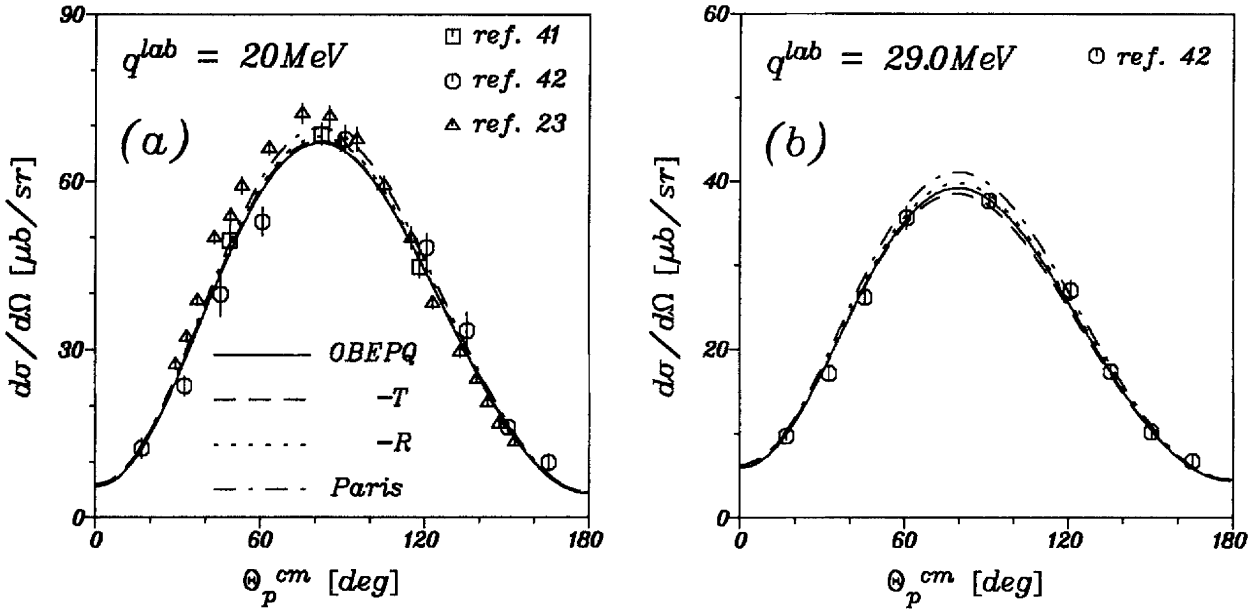

Figure 2.1: Unpolarized Differential Cross Section at 20 and 29 MeV. Where: q^{lab} is the lab energy (equal to the photon energy), and θ^{CM} is the center-of-mass/momentum polar angle. The different lines represent the potential used: OBEPQ, -T and -R are based on the Bonn potential [Mac87], and Paris is the Paris potential [Lac81]. The references are: 23: Skopik *et al.* [Sko74], 41: Fink *et al.* (1989), 42: De Pascale *et al.* (1985). Reference 23 is skewed in favour of small theta, and 42 is skewed in favour of large theta. No substantial discrepancy is observed. Image credit: Schmitt *et al.* [Sch91].

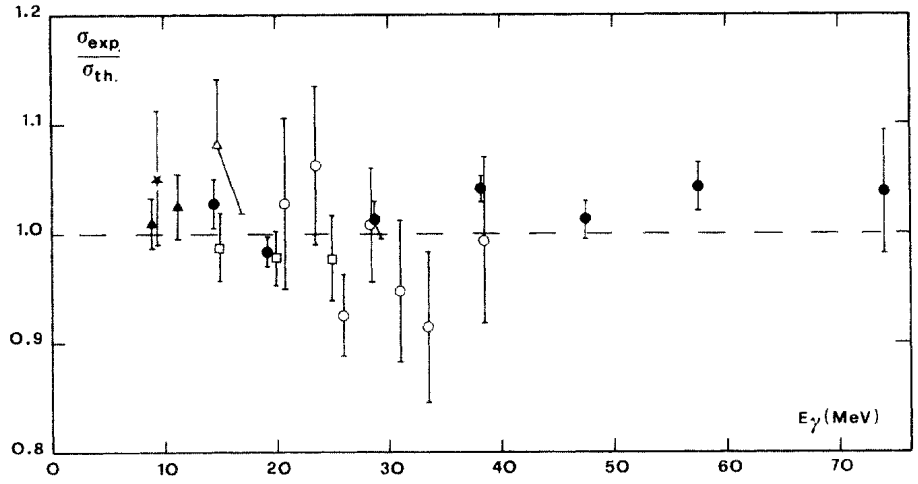

Figure 2.2: Comparison of Total Cross Section to Theory for Deuteron Photodisintegration from 0 to 75 MeV. The theoretical cross section was calculated using the Paris potential. Open squares: Bernabie *et al.* [Ber86] (laser Compton scattering beam), filled triangles: Ahrens *et al.* [Ahr74] (photon model independent bremsstrahlung beam), open circles: Birenbaum *et al.* (1985; neutron capture sources), open triangles: Bosman *et al.* (1979; inverse reaction), open triangles: Stiehler *et al.* (1985; inverse reaction), and stars: Tudoric-Ghemo (1967; inverse reaction). Bremsstrahlung experiments have been tactfully excluded (except Ahrens *et al.*) as there are substantial discrepancies between bremsstrahlung experiments. No substantial discrepancy is observed. Image credit: Bernabei *et al.* [Ber86].

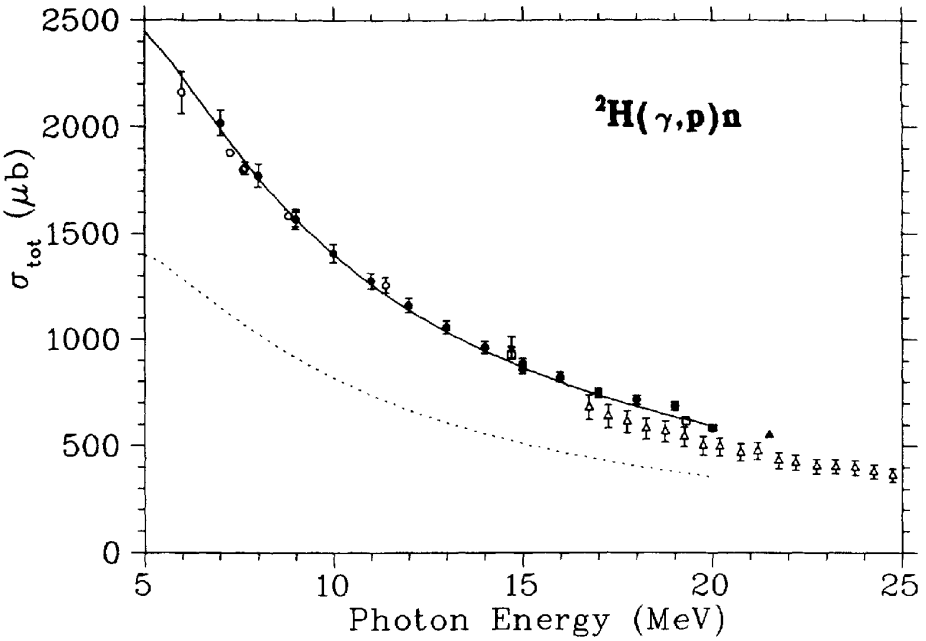

Figure 2.3: The Total Cross Section for Deuteron Photodisintegration from 5 to 25 MeV. The theoretical cross section (solid line) was calculated using the Paris potential. The dissenting data set (open triangles) are from Baglin *et al.* [Bag73], and were taken using an untagged bremsstrahlung beam. Closed circles: De Graeve *et al.* [DGr92] (tagged bremsstrahlung), open circle: Birenbaum *et al.* (1985; neutron capture sources), open triangles: Baglin *et al.* [Bag73] (bremsstrahlung), closed squares: Ahrens *et al.* [Ahr74] (photon model independent bremsstrahlung beam), closed triangles: Wauters *et al.* (1990; inverse reaction), open squares: Bernabie *et al.* [Ber86] (laser Compton scattering beam), and stars: Stiehler *et al.* (1985; inverse reaction). The dotted line is the "historical" value: the first deuteron photodisintegration prediction, calculated by Bethe and Peierls [Bet35]. Image credit: De Graeve *et al.* [DGr92].

The purported agreement between experiment and theory by: Schmitt *et al.* [Sch91] (figure 2.1 on page 16), Bernabei *et al.* [Ber86] (figure 2.2 on page 17), and De Graeve *et al.* [DGr92] (figure 2.3), was not without its detractors. Stephenson *et al.* [Ste87] offered a novel experimental technique: three bremsstrahlung radiators at three different angles and recorded by three detectors at three different angles. Their results disagree with then contemporary calculations done by Partovi (by a scaling factor), and also disagree both in

shape and magnitude with Arenhövel's calculation in 2000 [Are00] (figure 2.4 on the next page): which is similar to Schwamb and Arenhövel's calculation [Sch01c, Sch01a, Sch01b]. Hadjimichael *et al.* [Had87] rectified the discrepancy between theory and Stephenson *et al.*'s results by fitting the higher order parameters in their Legendre expansion of the differential cross section to Stephenson *et al.*'s results.

Birenbaum *et al.* [Bir88] followed up and performed differential cross section measurements between 6 and 9 MeV using various radioactive sources but were unable to fully replicate Stephenson *et al.*'s results (in particular at $\theta = 45°$), although their results also did not agree well with the calculations by Partovi nor recent calculations by Arenhövel (figure 2.4 on the next page). The discrepancy between Stephenson *et al.* and Birenbaum *et al.* may have been due to the systematic error which Stepheson *et al.* later discovered in their data: the bremsstrahlung beams were producing polarization from $\approx 25\%$ at 3.5 MeV to $\approx 0\%$ at 18 MeV [Kuc10]; because the partial polarization affected the detector calibration, this means that their results are not reliable at any energy.

Motivated by ambiguities in the few experimental data which were available at low energies, Sawatzky [Saw05] used the Blowfish detector array at the HI$\vec{\gamma}$S facility to measure the photodisintegration of the deuteron using: 3.5, 4, 6, and 10 MeV linearly polarized photons. His results (figure 2.4 on the next page and figure 2.5 on page 21) agree with Birenbaum *et al.*'s but disagree with Stephenson *et al.*'s (especially at $\theta = 45°$), possibly due to the systematic polarization in Stephenson *et al.*'s data.

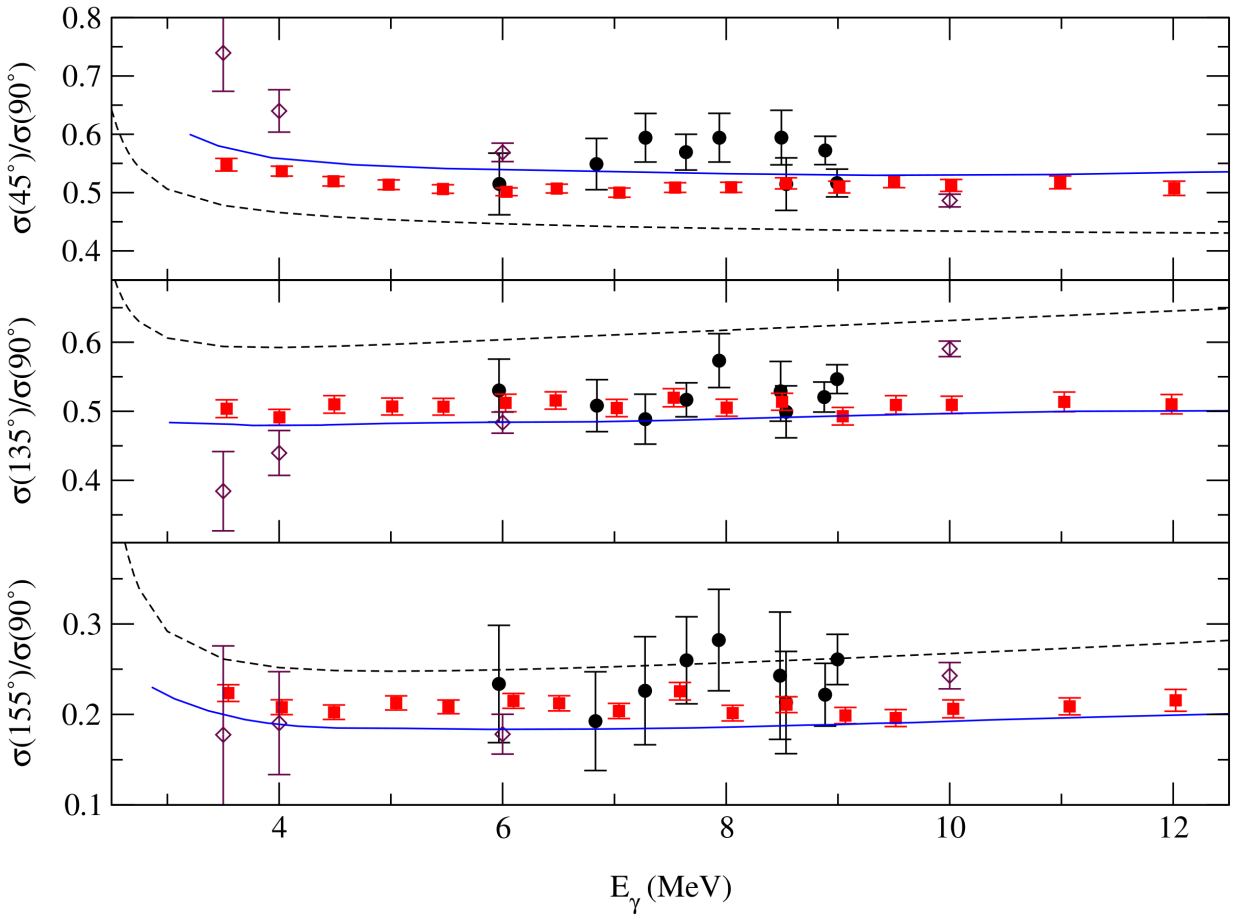

Figure 2.4: Ratio of Cross Section at Selected Neutron Lab Angles for Energy in Range: 3-12 MeV. Open diamonds: Sawatzky [Saw05], solid squares: Stephenson *et al.* [Ste87], solid circles: Birenbaum *et al.* [Bir88], blue line: indistinguishable theoretical calculations by Partovi [Par64] and Wiringa *et al.* [Wir84], dotted line: an earlier theoretical calculation by Arenhövel *et al.* [Are00]. Arenhövel's calculation clearly overestimates the backward scattering angles ($\theta > 90°$) or underestimates the forward scattering ($\theta < 90°$). Image credit: Sawatzky [Saw05].

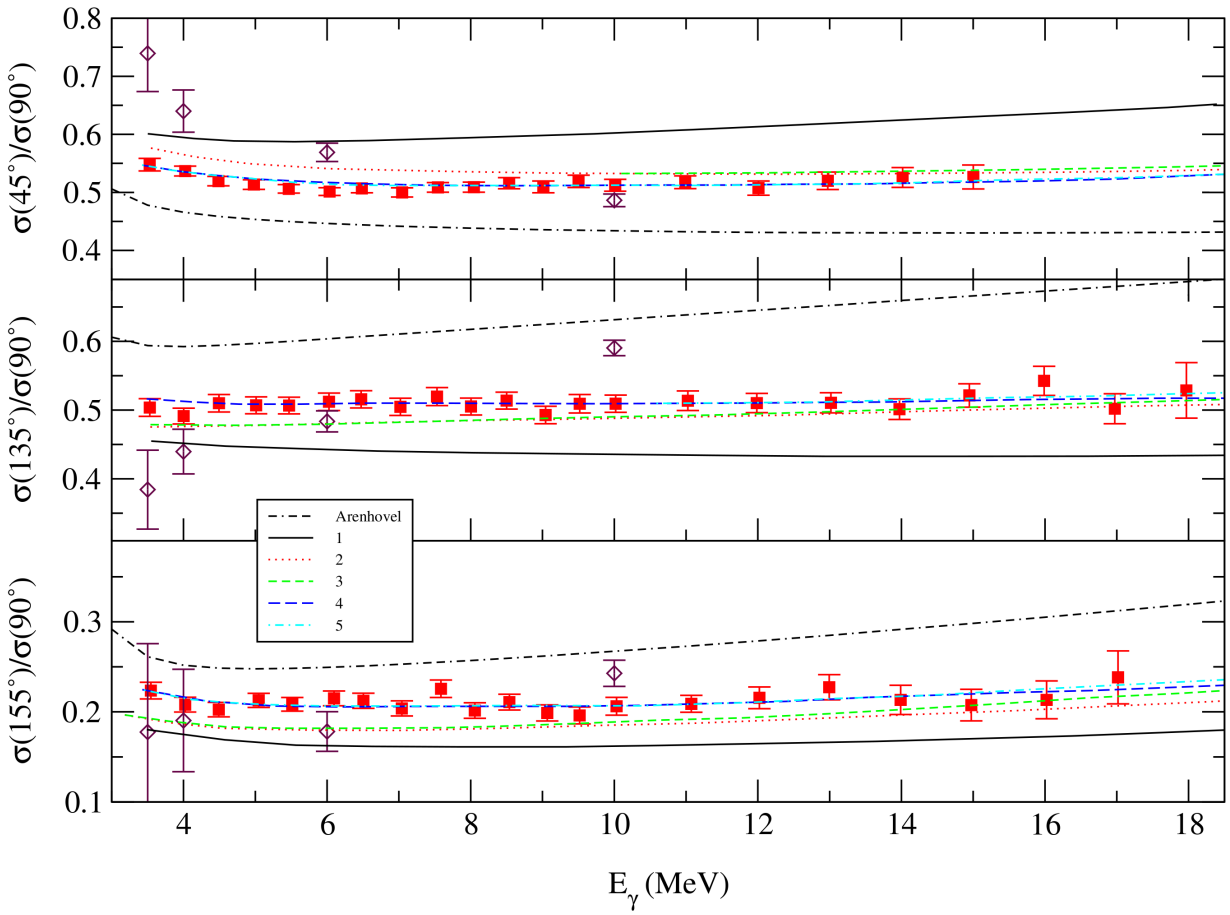

Figure 2.5: Ratio of Cross Section at Selected Neutron Lab Angles for Energy in Range: 3-18 MeV. Open diamonds: Sawatzky [Saw05], solid squares: Stephenson *et al.* [Ste87], the numbered lines are calculations performed by Hadjimichael *et al.* [Had87], and the dotted line labeled Arenhövel is an old calculation by Arenhövel *et al.* [Are00]. Arenhövel's calculation clearly overestimates the backward scattering angles ($\theta > 90°$) or underestimates the forward scattering ($\theta < 90°$). Image credit: Sawatzky [Saw05].

Subsequent research at HI$\vec{\gamma}$S using Blowfish has yielded similar results: Blackston [Bla07] used linearly polarized 14 and 16 MeV photons and found a forward scattering disagreement with Schwamb and Arenhövel's calculation similar to what Sawatzky observed [Saw05] (figure 2.6 on the next page). Since then, Kucuker [Kuc10] used circularly polarized photons

at 20 MeV but her results have an unaddressed inconsistency concerning results taken using different target lengths, and so are not discussed here.

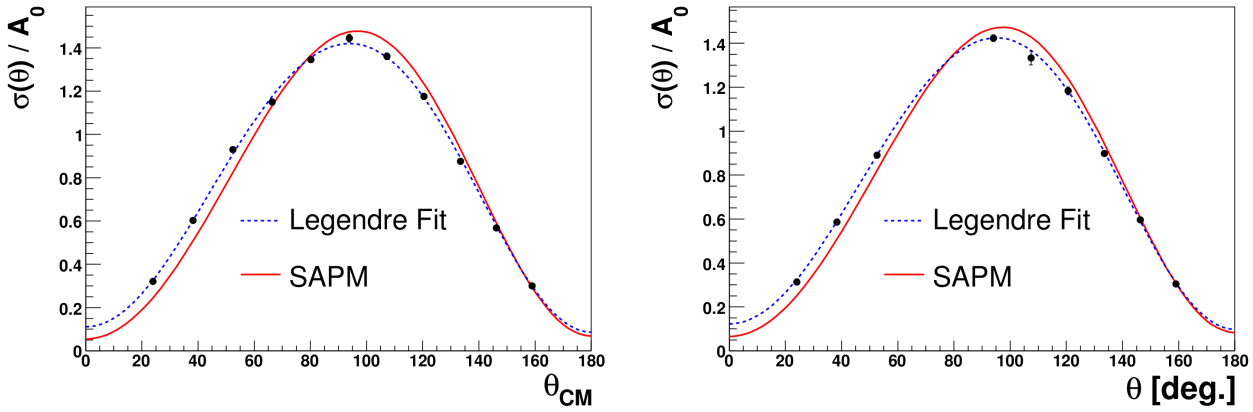

(a) 14 MeV Unpolarized Cross Section.

(b) 16 MeV Unpolarized Cross Section.

Figure 2.6: Unpolarized Differential Cross Section at 14 and 16 MeV. Notice that the experimental data (blue and black) disagrees with theory (red) at the forward scattering angles, this is consistent with Sawatzky's [Saw05] results. SAPM: Schwamb-Arenhövel potential model. Image credit: Blackston *et al.* [Bla08].

Both Sawatzky [Saw05], and Blackston [Bla07] used the same methodology, detector (Blowfish), and beam (HI$\vec{\gamma}$S), and found a similar discrepancy with theory: that the forward neutron yield is higher than theory and the backward neutron yield is lower than theory. Given the nearly identical setup of their experiments, it is *possible* that this discrepancy is due to a mutual systematic error, rather than a failure of the theoretical calculation.

The fundamental problem with testing the theoretical predictions for deuteron photodisintegration is that the experimental results do not agree well with each other and therefore the theorists are free to surmise which results to keep and which to throw away; not surprisingly this results in a very agreeable fit of selected data to their personal calculations. The reason for a lack of experimental consensus almost assuredly is due to the presence or absence of certain systematic errors. This was starkly demonstrated by Rossi *et al.* [Ros89] when they compared the total cross section data for deuteron photodisintegration with untagged bremsstrahlung sources versus "monochromatic" sources: the former show abject

disagreement with each other in the energy region ≈ 100-300 MeV while the latter show excellent agreement; Rossi *et al.* were even able to fit a simple phenomenological function to the "monochromatic" sources.

The solution is to replace old bremsstrahlung data with new, precise experimental data *with realistic error estimates*, especially where all models are known to struggle: at high energies, at extreme scattering angles, and using polarized observables. This experiment will: add data to the relatively sparse low energy region of polarized deuteron photodisintegration, test for inconsistencies in the differential cross section (such as those demonstrated at lower energies), and hopefully enable future high precision polarization measurements using Blowfish (e.g. fulfilling the original purpose of Blowfish by testing the Gerasimov-Drell-Hearn Sum Rule [Saw05, Bla07, Kuc10]).

2.3 Kinematics

In this experiment, the 18 MeV beam is below pion-threshold and so we assume that the process is elastic and two-body: a photon strikes a deuteron target producing a recoiling proton and an ejectile neutron. In this section we present the pertinent kinematic results, the calculation itself can be found in appendix C on page 284.

Assumptions:

1. The collision is elastic: i.e. the ejectile neutron and recoil proton are unbound and in their ground states, with $E_\gamma + E_D = E_n + E_p$.

2. The collision occurs in the xy-plane: this is purely for convenience sake since the z-axis is independent of the x and y coordinates and therefore can always be chosen to be perpendicular to the reaction plane.

3. The electron plays no role in the interaction: it is not accounted for in the mass of the deuteron target, and it is not accounted for in the mass of the recoil proton.

The kinematics for this experiment are summarized by eq. (2.1) on the next page.

Kinematics summary:

$$
\begin{aligned}
\beta &= \frac{E_\gamma}{E_\gamma + m_D c^2} \approx 0.0095 \text{ (for } E_\gamma = 18 \text{ MeV)} \\
E'_\gamma &= \gamma E_\gamma (1 - \beta) \\
E'_D &= \gamma m_D c^2 \\
E' &= E'_\gamma + E'_D \\
p'_n &= \frac{1}{c}\sqrt{(\frac{E'^2 + (m_p^2 - m_n^2)c^4}{2E'})^2 - m_p^2 c^4} \\
\mathbf{p}_n &= \begin{bmatrix} \frac{\gamma}{c}E'_n + \beta\gamma p'_n \cos\theta' \\ \frac{\gamma}{c}\beta E'_n + \gamma p'_n \cos\theta' \\ p'_n \sin\theta' \\ 0 \end{bmatrix} = \begin{bmatrix} \frac{E_n}{c} \\ p_{n,x} \\ p_{n,y} \\ 0 \end{bmatrix} \\
\theta &= \arctan\left(\frac{p_{n,y}}{p_{n,x}}\right) \\
E_n &= \sqrt{p_n^2 c^2 + m_n^2 c^4}
\end{aligned}
\tag{2.1}
$$

where: the primed variables are in the CM frame, the unprimed variables are in the lab frame, β is the CM frame velocity divided by c, E is the energy, p is the momentum, m is the mass, θ is the scattering angle, and the subscripts are: γ: photon, D: deuteron and n: neutron.

Notice that the momentum (and therefore energy) of the ejectile neutron depends only on: the beam energy (E_γ), the polar angle (θ), and known physical constants (see eq. (2.1)). Since we know the beam energy, the location of our detectors, and all of the physical constants: we can predict the energies for prompt neutrons in our detectors. This is the motivation for the time-of-flight cut: we know when the neutrons will arrive so we can simply ignore everything which arrives at an incompatible time (see section 5.4.4 on page 204 for details).

The kinematics calculated here were used for the simulation and the time-of-flight cut.

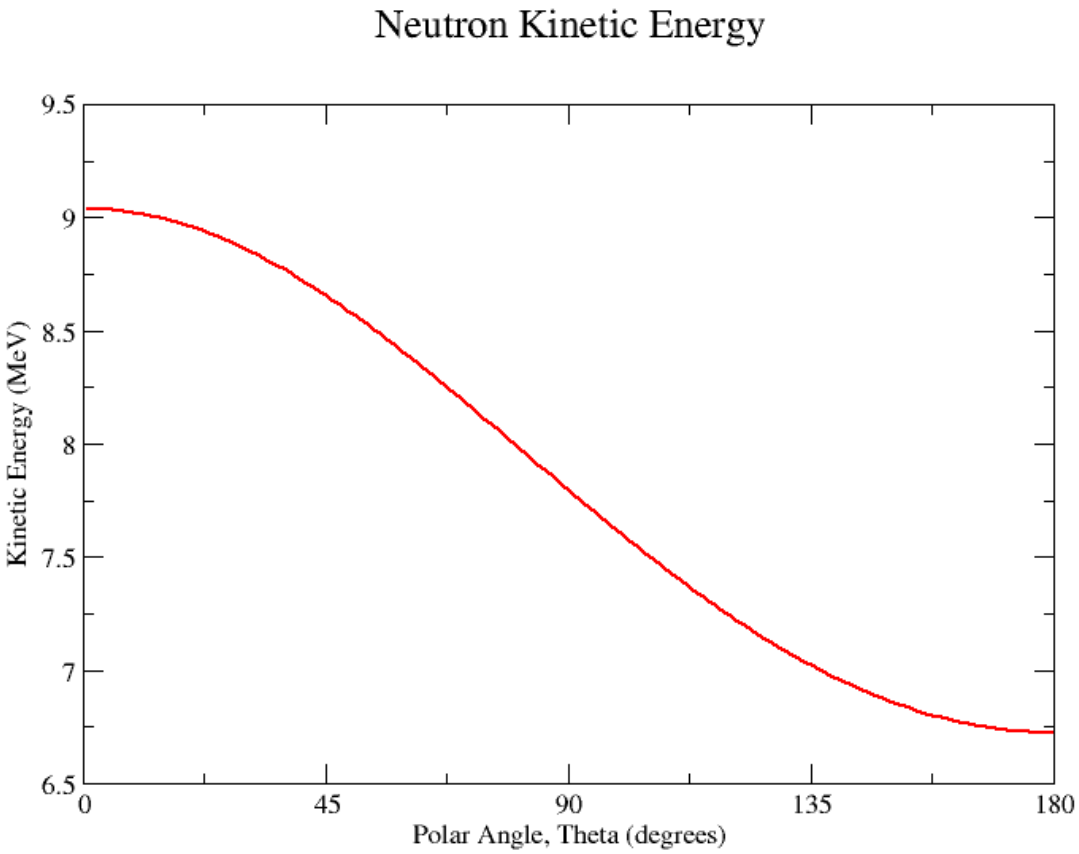

Figure 2.7: The neutron kinetic energy in the lab frame has been plotted using the kinematic relations derived in this section. Photon energy: 18 MeV.

Figure 2.7 illustrates the polar angle (θ) dependence of the ejectile neutron's energy.

2.4 Interactions of Particles with Matter

Detection is the fundamental goal of any experiment and; unless one wishes to be at the mercy of blind luck, the construction of an effective (and hopefully efficient) detector depends on a functional understanding of the measurability of the particular phenomenon being investigated. This experiment measured the spatial location and intensity of neutrons and photons: i.e. we measured particles, therefore it is appropriate to briefly describe how particles interact

with detectors i.e. matter.

We can quantitatively predict a detector's response using available theory, models, and measurements to describe the energy deposition i.e. $\frac{dE}{dx}$ and the relative probability of an interaction to occur i.e. cross sections. The energy deposition rate ($\frac{dE}{dx}$) is indicative of the type of particle incident, thus if our detector response is *proportional* to the energy deposition (see figure 2.8) then we can differentiate between particle types based on the detector response: this is the fundamental principle behind pulse-shape discrimination (section 5.3.9 on page 184).

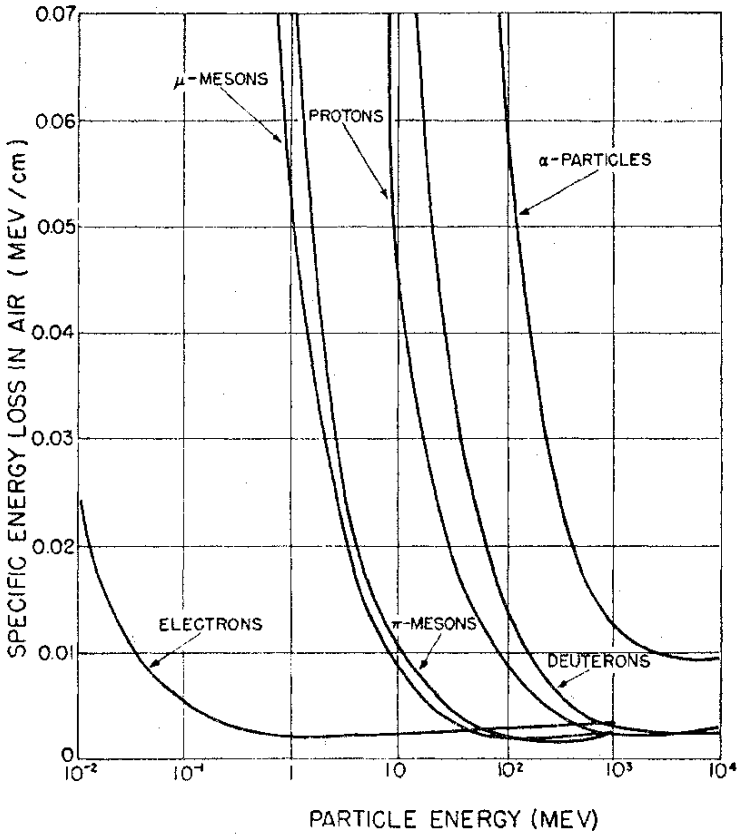

Figure 2.8: Energy loss ($-\frac{dE}{dx}$) of common particles in air. Energy deposition is clearly dependent on the particle, unless it is relativistic in which case the energy deposition is roughly constant (so called "minimum ionizing particles"). Image credit: Beiser [Bei52].

The probability for an interaction to occur is given by the cross section, which is defined

empirically as the probabilistically weighted area that a target occupies:

$$\frac{dN_D}{dx} = \sigma \rho n N \tag{2.2}$$

where: N_D is the number of daughter particles produced by an interaction, N is the number of incident particles at position x, σ is the reaction cross section as defined by this equation (cm^2/atom), ρ is the target mass density (g/cm^3), and n is the target number density (atoms/g).

Eq. (2.2) can be be used either to compute the number of products in a nuclear reaction (eq. (2.4)), or by substituting $dN_D \rightarrow -dN$ it yields the attenuation of an incident beam (eq. (2.3)); these equations hold probabilistically for a single particle.

Solving eq. (2.2) for the case where the parent and daughter are the same particle (i.e. $dN_D \rightarrow -dN$) yields the probability of penetration:

$$P = \frac{N}{N_0} = e^{-\mu x} \tag{2.3}$$

where: P is the probability of a particle reaching a position x without interacting, N_0 is the number of incident particles, N is the number of particles at position x, and $\mu \equiv \sigma \rho n$: σ is the total cross section for all reactions, ρ is mass density, and n is the number density [Pat11].

Alternatively, solving eq. (2.2) directly, by using eq. (2.3) to set $N = N_0 e^{-\mu x}$, yields the expected number of daughter products produced:

$$N_D = \frac{\sigma \rho n}{\mu} \cdot N_0 (1 - e^{-\mu x}) \tag{2.4}$$

where: N_D is the number of daughter particles produced by an interaction, x is the longitudinal position, N_0 is the number of particles incident at position $x = 0$, σ is the reaction cross section as defined by this equation (cm^2/atom), ρ is mass density (g/cm^3), and n is the number density (atoms/g).

Finally, using the variation of eq. (2.3): $N = N_0 e^{-\mu x}$, we can calculate the average

interaction point:

$$
\begin{aligned}
N &= N_0 e^{-\mu x} \\
P &= \frac{N}{N_0} = e^{-\mu x} \\
x &= -\frac{\ln(P)}{\mu} \\
\langle x \rangle &\equiv -\frac{\int_{x=0}^{x=l} \frac{\ln(P)}{\mu} dP}{\int_{x=0}^{x=l} dP} \\
\langle x \rangle &= \frac{1}{\mu} - \frac{l e^{-\mu l}}{1 - e^{-\mu l}}
\end{aligned}
\tag{2.5}
$$

where: μ is the linear attenuation coefficient, $\langle x \rangle$ is the average interaction location, and l is the target length.

A full discussion of the detection principles used in this experiment is presented in section 3.8 on page 73, thus it suffices to simply outline how the particles of interest in this experiment (MeV energy: photons and neutrons) interact with the material types present in the detectors used; this is covered in appendix A on page 278 (photons), and appendix B on page 282 (neutrons).

2.5 Theoretical Calculations

2.5.1 The Nucleon-Nucleon Interaction

"*In the past quarter century physicists have devoted a huge amount of experimentation and mental labour to this problem (the nucleon-nucleon interaction) probably more man hours than have been given to any other scientific question in the history of mankind.*"

H.A Bethe (1953) [Ari01]

When Bethe remarked about the intensive research being put into the nucleon-nucleon (NN) interaction, theoretical nuclear physics was at an impasse. The one pion exchange models first proposed by Yukawa in 1935; which had been successful in predicting NN scattering and deuteron binding [Mac11], proved to show severe signs of incompleteness at sufficiently

small nucleon separations.[6]

Taketani, Nakamura, and Sasaki provided a circumspect framework for the NN interaction in 1951; they identified three distinct regions in the binding of two nucleons which have persisted as useful distinctions [Mac87]:

Regions of Nucleon-Nucleon Binding

1. The *classical* region ($\gtrsim 2$ fm) where pion exchange dominates. Single pion exchange is still believed to be the dominant process in this region.

2. The *dynamical* region ($\approx$ 1-2 fm) where two pion exchange dominates. Contemporary models include multi-pion exchange (i.e. > 2) and some heavy meson exchange in this region as well.

3. The *phenomenological* region ($\lesssim 1$ fm). Since the acceptance of the quark-based Standard Model: quarks and gluons have been recognized as the fundamental degrees of freedom in the sub-nuclear regime which can be approximated in the nuclear regime by an effective field theory using multiple pion and heavy meson exchange.

The then inexplicable behaviour of NN binding in the phenomenological region was rescued by the discovery of heavy mesons in the 1960s, after which one boson exchange (OBE) models began to dominate [Mac87]. One boson exchange models have shown good agreement with empirical data for the deuteron at low energies (i.e. below pion-threshold) [Are91]. Skipping over the brief foray into dispersion relation potentials in the 1970s (e.g. the Paris potential), the acceptance of QCD in the 1980s inspired open speculation that mesons represented the effective degrees of freedom of the quarks inside nucleons [Mac87, Els88a] based on an essay by Weinberg [Wei79]; given in honour of Julian Schwinger's 60^{th} birthday in 1979, when he remarked:

"...one might imagine weakening the forces of QCD by introducing some sort of infrared cut-off, λ, and preserving the physical content of the theory by introducing the bound states

[6]For example, Brueckner and Watson demonstrated that if the nucleons get sufficiently close together then perturbation theory cannot be applied using pion exchange because the expansion of the potential diverges [Mac87].

of the theory as fictitious elementary particles. These bound states are just the ordinary hadrons, and they must be described by a chiral-invariant phenomenological Lagrangian."
Weinberg [Wei79]

"...if one writes down the most general possible Lagrangian, including all terms consistent with assumed symmetry principles, and then calculates the matrix elements with this Lagrangian to any given order of perturbation theory, the result will simply be the most general possible S matrix consistent with analyticity, perturbative unitarity, cluster decomposition, and the assumed symmetry principles." Weinberg [Wei79]

Weinberg's essay was used by others to conjecture the physical meaning of empirically fit cutoff parameters and coupling constants; the former were needed to enable the use of perturbative expansions in meson exchange models [Mac87, Els88a, Sch01c]. The 1980s also saw an increase in theoretical precision, for example: the inclusion of retarded meson propagators,[7] and off-shell corrections to the effective mass [Mac87, Els88a, Sch01c]. Weinberg eventually proved his conjecture over a decade later in 1990 [Wal04]: mesons are the effective degrees of freedom for nucleon binding *so long as the symmetries of QCD are appropriately preserved or broken* [Mac11].

The seminal work of Weinberg provided the theoretical bases for chiral effective field theories describing the NN interaction (for a review see Machleidt and Entem [Mac11]). These effective field theories use meson exchange, but constrained by chiral symmetry [Mac11].

Metaphorically speaking, it is a well known (though rarely acknowledged) fact that scientific theories and models obey Newton's first law of motion; theories being nominally relegated to models when acted upon by contradicting evidence: low energy theoretical nuclear physics will not advance beyond phenomenological one boson exchange potentials from the 1980s until a significant discrepancy with experiment is observed. This experiment tests a calculation performed by Schwamb and Arenhövel [Sch01c, Sch01a, Sch01b] based on two modernized phenomenological one meson exchange potential models: one based on the 1987 Bonn-OBEPR[8] [Mac87], and the other based on the Elster potential [Els88b, Els89]. An

[7] A retarded propagator accounts for the finite travel time of information.
[8] OBEPR: One Boson Exchange Parameterization in R(position)-space

inconsistency in Schwamb and Arenhövel's calculation below pion-threshold would be a blow to phenomenological one boson exchange potentials, and would help to inspire more rigorous calculations (such as those using an effective field theory).

2.5.2 Meson Exchange Potentials

Nucleon-nucleon (NN) interactions began being modeled via the exchange of mesons beginning with Yukawa's seminal paper in 1935 [Mac87] which modeled the nuclear force as the exchange of a then unknown massive scalar meson: the Yukawa potential. The Yukawa potential is derived from the scalar boson interaction Lagrangian:

$$\mathcal{L} = g_s \bar{\psi} \psi \phi \tag{2.6}$$

where: g_s is a coupling constant, $\bar{\psi}$ and ψ are fermion fields (e.g. nucleons), and ϕ is a scalar boson (e.g. a σ meson). In this section, "God-given units" (i.e. $\hbar = c = 1$) [Pes95] are particularly convenient and so they are used exclusively.

One can infer the non-relativistic potential by computing the S matrix for an arbitrary process involving two fermions using the Lagrangian (eq. (2.6)), and then infer an effective potential; then Fourier transform the effective potential into position-space (this is done in appendix A of Walecka [Wal04]). The effective Yukawa potential (see table 2.1 on the next page) can then be solved non-relativistically using the Schrödinger equation as a simple model for the NN interaction.

Yukawa's work has since been generalized to include vector, pseudoscalar, and pseudovector fields: these are summarized in table 2.1 on the next page [Wal04]. The basic concept remains the same: model the NN interaction using the exchange of mesons.

Exchange Particle Type	$\mathcal{L}$	$V_{effective}$
Isoscalar Scalar	$g_s\bar{\psi}\psi\phi$	$-\frac{g_s^2}{4\pi}\frac{e^{-m_s r}}{r}$
Isoscalar Vector	$ig_\nu\bar{\psi}\gamma_\mu\psi\omega_\mu$	$\frac{g_\nu^2}{4\pi}\frac{e^{-m_\nu r}}{r}$
Isovector Vector	$ig_\rho\bar{\psi}\gamma_\mu\frac{1}{2}\vec{\tau}\psi\cdot\vec{\rho}_\mu$	$\frac{g_\rho^2}{16\pi}\vec{\tau}_1\cdot\vec{\tau}_2\frac{e^{-m_\rho r}}{r}$
Isovector Pseudoscalar	$ig_\pi\bar{\psi}\gamma_5\vec{\tau}\psi\cdot\vec{\pi}$	$\frac{g_\pi^2}{4\pi}\left(\frac{m_\pi}{2M}\right)^2\frac{1}{3}\vec{\tau}_1\cdot\vec{\tau}_2$ $\left(\vec{\sigma}_1\cdot\vec{\sigma}_2+S_{12}\left[1+\frac{3}{m_\pi r}+\frac{3}{(m_\pi r)^2}\right]\right)\frac{e^{-m_\pi r}}{r}$

Table 2.1: Nucleon-Nucleon Lagrangians and Effective Potentials [Wal04]. Where: $\mathcal{L}$ is the Lagrangian, $V_{effective}$ is the non-relativistic effective potential associated with the Lagrangian, the g are coupling constants, $\vec{\tau}$ are the isospin matrices, $\vec{\sigma}$ are the Pauli spin matrices, m_α is the mass for a particle of type α, γ_μ are the Dirac matrices ($0 \leq \mu \leq 5$), $S_{12} \equiv \frac{3(\vec{\sigma}_1\cdot\vec{r})(\vec{\sigma}_2\cdot\vec{r})}{r^2} - \vec{\sigma}_1\cdot\vec{\sigma}_2$, $\vec{r}$ is the radial vector, $i = \sqrt{-1}$, M is the nucleon's mass, $\bar{\psi}$ and ψ are fermion fields (e.g. nucleons), ϕ is a scalar boson field (e.g. a σ meson), ω is a vector boson field (e.g. an omega meson), $\vec{\rho}$ is an isovector vector boson field (e.g. a rho meson), and $\vec{\pi}$ is an isovector pseudoscalar boson field (e.g. a pion).

The fundamental problem associated with one boson exchange Lagrangians is that they are not conducive to perturbative expansion. Although some quantum mechanical potentials can be solved exactly, many of them cannot be [Dic12], and thus developing the necessary tools to perform perturbative expansions is desirable. In order to perform perturbation theory, one must derive a sum of terms with decreasing magnitude, then the sum can be truncated to some desired level of precision. In QED the perturbative expansion is naturally regulated by the fine structure constant ($\alpha \approx \frac{1}{137}$), but the underlying theory of the NN interaction (QCD) contains momentum dependent coupling; worse yet, the coupling in QCD *increases* with increasing distance [Gri87] (so QCD coupling is > 1 in the nuclear regime).

Meson exchange models tackle this problem by introducing form factors at all meson-nucleon vertices representing the unknown underlying quark dynamics (illustrated in figure 2.9 on the next page), and introducing a counter term (i.e. cutoff) to the coupling constant so that perturbation theory can be applied [Mac87, Els88a, Sch01c].

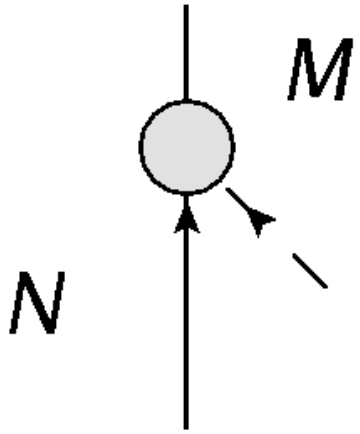

Figure 2.9: A Meson-Nucleon Vertex. A meson, M, interacts with a nucleon, N via some unknown quark-gluon process (grey circle). One boson exchange models insert a form factor at the grey circle.

The form factor may be incorporated in the propagator: e.g. by replacing the typical meson propagator to one with a cutoff, λ: $\frac{1}{q^2+m^2} \rightarrow \frac{1}{q^2+m^2}\frac{\lambda^2}{q^2+\lambda^2}$ [Bry72, Nag75], or by inserting a form factor at the vertex which contains a cutoff: e.g. $F(\mathbf{p}-\mathbf{q}) = \frac{\lambda^2}{\lambda^2+(\mathbf{p}-\mathbf{q})^2}$ [Ger71, Nag75] ($\mathbf{p}$ and $\mathbf{q}$ are momenta). This cutoff; λ, represents the scale at which the meson approximation fails and the quark-gluon interaction takes over, and consequently all meson exchange models must include it in one form or another (even effective field theories). The value of the cutoff, λ, is expected to be on the scale of the nucleon mass (i.e. $\approx$ 1-2 GeV) and must be extracted from empirical data.

The presence of cutoffs is expected based on the assumption that QCD is the underlying theory which governs the NN interaction, but it should be noted that the values are derived by fitting to the empirical data, rather than being based on some specific physical observation (e.g. like the charge). This means that different physical processes used to extract the same cutoffs may produce different results; even if the physical processes are very similar. For example, the pion-nucleon-nucleon form factor must have different cutoff parameters for elastic versus inelastic nucleon-nucleon scattering [Kuk01]. This has provided fodder for criticism of the use of modeling the NN interaction with mesons.[9] Though the most common criticism has always been the inclusion of mesons who's existence is questioned (i.e. the scalar-isoscalar σ/ϵ meson [Mac11]), or the equivalent use of resonant multi-pion exchanges (e.g. both are used in versions of the Bonn potential [Mac87]).

The best criticisms of one boson exchange models are provided by empirical data; thus

[9]Kukulin *et al.* [Kuk01] contains a brief review of criticisms of short range one boson exchange models.

high precision experiments, especially those above pion-threshold or utilizing polarized observables, will provide or eliminate the impetus for increasingly *ab initio* theoretical nuclear calculations.

2.5.3 The Schwamb and Arenhövel Model

In 1989 Schmitt and Arenhövel [Sch89] performed calculations of sub pion-threshold photodisintegration of the deuteron in order to test three versions of the 1987 Bonn potential [Mac87]: the OBEPQ,[10] OBEPT,[11] and OBEPR:[12] these are meson exchange parameterizations based on the "full" Bonn potential [Mac87]. Arenhövel has since returned to the problem with Schwamb [Sch01b] by incorporating full meson retardation effects (Schmitt and Arenhövel [Sch89] used only leading-order retardation corrections) and extending the calculations above pion-threshold by using a different potential: the Elster potential [Sch01c].

Schwamb and Arenhövel have also generalized a set of transformation operators to incorporate missing meson retardation corrections into both the T matrix and the NN potential up to the two pion threshold ($\approx$ 270 MeV) [Sch01c];[13] and used these generalizations to calculate a generalized effective current for electromagnetic reactions involving the deuteron [Sch01a].

The Elster and Bonn-OPEBR Potentials

Schwamb and Arenhövel performed calculations using two different one boson exchange potentials: the Bonn-OPEBR and the Elster potential [Sch01c, Sch01b]. These potentials are phenomenological one meson exchange potentials which use: $\pi, \omega, \delta/\mathrm{a}_0(980), \sigma, \eta$ and ρ meson exchange fitted with empirical coupling constants and cutoff parameters.

The Full Bonn potential [Mac87] is a relativistic model for the nucleon-nucleon interaction using $\pi, \omega, \delta/\mathrm{a}_0(980)$, and ρ meson exchange, and multi-meson exchanges (e.g. $\pi\pi$ and $\pi\rho$)

[10] OBEPQ: One Boson Exchange Parameterization in Q(momentum)-space.
[11] OBEPT: One Boson Exchange Parameterization with Time-dependence.
[12] OBEPR: One Boson Exchange Parameterization in R(position)-space.
[13] The two pion threshold: the energy threshold for two pion production. Schwamb and Arenhövel [Sch01c, Sch01a, Sch01b], and Elster *et al.* [Els88a, Els88b] only incorporated off-shell corrections for a single meson and thus their predictions are not expected to hold above the threshold for two pion production.

to compensate for not including the disputed σ meson (which is needed for the intermediate-range interaction [Kuk01]).[14] The Bonn-OPEBR potential is a simplification of the Full Bonn potential which has a relatively small loss of accuracy: designed to make calculations easier.

The Bonn-OPEBR is a one boson exchange parameterization: replacing the $2\pi + \pi\rho$ exchange with a σ meson and adding the η meson which was excluded in the Full Bonn. Retardation terms in the propagators cause an unwanted energy dependence, and therefore the static limit was taken for the propagators. Finally, the cutoff and coupling parameters were tweaked by refitting to empirical data [Mac87]. These simplifications were implemented to decrease the computing power needed for numerical solution of the deuteron wave function (such as the one performed from Schwamb and Arenhövel) [Bla07]. Due to the neglect of retardation in the propagators, the Bonn-OPEBR was used by Schwamb and Arenhövel to calculate the effect that retardation has on their calculations of deuteron photodisintegration [Sch01b].

The Elster potential [Sch01c] is similar to the Bonn-OPEBR in that it also started with a one boson exchange Bonn potential [Mac87]; however, the Elster potential was designed to extend above pion-threshold (up to the two pion threshold) and thus required additional considerations to improve accuracy. Extending the Elster potential beyond pion-threshold required: the incorporation of meson retardation (described in [Els88b]), mass corrections to nucleons due to off-shell (self-energy) contributions (described in [Els88a]), and the inclusion of Δ baryon intermediate states (so called "box diagrams"; described in [Els88b]).

In quantum field theory, particles interact with themselves, effectively increasing their mass [Gri87]: the self-interactions "dress" the "bare" mass. These so called "off-shell" effects must be taken into account in order to ensure consistency between the energy region where an exchange particle is forbidden from the final state and one where it is not [Els88a] (e.g. below and above pion-threshold, respectively). This means taking the bare mass and dressing it by computing the self-energy interactions (figure 2.10 on the next page illustrates the lowest order dressing). Since Elster *et al.* started from an already determined potential, this meant they had to infer a transformation from the previously determined potential, $\hat{V}$, to an effective potential, $\hat{V}^{eff}$ (i.e. a dressing operator, $\hat{R}$, such that $\hat{R}\hat{V} = \hat{V}^{eff}$).

[14] Törnqvist and Roos [Tor96] give a brief review of the σ meson dispute as well as evidence for its existence.

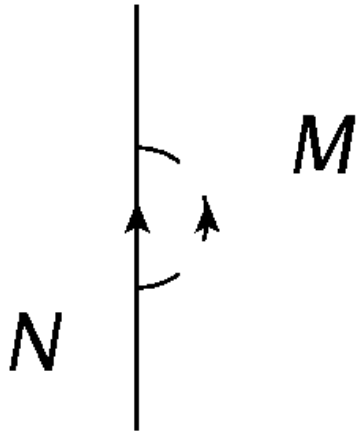

Figure 2.10: Nucleon Self-Energy. A nucleon, N, interacts with its own field via a meson, M. This is the first-order mass correction due to the self-energy.

The Elster potential also includes meson retardation effects and Δ baryon intermediate states. In order to implement the former: the meson propagators used must include a finite propagation speed; this can be included *ab initio* or *ad hoc* as an operator (Schwamb and Arenhövel have generalized the latter technique [Sch01c, Sch01a, Sch01b]). Δ baryon intermediate states are implemented similarly, but require computing the contributions due to "box diagrams": figure 2.11 on the next page; leading to dressing factors [Els88b].

The importance of meson retardation has been emphasized by Arenhövel [Lei87, Sch01c, Sch01a, Sch01b], who has made the argument that "one main reason" for discrepancies in the NN interaction is the neglect of meson retardation in the meson exchange operators [Sch01c]; citing deuteron photodisintegration as an example [Sch01b]. Deuteron photodisintegration also demonstrates the importance of including Δ baryon intermediate states (so called "isobar configurations"): the cross section differs by a factor of $\approx$ 2 in the isobar resonance range (240-320 MeV) due to its contribution [Are91]; see section 2.5.3 on page 38.

With these inclusions (meson retardation, nucleon self-energy, and Δ baryon intermediate states), the Elster potential is expected to describe the NN interaction up to the two pion threshold ($\approx$ 270 MeV).

Verification of these potentials requires using them to calculate some observables; such as those produced in a deuteron photodisintegration reaction, then comparing the results to experiment. This experiment uses the calculations performed by Schwamb and Arenhövel [Sch01b] in part to test the Elster potential below pion-threshold.

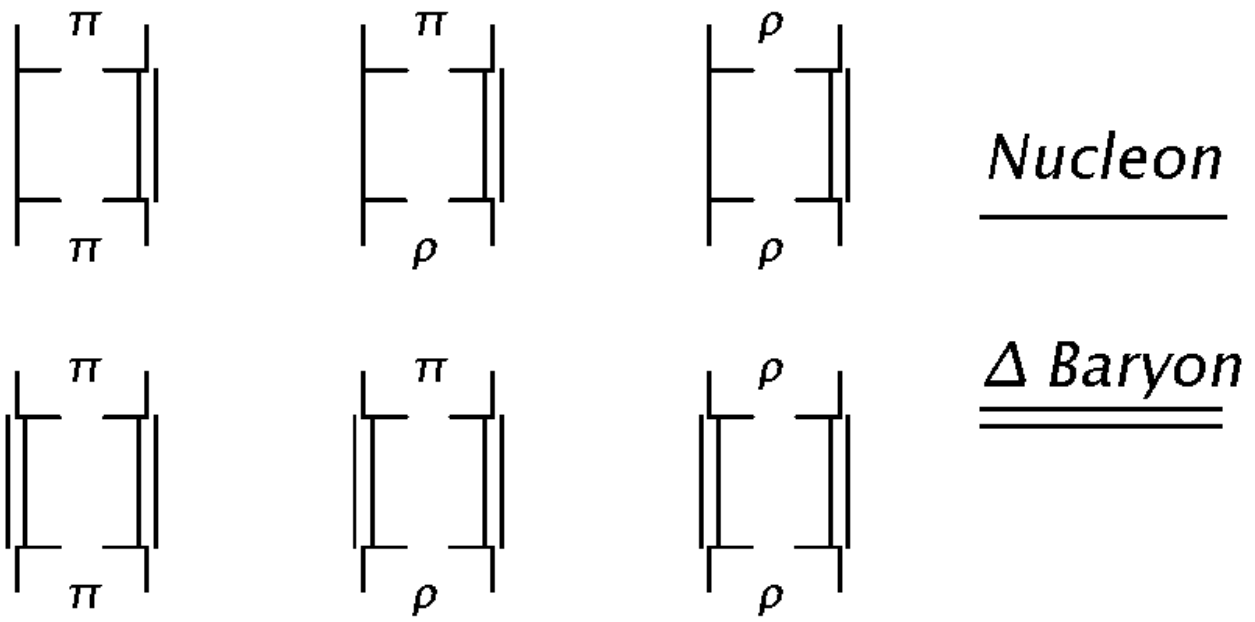

Figure 2.11: Box Diagrams of Δ Baryon Intermediate State. Two nucleons, N and N', form a Δ isobar resonance via a meson, ρ or π.

Retarded Meson Exchange Currents

Meson exchange potentials model the transfer of information between nucleons via the exchange of a meson propagator: i.e. meson exchange currents. In the limiting case where the kinetic energy transfer between the nucleons is 0, meson exchange is described by the static meson propagator approximation:

$$\frac{1}{(E-E')^2-(\vec{p}-\vec{p}')^2c^2-m^2c^4} \rightarrow -\frac{1}{(\vec{p}-\vec{p}')^2c^2+m^2c^4} \tag{2.7}$$

where: $E-E'$ is the progatator energy, $\vec{p}-\vec{p}'$ is the propagator momentum, and m is its mass. This is true in the limiting case $\Delta \mathrm{T}_{nucleon} \rightarrow 0$:[15] i.e. the nucleons the meson is mediating exchange no kinetic energy [Car11].

The use of the Static Meson Propagator Approximation was essentially invariable in calculations using meson exchange potentials up until Schwamb and Arenhövel [Sch01c].[16]

[15]This can be seen by considering a meson-nucleon vertex: the energy delta function forces the meson energy to be zero if the nucleon energy is the same going into and out of the vertex, assuming the mass doesn't change, this means that the change in nucleon kinetic energy is zero: $\Delta \mathrm{T}_{nucleon} \rightarrow 0$.

[16]Examples of the use of the Static Meson Propagator Approximation are supplied in Schwamb and

Motivated by earlier conjecture regarding its importance, Schwamb and Arenhövel have calculated observables for the photodisintegration of the deuteron both with and without the Static Meson Propagator Approximation [Sch01b].

The necessary interaction Hamiltonian for arbitrary NN (nucleon-nucleon) interactions were also derived by Schwamb and Arenhövel [Sch01c]; the parameters of their model were fit to NN scattering data and deuteron properties. For technical reasons, Schwamb and Arenhövel had to use the physical mass (rather than dressing) when considering meson exchange and Δ isobar resonance: this was then later rectified by use of dressing operators (discussed in section 2.5.3 on page 40).

The deuteron photodisintegration observables calculated by Schwamb and Arenhövel [Sch01b] used fully retarded meson exchange currents, including corrections due to the Siegert Operators to calculate the T matrix (see section 2.5.4 on page 44).[17]

Δ Baryon Degree-of-Freedom Corrections

Schwamb and Arenhövel have included the possibility that there may be up to one, non-relativistic, on-shell Δ baryon at any given time by expanding the Hilbert space to include a space consisting of n - 1 nucleons and a Δ baryon [Sch01c] and computing both its on-shell and off-shell contributions to deuteron photodisintegration [Sch01a, Sch01b]. The importance of the inclusion of the Δ baryon as both an intermediate and final state is illustrated by figure 2.12 on the next page.

Arenhövel [Sch01c].

[17] The Siegert Operators implicitly include contributions to the meson exchange currents and therefore a correction must be applied in order to prevent double counting. [Are91]

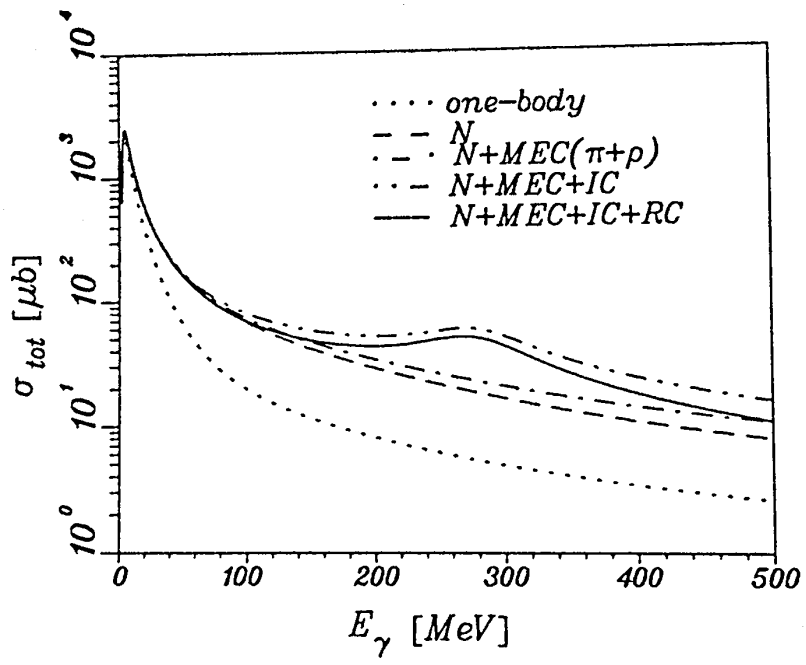

Figure 2.12: The Δ Isobar Contribution to the Deuteron Photodisintegration Cross Section. The inclusion of a Δ baryon as an intermediate state has a substantial affect on the total cross section in the Δ isobar resonance region. Definitions: N: nuclear potential, MEC($\pi + \rho$): π and ρ meson exchange currents, IC: isobar configurations (i.e. inclusion of the Δ baryon), and RC: relativistic corrections. Image credit: Arenhövel and Sanzone [Are91].

The on-shell affects of the Δ baryon were included by considering π and ρ meson exchange (figure 2.13 on the next page); the off-shell effects due to the Δ isobar are discussed in section 2.5.3 on the next page.

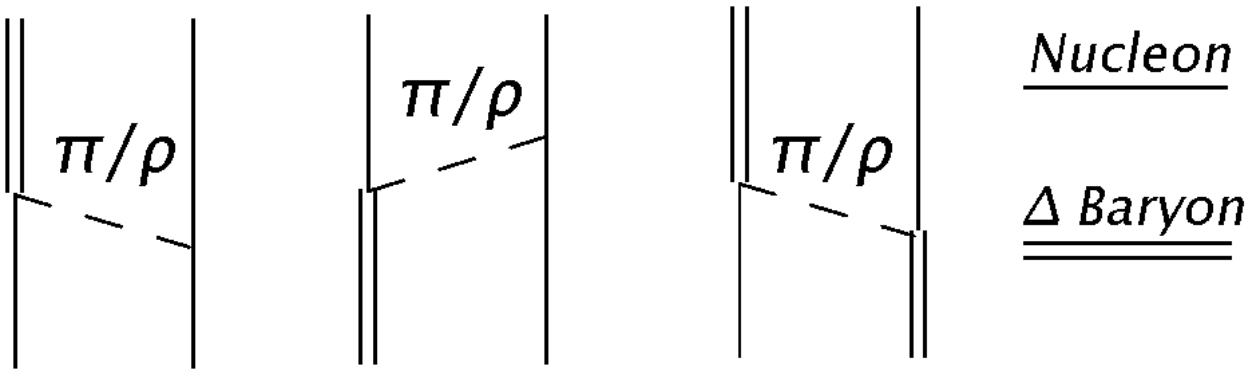

Figure 2.13: On-shell Δ Baryon Contributions. Feynman diagrams for the on-shell Δ baryon contributions to the nucleon-nucleon interaction.

Off-Shell Corrections

The observed mass of any nucleon is really a convolution of different processes which dress the bare mass [Gri87] via self-energy diagrams (e.g. the left image of figure 2.14 on the next page). A phenomenological calculation which utilizes the measured mass will encounter an ambiguity when faced with the prospect of an on-shell meson (e.g. M in the right image of figure 2.14 on the next page); this corresponds to the pion-threshold: where a pion can be in the final state. Failure to include self-energy diagrams leads to discrepancies above pion-threshold; for example, of: $25-30\%$ in the analyzing power for proton-proton bremsstrahlung, $\approx 20\%$ in the longitudinal response function for ^{12}C, and $\approx 8\%$ in the electron-nucleon cross section [Sch01a].

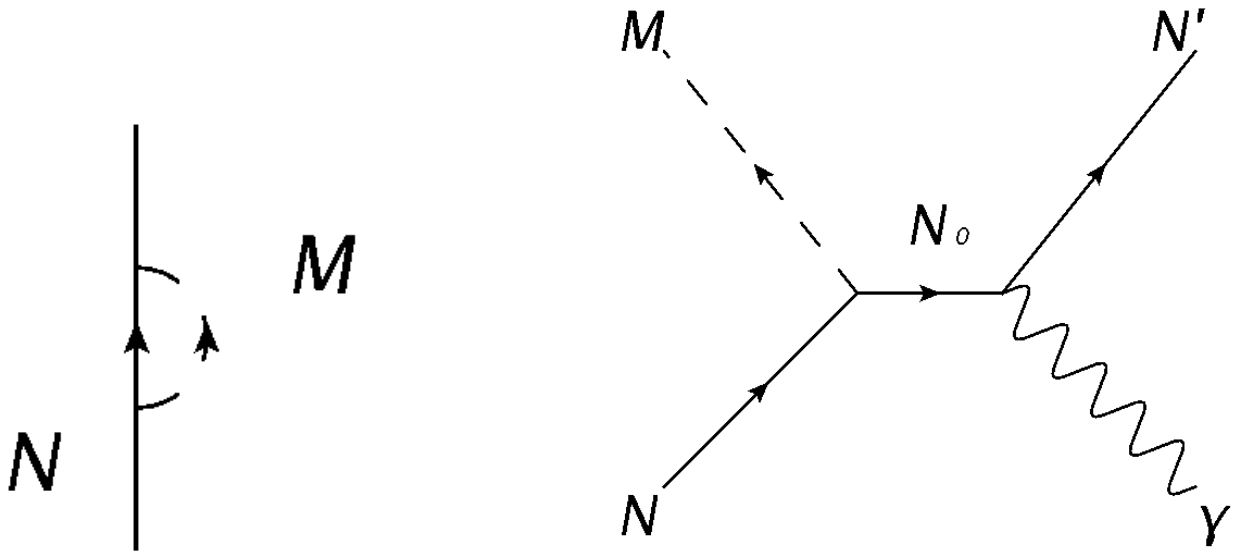

Figure 2.14: Meson Radiation and Nucleon Self-Energy. Left diagram: a nucleon, N, interacts with its own field via a meson, M. This is the first-order mass correction due to the self-energy. Right diagram: a photon, γ, is absorbed by a nucleon, N, producing a meson, M, and a final state nucleon, N' via a nucleon propagator N_0. Right adapted from Walker [Wal69].

Elster *et al.* [Els88a] performed off-shell corrections to the NN potential to first order via a dressing operator. Schwamb and Arenhövel [Sch01c] derived a similar dressing operator, $\hat{R}$ and applied it both to the NN (nucleon-nucleon) potential and T matrix:

$$(\hat{H}_0 + \hat{V}^{eff}_{\bar{N}\bar{N}}(M_d))|d\rangle = |d\rangle$$
$$\hat{V}^{eff}_{\bar{N}\bar{N}} = \hat{R}(V_{\bar{N}\bar{N}} + [\hat{V}_{\bar{B}X}\hat{G}\hat{V}_{X\bar{N}}]_{con})\hat{R}$$

where:

$$\hat{R}[\hat{V}_{\bar{B}X}\hat{G}\hat{V}_{X\bar{N}}]_{con}\hat{R} = \hat{V}^{Elster}$$

$\hat{V}^{eff}_{\bar{N}\bar{N}}$ is the meson retardation corrected potential using the bare nucleon masses, $\hat{R}$ are the dressing operators to convert the bare nucleon potential into a dressed nucleon potential, $\hat{G}$ is the retarded propagator operator, $\hat{V}_{\bar{B}X}$ is the meson/nucleon potential, and $\hat{V}^{Elster}$ is the Elster potential. The T matrix is then:

$$\hat{T}_{\bar{N}\bar{N}} = \hat{V}^{eff}_{\bar{N}\bar{N}} + \hat{V}^{eff}_{\bar{N}\bar{N}}\hat{G}\hat{T}_{\bar{N}\bar{N}} \tag{2.8}$$

We get a new recursive relation for our T matrix in terms of the effective potential: just like the normal T matrix (described in section 2.5.4 on page 44), and allowing any arbitrary NN process to be properly described past pion-threshold. In the static limit the effective potential just simplifies to the nucleon-nucleon potential, thus returning everything to normal (Schwamb and Arenhövel use the Bonn-OBEPR in that case).

Eq. (2.8) requires an effective NN potential which includes dressing of nucleons via mesons. Schwamb and Arenhövel used the Elster potential to calculate the contribution in electromagnetic reactions with the deuteron [Sch01a] and specifically the photodisintegration of the deuteron [Sch01b]. In addition to dressing factors, Schwamb and Arenhövel derived an effective nucleon current which includes off-shell electromagnetic effects (i.e. interactions with the "virtual meson cloud" and Δ isobar; e.g. figure 2.15 on the next page). The nucleon current is used to calculate observables for deuteron photodisintegration as discussed in section 2.5.4 on page 44.

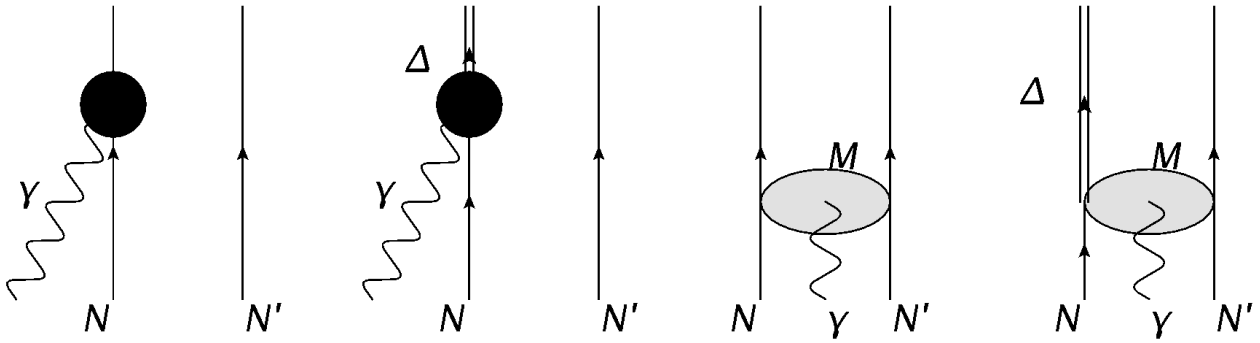

Figure 2.15: Off-shell Contributions to Nucleon Current [Sch01a]. Where: N and N' are nucleons, M is a meson cloud, γ is a photon, and Δ is a Δ isobar.

Relativistic Corrections

Deuteron photodisintegration was once believed to be adequately described non-relativistically, so Arenhövel and Sanzone [Are91] emphasize the "surprise" when Cambi *et al.* demonstrated that relativistic spin-orbit contributions to the cross section at 0°: at energies as low as 20 MeV were of "importance" [Are91]. The dominant electric transition (E1) depends on $a + b\sin^2\theta$ [Had87] and therefore reaches a minimum at 0° and 180° ($\theta \in [0, \pi]$), enabling the relatively small relativistic correction to provide a significant contribution to the precision of the calculation.

Relativistic corrections manifest in deuteron photodisintegration calculations via: the deuteron binding, Lorentz contraction of the deuteron when boosting in the center of momentum frame, relativistic corrections to the current operator [Are91], and retardation of the meson exchange currents [Bla07]. Of these manifestations, Schwamb and Arenhövel included relativistic effects: by performing relativistic corrections to the current operator [Sch01b], by using the fully relativistic energies of the final state nucleons, and by using retarded meson exchange currents [Sch01c, Sch01a, Sch01b]. These contributions are expected to be the dominant relativistic effects, but a discrepancy between our results and Schwamb and Arenhövel's calculation; in particular at the forward or backwards angles, could signify the need for additional relativistic corrections e.g. to the binding of the deuteron or in boosting

the center-of-momentum/mass frame.[18]

2.5.4 Deuteron Photodisintegration: the S and T Matrices

The S matrix or "Scattering Matrix" [Che97] is the probability amplitude for the time evolution of some initial state $|i\rangle$ to some final state $\langle f|$:

$$\langle f|\hat{S}_{fi}|i\rangle = \langle f|\hat{U}_I(-\infty,\infty)|i\rangle \tag{2.9}$$

where: $|i\rangle$ is the initial state, $\langle f|$ is the final state, $\hat{U}_I(-\infty,\infty)$ is the Interaction Picture time-evolution operator, and $\hat{S}_{fi}$ is the S matrix defined by this equation [Che97]. Thus, the S matrix describes how quantum mechanical systems evolve.

Given an interaction Hamiltonian, the time-evolution operator in eq. (2.9) ($\hat{U}_I$) can be calculated directly, or using quantum field theory by defining a field as the Hamiltonian density: $\hat{H}_I = \int \mathcal{H}_I d^3x = -\int \mathcal{L}_I d^3x$ [Pes95] (where I have included the Lagrangian for convenience).[19] When using quantum field theory to calculate observables, $\hat{U}_I$ generates a sum of terms which are readily represented by Feynman diagrams. Feynman rules can be deduced or referenced, and then used to calculate these diagrams. Arenhövel and Sanzone [Are91] discuss the use of Feynman diagrams to calculate deuteron photodisintegration observables, while Walecka [Wal04] provides a good description of a nucleon-nucleon meson exchange model including the necessary Feynman rules.

The first term in eq. (2.10) has no dynamical quantities to it: it is simply a comparison of the initial and final states and will always be 0 or 1 if the states are orthonormal. We define the T matrix or "Transition Matrix" [Che97] to be where the action happens in the transition from some initial state $|i\rangle$ to some final state $\langle f|$:

$$\hat{S}_{fi} = \langle f|i\rangle + (2\pi)^4 i\delta^{(4)}(\mathbf{p}_f - \mathbf{p}_i)\hat{T}_{fi} \tag{2.10}$$

[18]The lack of a Lorentz boost to the deuteron bound state into the center-of-mass/momentum frame seems reasonable for the energy region of our experiment: the deuteron only moves at 0.95% c in the center-of-mass/momentum frame, but it seems questionable that this approximation is valid near the upper limit of the model $\approx$ 500 MeV where the center-of-mass/momentum frame deuteron moves at 26% c.

[19]Note that I will refer to the Lagrange density as the Lagrangian.

where: $\mathbf{p}_f$ is the final 4-momentum, $\mathbf{p}_i$ is the initial 4-momentum, and T_{fi} is the T matrix defined by this equation [Are91].

Thus the T matrix incorporates all higher order (above 0^{th}) contributions to the S matrix. The definition of the T matrix using eq. (2.10) on page 44 incorporates the basis dependence, enabling general solutions for the cross section in terms of the T matrix that are independent of choice of basis.

The T matrix is used to calculate the cross section data via the Golden Rule for scattering of a two-body initial state into a two-body final state:

$$d\sigma = |\mathcal{M}|^2 \frac{(2\pi)^4 \hbar^2 S}{4\sqrt{(\mathbf{p}_1^i \cdot \mathbf{p}_2^i)^2 - (m_1^i m_2^i c^2)^2}} \frac{c\, d^3 p_1^f}{(2\pi)^3 2E_1^f} \frac{c\, d^3 p_2^f}{(2\pi)^3 2E_2^f} \delta^{(4)}(\mathbf{p}_i^1 + \mathbf{p}_i^2 - \mathbf{p}_f^1 - \mathbf{p}_f^2) \quad (2.11)$$

where: $\mathcal{M} = T$ is the scattering amplitude, $\mathbf{p}_f$ is the final 4-momentum, $\mathbf{p}_i$ is the initial 4-momentum, $S = 1$ is a statistical factor for identical particles in the final state [Gri87].

Using God-given units, eq. (2.11) for a photon plus one-body to two-body reaction in the CM (center-of-mass/momentum) frame can be simplified to:

$$\left(\frac{d\sigma}{d\Omega}\right)_{CM} = \left(\frac{1}{8\pi}\right)^2 \frac{|T_{fi}|^2}{E_{CM}^2} \frac{p^L}{E_\gamma^L} \quad (2.12)$$

where: $\hat{T}_{fi}$ is the T matrix, p^L is the final 3-momentum magnitude of either of the final state particles, E_{CM}^2 is the total energy of the CM frame, and E_γ^L is the lab frame energy of the incident photon. Note: $\hbar = c = 1$ [Gri87, Pes95].

Eq. (2.12) gives the cross section purely in terms of the T matrix and the kinematic variables. The kinematics can be computed exactly using conservation of energy and momentum (this was discussed in section 2.3 on page 23), while the T matrix was calculated by Schwamb and Arenhövel directly from their effective nucleon current [Sch01b] using:

$$T_{fi} = \sqrt{\frac{\alpha}{2\pi^2}} \langle n, p | \epsilon^\mu J_\mu | d \rangle \quad (2.13)$$

where: T_{fi} is the T matrix, ϵ^μ is the photon polarization vector, J_μ is the current density operator, $\alpha = \frac{e^2}{4\pi}$ is the fine-structure constant, $|d\rangle$ is the initial bound deuteron, and $\langle n, p|$ is the final unbound neutron + proton state [Are91].

The nucleon current can be expanded into a series of *multipole operators*:

$$\epsilon^{\mu}(\lambda)J_{\mu} = -\sqrt{2\pi}\sum_{L,m}\hat{L}(\hat{\mathrm{E}}^{L}_{m} + \lambda\hat{\mathrm{M}}^{L}_{m})D^{L}_{m\lambda}(R)$$

where: $\epsilon(\lambda)$ is the photon polarization, J_{μ} is the current operator as used in eq. (2.13) on page 45, $\hat{\mathrm{E}}$ is the electric multipole operator, $\hat{\mathrm{M}}$ is the magnetic multipole operator, and $D(R)$ is an Edmonds rotation matrix [Are91]. The magnetic multipole operator is defined by:

$$\hat{\mathrm{M}}^{L} \equiv \int \hat{j}\cdot\vec{A}^{l}_{m}d^{3}x = \int \hat{j}\cdot[\frac{i^{L-1}}{\sqrt{L(L+1)}}(\vec{r}\times\nabla)j_{L}\vec{Y}^{L}_{m}]d^{3}x \tag{2.14a}$$

where: $\hat{\mathrm{M}}$ is the magnetic multipole operator, $\hat{j}$ is the current density operator, $\vec{A}_{m}$ is the magnetic multipole field operator, $i = \sqrt{-1}$, r is the radial distance, and $\vec{Y}^{L}_{m}$ is the L, m spherical harmonic [Are91]. The electric multipole operator is defined by:

$$\hat{\mathrm{E}}^{L} \equiv \int \hat{j}\cdot\vec{A}^{l}_{e}d^{3}x = \int \hat{j}\cdot\frac{i}{\omega}\nabla\times\vec{A}^{l}_{m}d^{3}x \tag{2.14b}$$

where: $\hat{\mathrm{E}}$ is the electric multipole operator, $\vec{A}_{e}$ is the electric multipole field operator, and the other variables are defined by eq. (2.14a) [Are91].

Eq. (2.14a) and eq. (2.14b) are expanded perturbatively to some arbitrary precision, giving the T matrix via eq. (2.13) on page 45. The amplitudes calculated using these operators are colloquially referred to by their type (M or E) and their index (L)[20] e.g. E1 is the first-order electric multipole transition amplitude. The magnetic and electric multipoles can be used to calculate the differential cross section directly (via the T matrix), and they can be used to calculate the parameters for the Legendre expansion of the differential cross section, as is

[20]The multipole indices are equal to the angular momentum of the transition photon; the parity is related to the angular momentum and transition type as follows: the electric multipole parity is $(-1)^{L}$, and the magnetic multipole parity is $(-1)^{L+1}$.

discussed in section 2.5.5.

The time reversed reaction: n-p capture, can be conveniently described by:

$$\hat{T}^c_{fi} = \frac{p^L}{E^L_\gamma}(\hat{T}^\gamma_{fi})^* \tag{2.15a}$$

$$\frac{d\sigma^c}{d\Omega} = |\hat{T}^c_{fi}|^2 \tag{2.15b}$$

where: c is for capture, $\hat{T}^c_{fi}$ is the capture T matrix, $\hat{T}^\gamma_{fi}$ is the deuteron photodisintegration T matrix, p^L is the magnitude of the CM frame proton and neutron momenta, and E^L_γ is the lab frame energy of the incident photon [Are91]. The data from this experiment can therefore be applied to the inverse reaction.

2.5.5 Legendre Expansion of the Cross Section

Section 2.5.4 on page 44 covers what the T matrix is and how to get the desired observables (i.e. cross section data) from it. Ideally, this concludes the necessary calculations; however, interpolating the angular dependence of the cross section (i.e. the differential cross section $\frac{d\sigma}{d\Omega}$) from the experimental data using an arbitrary function or series would not be conducive to scientific discussion. The solution is to break up the differential cross section into a linear combination of functions which can easily be fit to experimental data, and can either be easily fit to theoretical data or (ideally) calculated directly.

It is clear that we want to describe the differential cross section using a simple linear combination of functions:

$$\frac{d\sigma}{d\Omega}(\theta,\phi) = \sum_k a_k f_k(\theta,\phi) \tag{2.16}$$

where: $\frac{d\sigma}{d\Omega}$ is the differential cross section, a_k are scale parameters to be extracted by fitting experimental data, and f_k are some known functions.

An early parameterization was performed by Partovi [Par64] who provided a framework

for deuteron photodisintegration reactions:

$$\begin{aligned}\frac{d\sigma}{d\Omega}(\theta,\phi) =& a + b\sin^2\theta \pm c\cos\theta \pm d\sin^2\theta\cos\theta + e\sin^4\theta \\ &+ \cos 2\phi[f\sin^2\theta \pm g\sin^2\cos\theta + h\sin^4\theta]\end{aligned} \tag{2.17}$$

where: $\frac{d\sigma}{d\Omega}$ is the differential cross section, a, b, ... and h are scale parameters to be extracted by fitting experimental data, $\pm$ refers to the outgoing neutron ($-$) versus proton ($+$), ϕ is the azimuthal angle, and θ is the polar angle relative to the incident photon [Saw05].

The problem with eq. (2.17) and similar expansions is that the terms of the expansion depend on the multipole transition amplitudes in a complicated manner. This problem was rectified in 1982 by Cambi *et al.* [Cam82] by using orthogonal Legendre functions in an expansion equivalent to eq. (2.17):

$$\frac{d\sigma}{d\Omega}(\theta,\phi) = \sum_{k=0} A_k P_k^0(\cos\theta) + \sum_{k=2} B_k \Sigma_l P_k^2(\cos\theta)\cos 2\phi \tag{2.18}$$

where: $\frac{d\sigma}{d\Omega}$ is the differential cross section, Σ_l is the degree of linear polarization of the incident beam, k is the total angular momentum, A_k and B_k are either calculated or treated as scale parameters to be extracted by fitting experimental data, P_k^L are associated Legendre polynomials, ϕ is the azimuthal angle, and θ is the polar angle relative to the incident photon [Cam82].

Cambie *et al.* showed the parameters in eq. (2.18) are closely tied to the initial (unprimed) and final (primed) electric and magnetic multipole operators:

$$A_k \propto \delta_{N,even}(\mathcal{E}^L\mathcal{E}^{L'} + \mathcal{M}^L\mathcal{M}^{L'}) - \delta_{N,odd}(\mathcal{E}^L\mathcal{M}^{L'} + \mathcal{M}^L\mathcal{E}^{L'}) \tag{2.19a}$$

$$B_k \propto \delta_{N,even}(\mathcal{M}^L\mathcal{M}^{L'} - \mathcal{E}^L\mathcal{E}^{L'}) + \delta_{N,odd}(\mathcal{M}^L\mathcal{E}^{L'} - \mathcal{E}^L\mathcal{M}^{L'}) \tag{2.19b}$$

where: A_k and B_k are the parameters from eq. (2.18), k is the indexing variable from eq. (2.18) (k is the total angular momentum) with the constraint $|L - L'| \leq k \leq L + L'$, the magnetic: $\mathcal{M}^L$ and electric: $\mathcal{E}^L$, reduced matrix elements are proportional to: $\mathcal{E}^L + \mu\mathcal{M}^L \propto \langle f|E^L + \mu M^L|i\rangle$, $\delta_{N,even} \equiv \frac{1+(-1)^N}{2}$, $\delta_{N,odd} \equiv \frac{1-(-1)^N}{2}$, $N \equiv L+L'+k$, and L (initial state) and L' (final

state) are the angular momenta (and multipole indices). Based on Cambie *et al.* [Cam82]. Unfortunately, there is no general way to invert the mapping such that a Legendre expansion can be used to give a multipole expansion.

The terms in eq. (2.19) on page 48 with mixed electric and magnetic reduced matrix elements or multipolarities are called "interference" [Cam82] terms. One can tell the pertinent contributions to a parameter from $\hat{\mathrm{E}}$ and $\hat{\mathrm{M}}$ by considering a particular value of k, for example: the first contribution to A_3 is $L = 1$, $L' = 2$ (because $|L-L'| \leq k \leq L+L'$), and therefore only the even terms contributes, leading to two interference terms: E1-E2 and M1-M2 [Cam82].

In our experiment, we: truncate, absorb the polarization (Σ_l) into the e_k fit parameters, and then add two additional terms to compensate for improper target alignment following Kucuker [Kuc10], yielding:

$$\begin{aligned}\frac{d\sigma}{d\Omega} \approx & \frac{\sigma}{4\pi}\left[1 + \sum_{k=1}^{4} a_k P_k^0(\cos\theta) + \sum_{k=2}^{4} e_k P_k^2(\cos\theta)\cos 2\phi \right. \\ & \left. + \sum_{k=1}^{2} c_k P_k^1(\cos\theta)\cos\phi + \sum_{k=1}^{2} d_k P_k^1(\cos\theta)\sin\phi\right] \end{aligned} \tag{2.20}$$

where: P_k^i are the associated Legendre polynomials, a_k are the A_l of eq. (2.18) on page 48, e_k are the $B_l\Sigma_l$ of eq. (2.18) on page 48, the c_k and d_k terms verify the target alignment, and σ is the total cross section.

Similar expansions have been applied by previous Blowfish researchers: e.g. Sawatzky [Saw05], Blackston [Bla07], Kucuker [Kuc10], and Wurtz [Wur10c]. Sawatzky [Saw05] has provided the necessary algebra to convert to the Partovi Expansion (eq. (2.17) on page 48), see his work for details.

Schwamb and Arenhövel [Sch01c, Sch01a, Sch01b] provided us the differential cross section, total cross section, photon asymmetry, and the multipole amplitudes up to $l = 4$ for 18 MeV deuteron photodisintegration. We perform a fit of eq. (2.20) to the differential cross section and photon asymmetry values given by Schwamb and Arenhövel in order to compare our results to their calculation.

We extract the same set of parameters from our experimental data by mapping eq. (2.20) into a probability density function and use the Monte Carlo Method to simulate the expected

neutron yield in each detector (described in section 4.4.2 on page 119). The simulated neutron yields are then used as the fitting functions to parameterize the experimental neutron yield and thus extract the parameters in eq. (2.20) on page 49.

Chapter 3

Experimental Apparatus

"...once in a while, though, the sticks go together and I reach the banana." -Richard Feynman [Fey]

3.1 Introduction

The data were recorded at the High Intensity Gamma Source (HI$\vec{\gamma}$S; section 3.3 on page 53) in Durham, North Carolina during October of 2010. The reaction tested was the photodisintegration of the deuteron at 18 MeV using linearly polarized photons: $d(\vec{\gamma},n)p$; the ejectile neutrons were measured by the Blowfish detector array.

The purpose of the experiment at the time was to test a few potential systematic errors in preparation for future high-precision experiments; consequently the experiment was not performed as carefully as possible and it is probable that the uncertainties estimated in this work are higher than they need be in future experiments with Blowfish.

The author of this thesis did not participate in the collection of the data, but instead inherited them in 2011 with the intent of extracting usable data.

3.2 Run Summary

Table 3.1 on the next page summarizes the experimental runs which were analyzed to provided the data for this thesis.

October 2010 Run Summary

Run	Run Time	Target/Source	Arm Up	Purpose
136	9-9:27 am	AmBe Source	3	Verify run 139 results.
139	10:11-10:32 am	AmBe Source	3	Calibrate gain and PSD (runs 142-143).
140	10:36-11:33 am	Background	3	Test gain linearity.
141	1:19-1:20 pm	10.7 cm D_2O	3	Align the TDCs.
142	1:22-2:05 pm	10.7 cm D_2O	3	Data run.
143	2:07-2:42 pm	10.7 cm D_2O	3	Data run.
149	3:51-4:28 pm	10.7 cm D_2O	2	Data run.
150	4:28-5:07 pm	10.7 cm D_2O	2	Data run.
152	5:51-6:35 pm	10.7 cm D_2O	4	Data run.
153	6:39-7:16 pm	10.7 cm D_2O	4	Data run at half photon flux.
154	7:33-8:18 pm	10.7 cm H_2O	4	Measure background neutrons.
155	8:27-9:14 pm	2.0 cm D_2O	4	Data run.
157	9:14-10:02 pm	2.0 cm D_2O	4	Data run.
158	10:20-11:08 pm	2.0 cm D_2O	2	Data run.
159	11:08-11:36 pm	2.0 cm D_2O	2	Data run.
165	12:09-12:15 am	AmBe Source	2	Calibrate gain and PSD (runs 158-159).

Table 3.1: List of runs used in this analysis. Runs were performed over a continuous period from 9:01 am October 29$^{\text{th}}$, 2010 12:34 am October 30$^{\text{th}}$.

3.3 The High Intensity Gamma Source (HI$\vec{\gamma}$S)

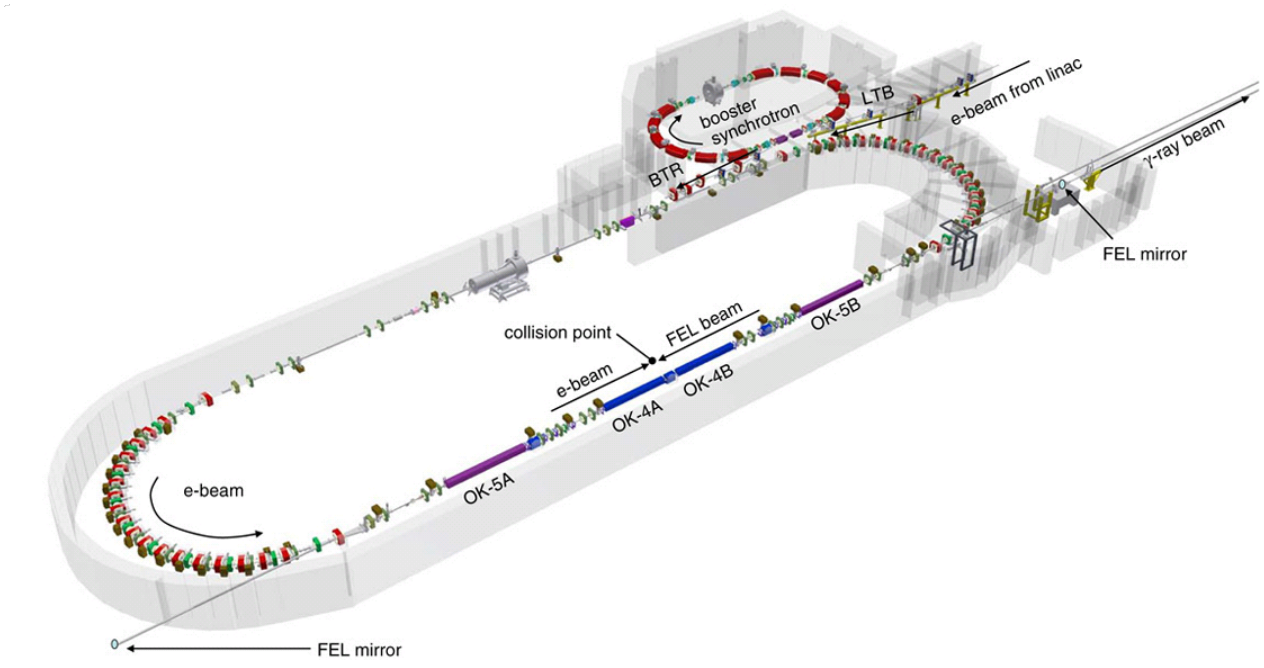

Figure 3.1: The HI$\vec{\gamma}$S Facility. Electrons enter from the linear accelerator (linac) in the top right, then they are stored in the booster synchrotron until demanded by the storage ring (main synchrotron). The free-electron laser operates via the OKs (Optical Klystrons) and the FEL mirrors; we used the OK-4 in this experiment which produces horizontally polarized photons. Definitions: LTB: Linear accelerator To Booster, BTR: Booster To Ring, OK-5A/B: Optical Klystron (helical polarizer), OK-4A/B: Optical Klystron 4 (linear polarizer), and FEL: Free-Electron Laser. Full discussion follows in text. Image credit: Weller et al [Wel09].

The High Intensity Gamma Source (HI$\vec{\gamma}$S) facility is located at Duke University in Durham, North Carolina; it is a joint project operated by the Triangle Universities Nuclear Laboratory.[1] HI$\vec{\gamma}$S uses a free-electron laser (FEL) capable of producing nearly 100% linear or

[1]The Triangle Universities are: Duke, North Carolina State and North Carolina at Chapel Hill.

circularly polarized photons[2] with high precision energy in the range of 1-95 MeV, at a flux of 10^8-$10^9 \frac{\gamma}{s}$ [DFE10] (full metrics can be found in appendix D on page 289).

The High Intensity Gamma Source is compared to its contemporaries in table 3.2: as you can see, HI$\vec{\gamma}$S has relatively high flux and energy precision at the expense of energy; the high flux compliments Blowfish well because Blowfish has a relatively low detection efficiency.

	ROKK-1M	GRAAL	LEPS	HI$\vec{\gamma}$S
Location	Russia	France	Japan	USA
γ beam energy (MeV)	100-1600	550-1500	1500-2400	1-100
Energy resolution, % ($\frac{\Delta E}{E}$)	1-3	1.1	1.25	0.8-10
Max flux at target ($\frac{\gamma}{s}$)	10^6	$3 \cdot 10^6$	$5 \cdot 10^6$	$10^4 - 5 \cdot 10^8$

Table 3.2: HI$\vec{\gamma}$S Contemporaries. HI$\vec{\gamma}$S compared with a few other Compton γ-sources. As you can see, HI$\vec{\gamma}$S is capable of high precision and flux at relatively low energies: ideal for low energy nuclear photodisintegration experiments. Adapted from Weller et al [Wel09].

Electrons are accelerated in groups of several electrons called *bunches* via a *lin*ear *ac*cellerator (*linac*) into a booster ring from which they are fed into the storage ring on demand. The booster ring was commissioned in 2006 in order to compensate for electron loss in the storage ring [Wel09] and to accommodate higher energy beams: above 20 MeV there is continuous loss of electrons in the storage ring [Mik07]. The booster ring is designed to inject new electrons in phase with the storage ring [Mik07] (for specifications, please see Mikhailov *et al.* [Mik07]).

Upon exiting the booster ring, the electron bunches are kept in the storage ring where they produce gamma rays via the FEL; until they eventually are attenuated from the synchrotron. The FEL operates by utilizing stimulated emission of polarized ultraviolet (UV) photons: this enables high flux, with high energy photons achieved via Compton backscattering.

[2]Degradation of the ultraviolet mirrors can cause a change in polarization: Sawatzky [Saw05] measured a 9° deviation in the polarization axis due to mirror degradation. We verify the polarization in section 6.4 on page 244 for this reason.

The approximate energy of a photon after backscattering from a highly relativistic electron ($E_e >> m_e c^2$) is:

$$E_{\gamma_f} \approx \frac{4\gamma^2 E_{\gamma_i}}{1 + (\gamma\theta)^2 + 4\gamma\frac{E_{\gamma_i}}{m_e c^2}} \tag{3.1}$$

where: E_e is the electron's total energy, m_e is the electron's rest mass, θ is the photon scatter angle, E_{γ_i} is the incident photon's energy, E_{γ_f} is the scattered photon's energy, and $\gamma = \frac{E_e}{m_e c^2}$ [Lit97]. The strong dependence on θ enables collimation to greatly reduce energy spread, resulting in high energy precision.

The energy spread of the process is approximately:

$$\frac{\Delta E_\gamma}{E_\gamma} \approx (\gamma\theta)^2 \tag{3.2}$$

where: E_e is the electron's total energy, m_e is the electron's rest mass, θ is the photon scatter angle, E_γ is the scattered photon's energy, ΔE_γ is the absolute uncertainty in the scattered photon's energy, and $\gamma = \frac{E_e}{m_e}$ [Lit97].

The initial polarized UV radiation in the FEL is emitted by "wiggling" the electrons via a graduated magnetic field in the Optical Klystrons (a.k.a wigglers); the Optical Klystron 4 (OK-4) was used in this experiment. The optical cavity is perfectly timed such that by the time an electron bunch has circumnavigated the storage ring: the UV photons have bounced off both mirrors and are in the same position as the electrons, this enables stimulated emission of additional UV photons in the wiggler. In order to produce gamma rays (i.e. high energy photons), a second bunch of electrons is stored in the storage ring exactly half the circumference away from the first, thus when the second bunch is in the middle of the optical cavity it is perfectly in time to meet the UV photons moving in the opposite direction: if a UV photon scatters from one of these electrons it will backscatter as a high energy photon (i.e. gamma ray). This process conserves the polarization and thus the final product is a photon with precise energy and polarization. This photon then penetrates the ultraviolet

mirror and travels down a vacuum, through the flux monitor, into the upstream, and then downstream target rooms where it impinges on the experimental target (depending on which target room it is in); the process is illustrated in figure 3.2 on the next page.[3]

[3]A video of the process can be viewed at `http://www.tunl.duke.edu/web.tunl.2011a.higs.php`.

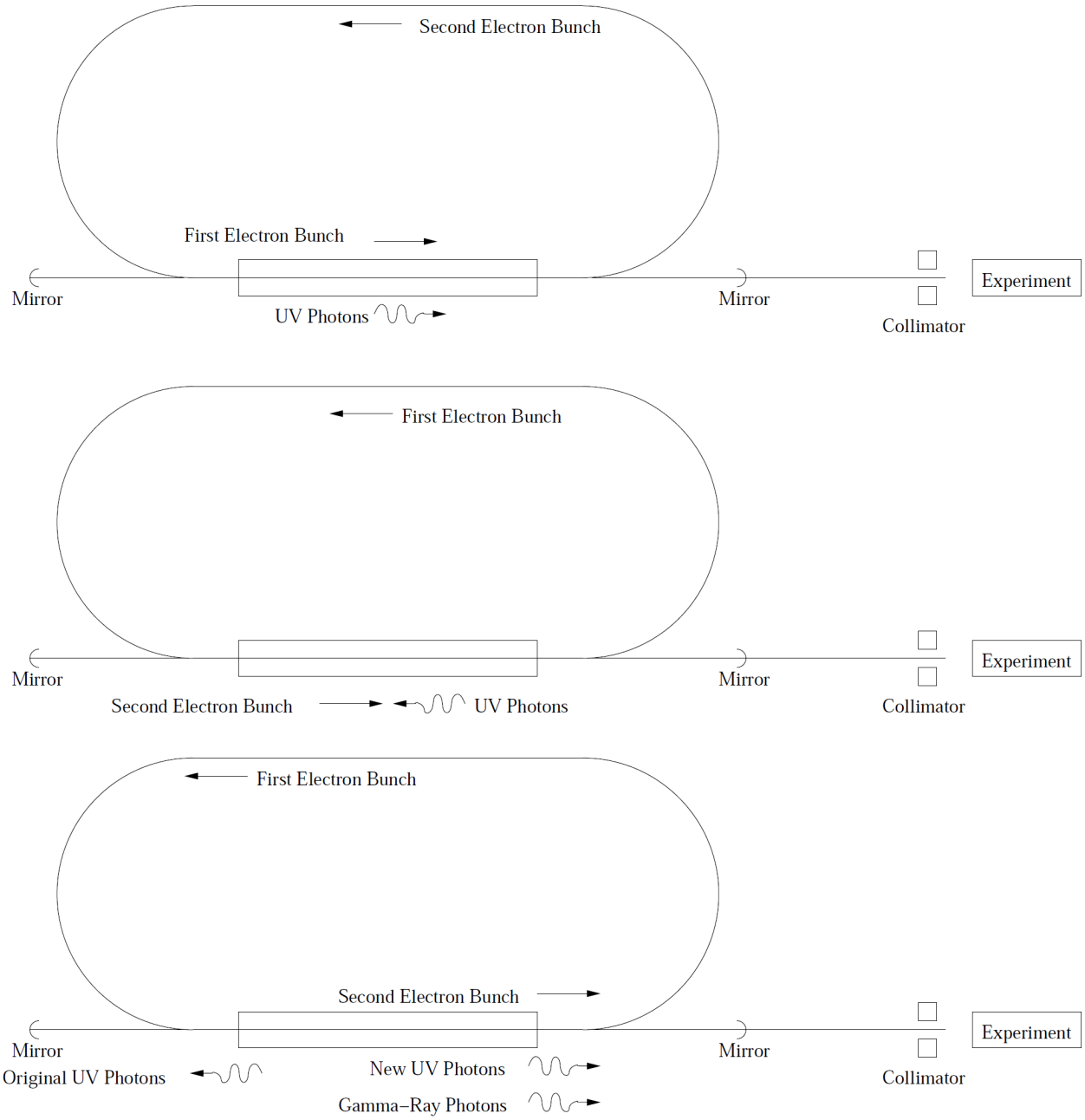

Figure 3.2: Operation of the Free-Electron Laser at HI$\vec{\gamma}$S [Wur10c]. This simplified diagram shows only the storage ring. Two bunches of electrons are stored at once: the first bunch radiates ultraviolet (UV) photons as it enters the wigglers. The second bunch may collide with the UV photons from the first bunch, and it produces UV photons of its own. The "gamma-ray photons" produced from Compton backscattering pass through the mirror undeflected and impinge on the target.

Under our experimental arrangement, the final result is a 5.58 MHz pulse laser (i.e. $\approx$ 1-2 photons every 179 ns) with energy 18.00 $\pm$ 0.27 MeV.[4] We receive a signal from the accelerator each time an electron bunch *should* be at the collision point i.e. the starting point for an 18 MeV photon, enabling us to time and shutter our data acquisition system with respect to the beam.

3.3.1 Synchrotrons

The HI$\vec{\gamma}$S FEL (free-electron laser) is driven by electrons: first electrons are accelerated by a linear accelerator, then they are kept in a synchrotron (i.e. the booster ring) until they are demanded by a second synchrotron where they perform the lasing (i.e. the storage ring). Synchrotron operation is discussed here in order to provide the necessary background to understand where the out-of-time photons (section 5.3.1 on page 152) are being produced.

*Synchro*trons use *synchro*nously oscillating electric and magnetic fields that are capable of increasing, decreasing or maintaining the energy of charged particles *while maintaining a uniform radius* [Pat11]. Maintaining a high precision energy and time spread is achieved by using a time oscillating potential to accelerate charged particles; this is performed in a radio-frequency[5] chamber section of the synchrotron; a simplified version of this potential is displayed in figure 3.3 on the next page.

[4] The uncertainty in the energy was estimated by linearly extrapolating the measured beam energy spread by Blackston [Bla07] at 16 MeV.

[5] The name comes from the fact that the necessary oscillations are on the order of MHz which is in the radio wave range of the electromagnetic spectrum. For example, HI$\vec{\gamma}$S operates at 178.55 MHz [Wel09].

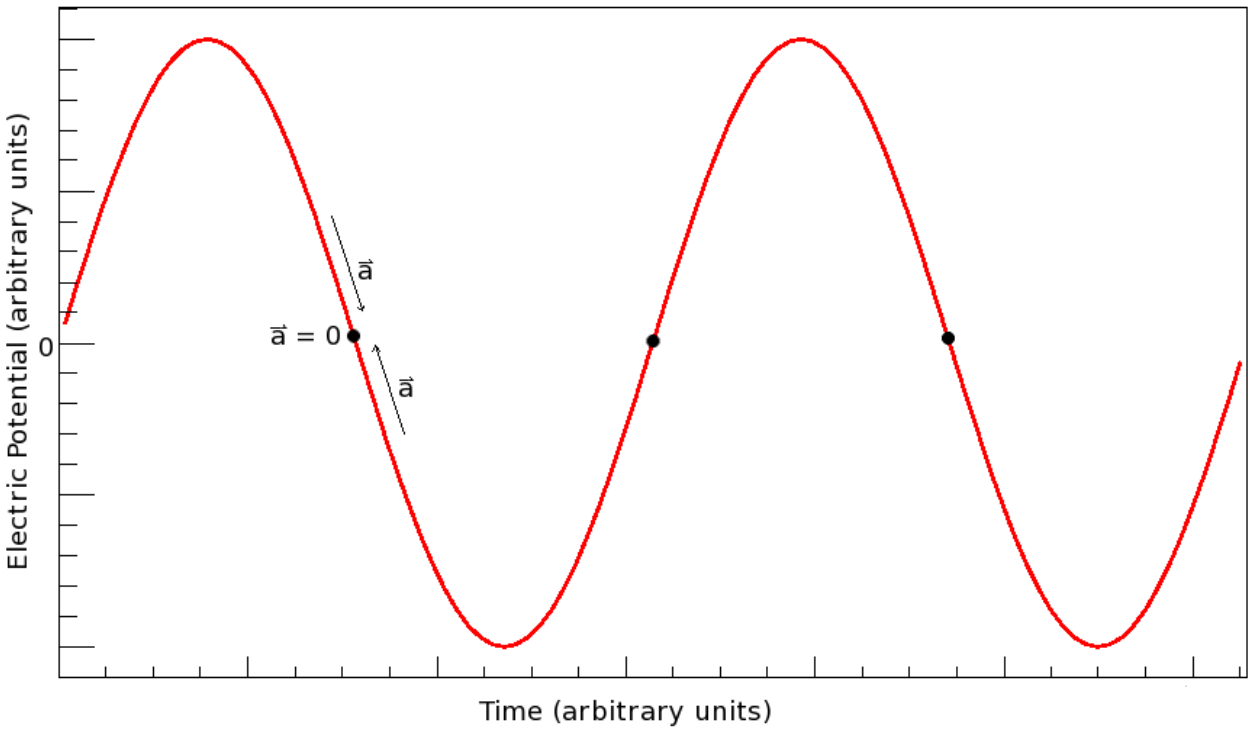

Figure 3.3: Idealized Synchrotron Potential, based on Patel [Pat11]. Charged particles (e.g. electrons) are stabilized at the black nodes (i.e. potential energy minimums): charged particles arriving early or late get accelerated by a potential towards the nearest node by an appropriately signed electric potential (as per $\vec{F} = q(\vec{E} + \vec{v} \times \vec{B})$). Illustrated is the steady state potential, in order to accelerate the synchrotron particles: a constant is added to the electric potential. The oscillating frequency is given by the circumference of the trajectory and energy of the charged particles.

As demonstrated in figure 3.3: there are many neighbouring stable potential minimums where charged particles are in a stable trajectory. The storage ring at HI$\vec{\gamma}$S has 64 potential energy minimums (called "buckets") each spaced 5.6 ns apart [Wel09]. In gamma ray operation: 2 of these potential energy minimums are occupied, each by a bunch of electrons. The data from this experiment imply that there are also additional potential energy minimums occupied as the electron bunches slowly spread into neighbouring potentials; this is discussed in section 5.3.1 on page 152.

3.4 Experimental Layout

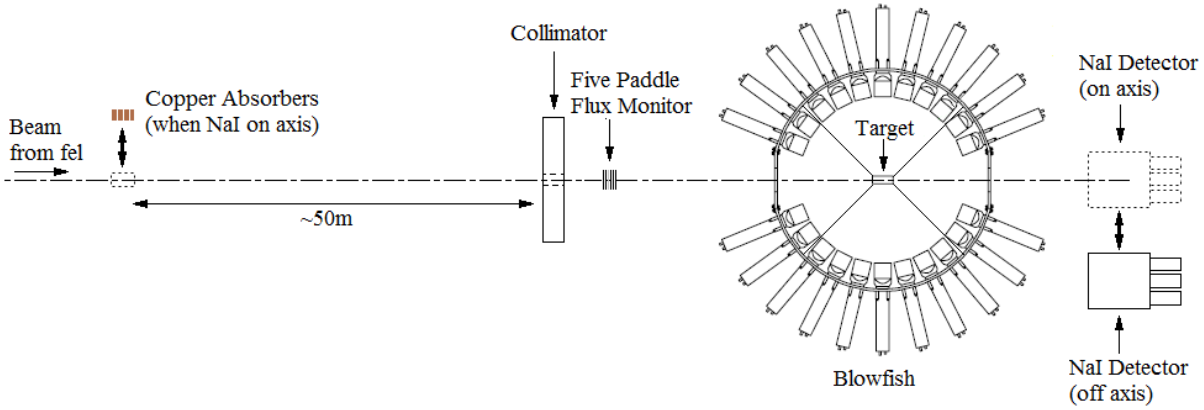

Figure 3.4: Experimental Layout. The beam enters from the free-electron laser (FEL) traveling left to right. The diagram represents the setup during a target run: the copper absorbers and sodium iodide (NaI) detector are both off axis and the target is in Blowfish. When we wanted to measure the NaI flux we added the copper absorbers and slid the NaI detector along its track onto the beam axis. Figure not to scale. Image adapted from Sawatzky [Saw05].

The key components of the experimental layout are diagrammed in figure 3.4. The beam was collimated before entering the Five Paddle Flux Monitor (section 3.9 on page 85), then it traveled some distance through the upper target room and into the lower (main) target room which contained Blowfish. The flux monitor remained on axis for all runs: it sampled the beam in order to determine the number of photons on target, which we use to compute the total cross section. The sodium iodide detector must be kept off axis when running at full flux to prevent damaging the crystal, so copper absorbers had to be added to attenuate the beam when we took sodium iodide flux measurements (used to calibrate the flux monitor).

In this experiment we utilized a 11 mm (≈0.5 inch) radius collimator.

3.5 Targets

Figure 3.5: Long Targets. Image credit: Kucuker [Kuc10]

The targets used in this experiment were built by Kucuker [Kuc10]. All targets were made of 0.2 mm wide Lucite containers with two possible contents: D_2O or H_2O, and two possible lengths: 10.7 cm (long) or 2.0 cm (short). The H_2O target run was performed in order to get an idea of the background neutrons produced from sources other than D.

Target Metrics

Target Contents	Target Length (cm)	Inner Diameter (cm)
D_2O	10.7 ± 0.1	3.6 ± 0.1
H_2O	10.7 ± 0.1	3.6 ± 0.1
Air	10.7 ± 0.1	3.6 ± 0.1
D_2O	2.0 ± 0.1	3.6 ± 0.1
H_2O	2.0 ± 0.1	3.6 ± 0.1
Air	2.0 ± 0.1	3.6 ± 0.1

Table 3.3: The 10.7 cm targets are referred to as the *long* targets and the 2.0 cm targets are referred to as the *short* targets. No uncertainty was provided by Kucuker [Kuc10], and so it had to be assumed to be 1 mm for the target lengths and inner diameters based on the number of significant digits provided.

The targets were held inside a Lucite frame and then suspended inside Blowfish by four wires; the targets were all placed at the center of Blowfish to a precision of 1 mm (see figure 3.6).

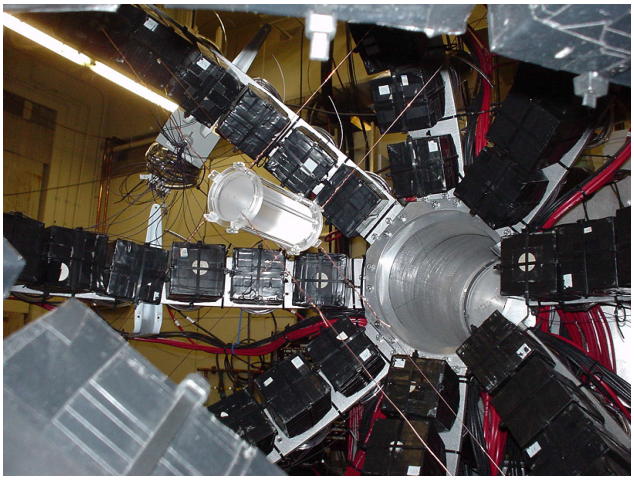

Figure 3.6: A Target Suspended in Blowfish. Image credit: Kucuker [Kuc10]

The Lucite frame was not simulated during the analysis of these data: its contribution was shown to be negligible for 20 MeV photons and therefore is expected to be negligible for 18 MeV photons as well.

3.6 Blowfish

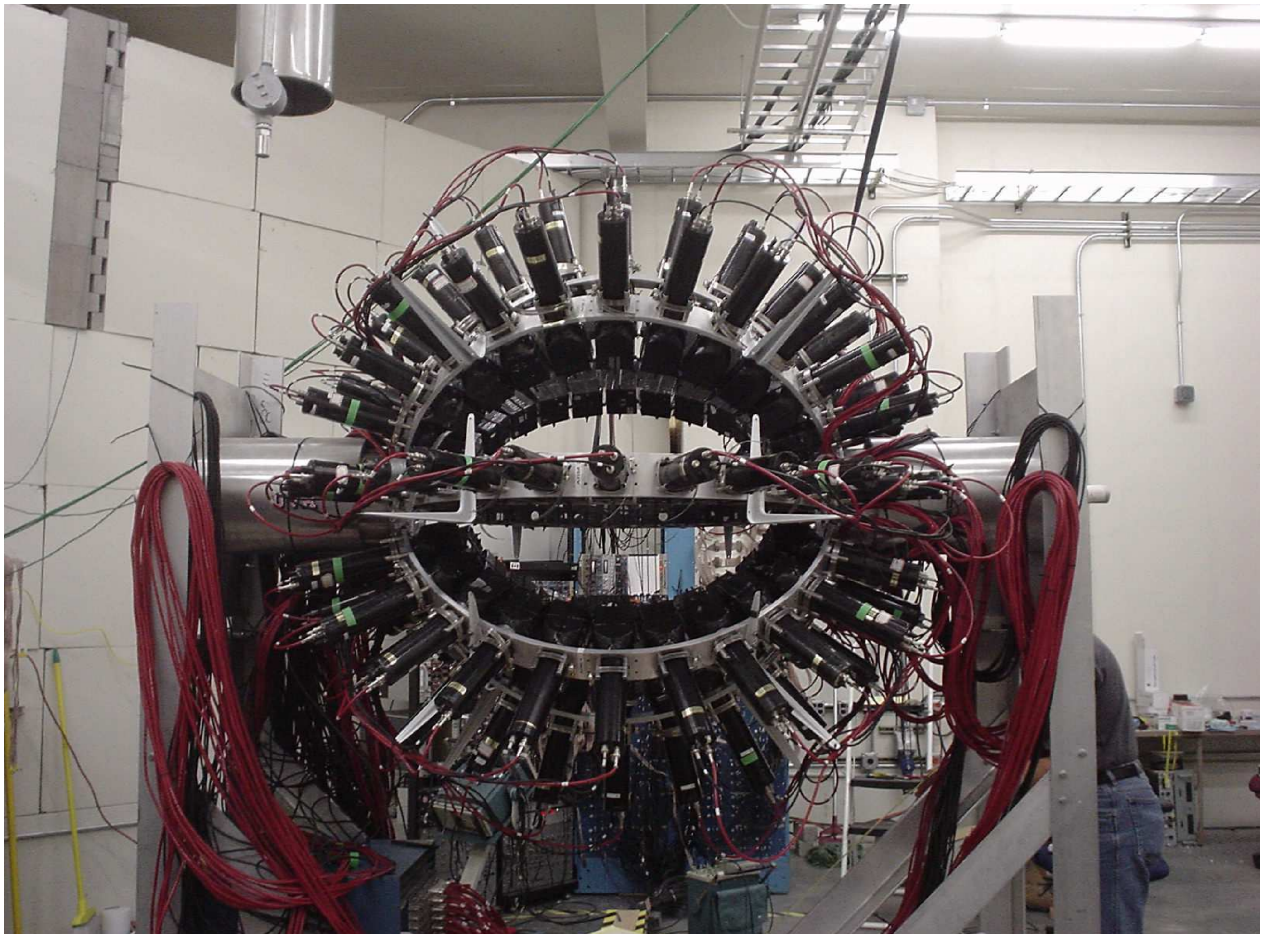

Figure 3.7: The Blowfish Detector Array positioned in the beam-line at HI$\vec{\gamma}$S. The beam enters from the left, travels through the aluminum port, potentially interacts with the target suspended in the middle (not shown), and then, if it fails to interact, exits through the port in the other side. Image credit: Sawatzky [Saw05].

Table 3.4: Blowfish Metrics

Coverage	$\approx \pi$ st, polar angle:$\theta \in [22.5°, 157.5°]$, azimuthal angle: $\phi \in [0°, 360°)$
Internal Radius	40.64 ± 0.30 cm
Num. Detectors	88
Num. Arms	8
Num. Rings	11
Detector Type	BC-505 Scintillator
Detector Surface	7.6 x 7.6 cm^2(active)
Detector Depth	6.4 cm (active)
Detector Surface	8.2 x 8.2 cm^2(external)
Detector Depth	7.1 cm (external)

Blowfish owes its memorable name to its spherical shape and analogous spines which are reminiscent of a blowfish in defensive posture. The spherical shape is designed to sample the entire target emission surface, while the protruding spines are photomultiplier tubes, connected to black detector cells on the inside of the metal arms that span longitudinally down Blowfish.

There are 88 detection cells in the Blowfish Array, each contains a liquid scintillator (BC-505) inside a Lucite container; the BC-505[6] is idealized to measure photons and neutrons, *and is able to differentiate between them.*[7]

The components of Blowfish were initially used in a detector system called Fly's Eye: the hardware was scavenged in 2000 by Brad Sawatzky and Blowfish was constructed from 2000-2001 in a joint effort between the University of Virginia and the University of Saskatchewan. Blowfish was "strongly influenced" [Saw05] by the desire to test the Gerasimov-Drell-Hearn sum rule at HI$\vec{\gamma}$S,[8] that requires measurement of the photodisintegration cross section parallel

[6]The BC name derives from the name of the subsidiary that produces them: Bicron, it has since been "united" under the Saint-Gobain brand.

[7]Even though BC-505 is considered one of the best detectors for pulse-shape discrimination of neutrons and photons: it is no trivial task, see section 5.3.9 on page 184 for more information.

[8]The Gerasimov-Drell-Hearn sum rule experiment *was* finally scheduled to run in November of 2013, but it has since been rescheduled as a yet to be defined run date sometime in 2014.

and anti-parallel to the photon's polarization. This requires measuring θ and ϕ at several positions, ideally symmetrically: hence the spherical distribution of detectors around the target.

In order to reduce spatial and cell biases, Blowfish is capable of being rotated, although this is known to cause problems with the Gain Monitoring System (section 3.10.3 on page 97).

Considered as a whole, Blowfish is well-suited for photodisintegration measurements because it samples a wide range of values in ϕ and θ and is able to differentiate neutrons and photons; unfortunately, it is not particularly efficient,[9] and thus is best used in conjunction with a high flux beam (such as HI$\vec{\gamma}$S).

3.6.1 Detector Coordinates

Blowfish has 88 detectors placed approximately uniformly over a spherical frame covering π steradians ($\frac{1}{4}$ of the surface of a sphere) from $\phi = 0°$ to $\phi = 360°$ and $\theta = 22.5°$ to $\theta = 157.5°$ (θ and ϕ are defined in figure 3.8 on the next page). The aluminum frame has an inner diameter of 40.64 ± 0.30 cm (16.00 ± 0.12 inches), it consists of 8 longitudinal arms; each $\Delta\phi = 45°$ apart and 11 transverse rings, each $\Delta\theta = 13.5°$ apart.

[9] The spatial coverage is $\approx 25\%$, and the neutron detection efficiency for this experiment was $\approx 10\%$, so the total neutron efficiency was $\approx 2.5\%$.

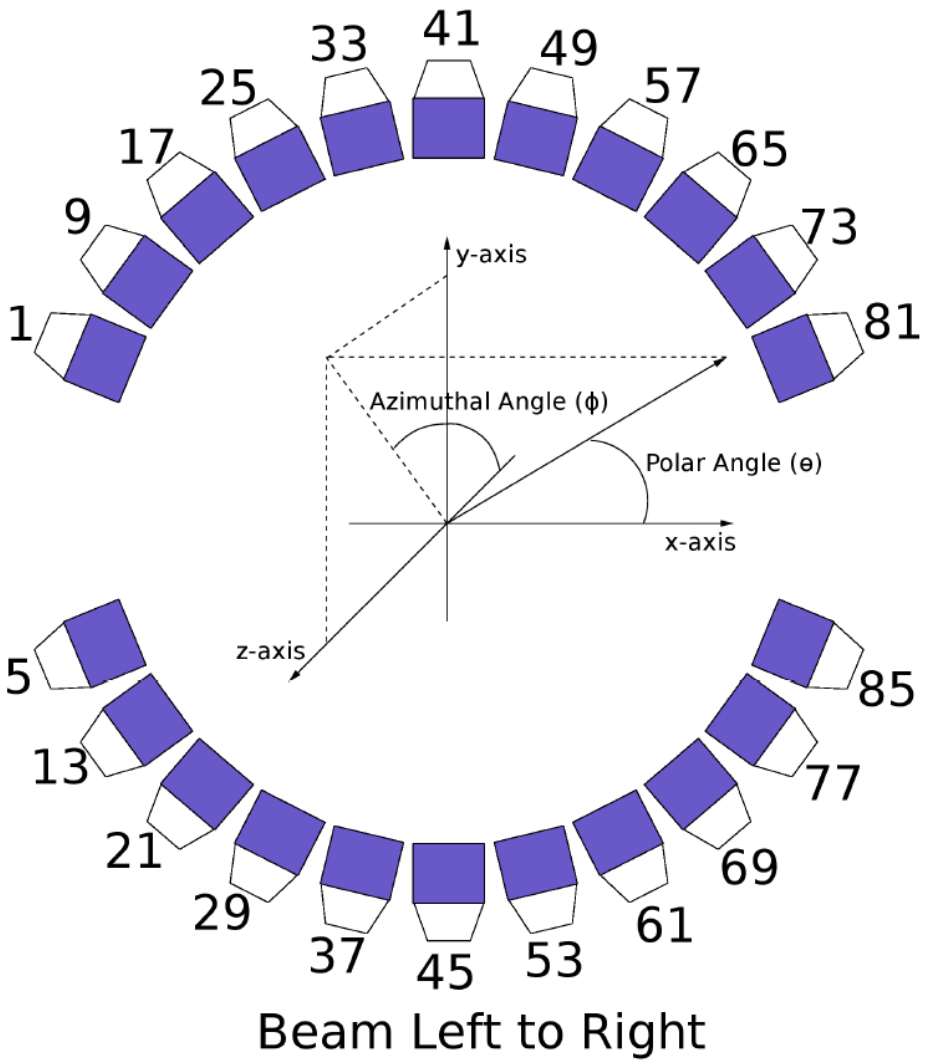

Figure 3.8: Blowfish Coordinates: the x-axis is aligned with the beam. The coordinate system was chosen such that it is harmonized with the GEANT4 simulation. Image credit: Wurtz [Wur10c].

We number the detectors starting at the upstream end[10] and enumerate sequentially in the clockwise direction from the perspective of the beam (see figure 3.9 on the next page).

[10]Upstream of the beam i.e. where the beam enters Blowfish.

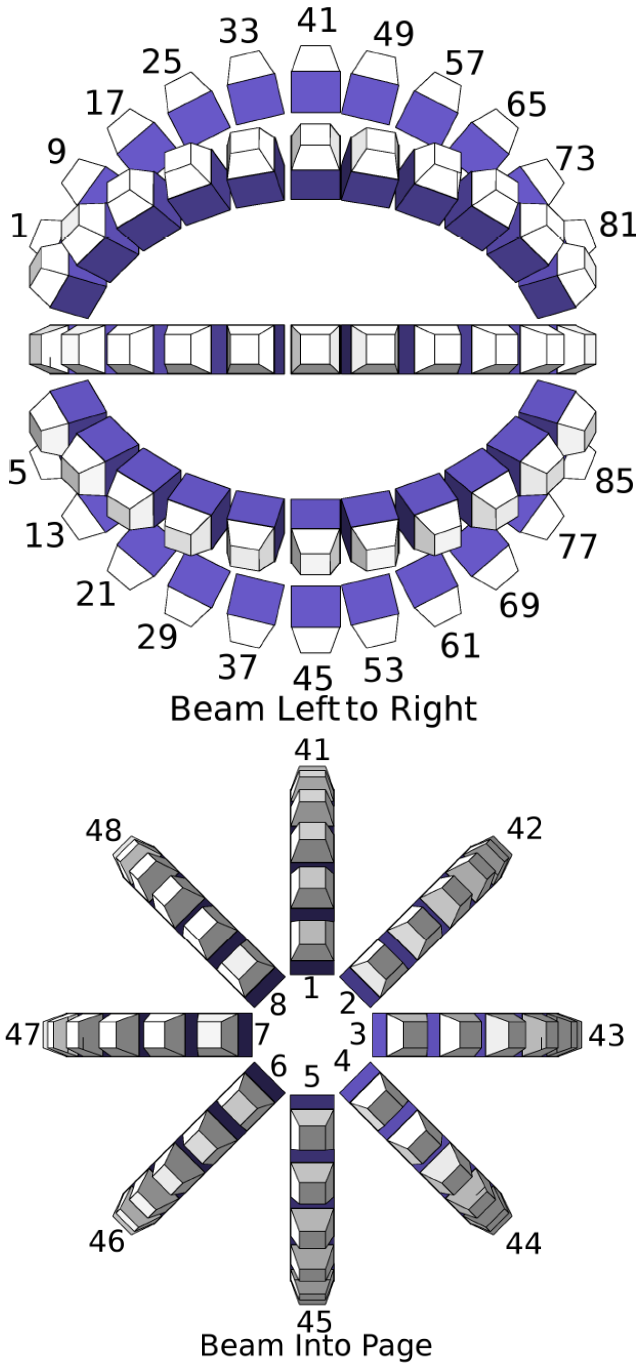

Figure 3.9: Blowfish Detector Numbering. Image credit: Wurtz [Wur10c].

One can convert from detector number to ring and arm number, then subsequently ϕ and θ, respectively.

ϕ is proportional to the arm number, which can be calculated using:

$$\text{arm} = (\text{detector} - 1) \bmod 8 + 1 \tag{3.3a}$$

$$\phi = 45^\circ(\text{arm} - \text{arm on top} + 2) \tag{3.3b}$$

where: ϕ has been defined relative to the beam axis in figure 3.8 on page 66 [Wur10c].

θ is proportional to the ring number, which can be calculated using:

$$\text{ring} = \lfloor \frac{\text{detector} - 1}{8} \rfloor + 1 \tag{3.4a}$$

$$\theta = 157.5^\circ - 13.5^\circ(\text{ring} - 1) \tag{3.4b}$$

where: $\lfloor\ \rfloor$ is the floor operator, and θ has been defined relative to the beam axis in figure 3.8 on page 66 [Wur10c].

When arm 3 is up, the detector locations are correctly described by table 3.5 on the next page.

		Arm Number ($\propto \phi$)							
Ring		1	2	3	4	5	6	7	8
Number	θ	ϕ: 0°	45°	90°	135°	180°	225°	270°	315°
1	157.5°	1	2	3	4	5	6	7	8
2	144.0°	9	10	11	12	13	14	15	16
3	130.5°	17	18	19	20	21	22	23	24
4	117.0°	25	26	27	28	29	30	31	32
5	103.5°	33	34	35	36	37	38	39	40
6	90.0°	41	42	43	44	45	46	47	48
7	76.5°	49	50	51	52	53	54	55	56
8	63.0°	57	58	59	60	61	62	63	64
9	49.5°	65	66	67	68	69	70	71	72
10	36.0°	73	74	75	76	77	78	79	80
11	22.5°	81	82	83	84	85	86	87	88

Table 3.5: Blowfish Detector Arrangement. The cell numbers are provided in the bottom right section. The values of ϕ are given for arm 1 in the horizontal position ($\phi = 0$) i.e. parallel to the beam alignment in this experiment. Table adapted from Blackston [Bla07].

In order to align the cells of Blowfish: a metal rod was inserted along the beam axis, attached to this rod was a second rod capable of swinging in a 180° arc of radius 15.75 inches: when the rotation axis of the second rod was aligned in the center of Blowfish, it was then used to set all of the cell distances to the same value. A spacer of approximately 0.25 inches was inserted between the rod and the Blowfish cells in order to prevent damaging the surface. The inner radius of 16.00 inches is simply the sum of the spacer and rod; the error is estimated at 0.12 inches (40.64 ± 0.30 cm).

3.7 Detector Structure

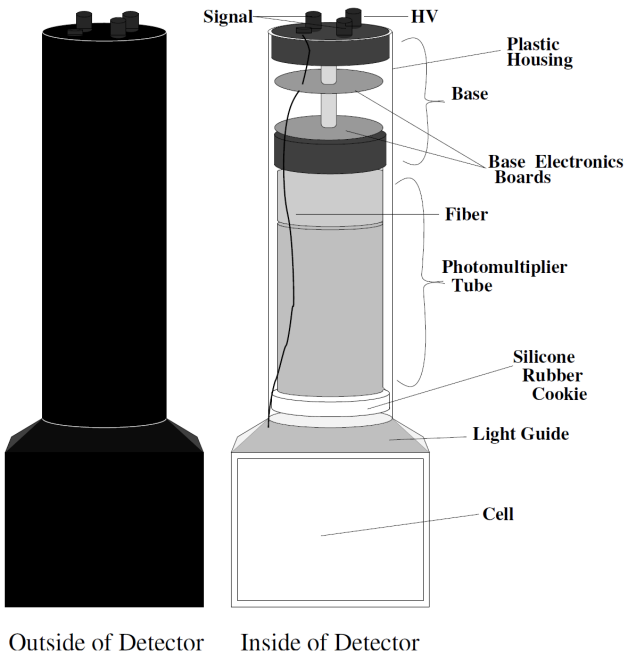

Figure 3.10: A Blowfish Cell. Image credit: Bewer [Bew05].

The 88 detector cells in the Blowfish array each look like figure 3.10 inside: the scintillator is housed in a Lucite box that is connected to a photomultiplier tube via a light guide, kept "optically tight" by the spring and a silicone rubber "cookie". The Lucite box is wrapped loosely in aluminum foil in an attempt to maximize internal reflection of fluorescence, then covered in black tape to keep out ambient visible wavelength light (the process is beautifully described pictorially in Leo [Leo87] pages 197-199).

The process of converting a neutron or photon into a pulse of light is covered in detail in section 3.8 on page 73; however, little attention is given to the step necessary to convert that light pulse into an electronic signal. A photomultiplier tube converts the light pulse into an analogue electronic signal, which then enters the electronics (section 3.10.1 on page 88) where it is converted into a digital electronic signal and, finally, into bits of machine-language data.

3.7.1 Photomultiplier Tubes (PMTs)

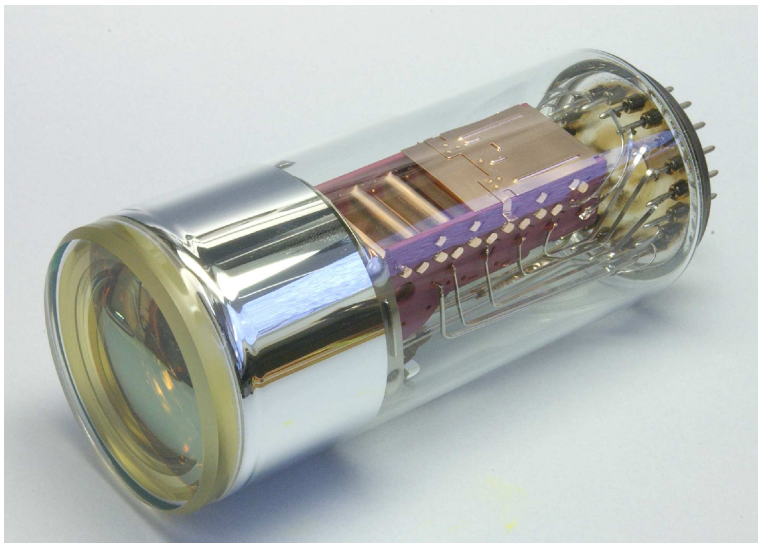

Figure 3.11: A Photonis XP2262 Photomultiplier Tube (PMT). Image credit: Photonis [XP06].

The photomultiplier tubes (PMTs) used in this experiment were Photonis XP2262/B, 12 dynode bi-alkali 51 mm detectors, its properties are summarized in table 3.6. A description of PMT operation follows in this section.

Table 3.6: HadronsPhotonis XP2262/B PMT Metrics [XP06]

Window Material	Lime Glass
Photocathode	Bi-alkali
Refractive Index	1.54 (at 420 nm)
Spectral Range	290-650 nm
Maximum Sensitivity	420 nm

In a Blowfish detector, when the scintillator fluoresces the photon travels down the light guide and into the photomultiplier tube (PMT) where it strikes a phosphorescent coating on the surface window and then, hopefully, the photoelectric effect occurs and liberates an electron that will subsequently start an electron cascade culminating in an electronic pulse

(see figure 3.12). In essence a *photomultiplier* tube *multiplies* the number of *photo*ns detected (i.e. the number of photoelectrons).

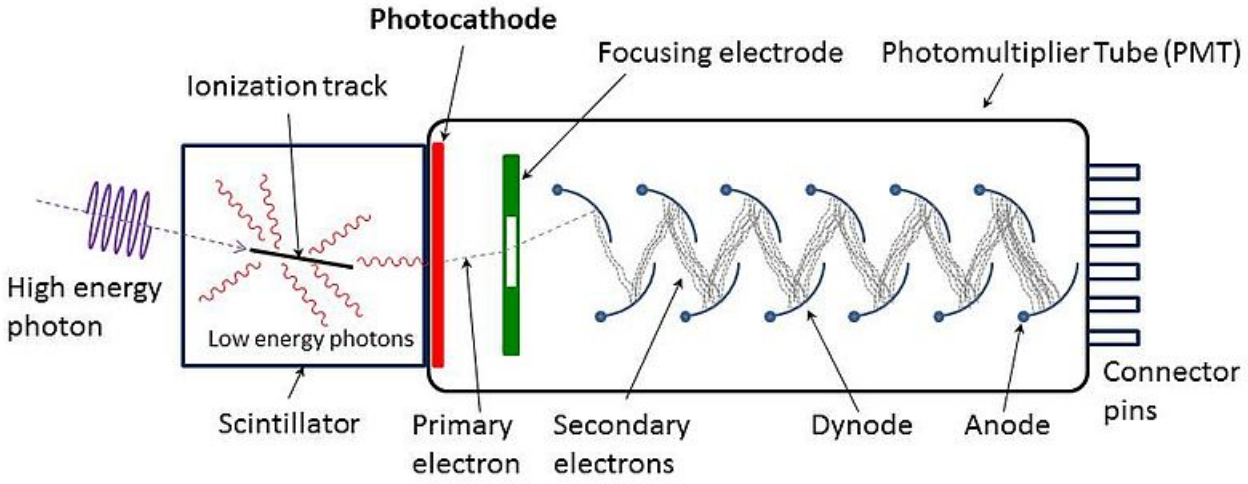

Figure 3.12: Photomultiplier tube operation. Description in text. Image credit: Wikipedia.

The process begins when electrons are generated inside a thin layer of either conductive or semi-conductive material just inside the window which is capable of generating photoelectric electrons: called the photocathode. The relatively small photon energy ($\approx$ eV for optical photons) is barely enough energy to get the electron out of the thin layer photocathode and into the vacuum, and so all PMTs have some threshold wavelength below which they are insensitive.[11]

The photo-electrons enter the vacuum with barely any energy ($\approx$ eV) and hence are readily collected by the focusing electrode and strike the first dynode, which is held at a high voltage ($\approx 140 \frac{\text{V}}{\text{dynode}}$[12]); each dynode is held at a decreasing voltage from cathode to anode. Once the electron strikes the first dynode it generates a spallation of electrons with

[11] Photomultiplier tubes are less sensitive near their energy threshold because there is some spread in electron distance traveled depending on whether the electron is generated on the outside or inside of the photocathode: the photo-electrons do not have enough energy to penetrate this layer.

[12] A typically voltage setting in our experiment was ≈ 1700 V across a total of 12 dynodes, so we expect a $\frac{1700}{12}$ V ≈ 140 V potential per dynode.

multiplicity δ, defined by [Kno00]:

$$\delta = \frac{\text{number of secondary electrons emitted}}{\text{number of incident electrons}} \tag{3.5}$$

Then the spallation of electrons proceeds towards the next dynode and the process repeats until the anode is finally reached and the cascade of electrons becomes an electronic signal that is sent out of the PMT. The electron kinetic energy (and hence the detector *gain*[13]) is a function entirely of the applied voltage: the progenitor photon energy is trivial with regards to the electron kinetic energy after accelerating through a dynode (≈ 140 eV[14]).

The entire process is typically linear [Kno00]: a single photoelectron gets multiplied into $10^7 - 10^{10}$ (approximately 5 per dynode: normal for PMTs like ours) final electrons. The efficiency is dependent on the quantum efficiency of the photocathode (the electron cascade is nearly 100% efficient) and is much less than 100%: we expect it to be on the order of $\approx 25\%$ for our Bi-alkali PMTs at the scintillator's typical wavelength (≈ 400 nm) [Kno00]. We do not account for the PMT efficiency in our simulations because we assume that we always have enough photons from the scintillator to produce a proportional electrical signal.

3.8 Principles of Detection

Recall that the reaction we measured in this experiment was $d(\vec{\gamma},n)p$: we use polarized photons to photodisintegrate the deuteron then measure the recoiling neutron. Thus we are ideally interested in measuring all of the neutrons produced from this process and nothing else. Unfortunately, any detector will be sensitive to particles other than those we desire to measure: we accept this as an inevitability and utilize a detector capable of differentiating between photon and neutron events i.e. one capable of pulse-shape discrimination (PSD; section 5.3.9 on page 184). Furthermore, we can utilize these formerly unwanted photons to: calibrate the gain of our detectors using the Compton continuum, and determine the time of

[13]The number of secondary electrons produced at each dynode is proportional to the kinetic energy of the incident electron, therefore the gain is proportional to the incident electron's kinetic energy.

[14]Assuming a typical voltage of $\approx 140 \frac{V}{dynode}$, after the electron's last dynode interaction it should have a final kinetic energy of ≈ 140 eV when it leaves the PMT.

flight for the particles we detect.

How then does one detect a neutron? A circumspect answer is to first consider how neutrons interact (i.e. deposit energy) in materials, then consider what the best way to observe data in a human-readable format is, then fill in the steps inbetween.

*Neu*trons are electromagnetically *neu*trally charged particles, and they are extremely light: thus if we are to measure neutrons we must either utilize a manifestation of: the weak interaction (e.g. beta decay) or the strong interaction i.e. the nuclear interaction. We want to perform data analysis with a computer, so we must convert the nuclear or weak interaction into an electronic signal which can be read by a computer, and finally converted into something meaningful for humans.

In Blowfish we utilize nuclear scattering between incident neutrons and the nuclei inside a scintillating detector (section 3.8.1) which converts these scattering events into pulses of light, these pulses of light are then collected by a light guide and enter a photomultiplier tube (PMT; see section 3.7.1 on page 71) where they are converted into an analogue electrical signal that can be converted via our data acquisition system (section 3.10 on page 88) into digital data to be manipulated using software into human-readable format.

3.8.1 Organic Scintillators

The first step in converting an incident neutron into human-readable data is the scintillator: in our detector a neutron is most likely to be measured if it has scattered off of a hydrogen nucleus: which recoils and; through a few molecular processes, eventually results in the emission of characteristic photons.

In general, a scintillator is any detector that absorbs energy from its surroundings and emits some portion of it as photons. Organic scintillators are those scintillators which are composed of aromatic hydrocarbons; they are desirable because they have a fast response time ($\approx$ ns), and are rich in hydrogen which; as is evident in eq. (3.6) on the next page, can absorb a large portion of the incident neutron's kinetic energy: thus the average neutron only has to hit a few times to deposit all of its energy in the detector; furthermore, hydrogen has

a relatively large cross section for neutron elastic scattering.[15]

The energy absorbed by a recoiling nucleus after being hit by a neutron in a non-relativistic elastic scattering event is:

$$E_{recoil} = \frac{4A}{(1+A)^2} cos^2\theta E_{neutron} \tag{3.6}$$

where: E_{recoil} is the kinetic energy of the recoiling nucleus hit, θ is the angle between the incident neutron and the recoiling nucleus, $E_{neutron}$ is the incident neutron kinetic energy, and $A = \frac{\text{mass of recoil}}{\text{mass of neutron}}$, which is approximately the atomic number of the recoiling nucleus [Kno00].

The process of conversion from neutron scattering inside the scintillator to emission of characteristic photons via fluorescence[16] is outlined as follows, and diagrammed using energy levels in figure 3.13 on page 77.

The process of neutron-induced scintillation:

1. The neutron scatters off of hydrogen or some other nucleus.

2. If the neutron scatters off of hydrogen causing ionization, this produces a proton with energy given by kinematics. The neutron could just as well scatter from a different nucleus, but we will focus on protons for argument's sake; neutron-proton scattering is the dominant process anyways (as shown in section 3.8.2 on page 80).

3. The liberated proton interacts readily with the electrons found inside the scintillator. Most of the proton's energy is lost due to *quenching*: non-radiative energy transfer [Kno00] (not measured).

4. Some of the electrons that interact are the π electrons from the *fluor* molecules,[17]thus exciting them to higher energy levels: we consider singlet and triplet states.

5. The excited π electrons either fluoresce promptly (from a singlet state), or enter quasi-stable triplet states.

[15]Hydrogen also has a well measured neutron scattering cross section: allowing for accurate/precise efficiency estimates.

[16]We use the definitions: fluorescence: de-excitation of *singlet* state via emission of a single photon; phosphorescence: de-excitation of *triplet* state via emission of a single photon [Kno00].

6. The excited triplet states may phosphoresce, or collide with other excited molecules [Kno00] and return to the singlet state, then emit delayed fluorescence. Quenching increases the rate of triplet state collisions by increasing local concentration of triplet states.

Photon-induced scintillation proceeds in the same manner with the exception that the photons are vastly more likely to interact with the atomic electrons rather than nuclei, and thus they cause recoiling electrons to interact with the scintillator's π electrons. By interacting via electrons, the photons cause much less quenching than neutrons do and therefore produce less delayed fluorescence.

[17]The *fluor* molecules are those that actually result in fluorescence; the other major components of scintillator are an absorber and a wavelength shifter (optional) [Kno00].

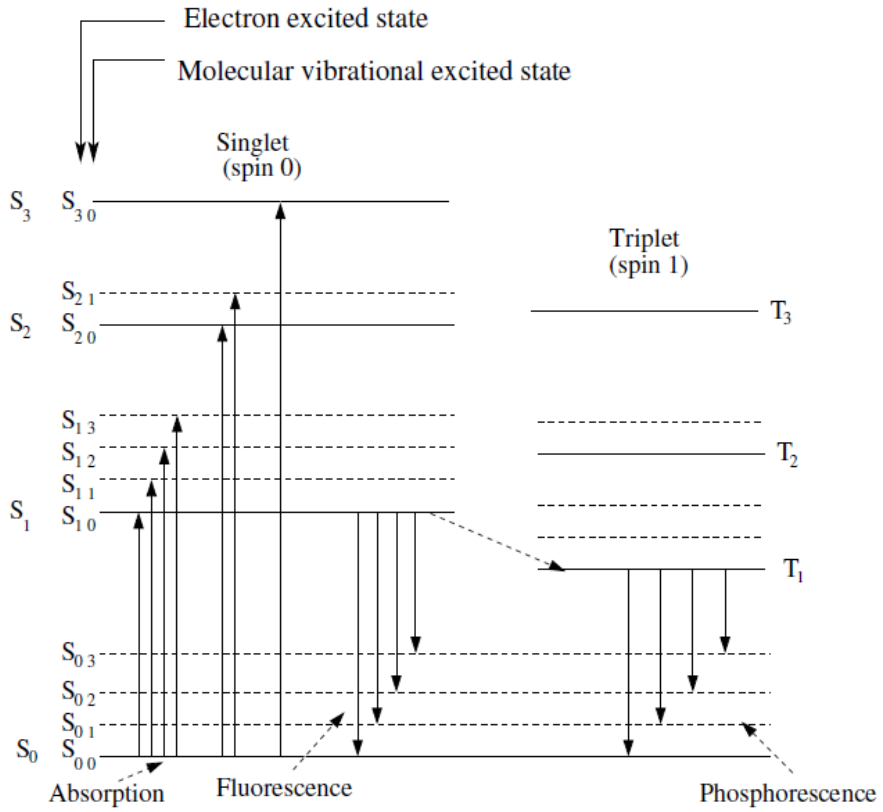

Figure 3.13: Scintillator Excitation (Energy Levels). The singlet state decays rapidly ($\tau \approx$ ns) while the triplet state remains meta-stable for a much longer time (up to ms). Pulse-shape discrimination (section 5.3.9 on page 184) relies on the excitation of triplet states back into singlet states which subsequently fluoresce (called *delayed fluorescence*) [Kno00]. Image credit: Bewer [Bew05].

The important difference between the scintillation processes induced by photons versus neutrons is the frequency of delayed fluorescence: it is more frequent when neutrons interact with the scintillator. It is important to note that when a particle interacts with a scintillator, it results in *many* excited π electrons, not just a few; and we therefore expect to see an emission spectrum that includes prompt and delayed fluorescence. Since neutrons result in more delayed fluorescence events than photons, we furthermore can expect to see that neutron interactions with a scintillator will result in longer light pulses than photons. This is exactly what is observed (see figure 3.14 on the next page) in organic scintillators, other types of scintillators tend to destroy this particle-type information or fail to produce it: hence our

motivation for using an organic scintillator.

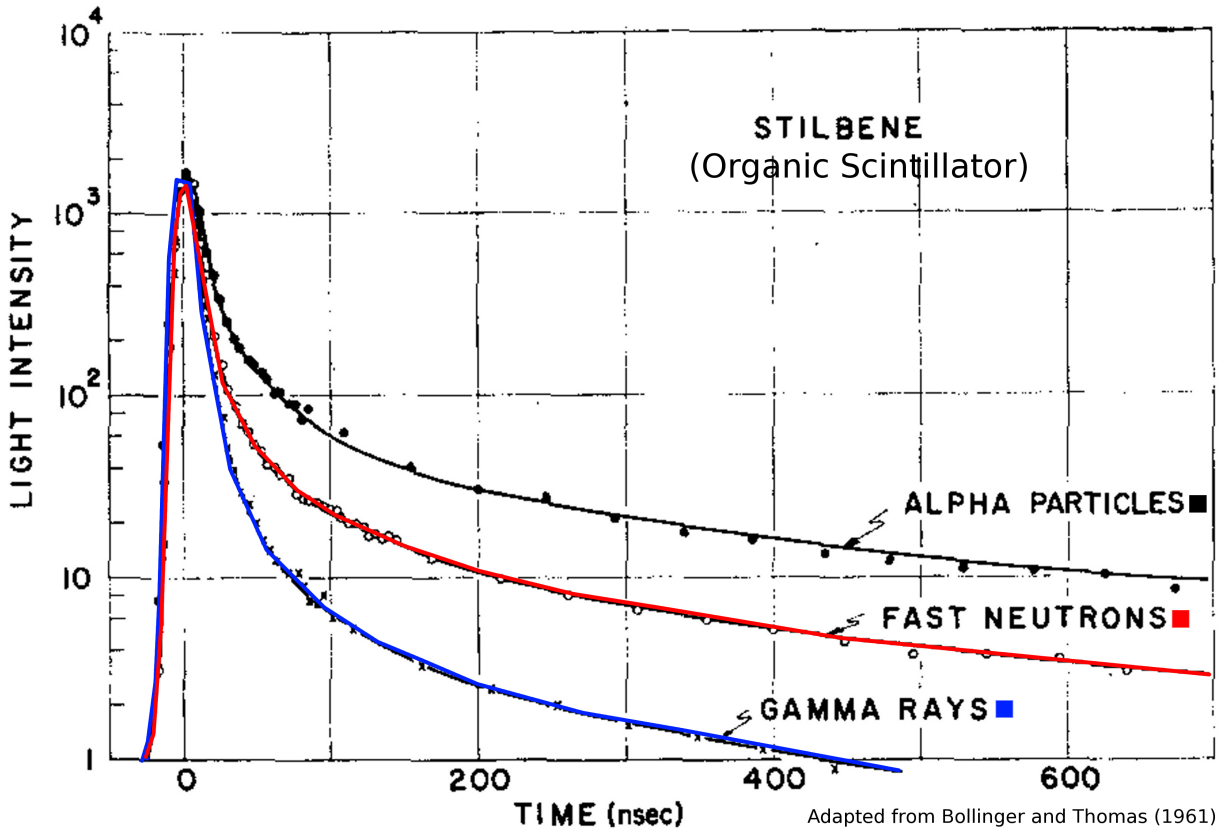

Figure 3.14: Light Response of Stilbene (normalized). As you can see, neutrons cause longer light pulses than gamma rays (photons): this difference in pulses can be used to discriminate between the two (i.e. pulse-shape discrimination: section 5.3.9 on page 184). Image credit: Bollinger and Thomas [Bol61].

BC-505 Liquid Organic Scintillator

BC-505 is formulated to provide the best overall performance of any liquid scintillator. It has the highest light output of any liquid (80% anthracene) and excellent light transmission. Its high flash point (48° C) renders it particularly suitable for use in large volume detectors such as anti-Compton and anti-coincidence shields and high energy neutron detectors. -Saint-Gobain Crystals (manufacturer) [Sai08]

The reader is advised to take Saint-Gobain Crystals' BC-505 sales-pitch with a grain of

salt; for instance, its purported "high flash point" of 48°C does not exactly instill confidence (it's really only "high" relative to other liquid organic scintillators). The full metrics of BC-505 as provided by Saint-Gobain Crystals [Sai08] are shown in table 3.7, and its emission spectrum is shown in figure 3.15.

Table 3.7: BC-505 Metrics [Sai08]

Light Output	80% of anthracene
Wavelength of Maximum Emission	425 nm
Decay Time (fast)	2.5 ns
Density (20°C)	0.887 gcm^{-3}
Ratio of H/C Atoms	1.331
Refractive Index	1.505
Flash Point	48°C

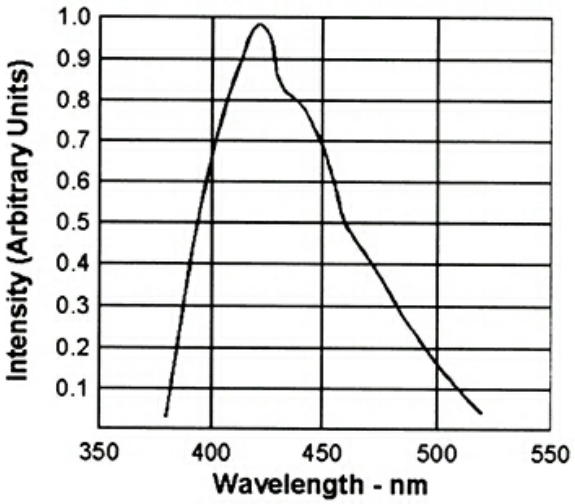

Figure 3.15: BC-505 Emission Spectrum. Image credit: Saint-Gobain Crystals [Sai08].

Sawatzky [Saw05] compared BC-505 to a few other liquid scintillators: a summary provides perspective for the BC-505 metrics (table 3.8 on the next page).

Table 3.8: BC-505 Comparison [Saw05]

Property	BC-505	NE-213	NE-102
Light Output(% anthracene)	80	78	65
Flash Point (°C)	48	26	N/A
Density (gcm^{-3})	0.877	0.874	1.03
Ratio of H/C Atoms	1.331	1.211	1.103

Reading table 3.8, it should be clear that BC-505 benefits from a relative high light output and flash point, both making it easier to work with. In fact, the relative ease with which BC-505 can be handled was the deciding reason for its choice over other liquid organic scintillators: specifically the fact the BC-505 doesn't dissolve Lucite and hence could be placed in Lucite containers [Pyw].

Relative to solid organic scintillators, liquid organic scintillators (like BC-505) have the advantages of: being far more resilient to radiation damage, being cheaper, and typically being superior at performing pulse-shape discrimination [Kno00]. The downside to liquid organic scintillators is the necessary use of a volatile and reactive solvent.[18]

3.8.2 Scintillator Light Output

The obvious importance of understanding the light output of our scintillators is that without it we would be unable to detect anything: what good is a scintillator that doesn't scintillate! What is not obvious is that the light output spectrum is an indispensable tool for determining the detector efficiency and validating the simulated detector response. The reason for this is that although the spectrum has a complex analytical structure to ensure that a serendipitous fit is unlikely, the physical processes are sufficiently simple that the spectrum can be parameterized and simulated.

Bormann *et al.* [Bor70] decomposed the light output spectrum from stilbene (a solid organic scintillator) into physical processes that were simulated using the Monte Carlo Method

[18]Liquid organic scintillators are, in fact, simply solid organic scintillators which have been dissolved in a solvent. Since solid organic scintillators are plastics this means it is very difficult to find a liquid organic scintillator that can be kept inside a plastic container.

(section 4.2.3 on page 109), their results are shown in figure 3.16.

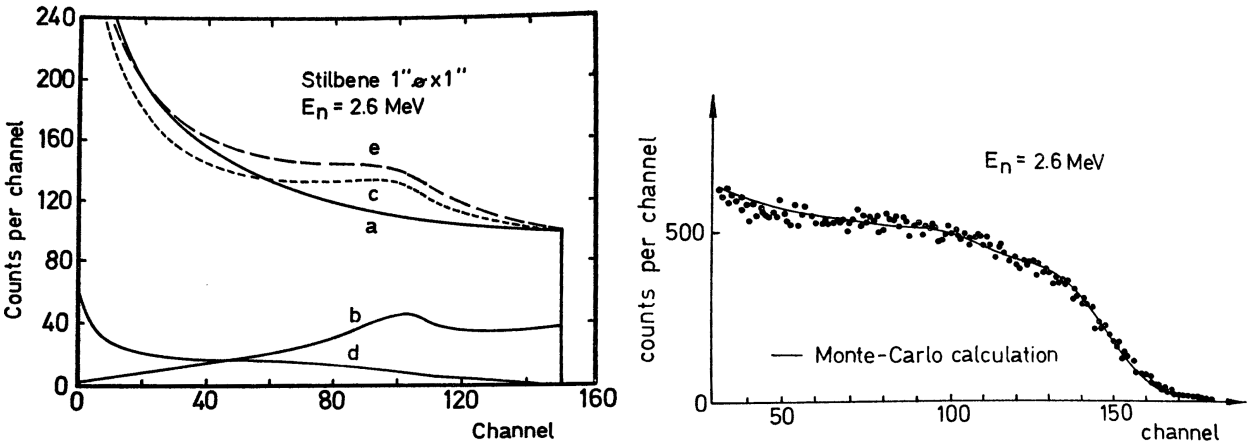

Figure 3.16: Stilbene Detector Response. Left: Bormann *et al.* [Bor70] calculated the separate effects of three processes occurring in the detector (a,b and d): (a) single n-p[19]scattering with edge-effects, (b) double n-p scattering, (c) a + b, (d) n-p scattering after the neutron has been scattered off of a carbon nucleus, and (e) sum of all effects. Right: their experimental results confirm their Monte Carlo calculation (the tail is a detector edge effect which has been suppressed in the left image).

The light output spectrum from Bormann *et al.* [Bor70] bears a resemblance to the light output of our scintillator, BC-505: figure 3.17 on the next page.

[19]n: neutron, and p: proton.

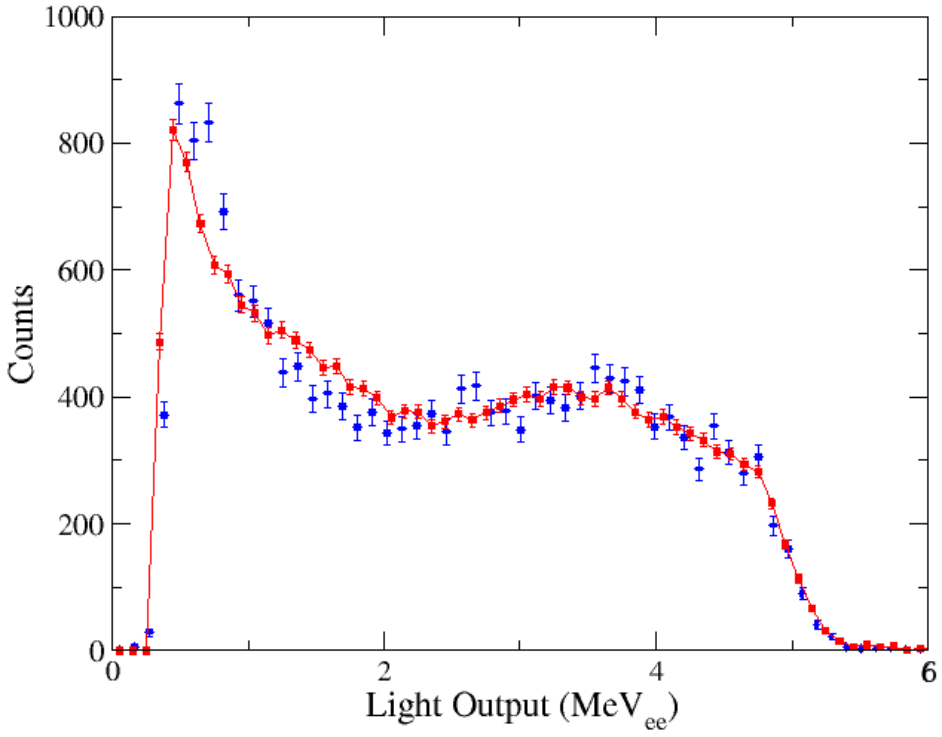

Figure 3.17: BC-505 Light Response [Pyw06] to 8.9 MeV neutrons. The experimental data (blue points) compared to the GEANT4 simulation (red points) which is based on the parameterization (solid red line). The simulation reproduces the experimental data well. Notice the qualitative similarity between this figure starting at $\approx$ 3 MeVee and figure 3.16 on page 81: evidently the dominant physical processes are still: n-p, n-carbon + n-p, and double n-p scattering, and edge effects. Image courtesy of Dr. Robert Pywell.

Figure 3.17 was used to validate the simulation when the efficiency of the detector was known [Pyw06] and thus can now be used to determine the efficiency of the detector using the simulation. The latter is done by simply applying the same light output cut (and all other cuts; section 5.4 on page 193) to the simulation and the experimental data then normalizing the number of simulated neutrons into an efficiency (via efficiency $= \frac{\text{neutrons measured}}{\text{neutrons emitted}}$).

Extraction of the light output parameters was performed in Pywell *et al.* [Pyw06] using the following derivation:

Pywell *et al.* start with the expression from Chou [Cho52]:

$$\frac{dL}{dx} = S\frac{dE}{dx}[1 + kB(\frac{dE}{dx}) + C(\frac{dE}{dx})^2]^{-1} \equiv Sf(\frac{dE}{dx}) \tag{3.7a}$$

Where: S is a scaling factor, $kB = 0.0061 \pm 0.0003$ gcm^{-2}MeV^{-1} and $C = (1.0 \pm 0.1) \cdot 10^{-5}$ g^{2}cm^{-4}MeV^{-2} are fit parameters, L is the light output, E is the energy, and x is the position.

Then a particle that stops at a distance R into the material will cause light output, L:

$$L(E) = \int_0^R \frac{dL}{dx}dx = S\int_0^R f(\frac{dE}{dx})dx \tag{3.7b}$$

A "*minimum ionizing particle*" has approximately constant energy loss: $\frac{dE}{dx}_{min} \approx$ constant $\implies f(\frac{dE}{dx}_{min}) \approx$ constant (as demonstrated at the highly relativistic energies in figure 2.8 on page 26) so the integral becomes:

$$L(E_{min}) = Sf(\frac{dE}{dx}_{min})\Delta x \tag{3.7c}$$

The energy deposited in this process must be:

$$E_{min} = \frac{dE}{dx}\Delta x \tag{3.7d}$$

Pywell *et al.* then defined the gain such that $L(E_{min}) = E_{min}$. This enables them to combine eq. (3.7c) on page 83 and eq. (3.7d) on page 83 and solve for the scaling parameter, S:

$$S = \frac{dE/dx_{min}}{f(dE/dx_{min})} \tag{3.7e}$$

Substituting in the scaling parameter, S, into eq. (3.7b) on page 83:

$$L(E) = \frac{dE/dx_{min}}{f(dE/dx_{min})} \int_0^R f(\frac{dE}{dx})dx \tag{3.7f}$$

where: dE/dx_{min} is a measured parameter of the scintillator and f is given by eq. (3.7a) on page 83.

The minimum ionizing energy (dE/dx_{min}) is considered a property of the scintillator; not the incident particle type, it was calculated using the Bethe-Bloch formula with shell corrections at low energies; the other parameters of f (i.e. kB and C) were measured using neutrons of known energy [Pyw06]. Eq. (3.7f) can now be simulated in GEANT4 using the Monte Carlo Method i.e. evaluating the expression at each step, Δx, the particle takes through the scintillator.

In this experiment, we used the parameters from Pywell *et al.* [Pyw06]: $kB = 0.0061 \pm 0.0003$ gcm^{-2}MeV^{-1}, $C = (1.0 \pm 0.1) \cdot 10^{-5}$ g^{2}cm^{-4}MeV^{-2}, and $\frac{dE}{dx}_{min} = 2.00$ MeVg^{-1}cm^2. We also used the GEANT4 implementation based on these parameters; written by Pywell et al [Pyw06].

3.9 The Five Paddle Flux Monitor

Figure 3.18: The Five Paddle Flux Monitor.

In this experiment we utilized the third generation of flux monitors at HI$\vec{\gamma}$S: the Five Paddle Flux Monitor. The Five Paddle Flux Monitor (Five Paddle) was constructed by Octavian Mavrichi as his MSc project [Mav10] (its design was published in 2009 [Pyw09a]), it was an improvement on the Three Paddle Flux Monitor, which was itself an improvement upon the initial One Paddle Flux Monitor. Five Paddle is capable of measuring the beam flux at HI$\vec{\gamma}$S to within 2% systematic error [Mav10] (using eq. (5.8) on page 212).

Five Paddle is, appropriately, composed of five detecting paddles: each paddle is a 2 mm BC-400 solid plastic organic scintillator coupled to a PMT [Mav10]. The particles it is designed to detect are electrons and positrons produced by the radiator: a 2 mm sheet of aluminum located between the 2nd and 3rd paddles (counting from upstream). High energy electrons/positrons are highly interacting[20] but they are virtually undeflected by each interaction (until they slow down) and will usually penetrate through all three of the downstream paddles.[21]

[20]For example, the likelihood of a 9 MeV electron interacting with one of the paddles is very close to 1: $\approx 1 - e^{-10000}$ [Rud04].

[21]For example, the likelihood of a 9 MeV electron being absorbed by one of the paddles is only $\approx 4\%$. The likelihood of the same electron being absorbed by the air gap between paddles is negligible $\approx 0.05\%$ [Zuc11].

This means that the electrons/positrons produced by the radiator will have a high probability of traveling in a straight line: through each of the three paddles, and depositing some of their energy in each paddle. In contrast, a photon has only a $\approx 1\%$[22] chance of interacting with a paddle, meaning that the likelihood of interacting with three has a probability of $\approx \frac{1}{1000000}$. What this all means is: *the Five Paddle Flux Monitor is simultaneously non-intrusive (it barely attenuates the beam) and efficient (the photons it does attenuate are almost all measured).*

In order to compensate for other highly interacting charged particles e.g. cosmic ray muons and electrons/positrons from other sources,[23] a veto paddle is placed in front of the radiator. Events are recorded which include a coincidence between paddle 3, 4 and 5, and an anti-coincidence with paddle 2: the veto paddle; the number of veto events is also recorded in order to perform a flux correction. An example of which events would be counted or excluded is diagrammed in figure 3.19 on the next page.

[22]The probability of an 18 MeV photon interacting with a 2 mm paddle of BC-454 (a different solid organic scintillator) is 1.04% [Sai11], we assume that interacting with BC-400 would have a similar likelihood.

[23]When in the beam-line, the Five Paddle Flux Monitor is sandwiched between two beam attenuators capable of producing fast electrons.

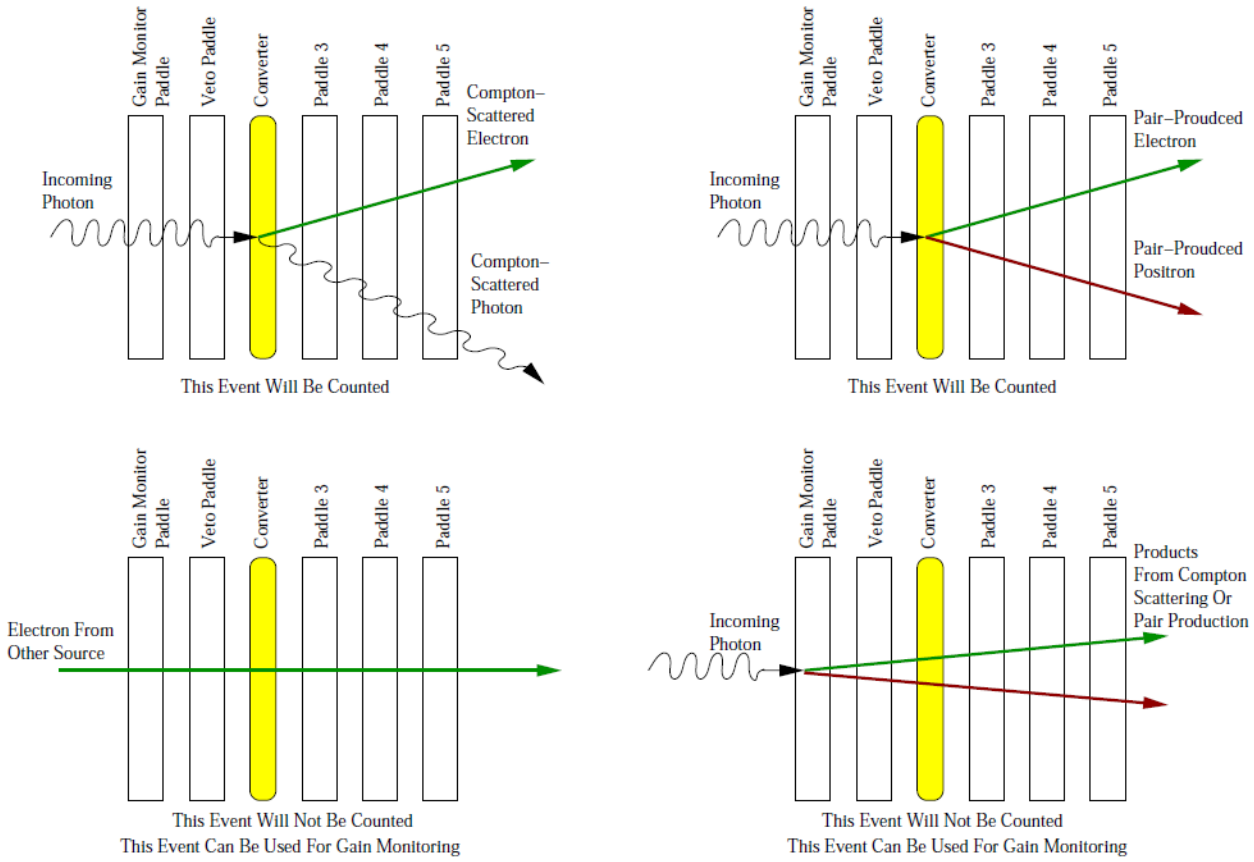

Figure 3.19: Five Paddle Flux Monitor Acceptance. Only those events which interact with paddles 3, 4, and 5 are measured; if they interact with paddle 2 (the veto paddle) then they are automatically excluded. The converter (i.e. radiator) is designed to produce high energy electrons in order to sample the beam flux. Image credit: Wurtz [Wur10c]

In order to compute the beam flux we need a calibration factor (f'_m in eq. (5.8) on page 212), extracted using the sodium iodide detector flux data along with the Five Paddle flux data. The sodium iodide detector measures the beam intensity directly from the HI$\vec{\gamma}$S beam by being placed in the beam-line; its position is diagrammed in figure 3.4 on page 60.

3.10 Data Acquisition System

Once an analogue electrical signal has been generated by the detectors, their job is done. The signal travels into the electronics of the data acquisition system where useful information is extracted from the analogue signals and converted into digital signals to be: read, converted into software variables, and then saved by the data acquisition software: Lucid (section 3.10.6 on page 102).

3.10.1 Circuit Logic

Electronic logic modules are used to increase data acquisition efficiency, for example by doing basic exclusions and coincidence registries in order to properly characterize Blowfish's live-time. Raw data enter the electronics in analogue electronic form directly from the detectors and into the CF8000 discriminators where they begin their circuit logic path: eventually being stored in the time-to-digital converters (TDCs) and analogue-to-digital converters (ADCs) as digital signals to be read out by Lucid. The logic circuits used in this experiment for data collection are provided in full in this section together with brief overviews for each.

Additional circuit logic is discussed in: section 3.9 on page 85 (The Five Paddle Flux Monitor), and section 3.10.3 on page 97 (The Gain Monitoring System).

The circuit diagram labeling convention is provided in figure 3.20 and figure 3.21 on the next page

Figure 3.20: Circuit Symbol Legend. The veto windows are continuous yes/no logic signals, the trigger signals are toggle yes/no logic signals, and the software signals are toggle yes/no logic signals sent by the front-end computer.

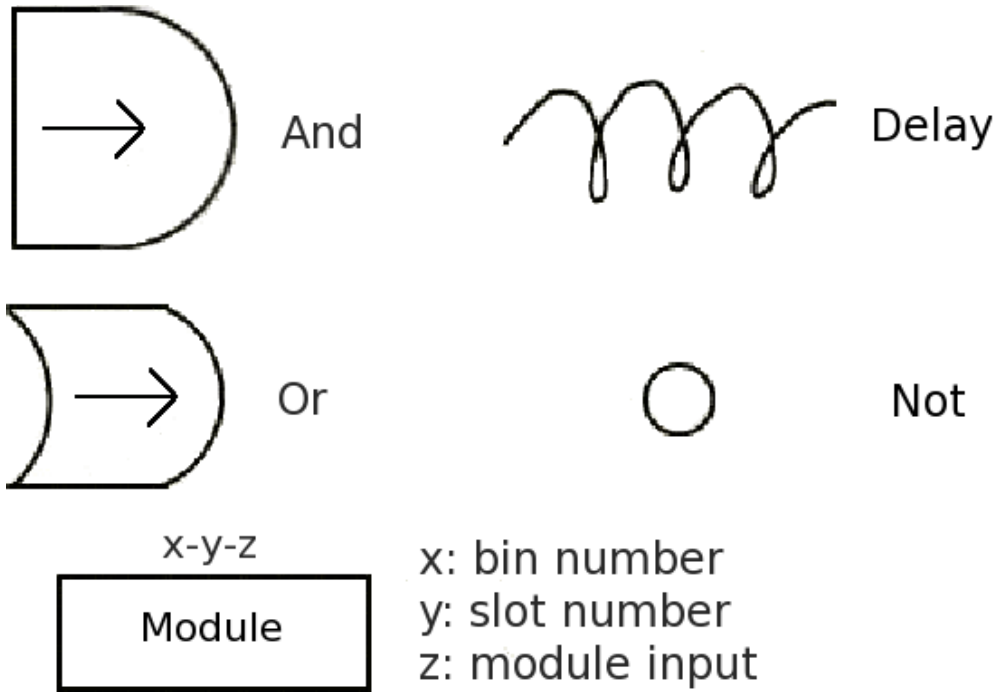

Figure 3.21: Logical Symbols Used for Circuit Diagrams: symbol with meaning to right of it. Note: a 'not'+'or' symbol with only one input is drawn instead of simply a 'not' symbol.

The Data Acquisition Windows

The first logical circuit to consider handles the acquisition windows (figure 3.22 on the next page): these determine whether or not data are able to enter the electronics.

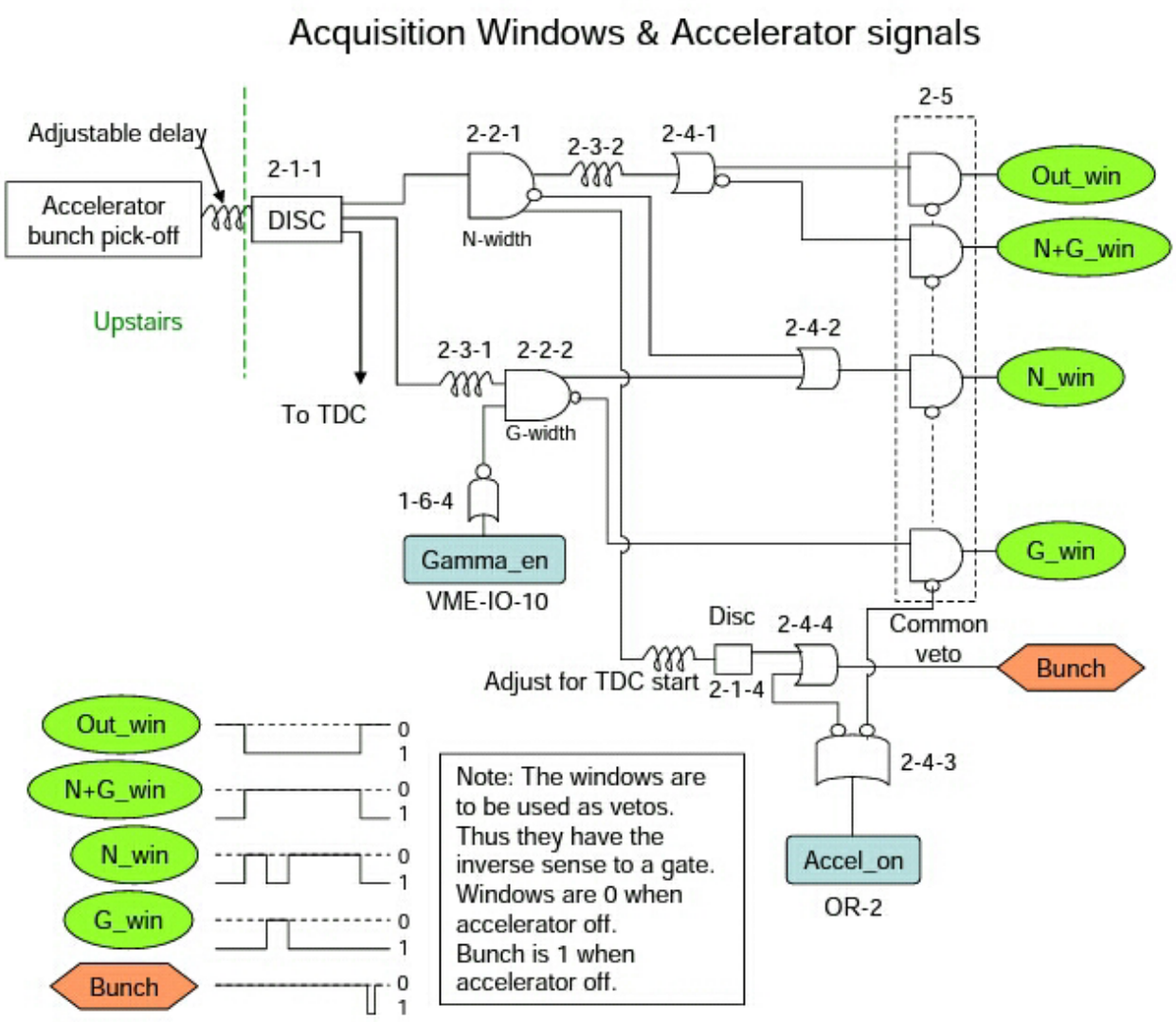

Figure 3.22: Data Acquisition Windows. These *veto* windows determine when data should be accepted or not: 0: data in/off, 1: no data/on. Data are allowed to enter when windows are closed (i.e. 0). Definitions: N: neutron, G: gamma ray, win: veto window, Gamma_en: gamma enabled, and Accel_on: accelerator on. All windows start with a suitably delayed signal from the accelerator (the bunch pick-off signal): this is when electrons are expected to be in position to produce gamma rays. N_win is used to accept data normally; the notch in time with G_win is used to pre-scale the number of hits in the region where the beam is expected. These windows are adjusted using N-width and G-width. Gamma_en and Accel_on are commands executed by the reader running on the front-end computer (see section 3.10.6 on page 102).

We know that the photon beam at HI$\vec{\gamma}$S operates (ideally) with a definite frequency: 5.58 MHz, and we furthermore know the time when the FEL is able to produce gamma rays. We use these data in the form of the "bunch pick-off" signal i.e. a logic signal sent from the accelerator indicating that gamma rays may have just been produced. After a suitable delay (allowing the gamma rays to travel the rest of their path and hit the target), we allow this signal to enter the logic circuits in order to determine an appropriate start time for the data acquisition system to begin accepting data. This results in: (1) an appropriate start time to turn on the TDCs, and (2) the four data acquisition *veto windows*.[24]

The four windows are: Out_win, N+G_win, N_win (i.e. the neutron window), and G_win (i.e. the gamma window); their respective purposes are: accept no data, accept all data, accept all data except the data near the arrival time of the beam, and accept just the data near the arrival time of the beam (these windows are diagrammed on figure 3.22 on page 90). G_win can be enabled periodically by Lucid to send a Gamma_en signal so that beam photons can be used to calibrate the time-of-flight. The accelerator can be enabled or disabled using Lucid to toggle Accel_on: when the accelerator is disabled all of the windows are vetoed i.e. data are always accepted.

The Detector Circuits

The next logical circuit (figure 3.23 on the next page) handles the actual detector data from the cells. The purpose of this circuit is to apply basic exclusions and classifications, then send the data to the TDCs and ADCs where they are digitized and recorded.

[24]When a veto window is disabled: data can come in, when the veto window is enabled: data can't come in. The windows work the way you would expect them to e.g. N_win (the neutron window) allows data to enter only at times when neutrons should be observed.

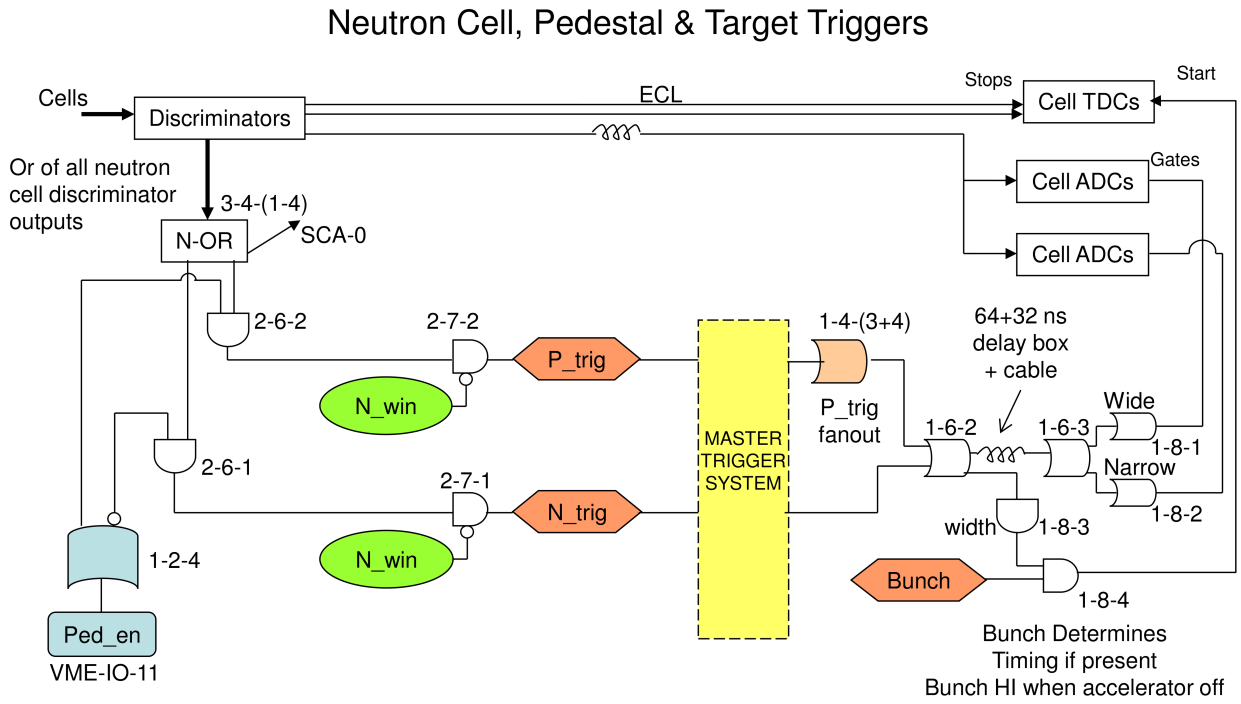

Figure 3.23: Detector Circuit. The Neutron Cell, Pedestal and Target Triggers handle acquisition of the detector data: it determines whether or not the analogue electronic signal from the detectors are stored as digital values in the TDCs and ADCs. Definitions: IGOR: independent-gate ADC 'or', IG: independent-gate ADC, N-OR: 'or' from all of the cells combined, ECL: emitter-coupled logic,[25]Ped_en: enable pedestals, and SCA: scaler.

The logic circuit starts at the discriminators where the raw analogue signal enters from the detectors. The raw signals entering the discriminators are allowed to pass through to the TDCs and ADCs directly after running through a delay: the ADCs can then integrate the amount of charge in the pulse which arrives within the time interval defined by a gate supplied to the ADC; in the event that a discriminator receives a raw signal above its threshold, it also outputs a logical signal to the N-OR (neutron master 'or') module informing the data acquisition system that an event has occurred, and a second signal to the TDCs providing

[25]Emitter-coupled logic is a logic signal that operates based on the relative voltage difference between two signals instead of relative to 0.

the arriving time for the detected particle (by stopping the cell's TDC channel).

The TDC signals are a bit confusing because there are several delays involved which result in the particle being measured by the discriminator before the TDC is actually started. In simplest terms: the bunch signal from the accelerator starts the TDCs and the discriminators stop a specific TDC channel if an event is detected in that TDC channel's respective Blowfish cell; appropriate delays are put in place so that the bunch signal only starts the TDCs if there is a particle in one of the cells, but the relative time between the bunch signal and the particle's detection time is preserved. All TDCs are started after any one cell records a hit above the discriminator's threshold which was in coincidence with the delayed bunch signal from the accelerator (if enabled), the stop signal is given the same delay (approximately) so that it arrives some time after the bunch signal which is proportional to the detected particle's time-of-flight. The beam photons which scatter from the target arrive at approximately the same time in the TDC and can be used as a reference time for the other signals in the TDC spectrum, thus allowing the conversion of the TDC spectrum into a time-of-flight spectrum.

The P_trig is initiated by Lucid sending a Ped_en signal to the ADCs; the next event recorded by a discriminator results in pedestal events for each cell which are a record of the DC (direct current) offset of the ADC (see section 5.3.2 on page 158).

The N_trig is a neutron trigger event which corresponds to real data arriving at an appropriate time.

A logic pulse passing through either the neutron or pedestal trigger enters the Master Trigger System (see section 3.10.1 on the next page) where it is vetoed if the data acquisition system is not ready to accept it, or allowed to pass otherwise. In the event that the pulse passes through the master trigger system, it is delayed and then split into a "wide" logic pulse and a "narrow" logic pulse telling the ADC to integrate the raw signal that passed through the discriminator over a long or short gate period, respectively; a logic pulse is also sent to the TDC telling it that there is something worth recording and giving a start time. A delayed logical signal then comes from the discriminator telling the TDC the correct stop time.

When this circuit is complete the analogue signal from the electronics has been converted into: a short gate digital value proportional to the integrated charge of the signal, a long gate

digital value proportional to the integrated charge of the signal, and a digital value for the relative arrival time. These values are then read-out by Lucid (section 3.10.6 on page 102) and saved.

The Master Trigger System

The Master Trigger System (figure 3.24 on the next page) serves to prevent signals from entering the electronics while the data acquisition system is busy, and thus rigidly enforces the DAQ live-time: when the DAQ is busy, no data are recorded.

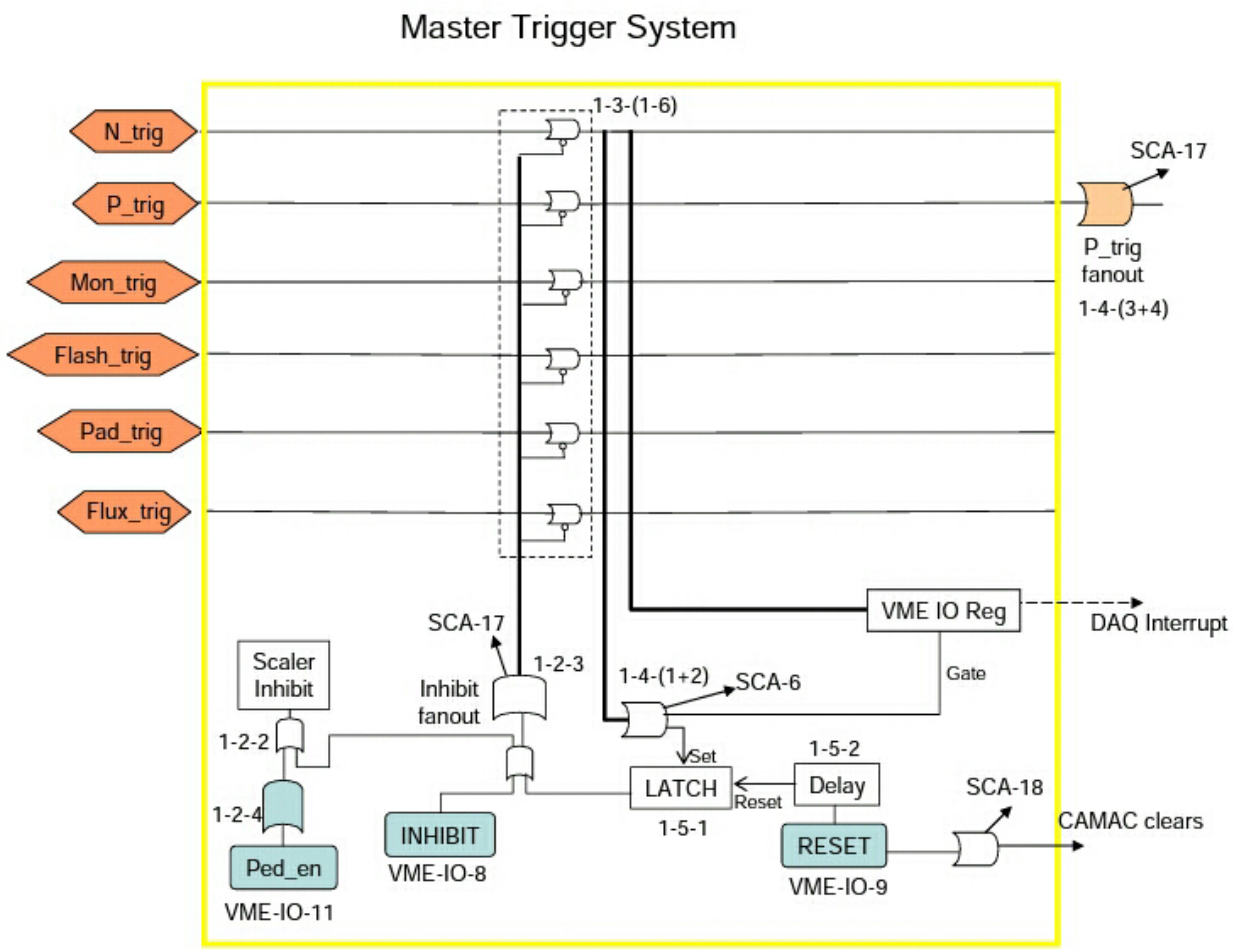

Figure 3.24: The Master Trigger System. All of the triggers enter here from the left; they set the "LATCH" which prevents new data from entering while the data acquisition system is busy. When Lucid finishes reading data it sends a RESET signal that opens the LATCH. The system can also be inhibited by Lucid via Ped_en or INHIBIT. Definitions: N_trig: neutron trigger, P_trig: pedestal trigger, Mon_trig: flash monitor trigger, Flash_trig: flasher trigger, Pad_trig: Five Paddle Flux Monitor trigger, Flux_trig: sodium iodide crystal trigger, DAQ: data acquisition system, CAMAC/VME: types of electronics (crate/bus types), and SCA: scaler.

Each possible trigger enters in the form of a logic pulse into an inhibit module that stops the pulse if the data acquisition system is busy (i.e. the system is *latched*). If a trigger is not inhibited, then *it* inhibits the data acquisition (it latches the system shut) and sends

a look-at-me signal informing the data acquisition system of the inhibition; the trigger can then proceed as it normally would in its respective circuit.

While the system is inhibited, the scalers do not count events and no new triggers can enter the electronics. The latch can be lifted by receiving a RESET signal from Lucid. Since all data are latched together, we need not worry about dead-time: Blowfish is never partially active, and all the data collected are complete. The system can also be inhibited by Lucid, which occurs both: when it sends an INHIBIT signal, and when the pedestals are measured via Ped_en (pedestals enabled).

3.10.2 Gain

In general terms, gain is the change in a signal due to the influence of some agent, usually a piece of electronics:

$$\text{gain} \equiv \frac{\text{input signal}}{\text{output signal}} \tag{3.8}$$

noting that the inverse of our definition is often used by other researchers: so it is important to take note of the units given.

Controlling gain is important insomuch as it may be necessary to amplify a signal in order to keep it above noise, or to attenuate a signal in order to prevent it from overflowing or damaging a piece of electronics. Usually, though, it is unimportant what exactly the gain is so long as it is known exactly for all inputs at all times. Realistically, we settle for electronics that are relatively stable over time and have simple functions describing how they change with respect to input (i.e. linear functions).

Analogue-to-digital converters aren't the only things that have a gain associated with them in our experimental setup: every piece of electronics we use will have some gain associated with it, as will the wires inbetween them; most of these contributions are trivial, though. We have no desire, nor reason, to keep track of the gain of every piece of electronics: instead we elect to treat the entire detector and data acquisition system as a single entity with a single gain for each type of data it produces. This means that we only need to worry about the gains of the time-to-digital converters (TDCs) and ADCs.

The TDC gains were determined by measuring an event of a known time interval i.e. a cable of a known signal propagation time was inserted into the wiring and the change in the stop time was recorded: the TDC bin value is then used to divide the actual time in order to determine the correct gain (see section 5.3.5 on page 172).

The ADC gains were determined by using radioactive sources with known energy spectrum features e.g. the Blowfish cells were calibrated using a known relationship between the inflection point from the end of the Compton continuum and the Compton edge,[26] then the literature value for the Compton edge was used to determine the gain. Three radioactive sources were used: AmBe to determine the gain (see section 5.3.2 on page 158), and ^{40}K and ^{228}Th to verify the gain is linear with zero intercept (see section 5.3.2 on page 163).

For the rest of this thesis it should be assumed that when referring to the gain it is the ADC gain which is being referenced unless explicitly stated otherwise.

3.10.3 The Gain Monitoring System

It is an empirical fact that the ADC detector gains of Blowfish drift over time (e.g. figure 3.25 on the next page). The Gain Monitoring System was designed and installed on Blowfish by Bewer [Bew05]: it enables the continuous tracking of gains inbetween calibration runs.

[26] BC-505, just like other liquid scintillators [Kno00], cannot resolve a photopeak.

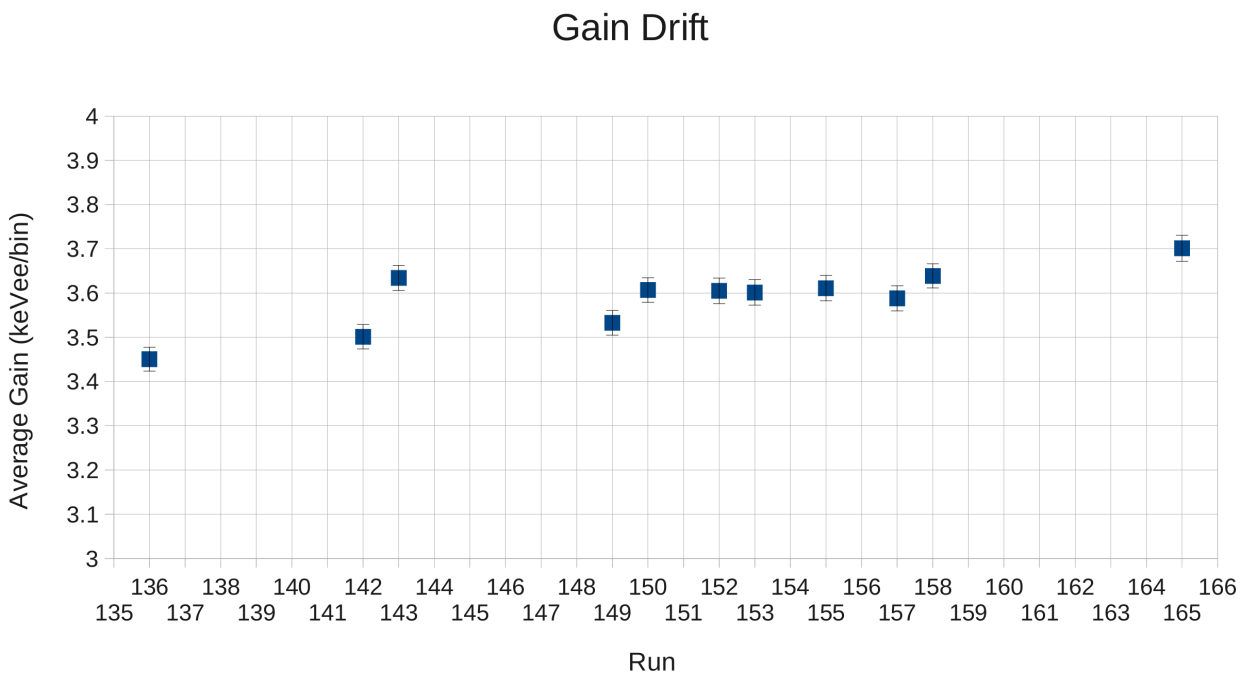

Figure 3.25: Gain Drift During the Experiment. The average gain (for all cells) was observed to drift over the course of the experiment, using the Gain Monitoring System. Run 136 and 165 are calibration runs, while the gains for the intermediate runs were computed using the Gain Monitoring System and the gain from run 136.

The Gain Monitoring System is designed to monitor the detector ADC gain using a system of continuously calibrated light-emitting diodes (LEDs). Four LEDs are mounted on Blowfish inside light-tight metal containers (called *flashers*) with a bundle of fiber optic cables carrying the LED light into each Blowfish cell and four gadolinium-silicon-trioxide (GSO) inorganic crystals (figure 3.26 on the next page). Each fiber optic bundle splits the LED light into 30 strands: 1 is sent to a GSO crystal, 22 are sent to the Blowfish cells of 2 full arms, and 7 spares remain; the four flashers are able to cover all 88 Blowfish cells and 4 GSO crystals.

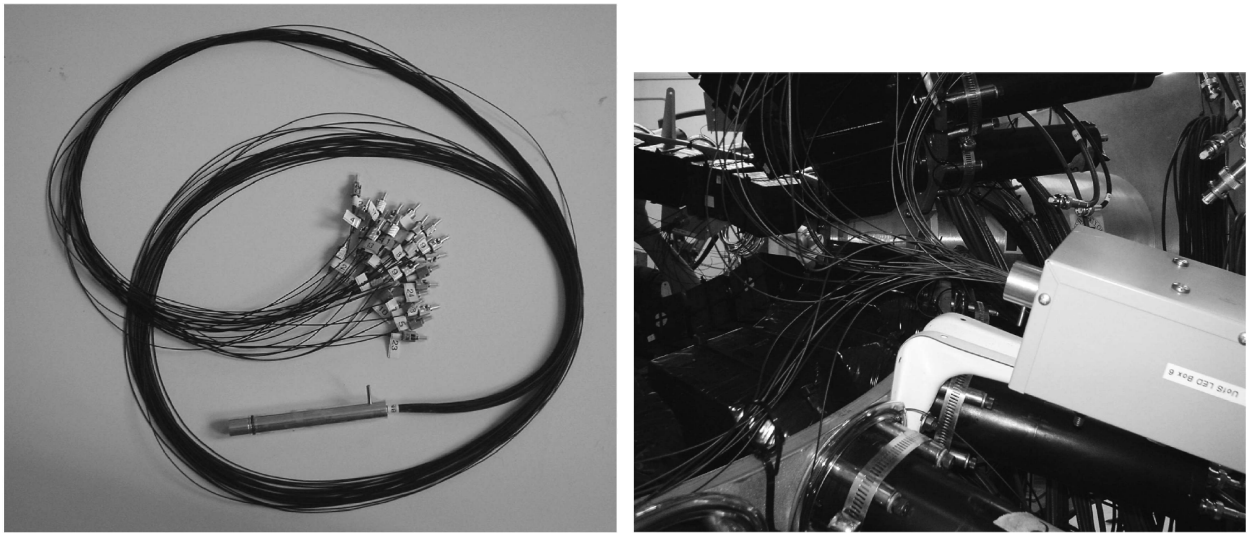

Figure 3.26: LED Flashers. To the left is a bundle of the fiber optic cables used; to the right is a LED flasher box; with fiber optic cable bundle outgoing to cells and a GSO crystal. The flasher box is mounted on one of Blowfish's arms. Image credit: Bewer [Bew05].

Each Blowfish cell has a hole drilled into the light guide and a fiber optic bundle glued into that hole so that it can carry light from the flasher directly into the detector (recall figure 3.10 on page 70).

The GSO crystals are used to continuously measure the LED light output in order to detect any drifting of the LED intensity. In order to make sure the GSO detectors aren't drifting: a radioactive source is placed in a light-tight box with the 4 GSO crystals so that they can be continuously monitored for their own gain. This system is referred to as the *flash monitoring system*.

The flashers are driven by a simple pulse generator (called the *pulser*) which is, in turn, enabled or disabled by the data acquisition system.

With everything installed we can continuously monitor the gain of each cell using the flashers, so long as we can continuously monitor the output of the LEDs; the latter requires that we assume the portion of light each cell receives relative to its corresponding flasher's GSO detector remains constant: this is approximately true, unless Blowfish is rotated (see section 5.3.4 on page 170). The calculations necessary for tracking the gain are discussed in

section 5.3.3 on page 165.

3.10.4 Analogue-to-Digital Converters (ADCs)

Analogue-to-digital converters (ADCs) are aptly named modules that convert the analogue electrical signals coming from our detectors into digital machine-language.[27] In this experiment, we used 6 32-channel 12-bit v792 charge integrating ADC modules,[28] a 12-channel 11-bit LeCroy 2249W charge integrating ADC, and an independent gate (IG) ADC model. The independent gate ADC and 2249W handled miscellaneous signal integration while the v792 ADCs integrated the Blowfish detector signals over a short and a long gate (i.e. time interval).

Our primary concern in this experiment was the performance of the v792 ADCs rather than the IG ADCs because the most important energy data (i.e. from Blowfish's cells) was recorded by the v792, therefore our discussion in this section will focus on the v792, although much of what is discussed is analogously true for the other ADCs.[29]

Each channel of the v792 ADC module has 4096 ($4096 = 2^{12}$ i.e. 12 bit) Boolean bins: the number of filled bins is proportional to the total charge which was integrated over the gated time interval: the data readout by Lucid are thus simply integer values between 0 and 4095. The v792 ADCs are integrating threshold ADCs, meaning that they integrate the total amount of charge of an electronic pulse over a given time period (supplied by a logical pulse) then choose a proportionate bin to place that integral based on a series of if-greater-than-or-equal-to sequences e.g. an integral of charge 100.9 bins would be recorded in bin 100.

There is a certain subtlety to getting the best performance out of a set of ADCs. Our experimental resolution is proportional to the number of bins we use: e.g. if we have some energy range ΔE and spread it over 100 bins then our resolution is 1%, but if we spread it over

[27] When the ADCs are used to calculate the total charge in a pulse they are alternatively referred to as QDCs: q is for charge: charge-to-digital converters.

[28] Each Blowfish cell requires two channels in the v792 ADC: one for the short and one for the long gate. Since the v792 ADC modules can only have one gate width per module, this means we need $2 \cdot \lceil \frac{88}{32} \rceil = 6$ modules.

[29] Information on the LeCroy 2249W can be found at `http://teledynelecroy.com/lrs/dsheets/2249.htm`.

1000 bins then our resolution is now 0.1%. In contrast, we must also consider the possibility of overflow occurring: if a charge is greater than the largest bin it will overflow and the energy information will be lost completely.[30] Ideally, then, we would like the most probable energy measured to be at the highest possible bin number with the maximum energy below the maximum bin (4095). The voltages supplied to the photomultiplier tubes were tweaked so that each cell's event signals were using as many of the ADC bins as possible for this experiment: this effectively alters the ADC gain.

A second performance consideration is the linearity of the ADCs used.[31] Our modules use the sliding-scale technique, which reduces the differential non-linearity[32] but it effectively reduces the maximum bin to 3840 [CAE10] (from 4096); furthermore, we observe suspicious activity in bins less than that ($\gtrsim$ 3650) and so we don't trust bins $\geq$ 3500 in order to be conservative.

The module also automatically applies a constant DC voltage to improve ADC linearity; this results in a pedestal: a minimum charge level for every integral of the ADC. The pedestal must be determined precisely then subtracted from the raw ADC data during data analysis in order to get the true pulse integral (see section 5.3.2 on page 158).

3.10.5 Time-to-Digital Converters (TDCs)

Time-to-digital converters (TDCs) convert the time difference between two signals into a digital bin number proportional to the time. Our TDCs have a nominal gain of 0.1 $\frac{ns}{bin}$ and a measured gain within about 5% of that (see section 3.10.2 on page 96 for more information).

In order to get the time-of-flight spectrum, we made regular measurements of the arrival time of photons scattered from the target via the G_win window (see figure 3.22 on page 90). Run 141 was taken entirely with G_win enabled (i.e. no pre-scaling of the expected beam photon arrival time): it was used to align the experimental runs. The HI$\vec{\gamma}$S FEL operates in pulses, so we can align our TDCs by assuming a mean free path for the scattered beam photons, then we can deduce the neutron time-of-flight for neutrons produced by the beam.

[30] The v792 has an overflow bit in its readout which signifies whether an overflow has occurred [CAE10].
[31] We verify that they are linear during data analysis, this is discussed in section 5.3.2 on page 163.
[32] Differential non-linearity is a measure of the actual bin widths of adjacent bins.

During normal data runs, G_win was enabled for approximately 1 in every 1000 events, resulting in a small peak at the beam photon arrival time; unfortunately, because of the angular dependence of the scattering probability ($\propto \theta$) there were insufficient data in the upstream cells. The downstream cells were used to track changes in the TDC alignment as well as the presence of out-of-time photons (section 5.3.1 on page 152).

With the gains correctly determined and the time-of-flight spectrum aligned (section 5.3.5 on page 172) we can proceed to make accurate time-of-flight cuts to exclude neutrons that are energetically forbidden by kinematics. We can also use the TDC spectra to: estimate the number of out-of-time photons in the beam (section 5.3.1 on page 152), detect TDC drift, and make necessary cell exclusions in the event of an irreconcilable presence of one of the former two (section 5.4.7 on page 209).

3.10.6 Lucid

Lucid handles the interface between machine and human language within the data acquisition system, it provides the electronics computer with commands to be sent to the electronics, and it receives data from the front-end, then it: sorts the data into human-readable format, does a few basic operations, and finally saves it all to disc.

Lucid operates using three primary programs the: *reader*, *looker*, and *writer* [Mur95].

The reader is the only mandatory program that must be built; it *reads* data from the electronics (i.e. in CAMAC/VME data format), stores it in variables as defined in the user-supplied *.r* reader file, and may perform a few rudimentary calculations on these variables. At the beginning of an experiment, a copy of the reader file is downloaded onto the front-end computer (running on the RTEMS operating system) to provided it with online commands for the electronics.

The optional *looker* receives data in the form of Lucid variables from the reader, it is designed to passively view the data stream so that more complex or frivolous calculations may be performed on the data without increasing dead-time. The looker produces human-readable format data (e.g. histograms) via a rudimentary window-based interface; data analysis *could* be done using the looker, but in practice we convert to ROOT and use it instead, as it is a more powerful option (section 5.2 on page 146).

The other optional piece of software is the *writer* which receives data from the reader and then saves it to disk.

The conceptual overview of Lucid is provided in figure 3.27.

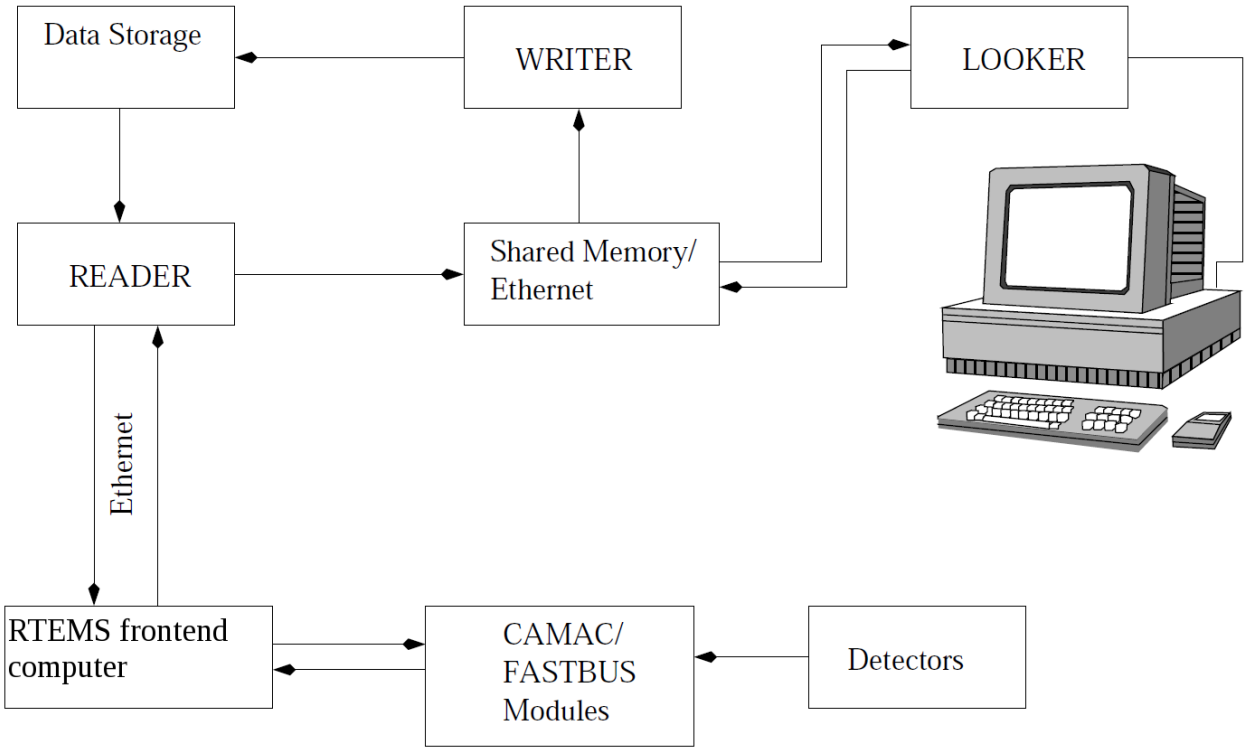

Figure 3.27: Conceptual Overview of Lucid Integrated with Blowfish. Image adapted from Sawatzky [Saw05].

The data from this experiment were recorded using Lucid; then, using RLucid (section 5.2.1 on page 151), the data were converted to ROOT format (section 5.2 on page 146) and analyzed using BFROOT (section 5.2.1 on page 149).

Chapter 4

Simulation

4.1 Introduction

Reliable and realistic simulation software is a valuable tool capable of accounting for a breadth of confounding experimental variables that we, for practical reasons, are uninterested in clarifying experimentally. The underlying physics in the simulation software has already been determined experimentally, placed on a sound model or theoretical basis, and the simulation itself has been consistently validated:[1] there is little merit in toiling in the lab to verify each step we must take to reach our results when we can simply use the simulation.

The key simulations we performed were: the probability density functions needed for the parameterized differential cross section, the Five Paddle Flux Monitor efficiency [Pyw09c], the detector efficiency (including geometric effects) for the total cross section, and errors, especially those associated with detector geometry. Stated concisely: efficiencies, errors, and geometric effects were simulated.

The simulations were performed using the GEANT4 Monte Carlo simulation toolkit [Ago03] and the BlowfishX package [Wur10a].

GEANT4 is a modular,[2] object-orientated[3] `C++` toolkit that contains contemporary models and empirical data ranging from the energy domain of eV up to PeV.[4]

BlowfishX is a package which contains all of the detector geometry and physics for an implementation of the Blowfish detector array in GEANT4; the X stands for: fill in the blank

[1] See section 4.2.4 on page 110 for details.

[2] The modular, object-orientated design allows users to be developers: they can replace or update 'modules' via the classes.

[3] Based on the Booch object-orientated methodology [Boo94].

[4] 1 PeV = 10^{15} eV

[Wur10a].

4.2 GEANT4

GEANT4: **Ge**ometry **An**d **T**racking, Version **4**.

We performed simulations of our experimental conditions using the GEANT4 toolkit [Ago03]. The GEANT4 acronym was contrived for a good reason: GEANT4 was designed to incorporate "*geometry*, *tracking*, detector response, run event and track management, visualization, and user interface" [Pia99]; we take advantage of all of these virtues.

The primary lesson learned from previous implementations of GEANT was that GEANT4 must be *modular* and *flexible* so that the underlying physics is transparent (for validation) and easily modified should it need to be supplemented or outright replaced [Ago03]. The software language `C++` is a versatile tool: it allows both high and low level user interfacing,[5] there are compilers on virtually every operating system (e.g. Mac, Windows and Linux) allowing `C++` programs to be highly *flexible* and portable, it also has additional object-oriented features not found in `C` (making it ideal for *modular* software), and; likely because of the former reasons: `C++` is *popular*, so many physicists (and other people) are familiar with the language [Gad09]. It should thus come as no surprise that `C++` is the underlying software language of GEANT4 [Ago03].

GEANT4 is a "toolkit" [Ago03], meaning that it provides the tools (i.e. the classes: including pertinent physics) necessary for constructing simulation software; the onus is on the user to construct simulations using the tools GEANT4 has provided, and then verify that simulation is consistent with empirical results [Apo08]. The implementation for this experiment was performed using BlowfishX with full considerations discussed in section 4.3 on page 114.

What follows is a brief description of how GEANT4 works: in an attempt to familiarize the reader with what considerations must be made by the user during an implementation, and (hopefully) to elucidate potential sources of incongruency between GEANT4 simulations

[5]For example, one can micro-manage memory on the heap while simultaneously utilizing black-box class implementations.

and nature. The best way to understand the following description is to supplement it with a sample of GEANT4 output, found in appendix E on page 291.

GEANT4 is fundamentally based on materials,[6] particles[7] and the interactions between them. The user must therefore hard-code these three things; either *ab initio* or from pre-defined libraries, along with desired output; then the simulation is ready to be run.

A simulation *run* begins when a particle is generated at some point in space (as described by floating point numbers: x, y and z) with definite momentum and energy, then it is tracked step-by-step: measured either as a distance (for particle velocity > 0) or as a time (for particle velocity $= 0$); if the particle would cross a boundary between materials (the transportation class is forbidden from crossing material boundaries) or run out of energy (due to a continuous energy loss process like bremsstrahlung) then the step is stopped short. During a particle's step, the probability of an interaction occurring via any available physical process is computed and the Monte Carlo method (section 4.2.3 on page 109) is used to determine which, if any, interaction (called an *event*) occurs;[8] if no interaction occurs then the transportation class is called and the particle moves through the interval of space (or time) [Ago03].

This step-by-step tracking occurs for each particle generated: the particle initially created by the user's generation parameters,[9] and any particles subsequently generated by interactions. A particle is tracked from generation until it is destroyed, either by: an interaction (e.g. absorption or decay), running out of kinetic energy,[10] being transported outside of the world volume, or by any user-defined criteria. A run starts when the initial particle is generated, and it ends when the last particle is destroyed.

The interaction data is computed at each step, then when the run has finished, a simplified data set representing the trajectory taken is outputted in human-readable format:[11] in text (table E.1 on page 292) and as a graphic (figure E.1 on page 291) with highlighted particle

[6] The materials are of user defined elemental composition.

[7] Anything recognized by the Particle Data Group [Ber12] is considered a particle, be it: hadron, lepton or boson.

[8] A particle only ever participates in one interaction during a step (i.e. no superpositions) and it is chosen by a properly weighted random number generated.

[9] This takes place in G4PrimaryGeneratorAction::GeneratePrimaries().

[10] If it is stable, otherwise it will remain 'at rest' until it decays

[11] When run in GUI mode.

trajectories; and in user-defined format. The BlowfishX [Wur10a] package tells GEANT4 to output data in Lucid (section 3.10.6) format. Finally, the user may queue runs in which case GEANT4 calls the next run in the queue. Once all of the runs have finished, the simulation data can be compressed and stored for future analysis.

4.2.1 Physics Lists

It should come as no surprise that the physics *lists* provide GEANT4 simulations with a *list* of formulae, models and empirical data to use when simulating interactions. GEANT4 developers validate their models using published thin-target data, but once they have completed a physics list it is the user's responsibility to validate the list in their domain of application [Apo08].[12]

The physics list used in this analysis was the `QGSP_BERT_HP` physics list [Wel02]: the safest choice though not the most efficient. The `QGSP_BERT_HP` physics list has the slowest CPU performance, but it also has the best agreement with test-beam data, which is why it's the default choice for both the ATLAS and CMS collaborations [Apo08].

Table 4.1: `QGSP BERT HP` Physics List

`QGSP`	**Q**uark-**G**luon **S**tring **P**recompounded.	Only active in 12 GeV-100 TeV range.
`BERT`	**Bert**ini cascade.	Follows INUCL implementation [Ste88].
`HP`	**H**igh **P**recision.	High precision neutron package used for 0-20 MeV range.

Since we are well below pion-threshold at the beam energy of 18 MeV: we don't need to worry about mesons and we can easily enumerate all of the possible particles involved in our simulation and the libraries used by `QGSP_BERT_HP` in our energy region [QGS].[13]: table 4.2 on the next page

[12] More on this in appendix J on page 302.
[13] A full list is provided by the GEANT4 collaboration [QGS].

Table 4.2: `QGSP BERT HP` Libraries

Particle	Interaction	Library(ies) Used
Hadrons	Elastic	hElasticCHIPS
	Inelastic	BertiniCascade[1]
	Neutron Transportation	NeutronHP
	Neutron Capture	G4LFission or GheishaFissionXS[2]
	Fission[3]	G4LFission or GheishaFissionXS
Photons	Inelastic	CHIPSGammaNuclear or PhotoNuclearXS
Electrons/ Positrons	Inelastic	CHIPSElectroNuclear or ElectroNuclearXS
Any	Electromagnetic	G4StEm with sub-package for optical photons [Bur04]

Note: in the event of an overlap between libraries in an energy region: a random number is generated and a linearly[14] weighted selection is made between the two [Apo08]; we don't simulate any physics near a region of overlap [QGS].

4.2.2 Using GEANT4

Before using GEANT4, one must program a few key classes and integrate them into a single `int main()` class containing the G4RunManager: this handles the time evolution of the simulations. Once a functional piece of GEANT4 software has been created: the user can implement specific details for the particles being simulated (e.g. initial particle position and

[1] A Bertini cascade consists of a cascade of individual scattering events using nuclear medium corrected cross sections. Nuclei are modeled as a set of spherical shells.

[2] GheishaFissionXS lacks low energy resonances.

[3] Neutron induced.

[14] As a function of energy.

energy) via: hard-coding it into the software, running a command-line macro, or using a GUI.

How it works at a low level (skeleton):

1. Build a world volume and materials inside (G4VUserDetectorConstruction class).
2. Specify the physics involved (G4UserPhysicsList class).
3. Specify how particles are to be created (G4UserPrimaryGeneratorAction).
4. Specify how particles are tracked: between runs (G4UserRunAction) and between steps (G4UserSteppingAction).
5. Specify what actions to perform when an interaction occurs, and what output is desired (G4UserEventAction).
6. Provide a user interface for building the above and (contained in your `int main()` via G4RunManager class) for executing commands (i.e. how to handle macros, a GUI or simply hard-code) and managing events.

How it works at a high level (macro and GUI commands are entered via a Linux-emulating terminal):

1. Pick a particle from the particle table (G4ParticleTable).
2. Define energy and momentum (G4ParticleGun or G4GeneralParticleSource).
3. Generate the particle (`\run\beamOn`) and watch what happens (G4RunManager).
4. Repeat (if desired).

4.2.3 The Monte Carlo Method

The predicted dynamics of nature will invariably be described by a set of equations, and yet the first step a physicist takes when attempting to predict nature is typically to solve them, regardless of how unpleasant the solution may be. The Monte Carlo method [Met49] circumvents this by emulating nature: each equation is simulated with some kind of probabilistic

degree of freedom in order to deduce a heuristic prediction (or approximate solution). Similarly, probabilistic predictions (such as those produced by quantum theory) can be simulated using pseudo-random number generators with appropriate weighting: in order to predict what an experiment might produce. GEANT4 uses the Monte Carlo method for the latter: particles are generated at a position in space with a definite energy and momentum specified by the user, then they move through the virtual world and interact with its virtual materials probabilistically, losing energy and momentum until eventually they are absorbed or their energy goes below the user-imposed threshold (or they leave the world volume altogether).

4.2.4 Simulation Consistency Checks

Our research group has performed consistency checks on: the GEANT3 implementation of Blowfish [Saw05], the Blowfish detectors [Kor99, Pyw06], and the flux monitor [Pyw09c], using empirical data; and: the physics list used [Wur10c], and the sampling technique, using internal consistency checks on the simulated data. The physics list (`QGSP_BERT_HP`) has also been verified at higher energies by both the ATLAS and CMS collaborations [Apo08].

GEANT4 is a popular simulation toolkit: the primary reference has over 8000 citations [Gea]. We have little reason to doubt the validity of the mutual interactions simulated by the majority of users e.g. photon interactions with common materials like aluminum; however, we do have reason to believe that the simulation may be invalid for less commonly used materials: namely, BC-505. Consequently most of the concern by our research group has been on the performance of the detectors, specifically their light output efficiencies, although Sawatzky [Saw05] performed some other fundamental tests on GEANT3.

The first experimental test of the simulated light output response of Blowfish's detectors (i.e. BC-505) was performed by Korkmaz *et al.* [Kor99] in 1999 at TRIUMF using the $p(\gamma,n)\pi^+$ reaction to produce neutrons of energies 6-13 MeV. The results showed a 9% discrepancy between the experimental and simulated light output efficiencies of the BC-505 cells. Pywell *et al.* [Pyw06] re-analyzed the data in 2006; they discovered an error in the previous analysis' gain determination, and were able to deduce new light output parameters for BC-505 such that the experimental and simulated light output responses were found to agree within errors (figure 4.1 on the next page).

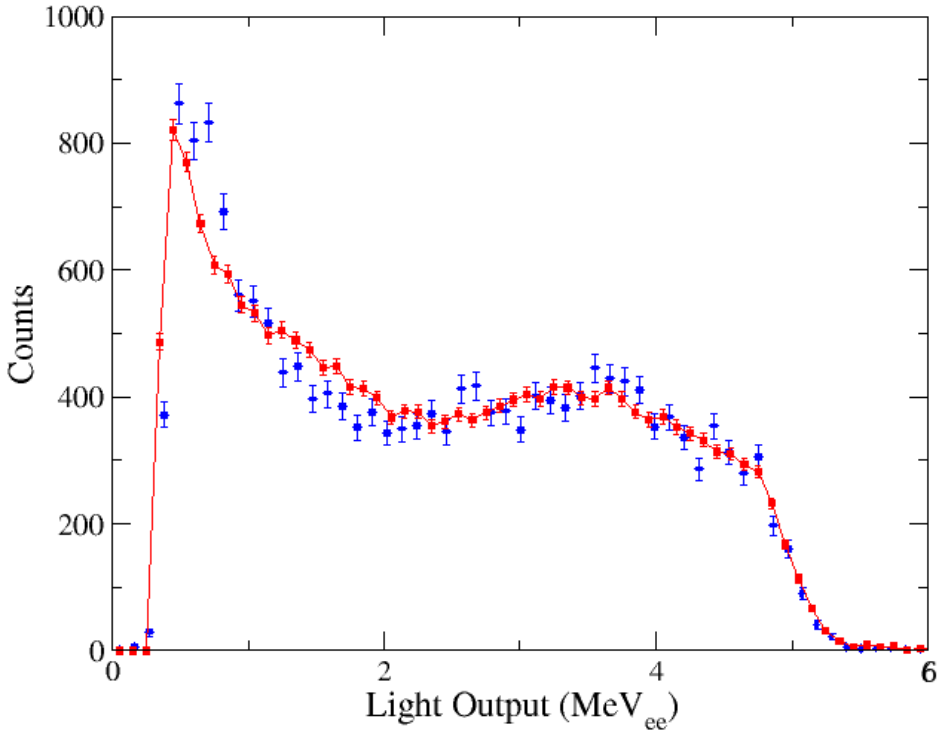

Figure 4.1: Simulated BC-505 Light Output spectrum for 8.9 MeV neutrons incident on a Blowfish detector (BC-505). Blue are the measured data; red are the GEANT4 simulated data. The data appear to be consistent with the simulation. Fits of this type were performed for neutrons of energies 6-12 MeV (see Pywell *et al.* [Pyw06]). Image courtesy of Dr. Robert Pywell.

In this experiment, kinematics limited the neutrons to energies less than 9 MeV and we performed a time-of-flight cut that would eliminate neutrons below 2 MeV. Therefore, it is pertinent to mention low energy detector response (from 2-6 MeV) as well as the 6-13 MeV response studied by Pywell *et al.* [Pyw06]. Ives [Ive03] used a ^{252}Cf radioactive source[15] to verify the light response and efficiencies of a BC-519,[16] detector for neutrons of energies 0-6 MeV: his results showed a perfect agreement within error. It should be noted that Ives' data were plagued by large uncertainties for neutron energies greater than 2 MeV, and Ives did not simulate the scintillator used in this experiment. Wurtz [Wur10c] notes that an

[15]Californium-252 is an alpha emitter (96.% of the time) and a spontaneous fission source (3.09% of the time) that produces neutrons with an average energy of 2.1 MeV [Mar00].

[16]BC-519 is a liquid organic scintillator produced by Saint-Gobain Crystals [Sai09] that is similar to the scintillator used in this experiment: BC-505.

attempt was made in 2005 to continue Ives' work, but it was unable to improve upon Ives' precision.

The flux monitor was also verified for consistency between experiment and simulation at 20, 25, 30 and 35 MeV beam energies [Pyw09c]. Good agreement was found at all energies (e.g. figure 4.2 on the next page) and we extrapolate that for the beam energy used in the current experiment (18 MeV), the flux monitor most likely shows good agreement as well.

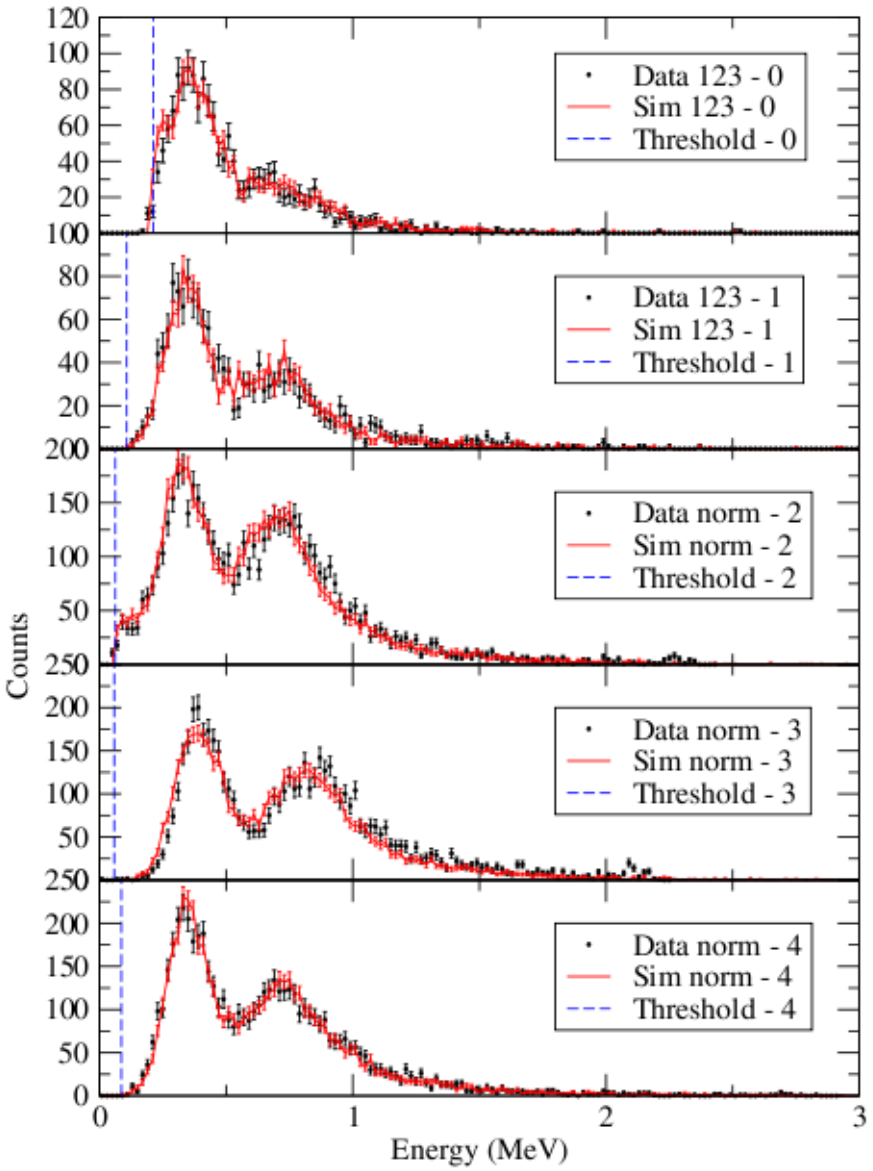

Figure 4.2: Simulated Flux Monitor Light Output energy spectra for photons at 25 MeV. 0, 1, 2, 3, and 4 are the paddle numbers indexed from 0 (paddle 0 is upstream; the aluminum radiator is inbetween paddles 1 and 2). Paddle 0 and 1 data required a triple coincidence between paddles 0, 1 and 2 (hence the "123" label: these are the paddle numbers indexed from 1 instead of 0), while paddle 2, 3 and 4 data used the normal condition: i.e. paddle 1 acts as a veto (hence the "norm" label: for normal). Black are experimental data points, red are simulation; the dotted blue line is the hardware threshold. The data appear to be consistent with the simulation. Image credit: SPIR-140 [Pyw09c].

Internal consistency checks of the simulation were also performed in a few cases. Wurtz [Wur10c] performed a consistency check on neutrons up to ≈ 35 MeV for the physics lists: `LHEP_PRECO_HP`, `LHEP`, and `QGSP_BERT_HP`. He found that only `QGSP_BERT_HP` produced possible results: this isn't surprising since GEANT4 doesn't recommend LHEP for any use other than high energy calorimetry.[17]

In this work, several internal consistency checks of the simulation were performed (and verified); these are discussed and compared to the experimental results in appendix J on page 302.

4.3 Simulation Implementation

The GEANT4 simulation of our experiment was performed using BlowfishX (section 4.3.1) as the framework and adding the necessary specifics of this experiment: the result was BlowfishXI.

The experiment specific updates included considerations of: beam attenuation in the target via a probability density function (PDF) (section 4.4.1 on page 118), the Legendre probability density functions (section 4.4.2 on page 119); and the tools necessary to access these: the analytical functions derived for the inverse transform sampling method (section 4.4.3 on page 141) and the numerical algorithms necessary to invert the non-analytical functions: Newton's method (section 4.4.5 on page 144) and the Bisection method (section 4.4.4 on page 143).

4.3.1 BlowfishX

The BlowfishX package for GEANT4 contains all of the basic requirements for GEANT4 simulations performed using the Blowfish detector array, and; with the BXLucid package installed, will automatically convert GEANT4 output into Lucid format. Explicitly, the package includes: detection properties of BC-505 [Pyw06] and the correct digital output

[17] `http://geant4.org/geant4/support/physicsLists/referencePL/useCases.shtml`

[Wur10a],[18] realistic time-to-digital converter output [Wur10a][19], geometry and materials for the entire detector array (including mount), sources ("Geantino",[20] americium-beryllium, Na-22, Th-228, Th-232 and Cs-137), Lucid event types,[21] and all of the necessary classes to produce an executable file that is functional in GEANT4.

The BlowfishX package lacks experimental specifics because it was designed to be as general as possible. The necessary implementations for the current experiment were carried out, they include: target self-absorption attenuation, and probability density function.[22] A new particle generation class (G4GeneralizedParticleSource) was also implemented in order to verify the previous particle generation class' results. Both classes produced equivalent results (see appendix J on page 302 for details).

A critical update was performed on the BlowfishX implementation of the G4HitsCollection class (i.e. the BXHitsColletion class). BlowfishX *was* assuming that the array of hits inside the G4HitsCollection class were ordered in time and calibrated the TDCs (time-to-digital converters) based on this assumption: which is incorrect.[23] What this means practically is that when a particle interacts with the detector; e.g. if an incident neutron interacts with multiple particles then it will take the *last* particle it interacts with as having been the earliest and set the TDC value accordingly e.g. if that neutron hit three protons then it would think that the third proton it hit was the first. This manifested itself in the data as what appeared to be abnormally high energy particles arriving late in time (we would normally expect later neutrons to be of lower energy because they either travel slower or have scattered, or both), and consequently gave a skewed TDC spectrum (see figure 4.3 on the next page).

[18] That is: the correct digital output from the analogue/charge-to-digital converters.
[19] Please see Wurtz [Wur10a] for more information.
[20] The Geantino is a fictional non-interacting particle used in GEANT4 to track geometries.
[21] If BXLucid is installed.
[22] Based on Wurtz [Wur10a]; using the G4ParticleGun class.
[23] According to Geant v4.9.4.

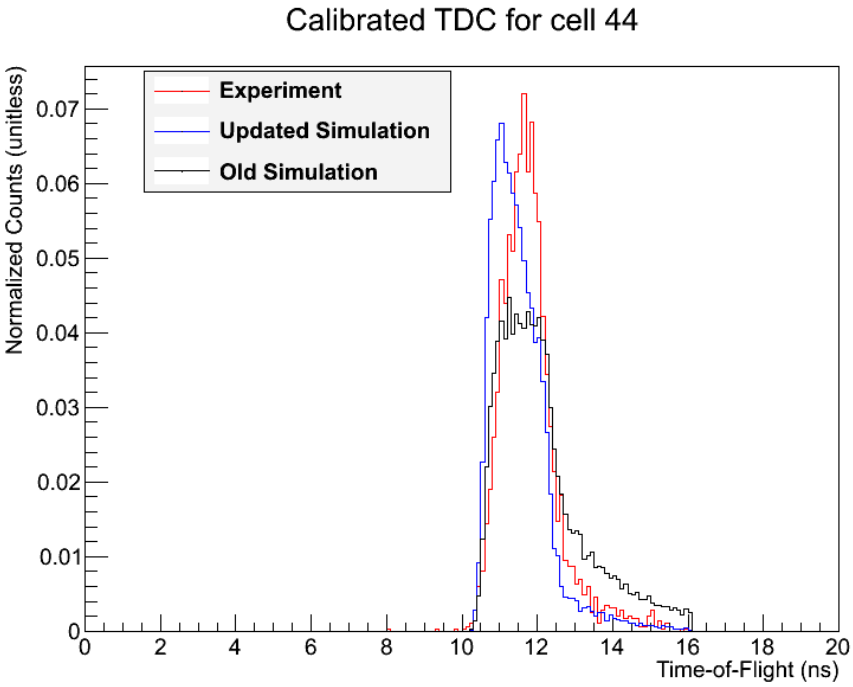

Figure 4.3: BlowfishX Update. A comparison of the TDC spectra for the experimental data, and the simulation before and after the update to BlowfishX' G4HitsCollection implementation.

With BlowfishX updated, the simulations now show consistencies in all of the raw data they output: ADC (analogue-to-digital converter) spectra and TDC spectra (see appendix J on page 302).

4.4 Probability Density Functions

GEANT4 is a Monte Carlo simulation toolkit and as such it requires probabilistic rules, specifically for this experiment, for: target attenuation (section 4.4.1 on page 118) and the Legendre probability density functions (section 4.4.2 on page 119). Using differential calculus, we can define the correct probabilistic rules for the simulation to follow as probability density functions (PDFs) with the properties outline in theorem 1.

Theorem 1. ***PDF Criteria***

For a function, f, to be a probability density function, the following must be true [Gha96]:

1. *f must always be positive.*

$$f : \mathbb{R} \mapsto [0, \infty)$$

2. *f must be normalized to unity.*

$$\int_{-\infty}^{\infty} f(x)dx = 1$$

We constructed analytical PDFs for both the target attenuation and Legendre probability density functions, then we used inverse transform sampling (section 4.4.3 on page 141) to implement them in the GEANT4 simulation and thus, via the Monte Carlo method, the pertinent heuristic result was extracted.

The inverse transform sampling method requires the cumulative distribution function (CDF) for a given PDF as well as the inverse function: CDF^{-1}. The analytical CDF exists for all PDFs in this experiment, however, many of the PDFs do not have analytical inverse CDFs: these are inverted numerically using Newton's method (section 4.4.5 on page 144) or the Bisection method (section 4.4.4 on page 143) when the former fails. This means that for the target attenuation PDF, and each Legendre PDF the following functions needed to be constructed:

1. Construct the PDF, $f(x)$, using the PDF criteria (theorem 1 on page 116): any function that obeys these two criteria is a PDF.

2. Calculate the CDF, noting that it must be normalized: $C(x) \equiv \int_{-\infty}^{x} f(x')dx'$.

3. Invert the CDF, either numerically via Newton's method or the Bisection method, or analytically.

Once the inverse CDFs have been computed, they are implemented into the simulation by supplying a uniformly sampled domain via a pseudo-random number generator as is discussed in full in section 4.4.3 on page 141.

4.4.1 Target Attenuation

PDF	$f(x) = \frac{\sigma\rho e^{-\mu x}}{1-e^{-\mu l}}$
CDF	$C(x) = \frac{1-e^{-\mu x}}{1-e^{-\mu l}}$
CDF^{-1}	$C^{-1}(u) = -\frac{1}{\mu}\ln(1-u+ue^{-\mu l})$

Table 4.3: Target Attenuation Functions. Where: σ is the total cross section, ρ is the target number density, μ is the photon linear attenuation coefficient for the target material, and l is the target length.

When a beam of photons enters the target, most of the photons simply travel right through unimpeded; the vast majority of the photons that *do* interact, interact with electrons in the target and are removed from the beam-line:[24] thus preventing them from causing nuclear photodisintegration reactions. The simulation initiates by considering a neutron being ejected from the target, thus the correct description of the experiment must include the photon attenuation effect. Nuclear photo-processes are extremely rare relative to atomic photo-processes so we simply neglect the former and consider it accounted for in the uncertainty of the latter.[25]

The beam attenuation in the target was implemented using the particle absorption equation to construct the predictive PDF, and the inverse transform sampling method to implement it into the simulation. This required a function to describe the PDF, CDF and inverse CDF: these are all given in table 4.3; the derivation of these functions is given in appendix F on page 293.

[24] See appendix A on page 278 for details.

[25] One can demonstrate how trivial the contribution of nuclear photo-processes is by contrasting the total atomic attenuation of H_2O (μ) to the nuclear attenuation of the deuteron (σn) : $\mu \approx 0.02\ cm^{-1}$ [Mic89, Sko74, Ahr74, DGr91]; $\sigma n \approx 3 \cdot 10^{-6}\ cm^{-1} \implies \mu >> \sigma n$.

4.4.2 Legendre Probability Density Functions

Recall from section 2.5.5 on page 47 that the differential cross section can be expanded in terms of associated Legendre polynomials as a function of $\cos(\theta)$:

$$\frac{d\sigma}{d\Omega} \approx \frac{\sigma}{4\pi}\left[1+\sum_{k=1}^{4} a_k P_k^0(\cos\theta)+\sum_{k=2}^{4} e_k P_k^2(\cos\theta)\cos 2\phi + \sum_{k=1}^{2} c_k P_k^1(\cos\theta)\cos\phi+\sum_{k=1}^{2} d_k P_k^1(\cos\theta)\sin\phi\right] \tag{4.1}$$

where: P_k^i are the associated Legendre polynomials, and σ is the total cross section.

Although the data *could* be fit to this expansion directly, it would require a complete description of the geometric effects. Alternatively, since GEANT4 contains all of the necessary physics and BlowfishX contains all of the necessary detector information: the Legendre polynomials can be simulated, then the detector neutron yields can be used to fit to the data: this is what was done, following in the footsteps of: Kucuker [Kuc10], Wurtz [Wur10c], Blackston [Bla07] and Sawatzky [Saw05].

The Legendre polynomials were converted to PDFs (probability density functions), then they were simulated using inverse transform sampling (section 4.4.3 on page 141). In order to construct PDFs from Legendre polynomials, the PDF criteria (theorem 1 on page 116) must be met: the PDFs must be positive (and finite) over their entire domains and they must be normalized to unity. This is readily achieved by adding a term to each Legendre polynomial to ensure it is always positive, then add the negative of that term to the expansion and include it in the 0^{th} Legendre polynomial PDF and, finally, normalize the remaining function:

$$f = \frac{d\sigma}{d\Omega}\frac{1}{\sigma} = \frac{1}{4\pi}\left[(1-\sum_{k=1}^{4} a_k - 3e_2 - 6e_3 - 10e_4 - c_1 - \frac{3}{2}c_2 - d_1 - \frac{3}{2}d_2)\rho_{00} + \sum_{k=1}^{4} a_k\rho_{0k} + 3e_2\rho_{22} + 6e_3\rho_{23} + 10e_4\rho_{24} + c_1\rho_{11} + \frac{3}{2}c_2\rho_{12} + d_1\rho_{11'} + \frac{3}{2}d_2\rho_{12'}\right] \tag{4.2}$$

where: $k, l \in \{\mathbb{Z} | 0 \leq k \leq 4, 0 \leq l \leq 2\}; \rho_{lk} : (R) \mapsto (R)^+ \; \forall \; k, \; l$

$\int_{\phi=0}^{\phi=2\pi} \int_{\cos\theta=-1}^{\cos\theta=1} \rho_{lk} d\cos\theta d\phi = 1 \; \forall \; k, \; l,$ and:

$$\begin{aligned}
\rho_{00}(\cos\theta, \phi) =& \frac{1}{4\pi} \\
\rho_{0k}(\cos\theta, \phi) =& \frac{1}{4\pi}[1 + P_k^0(\cos\theta)] \text{for} 1 \leq k \leq 4 \\
\rho_{22}(\cos\theta, \phi) =& \frac{1}{12\pi}[3 + P_2^2(\cos\theta)\cos 2\phi] \\
\rho_{23}(\cos\theta, \phi) =& \frac{1}{24\pi}[6 + P_3^2(\cos\theta)\cos 2\phi] \\
\rho_{24}(\cos\theta, \phi) =& \frac{1}{40\pi}[10 + P_4^2(\cos\theta)\cos 2\phi] \\
\rho_{11}(\cos\theta, \phi) =& \frac{1}{4\pi}[1 + P_1^1(\cos\theta)\cos\phi] \\
\rho_{12}(\cos\theta, \phi) =& \frac{1}{6\pi}[\frac{3}{2} + P_2^1(\cos\theta)\cos\phi] \\
\rho_{11'}(\cos\theta, \phi) =& \frac{1}{4\pi}[1 + P_1^1(\cos\theta)\sin\phi] \\
\rho_{12'}(\cos\theta, \phi) =& \frac{1}{6\pi}[\frac{3}{2} + P_2^1(\cos\theta)\sin\phi]
\end{aligned}$$

P_k^l are the associated Legendre polynomials. Note the normalization factor is exactly σ by definition.

Eq. (4.2) on page 119 can be used to simulate an entire run (by supplying the values of the 11 parameters) or a single distribution by setting the parameters to an appropriate set of values such that one of the distributions is singled out.[26] In order to apply eq. (4.2) on page 119 to the simulation though, the CDFs (cumulative distribution functions) and inverse CDFs had to be determined so that inverse transform sampling could be used.

The CDFs are a bit different for each parameter type because of their ϕ dependence. The ρ_{0k} PDFs and ρ_{00} are uniform in ϕ, so the total CDF is separated into two CDFs, one for ϕ

[26]For example, by setting all parameters to 0, except for $e_2 = \frac{1}{3}$ one would have $f = \rho_{22}$.

and one for θ:

$$C_{0k} \equiv \frac{\int_{\phi'=0}^{\phi'=\phi} \int_{\cos\theta'=-1}^{\cos\theta'=\cos\theta} \rho_{0k} d\cos\theta' d\phi'}{\int_{\phi'=0}^{\phi'=2\pi} \int_{\cos\theta'=-1}^{\cos\theta'=1} \rho_{0k} d\cos\theta' d\phi'}$$

$$C_{0k}^{\phi}(\phi) = \frac{\phi}{2\pi}$$

$$C_{0k}^{\cos\theta}(\cos\theta) = \frac{\int_{\cos\theta'=-1}^{\cos\theta'=\cos\theta} \rho_{0i} d\cos\theta'}{\int_{\cos\theta'=-1}^{\cos\theta'=1} \rho_{0i} d\cos\theta'}$$

$$C_{00}^{\cos\theta}(\cos\theta) = \frac{1}{2} \tag{4.3a}$$

$$C_{01}^{\cos\theta}(\cos\theta) = \frac{1}{4}(\cos^2\theta + 2\cos\theta + 1) \tag{4.3b}$$

$$C_{02}^{\cos\theta}(\cos\theta) = \frac{1}{4}(\cos^3\theta + \cos\theta + 2) \tag{4.3c}$$

$$C_{03}^{\cos\theta}(\cos\theta) = \frac{1}{16}(5\cos^4\theta - 6\cos^2\theta + 8\cos\theta + 9) \tag{4.3d}$$

$$C_{04}^{\cos\theta}(\cos\theta) = \frac{1}{16}(5\cos^5\theta - 10\cos^3\theta + 11\cos\theta + 8) \tag{4.3e}$$

where: C_{0k}^{ϕ} are the ρ_{0k} CDFs with respect to ϕ and $C_{0k}^{\cos\theta}$ are the ρ_{0k} CDFs with respect to $\cos\theta$.

The e, c and d parameters are most certainly not independent in ϕ and θ, so their CDFs must be computed over both parameters. Fortunately, sampling θ over the average value of ϕ removes the ϕ dependence in the θ CDF. The θ CDF can then be sampled for θ_s which is

subsequently used in the ϕ CDF:

$$\text{l} = 1 \text{ or } 2;\ \text{k} = 1,\ 2,\ 3 \text{ or } 4;\ \text{l,k} \in \mathbb{Z}$$

$$C_{lk} \equiv \frac{\int_{\phi'=0}^{\phi'=\phi} \int_{\cos\theta'=-1}^{\cos\theta'=\cos\theta} \rho_{lk} d\cos\theta' d\phi'}{\int_{\phi'=0}^{\phi'=2\pi} \int_{\cos\theta'=-1}^{\cos\theta'=1} \rho_{lk} d\cos\theta' d\phi'}$$

$$C_{lk}^{\cos\theta} \equiv \frac{\int_{\cos\theta'=-1}^{\cos\theta'=\cos\theta} \int_{\phi'=0}^{\phi'=2\pi} \rho_{lk} d\phi' d\cos\theta'}{\int_{\cos\theta'=-1}^{\cos\theta'=1} \int_{\phi'=0}^{\phi'=2\pi} \rho_{lk} d\phi' d\cos\theta'} = \frac{1+\cos\theta}{2}$$

$$C_{lk}^{\phi}(\cos\theta_s, \phi) \equiv \frac{\int_{\phi'=0}^{\phi'=\phi} \rho_{lk} d\phi'}{\int_{\phi'=0}^{\phi'=2\pi} \rho_{lk} d\phi'} = 2\int_{\phi'=0}^{\phi'=\phi} \rho_{lk} d\phi'$$

$$C_{22}^{\phi}(\cos\theta_s, \phi) = \frac{\phi}{2\pi} + \frac{P_2^2(\cos\theta_s)\sin 2\phi}{12\pi} \tag{4.4a}$$

$$C_{23}^{\phi}(\cos\theta_s, \phi) = \frac{\phi}{2\pi} + \frac{P_3^2(\cos\theta_s)\sin 2\phi}{24\pi} \tag{4.4b}$$

$$C_{24}^{\phi}(\cos\theta_s, \phi) = \frac{\phi}{2\pi} + \frac{P_4^2(\cos\theta_s)\sin 2\phi}{40\pi} \tag{4.4c}$$

$$C_{11}^{\phi}(\cos\theta_s, \phi) = \frac{\phi}{2\pi} + \frac{P_1^1(\cos\theta_s)\sin\phi}{2\pi} \tag{4.4d}$$

$$C_{12}^{\phi}(\cos\theta_s, \phi) = \frac{\phi}{2\pi} + \frac{P_2^1(\cos\theta_s)\sin\phi}{3\pi} \tag{4.4e}$$

$$C_{11'}^{\phi}(\cos\theta_s, \phi) = \frac{\phi}{2\pi} + \frac{P_1^1(\cos\theta_s)\cos\phi}{2\pi} \tag{4.4f}$$

$$C_{12'}^{\phi}(\cos\theta_s, \phi) = \frac{\phi}{2\pi} + \frac{P_2^1(\cos\theta_s)\cos\phi}{3\pi} \tag{4.4g}$$

where: P_k^l are the Associated Legendre polynomials, C_{lk}^{ϕ} are the ρ_{lk} CDFs with respect to ϕ, and $C_{lk}^{\cos\theta}$ are the ρ_{lk} CDFs with respect to $\cos\theta$.

Taking all of these CDFs into consideration, the full CDF for the entire differential cross section has two parts (like eq. (4.4)): a CDF to sample $\cos\theta$ from ($\mathrm{C}_{\frac{d\sigma}{d\Omega}}^{\cos\theta}$) and a CDF to sample an appropriate ϕ from ($C_{\frac{d\sigma}{d\Omega}}^{\phi}$). As demonstrated earlier, the ϕ and $\cos\theta$ dependencies can be separated if $\cos\theta$ is sampled from the *average* ϕ.

Starting from the definition of the normalized CDF:

$$C_{\frac{d\sigma}{d\Omega}} \equiv \frac{\int_{\phi'=0}^{\phi'=\phi} \int_{\cos\theta'=-1}^{\cos\theta'=\cos\theta} \frac{d\sigma}{d\Omega} d\cos\theta' d\phi'}{\int_{\phi'=0}^{\phi'=2\pi} \int_{\cos\theta'=-1}^{\cos\theta'=1} \frac{d\sigma}{d\Omega} d\cos\theta' d\phi'}$$

we sample $\cos\theta$ over average ϕ to get the $\cos\theta$ CDF:

$$\begin{aligned} C_{\frac{d\sigma}{d\Omega}}^{\cos\theta} &\equiv \frac{\int_{\cos\theta'=-1}^{\cos\theta'=\cos\theta} \int_{\phi'=0}^{\phi'=2\pi} \frac{d\sigma}{d\Omega} d\phi' d\cos\theta'}{\int_{\cos\theta'=-1}^{\cos\theta'=1} \int_{\phi'=0}^{\phi'=2\pi} \frac{d\sigma}{d\Omega} d\phi' d\cos\theta'} \\ &= (1 - a_1 - a_2 - a_3 - a_4) C_{00}^{\cos\theta} \\ &+ a_1 C_{01}^{\cos\theta} + a_2 C_{02}^{\cos\theta} + a_3 C_{03}^{\cos\theta} + a_4 C_{04}^{\cos\theta} \end{aligned} \tag{4.5a}$$

we use the standard algorithm to construct the ϕ CDF:

$$\begin{aligned} C_{\frac{d\sigma}{d\Omega}}^{\phi} &\equiv \frac{\int_{\phi'=0}^{\phi'=\phi} \frac{d\sigma}{d\Omega} d\phi'}{\int_{\phi'=0}^{\phi'=2\pi} \frac{d\sigma}{d\Omega} d\phi'} \\ &= \frac{(1 - a_1 - a_2 - a_3 - a_4 - 3e_2 - 6e_3 - 10e_4 - c_1 - \frac{2}{3}c_2 - d_1 - \frac{2}{3}d_2)\phi\rho_{00}}{(1 - a_1 - a_2 - a_3 - a_4)2\pi\rho_{00} + a_1 2\pi\rho_{01} + a_2 2\pi\rho_{02} + a_3 2\pi\rho_{03} + a_4 2\pi\rho_{04}} \\ &+ \frac{a_1\phi\rho_{01} + a_2\phi\rho_{02} + a_3\phi\rho_{03} + a_4\phi\rho_{04} + 3e_2\frac{1}{2}C_{22}^{\phi} + 6e_3\frac{1}{2}C_{23}^{\phi} + 10e_4\frac{1}{2}C_{24}^{\phi}}{(1 - a_1 - a_2 - a_3 - a_4)2\pi\rho_{00} + a_1 2\pi\rho_{01} + a_2 2\pi\rho_{02} + a_3 2\pi\rho_{03} + a_4 2\pi\rho_{04}} \\ &+ \frac{c_1\frac{1}{2}C_{11}^{\phi} + \frac{2}{3}c_2\frac{1}{2}C_{12}^{\phi} + d_1\frac{1}{2}C_{11'}^{\phi} + \frac{2}{3}d_2\frac{1}{2}C_{12'}^{\phi}}{(1 - a_1 - a_2 - a_3 - a_4)2\pi\rho_{00} + a_1 2\pi\rho_{01} + a_2 2\pi\rho_{02} + a_3 2\pi\rho_{03} + a_4 2\pi\rho_{04}} \end{aligned} \tag{4.5b}$$

where (consistent with earlier):

P_k^l are the Associated Legendre polynomials.

$$
\begin{aligned}
\rho_{00}(\cos\theta,\phi) &= \frac{1}{4\pi} \\
\rho_{0k}(\cos\theta,\phi) &= \frac{1}{4\pi}[1+P_k^0(\cos\theta)]\ \forall\ 1\leq k\leq 4, k\in\mathbb{R} \\
C_{00}^{\cos\theta}(\cos\theta) &= \frac{1}{2} \\
C_{01}^{\cos\theta}(\cos\theta) &= \frac{1}{4}(\cos^2\theta+2\cos\theta+1) \\
C_{02}^{\cos\theta}(\cos\theta) &= \frac{1}{4}(\cos^3\theta+\cos\theta+2) \\
C_{03}^{\cos\theta}(\cos\theta) &= \frac{1}{16}(5\cos^4\theta-6\cos^2\theta+8\cos\theta+9) \\
C_{04}^{\cos\theta}(\cos\theta) &= \frac{1}{16}(5\cos^5\theta-10\cos^3\theta+11\cos\theta+8) \\
C_{22}^{\phi}(\cos\theta_s,\phi) &= \frac{\phi}{2\pi}+\frac{P_2^2(\cos\theta_s)\sin 2\phi}{12\pi} \\
C_{23}^{\phi}(\cos\theta_s,\phi) &= \frac{\phi}{2\pi}+\frac{P_3^2(\cos\theta_s)\sin 2\phi}{24\pi} \\
C_{24}^{\phi}(\cos\theta_s,\phi) &= \frac{\phi}{2\pi}+\frac{P_4^2(\cos\theta_s)\sin 2\phi}{40\pi} \\
C_{11}^{\phi}(\cos\theta_s,\phi) &= \frac{\phi}{2\pi}+\frac{P_1^1(\cos\theta_s)\sin\phi}{2\pi} \\
C_{12}^{\phi}(\cos\theta_s,\phi) &= \frac{\phi}{2\pi}+\frac{P_2^1(\cos\theta_s)\sin\phi}{3\pi} \\
C_{11'}^{\phi}(\cos\theta_s,\phi) &= \frac{\phi}{2\pi}+\frac{P_1^1(\cos\theta_s)\cos\phi}{2\pi} \\
C_{12'}^{\phi}(\cos\theta_s,\phi) &= \frac{\phi}{2\pi}+\frac{P_2^1(\cos\theta_s)\cos\phi}{3\pi}
\end{aligned}
$$

With the CDFs delineated, we can now consider the respective inverses. Three of the CDFs are invertible analytically: l = 0, k = 0, 1 and 2 i.e. ρ_{00}, ρ_{01}, and ρ_{02}. The analytical inverses are outlined in table 4.4 on the next page.

k	l	Inverse CDF ($\mathbf{C^{-1}(u)}$)
0	0	$2u$
0	2	$2\sqrt{u}-1$
0	1	$\sqrt[3]{2u-1+2\sqrt{u^2-u+\frac{7}{27}}}-\sqrt[3]{1-2u+2\sqrt{u^2-u+\frac{7}{27}}}$

Table 4.4: Analytical CDF Inverses for Invertible Legendre Probability Density Functions. Using the inverse transform sampling method, we used a uniformly distributed u generated by a pseudo-random number generator in order to sample the correctly distributed values of $\cos\theta$ i.e. $\cos\theta_s = C^{-1}(u)$ where $u \in$ [0,1] is uniformly distributed.

The rest of the CDFs are inverted using Newton's method: if Newton's method fails to converge[27] then the Bisection method is employed. Since the CDFs are all monotonically increasing functions: their respective inversion algorithms must always yield unique solutions for ϕ and $\cos\theta$. Using Newton's method (section 4.4.5 on page 144) or the Bisection method (section 4.4.4 on page 143) we can invert the CDFs numerically using Eq. (4.6).

We need to know ϕ and $\cos\theta$. We sample either ϕ or $\cos\theta$ (depending on the CDF), then determine the unknown by finding the root of:

$$C(\cos\theta, \phi) - u = 0 \tag{4.6}$$

where: u is a pseudo-randomly generated number from 0 to 1.

Using these inversion algorithms (table 4.4 and eq. (4.6)), each probability density function ρ_{lk} was simulated for 50 million[28] neutron generation events for both the short and long target (because they have different geometries).

It is important to note that the ρ_{lk} PDFs are in the *center-of-mass/momentum (CM) frame* while the simulation takes place in the *lab frame*; therefore, the sampled ϕ and $\cos\theta$

[27]Newton's method converges monotonically (if it converges), so if the algorithm goes out of the domain for $\phi \in [0, 2\pi]$ or $\cos\theta \in [-1, 1]$ then it is known to have failed.

[28]Why 50 million? Lucid format data has a file size limit that is around the size of a 50 million event simulation ($\approx$ 2GB). Investigation into the file size limit found no user code implementing this limit: the file size limit remains of unknown ontogeny.

values provided by the CDF inverses needed to be Lorentz boosted into the lab frame: this was done using kinematics to provide the necessary transformation (see appendix C on page 284 for details).

The simulation outputs a simulated detector response which is then analyzed using the same data analysis procedure as the actual experimental data. We do this so that we can make the necessary assumption that the simulated efficiency is identical to the experimental efficiency. This necessitates applying identical cuts (when possible[29]) to both data sets: the simulated data and the experimental data.

Once all of the cuts have been applied and the data analysis is complete, the result is a neutron yield in each detector. The Legendre expansion of the cross section is assumed to be a homeomorphism of the neutron yields using the following derivation by Wurtz [Wur10c].

In the absence of geometric effects, the number of neutrons, N, passing through each detector is:

$$\frac{dN}{d\Omega}(\theta,\phi) = \Phi n l \frac{d\sigma}{d\Omega}$$

Let G be the function that describes the geometric effect of the experimental arrangement, then what we measure is:

$$G(\frac{dN}{d\Omega}(\theta,\phi)) = \Phi n l G(\frac{d\sigma}{d\Omega})$$

Where: Φ is the photon flux as a function of target depth, n is the atomic number density and l is the target length. The yield in a specific detector, N_d is:

$$N_d \approx \epsilon_d \int_{\Omega_d} G(\frac{dN}{d\Omega}(\theta,\phi))d\Omega$$

[29]For example, the background radiation cut cannot be performed on the simulation because there is no background radiation.

Where: Ω_d represents the effective detector surface area in spherical coordinates and ϵ_d is the detector's efficiency.

Now we simply do a few substitutions and using the linearity of the integral operator we find:

$$N_d \approx \epsilon_d \int_{\Omega_d} \Phi n l G(\frac{d\sigma}{d\Omega}(\theta,\phi))d\Omega$$

We sub in eq. (4.2) on page 119 for the differential cross section and multiply by σ:

$$\begin{aligned} N_d \approx \epsilon_d \Phi n l \sigma \int_{\Omega_d} G(\frac{1}{4\pi} \Bigg[& (1 - \sum_{k=1}^{4} a_k - 3e_2 - 6e_3 - 10e_4 - c_1 - \frac{3}{2}c_2 - d_1 - \frac{3}{2}d_2)\rho_{00}(\theta,\phi) \\ & + \sum_{k=1}^{4} a_k \rho_{0k}(\theta,\phi) + 3e_2\rho_{22}(\theta,\phi) + 6e_3\rho_{23}(\theta,\phi) + 10e_4\rho_{24}(\theta,\phi) \\ & + c_1\rho_{11}(\theta,\phi) + \frac{3}{2}c_2\rho_{12}(\theta,\phi) + d_1\rho_{11'}(\theta,\phi) + \frac{3}{2}d_2\rho_{12'}(\theta,\phi) \Bigg])d\Omega \end{aligned}$$

We assume the geometric function, G, is a linear function of the parameterization[30]and therefore:

$$\begin{aligned} N_d \approx \epsilon_d \Phi n l \sigma \frac{1}{4\pi} \Bigg[& (1 - \sum_{k=1}^{4} a_k - 3e_2 - 6e_3 - 10e_4 - c_1 - \frac{3}{2}c_2 - d_1 - \frac{3}{2}d_2) \int_{\Omega_d} G(\rho_{00}(\theta,\phi))d\Omega \\ & + \sum_{k=1}^{4} a_k \int_{\Omega_d} G(\rho_{0k}(\theta,\phi))d\Omega + 3e_2 \int_{\Omega_d} G(\rho_{22}(\theta,\phi))d\Omega + 6e_3 \int_{\Omega_d} G(\rho_{23}(\theta,\phi))d\Omega \\ & + 10e_4 \int_{\Omega_d} G(\rho_{24}(\theta,\phi))d\Omega + c_1 \int_{\Omega_d} G(\rho_{11}(\theta,\phi))d\Omega + \frac{3}{2}c_2 \int_{\Omega_d} G(\rho_{12}(\theta,\phi))d\Omega \\ & + d_1 \int_{\Omega_d} G(\rho_{11'}(\theta,\phi))d\Omega + \frac{3}{2}d_2 \int_{\Omega_d} G(\rho_{12'}(\theta,\phi))d\Omega \Bigg] \end{aligned}$$

If our simulation has perfectly incorporated all of the geometric effects in our experimental arrangement, then a simulation of N^{sim} neutrons with the probability density functions ρ_{lk} will yield:

$$N^{sim}_{d,lk} = \epsilon^{sim}_d N^{sim} \int_{\Omega_d} \Phi n l G(\rho_{lk}(\theta,\phi))d\Omega$$

If we assume $\frac{\epsilon_d}{\epsilon_d^{sim}}$ is the same for all of the detectors,[31] then lump together all of the factors into a new parameter, A, and sub in the $N_{d,lk}^{sim}$ for the ρ_{lk} to get an expansion in terms of neutron yields:

$$\begin{aligned} N_d \approx & A[(1 - \sum_{k=1}^{4} a_k - 3e_2 - 6e_3 - 10e_4 - c_1 - \frac{3}{2}c_2 - d_1 - \frac{3}{2}d_2)N_{d,00}^{sim} \\ & + \sum_{k=1}^{4} a_k N_{d,0k}^{sim} + 3e_2 N_{d,22}^{sim} + 6e_3 N_{d,23}^{sim} + 10e_4 N_{d,24}^{sim} \\ & + c_1 N_{d,11}^{sim} + \frac{3}{2}c_2 N_{d,12}^{sim} + d_1 N_{d,11'}^{sim} + \frac{3}{2}d_2 N_{d,12'}^{sim}] \end{aligned} \tag{4.7}$$

where: N_d is the neutron yield in a detector, d, and $N_{d,lk}^{sim}$ is the simulated neutron yield for the probability density function ρ_{lk}.

Therefore once we've simulated the probability density functions, ρ_{lk}, and applied all of the data analysis cuts to get the neutron yields, $N_{d,lk}^{sim}$, for each l and k: we can use eq. (4.7) to extract the parameters for the Legendre expansion of the cross section using the 88 detectors on Blowfish (N_d, $\{d|d \in \mathbb{Z} \wedge d \in [1, 88]\}$).

The results of the ρ_{lk} PDF simulations for the long target follow;[32] starting with figure 4.4 on the next page, and including the analytical plots for the respective ρ_{lk} in the CM frame. Blowfish, the target and the probability density function are all symmetric in phi so the 'bumpiness' with respect to ϕ (in the figures) must be caused by the counting error.[33]

[30] We later verified this is the case by simulating the experimental parameters and extracting new parameters from the simulated data: the parameters are the same (see appendix J on page 302 for details).

[31] We test this assumption was well founded by rotating Blowfish during the experiment: so that different detectors were at the same position.

[32] The short target simulations have similar overall shapes, but they have significantly different neutron detector yields.

[33] The counting error is a statistical error of magnitude $\sqrt{N}$: where N is the number of events measured. The relative error in each cell for the ρ_{00} simulation is approximately 0.1%.

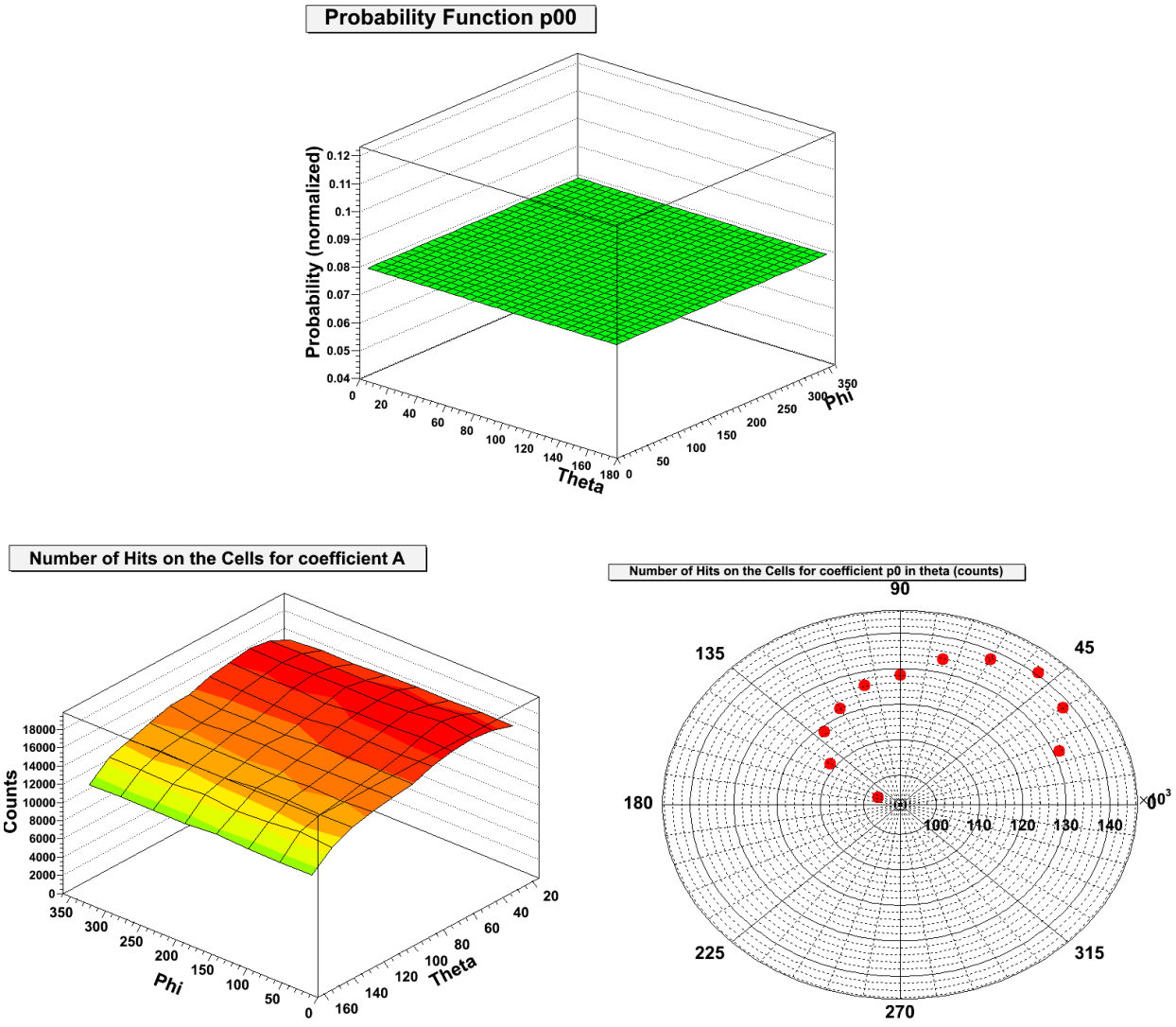

Figure 4.4: Simulated Neutron Yields from the ρ_{00} PDF. The top plot is the analytical function ρ_{00} (CM frame), while the bottom two are plots of the neutron yields from the simulation of ρ_{00} (lab frame). The polar plot (bottom right) has had the neutron yield averaged over ϕ. The Lorentz transformation into the lab frame causes the forward biasing (towards $\theta = 0$). The dip at the first ring ($\theta = 22.5°$) is due to the target's geometry: the short target doesn't show this feature. Note: $\theta \in [0°, 180°]$ (polar angle) is measured from the downstream beam axis (0°) up to the upstream beam axis (180°), $\phi \in [0°, 360°)$ is measured transverse to the beam axis (starting at the left horizontal from the beam's perspective).

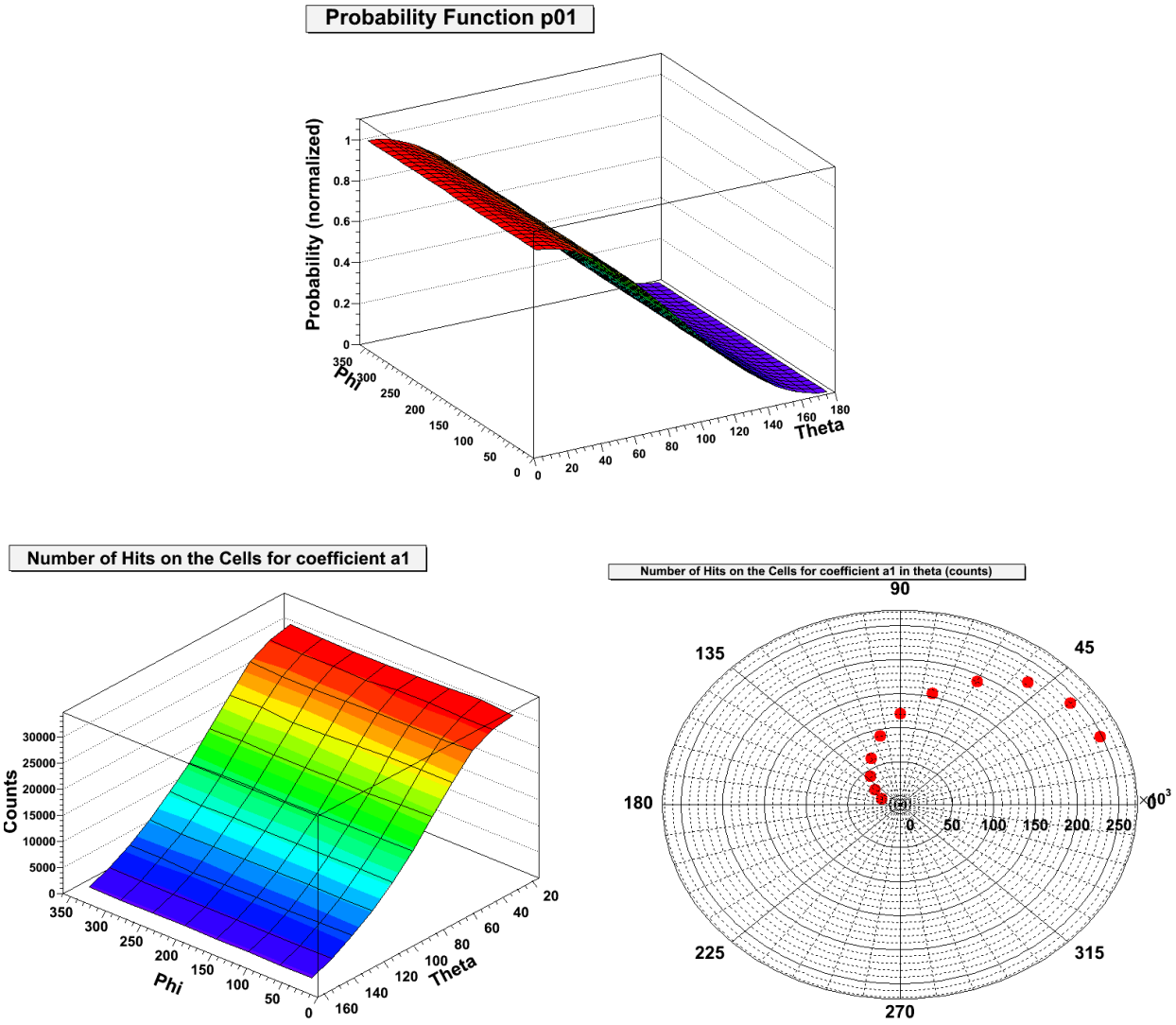

Figure 4.5: Simulated Neutron Yields from the ρ_{01} PDF. The top plot is the analytical function ρ_{01} (CM frame), while the bottom two are plots of the neutron yields from the simulation of ρ_{01} (lab frame). The polar plot (bottom right) has had the neutron yield averaged over ϕ.

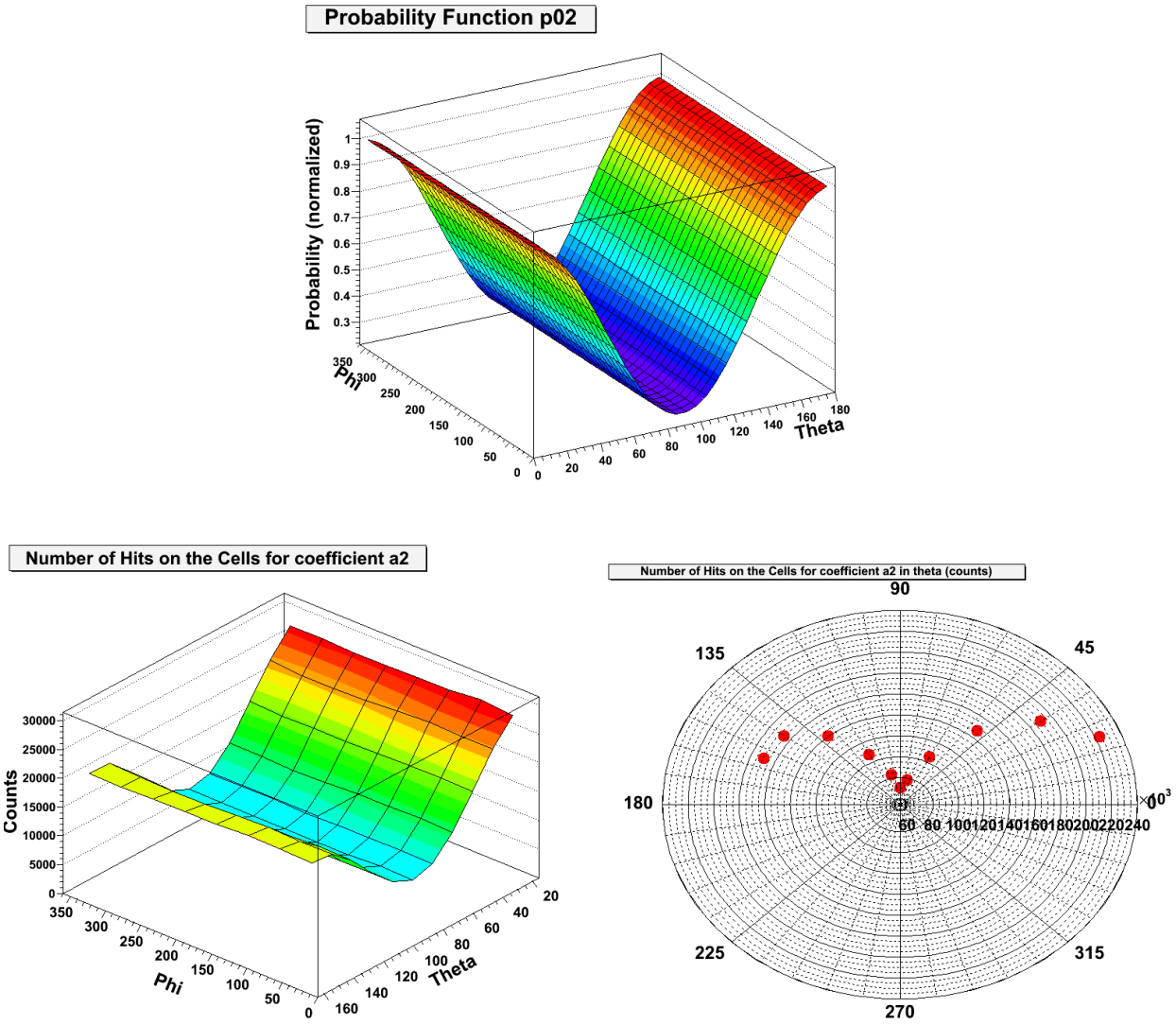

Figure 4.6: Simulated Neutrons Yields from the ρ_{02} PDF. The top plot is the analytical function ρ_{02} (CM frame), while the bottom two are plots of the neutron yields from the simulation of ρ_{02} (lab frame). The polar plot (bottom right) has had the neutron yield averaged over ϕ.

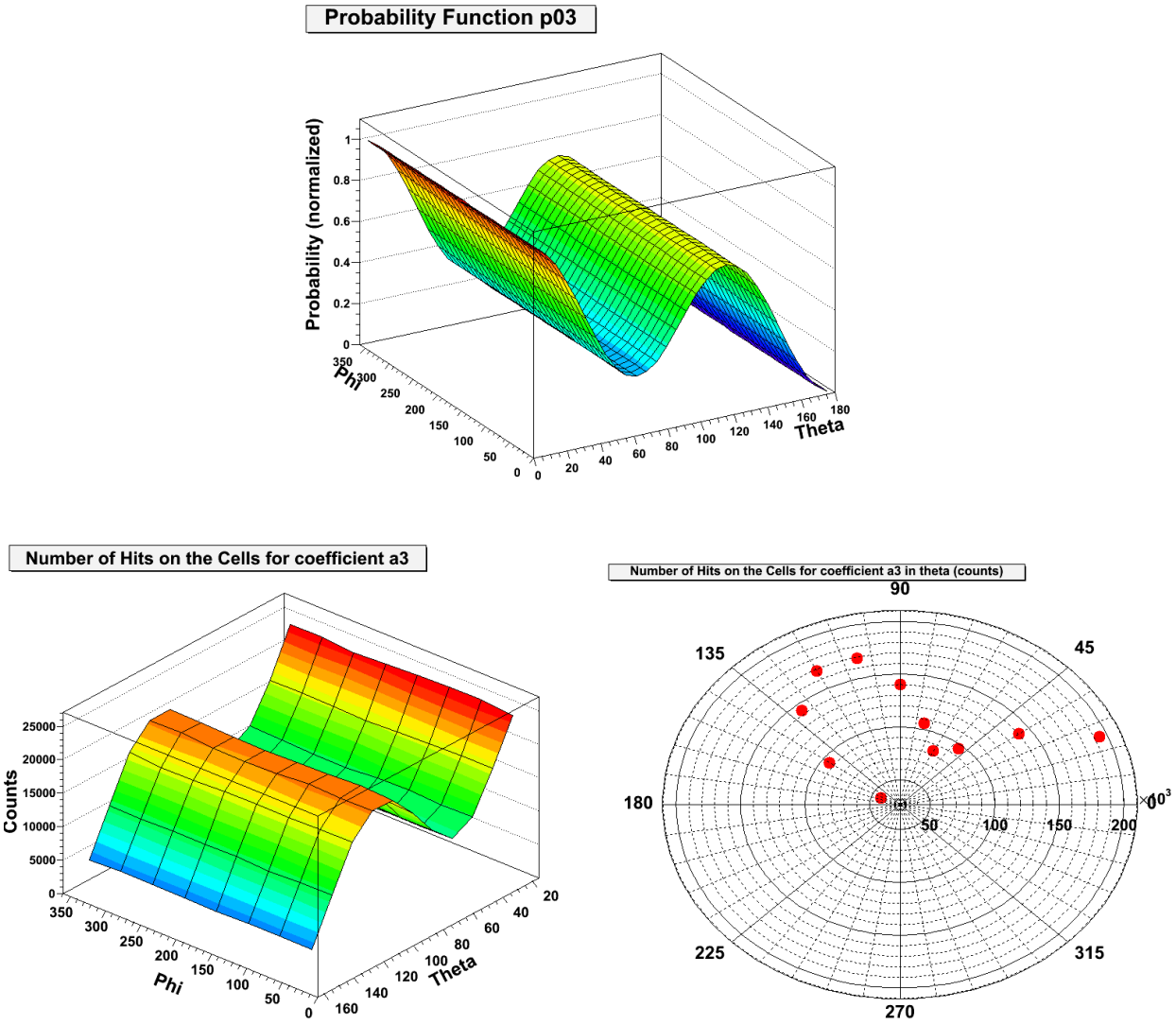

Figure 4.7: Simulated Neutrons Yields from the ρ_{03} PDF. The top plot is the analytical function ρ_{03} (CM frame), while the bottom two are plots of the neutron yields from the simulation of ρ_{03} (lab frame). The polar plot (bottom right) has had the neutron yield averaged over ϕ.

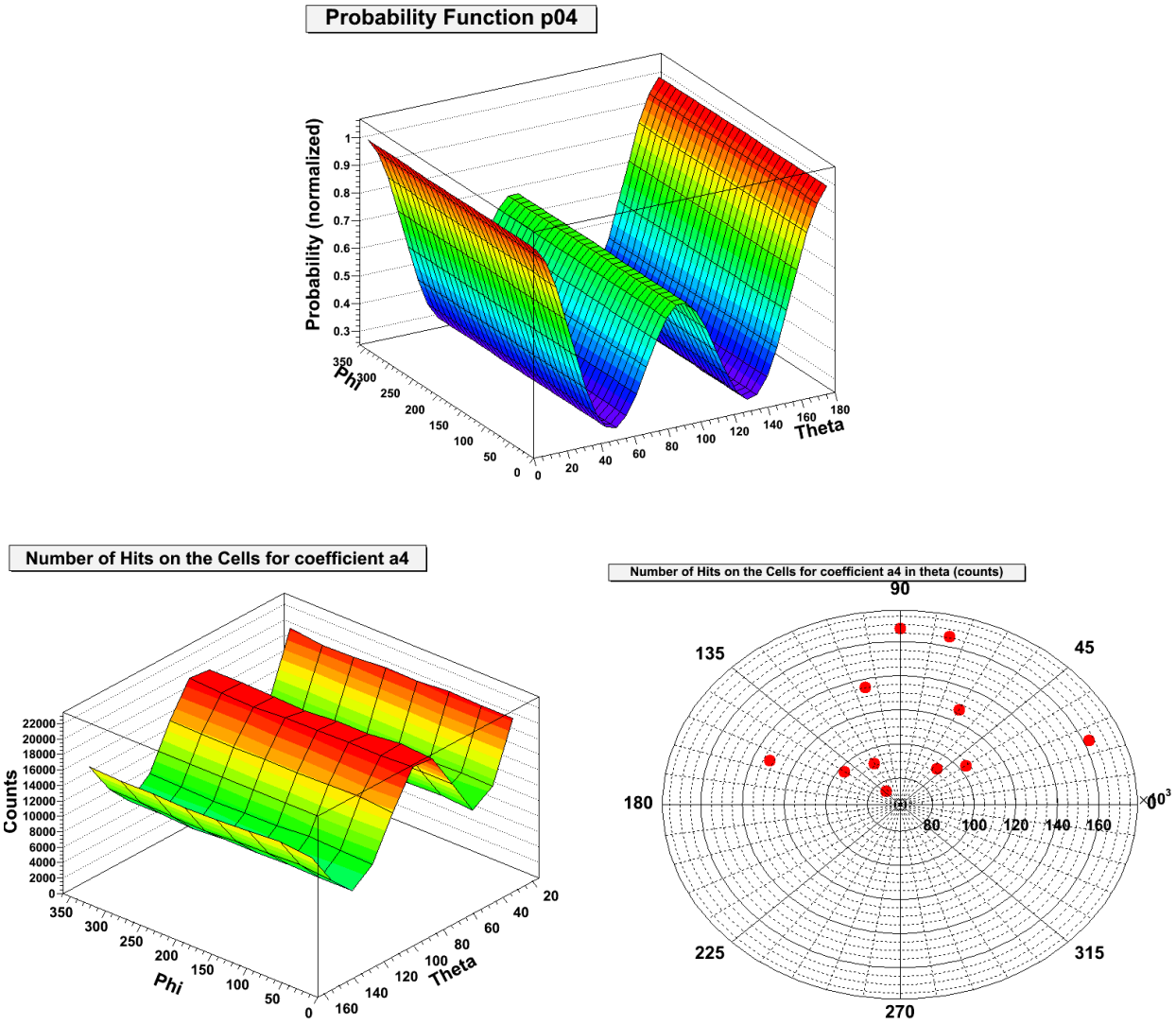

Figure 4.8: Simulated Neutrons Yields from the ρ_{04} PDF. The top plot is the analytical function ρ_{04} (CM frame) (CM frame), while the bottom two are plots of the neutron yields from the simulation of ρ_{04} (lab frame). The polar plot (bottom right) has had the neutron yield averaged over ϕ.

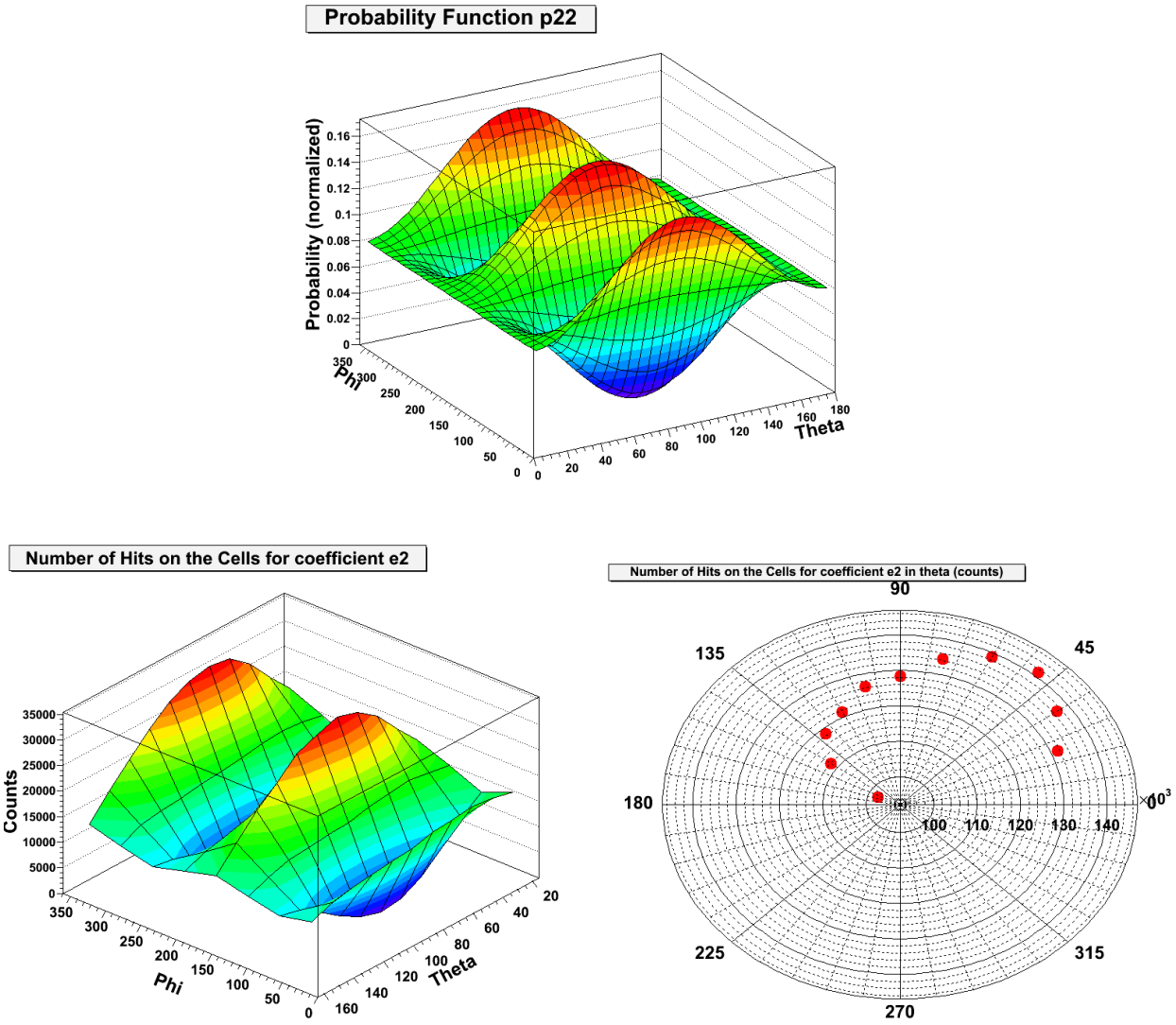

Figure 4.9: Simulated Neutrons Yields from the ρ_{22} PDF. The top plot is the analytical function ρ_{22} (CM frame), while the bottom two are plots of the neutron yields from the simulation of ρ_{22} (lab frame). The polar plot (bottom right) has had the neutron yield averaged over ϕ.

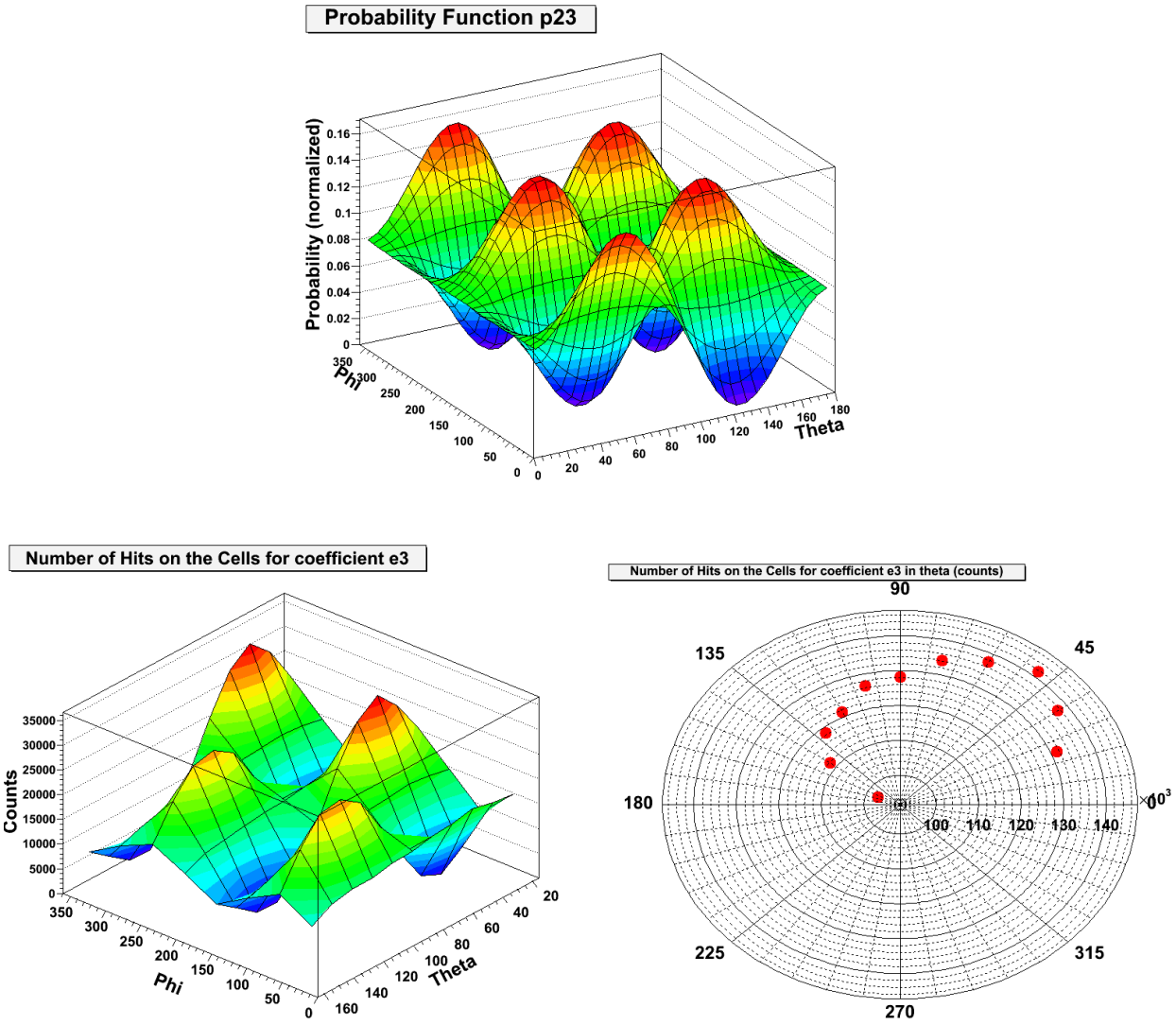

Figure 4.10: Simulated Neutrons Yields from the ρ_{23} PDF. The top plot is the analytical function ρ_{23} (CM frame), while the bottom two are plots of the neutron yields from the simulation of ρ_{23} (lab frame). The polar plot (bottom right) has had the neutron yield averaged over ϕ.

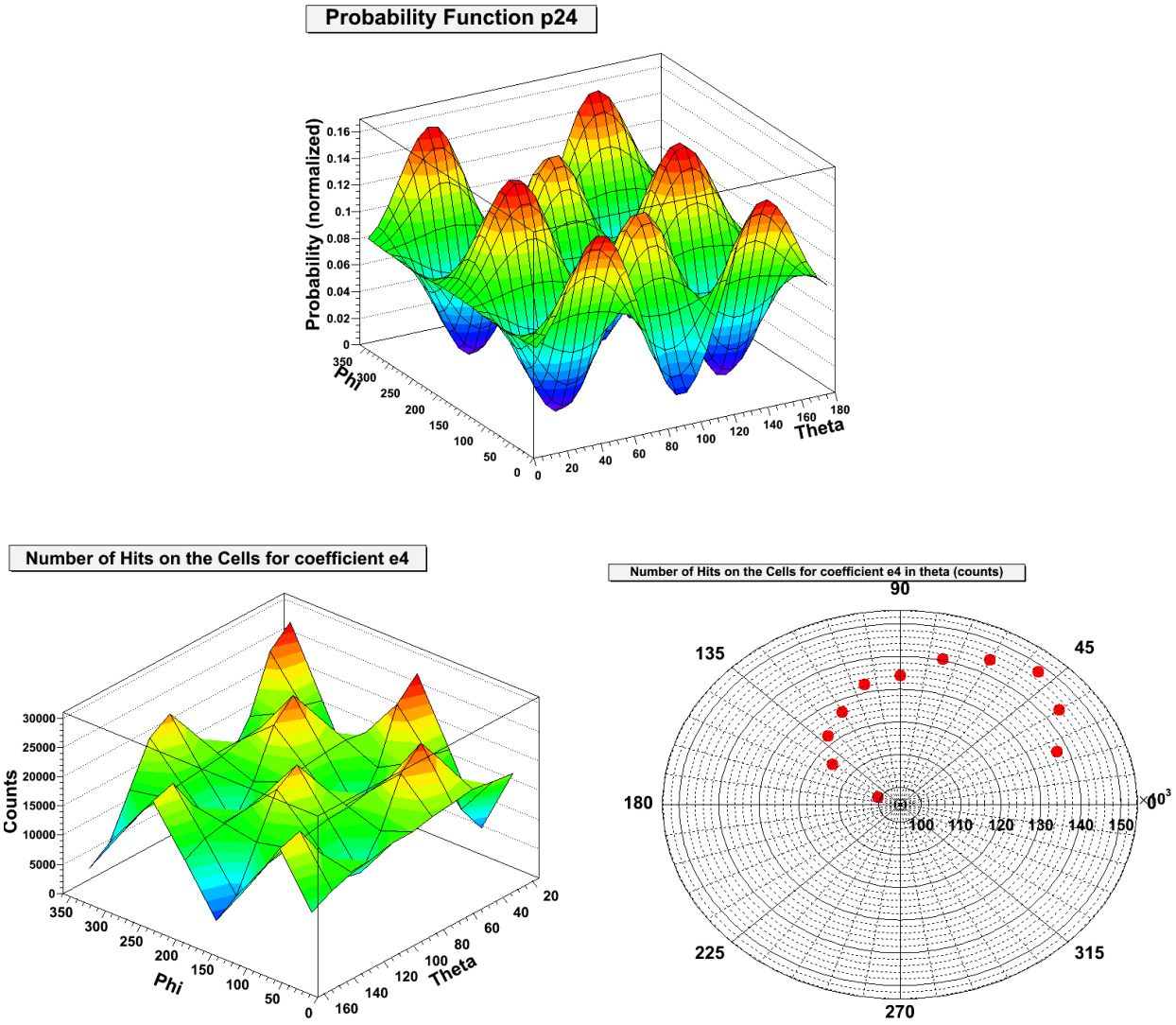

Figure 4.11: Simulated Neutrons Yields from the ρ_{24} PDF. The top plot is the analytical function ρ_{24} (CM frame), while the bottom two are plots of the neutron yields from the simulation of ρ_{24} (lab frame). The polar plot (bottom right) has had the neutron yield averaged over ϕ.

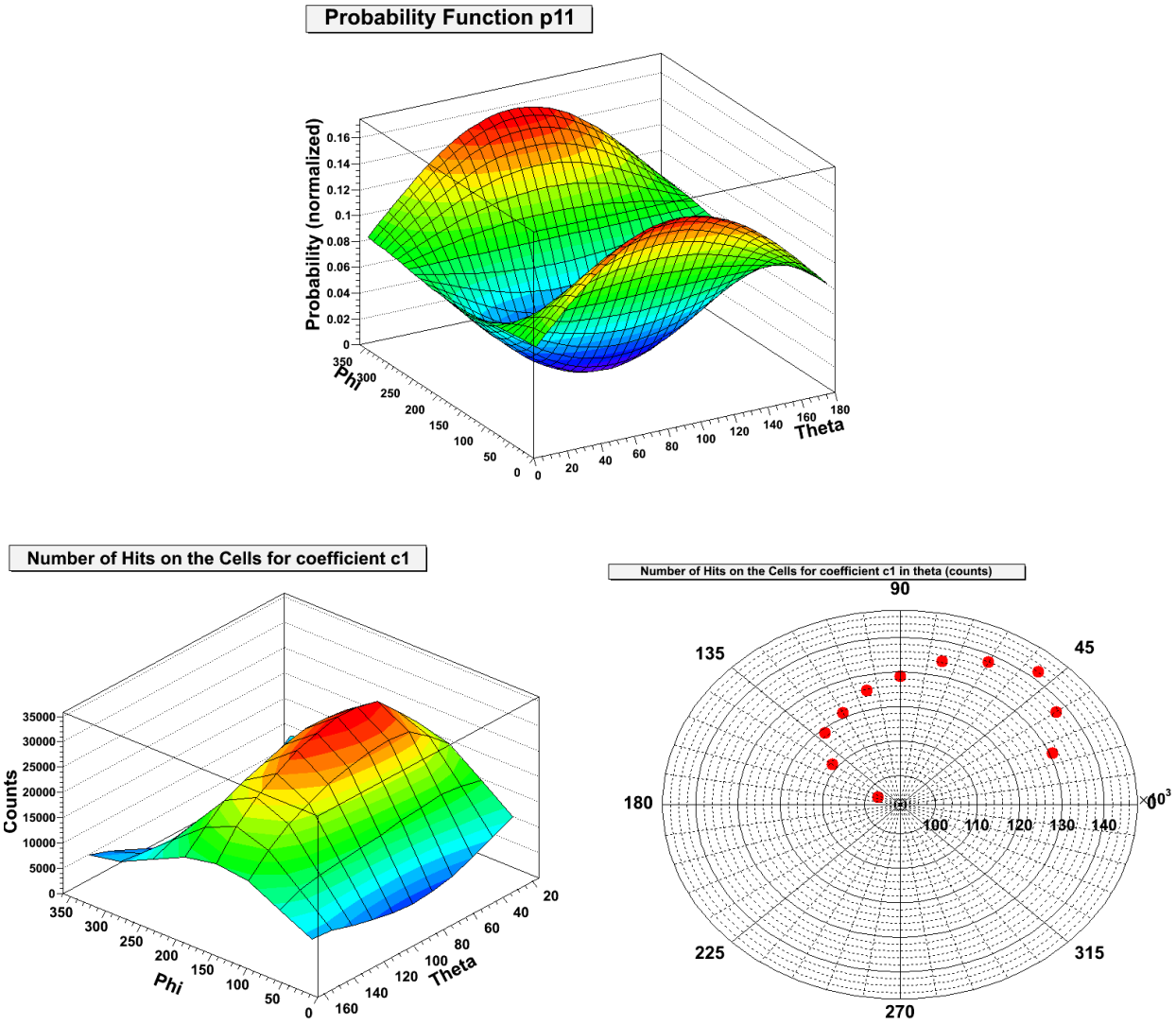

Figure 4.12: Simulated Neutrons Yields from the ρ_{11} PDF. The top plot is the analytical function ρ_{11} (CM frame), while the bottom two are plots of the neutron yields from the simulation of ρ_{11} (lab frame). The polar plot (bottom right) has had the neutron yield averaged over ϕ.

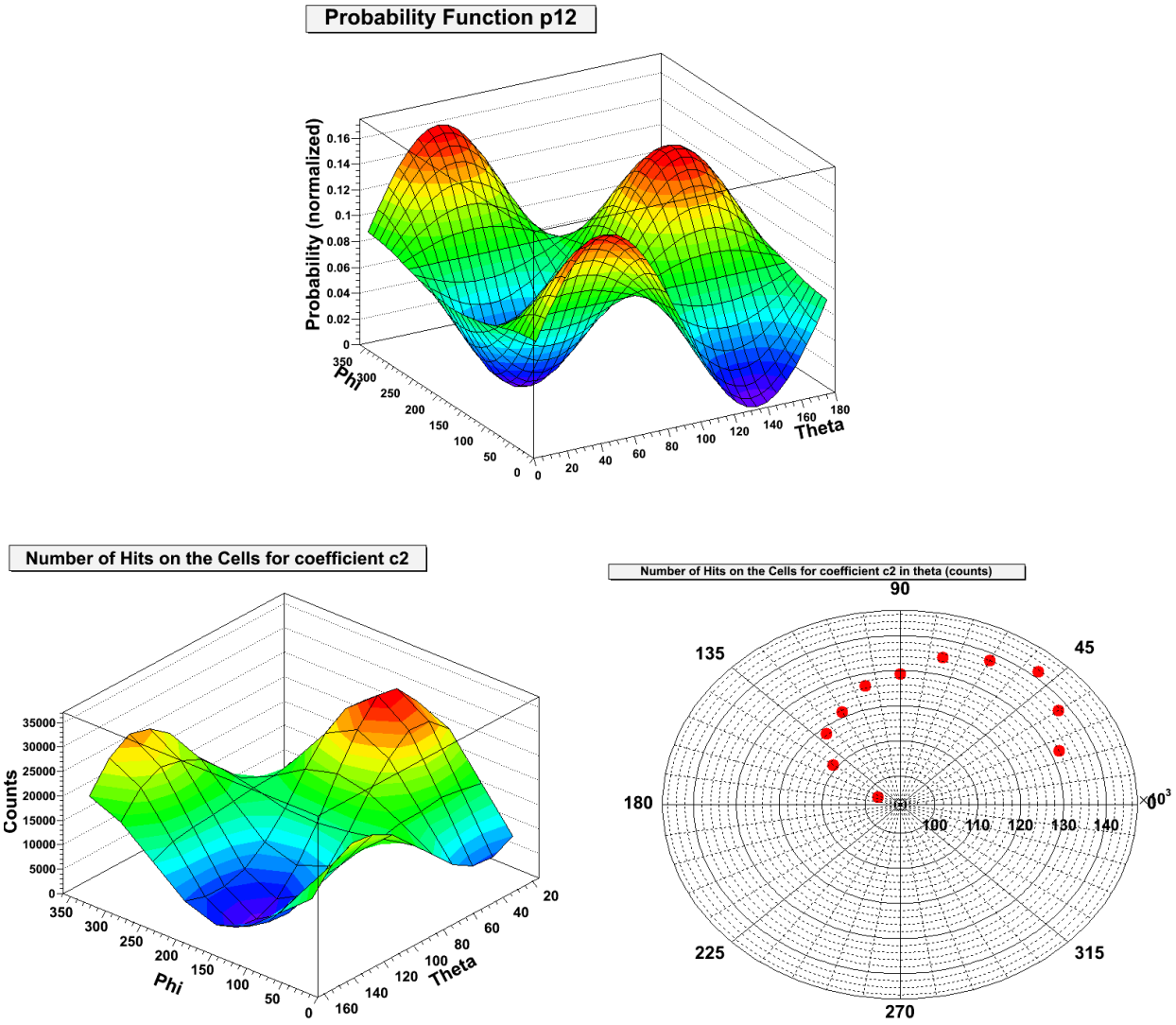

Figure 4.13: Simulated Neutrons Yields from the ρ_{12} PDF. The top plot is the analytical function ρ_{12} (CM frame), while the bottom two are plots of the neutron yields from the simulation of ρ_{12} (lab frame). The polar plot (bottom right) has had the neutron yield averaged over ϕ.

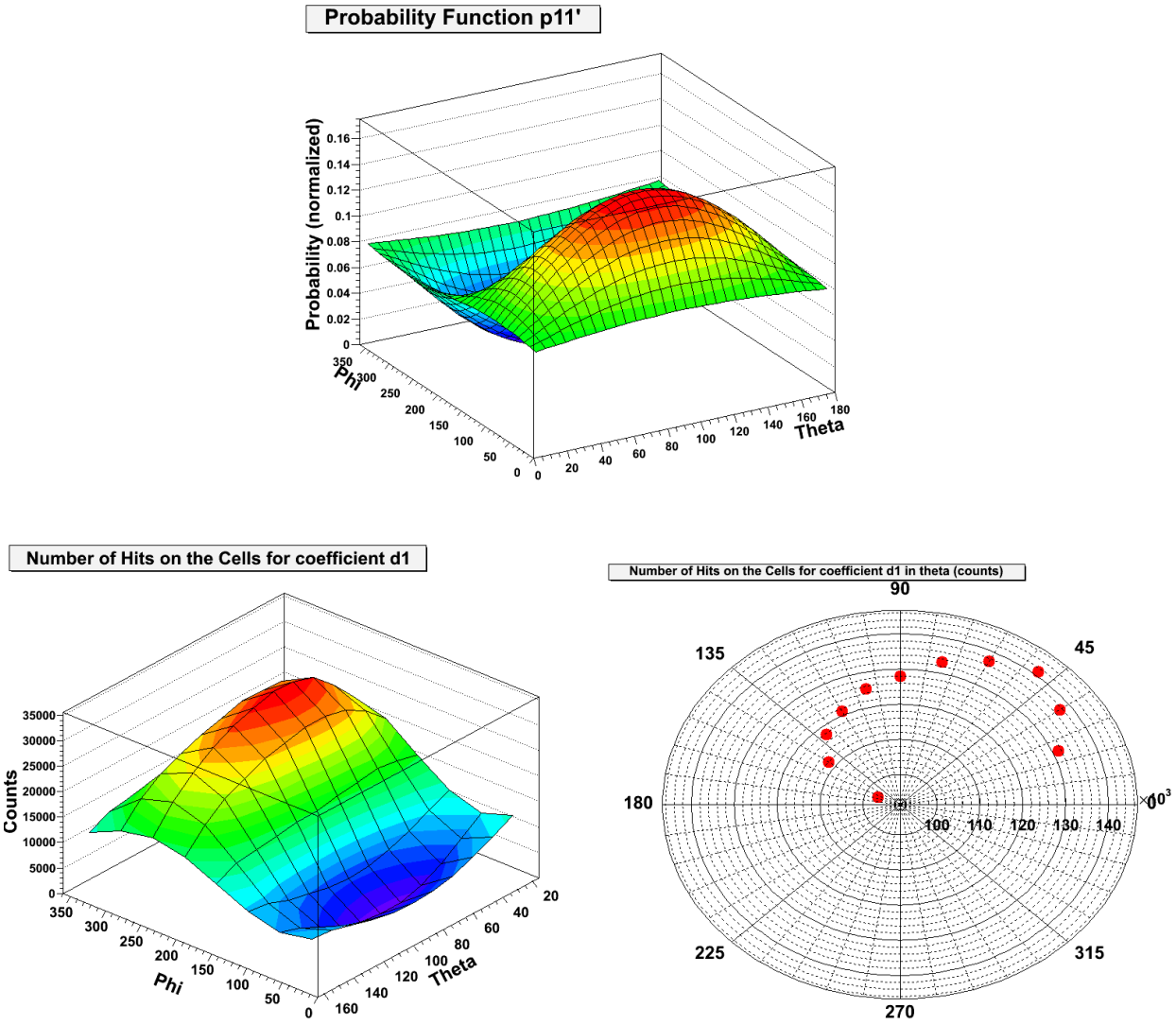

Figure 4.14: Simulated Neutrons Yields from the ρ_{11}' PDF. The top plot is the analytical function ρ_{11}' (CM frame), while the bottom two are plots of the neutron yields from the simulation of ρ_{11}' (lab frame). The polar plot (bottom right) has had the neutron yield averaged over ϕ.

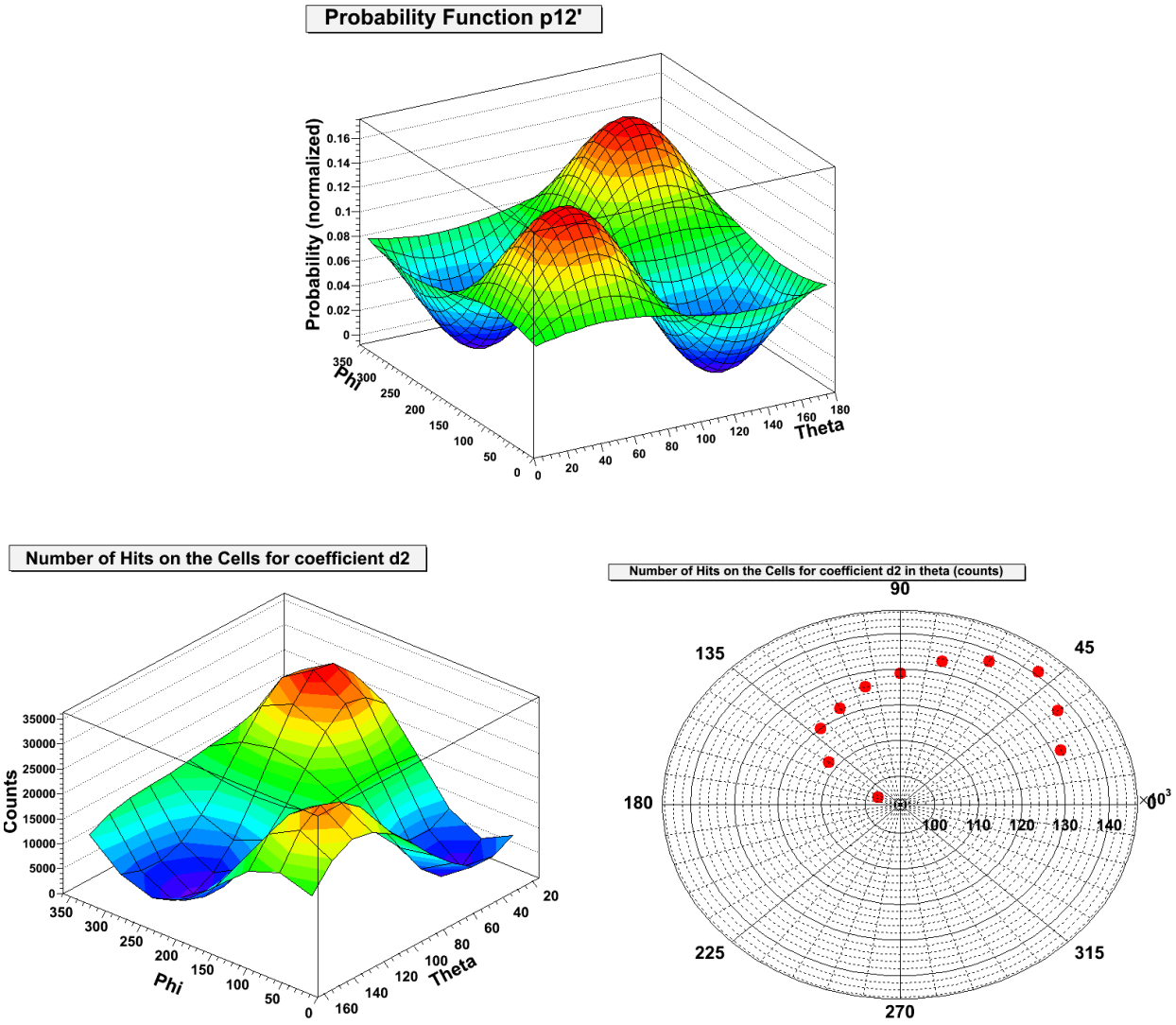

Figure 4.15: Simulated Neutrons Yields from the ρ_{12}' PDF. The top plot is the analytical function ρ_{12}' (CM frame), while the bottom two are plots of the neutron yields from the simulation of ρ_{12}' (lab frame). The polar plot (bottom right) has had the neutron yield averaged over ϕ.

Figures 4.4 through 4.15 illustrate how the Legendre PDFs transform when Lorentz boosted, then simulated. It should be clear from a geometric point of view that all of the Legendre PDFs could be homeomorphisms to the simulated neutron yields, something which was tested empirically in appendix J on page 302. So long as a homeomorphism exists

between the Legendre PDFs and the neutron yields we can safely assume that the parameters extracted from fitting to the neutron yields will be the same as those used to describe the differential cross section.

4.4.3 Inverse Transform Sampling

When dealing with software that utilizes probabilities, one invariably encounters the problem of sampling some probabilistic function (e.g. a PDF) with an appropriately weighted algorithm. In this experiment, this fundamental problem was manifested as sampling the target attenuation (section 4.4.1 on page 118) PDF and the Legendre PDFs (section 4.4.2 on page 119) in the simulation. One method for tackling this problem is inverse transform sampling.

Inverse transform sampling proceeds as follows:

1. Find a PDF: $f(x)$.
2. Calculate its CDF: $C(x)$
3. Invert the CDF: $C^{-1}(x)$
4. Use some uniformly sampled $u \in [0, 1]$ as input to the inverse CDF: $C(u) = x$ and the resulting distribution of x is identical to the PDF: f(x) [Dev94].

Inverse transform sampling is made possible by two theorems: theorem 2 and theorem 3 on the next page.

Theorem 2 (Devroye [Dev94])**.** ***Inverse Transform Sampling (1)***
Let $C(x)$ be an invertible cumulative distribution function defined on $x \in \mathbb{R}$, then if u is a uniformly distributed random variable in $[0, 1]$ then $C^{-1}(u)$ has cumulative distribution function $C(x)$.

Proof.
Let C be a cumulative distribution function defined on $\mathbb{R}$, then:
$C : \mathbb{R} \mapsto [0, 1]$
$C(x) = \int_{-\infty}^{x} f(x')dx' =$ probability that an arbitrary x' is $\leq x$

where f is the probability density function corresponding to C.

C is invertible, so its inverse C^{-1} must be defined by:

$C^{-1}(u) = infimum\{x : C(x) = u, u \in [0,1]\}$

Let $P(y)$ denote the probability of an event: y, occurring.

$P(C^{-1}(u) \leq x) = P(infimum\{y : C(y) = u\} \leq x)$

$= P(u \leq C(x))$ because C is monotonically increasing (it must be because it is defined as an integral of a universally positive function).

$= P(u \leq C(x)) = C(x)$ □

Theorem 3. ***Inverse Transform Sampling (2)***

Let f be a probability density function defined on $x \in \mathbb{R}$, if the cumulative distribution function of f: C, satisfies theorem 2 on page 141 and u is a uniformly distributed random variable in $[0,1]$ then sampling $C^{-1}(u)$ gives probability density function $f(x)$.

Proof.

Let f be a probability density function defined on $\mathbb{R}$, then:

1) $f : \mathbb{R} \mapsto [0, \infty)$ and 2) $\int_{-\infty}^{\infty} f(x)dx = 1$

By analogy with discrete probability distribution functions, $\lim_{dx \to 0} f(x)dx \propto$ probability that an event near x occurs.

The cumulative probability function is defined as:

$C(x) = \int_{-\infty}^{x} f(x')dx'$

or, by the Fundamental Theorem of Calculus (FTC): $dC(x) = f(x)dx$.

I will show that $\lim_{dx \to 0} f(x)dx = \lim_{du \to 0} C^{-1}(u)du$ given $C^{-1}(u) = infimum\{x : C(x) = u, u \in [0,1]\}$ is the relationship between u and x: i.e. sampling $C^{-1}(u)$ over $u \in [0,1]$ is equivalent to sampling $f(x)$ over $x \in \mathbb{R}$ in the limit $du \to 0$.

Case 1: $x \neq 1$.

Consider some arbitrary $\epsilon > 0$, then let $\delta = \frac{\epsilon}{|1-x|}$ $\forall$ $x \neq 1$.

$|f(x)dx - \lim_{du \to 0} C^{-1}(u)du| = |f(x)dx - xf(x)dx|$ using the FTC.

$= |1 - x|f(x)dx$ using condition (1) of f.

Now, suppose $0 < f(x)dx < \delta$, i.e. $0 < f(x)dx < \frac{\epsilon}{|1-x|}$,

then $|1 - x|f(x)dx < \epsilon$.

Case 2: $x = 1$

Consider some arbitrary $\epsilon > 0$, then let $\delta = \epsilon \; \forall \; x = 1$.

$|f(x)dx - \lim_{du \to 0} C^{-1}(u)du| = |f(x)dx - xf(x)dx|$ using the FTC.

$= |1 - x|f(x)dx = 0$ using condition (1) of f and substituting $x = 1$.

Now, suppose $0 < f(x)dx < \delta$, i.e. $0 < f(x)dx < \epsilon$,

then $|1 - x|f(x)dx < \epsilon$.

This covers all possible values of x, therefore $\lim_{dx \to 0} f(x)dx = L = \lim_{du \to 0} C^{-1}(u)du$ by the ϵ/δ definition of a limit. □

The necessary functions (i.e. the inverse CDFs) for the target attenuation PDF and the Legendre PDFs have already been outlined in their respective sections: these were the functions used to implement the PDFs into the simulation. For those CDFs that could not be analytically inverted, we used eq. (4.6) on page 125 to numerically invert them via Newton's method (section 4.4.5 on the next page) and the Bisection method (section 4.4.4).

4.4.4 The Bisection Method

The Bisection method is a simple application of the *Intermediate Value Theorem*, which states that if f is continuous on an interval [a, b] and changes sign during that same interval exactly once then f must cross 0 in the interval exactly once i.e. $\exists$ *exactly one* $c \in$ [a, b] such that $f(c) = 0$ [Tur01]. If we considered some sub-interval of [a, b], say [a +Δx, b] and we found that f changed sign within this sub-interval, then the root must exist in the new interval [a +Δx, b].

The bisection method takes the step, Δx, to be half of the length of the interval: Δx = (b - a)/2 then proceeds by testing whether the root occurs in the left half i.e. [a, b - Δx] or right half i.e. [a +Δx, b] of the interval: the root must be in one of the halves,[34] the one which it resides in is kept and the other interval is thrown away, then the algorithm repeats until the final interval is arbitrarily small around the root. Achieving a desired precision, say δx, for a root x is achieved by iterating until the final interval is [x $-\delta$x, x $+\delta$x] (which can

[34] In the unlikely, though possible (because we use floating point numbers) event that the root falls in both intervals i.e. at a + Δx = b $-\Delta$x then that value (a +Δx = b $-\Delta$x) is taken as being the correct root; to floating point precision.

be tested for by simply taking the length of the interval). Note that for a piece of software, any real number is only approximated to some precision defined by the amount of available memory: by setting the desired precision to the precision of the floating point number one can find the root of f without any loss of accuracy compared to the analytical root (although it will almost certainly be slower).[35]

Outline of Bisection method: Given a continuous function $f(x) = 0$ over some domain [a, b] with exactly one root, the root can be found by the following steps:

1. Select the midpoint: c = (a + b)/2.

2. Test to see if the root is in [a, c] or [c, b]: we know by the *Intermediate Value Theorem* that if f(a) $>$ 0 and f(c) $>$ 0 or f(a) $<$ 0 and f(c) $<$ 0 then there is no root on the interval [a, c], therefore the root must be in [c, b], but if f(a) $<$ 0 and f(c) $>$ 0 or f(a) $>$ 0 and f(c) $<$ 0 then we know the root must be in [a, c]. If f(c) = 0 then we are done.

3. Shrink the interval by setting a = c if the root is in [c, b] or b = c if the root is in [a, c] and repeat.

4.4.5 Newton's Method

The Bisection method is a rigorous and stable algorithm for finding the root of a continuous function on a closed interval, but it isn't particularly fast: the interval converges *linearly* at a rate of $\frac{1}{2}$ per iteration. Newton's method converges faster: *quadratically* [Tur01] (when it converges); we attempt to use Newton's method first in order to (hopefully) save time on computations, then resort to the Bisection method if it fails.

Newton's method is essentially an application of the local linear approximation (i.e. the first-order Taylor series) near a root. The local linear approximation of f(x) is:

$$f(x) \approx f(x_0) + (x - x_0)f'(x_0)$$

[35]The actual precision used for both numerical methods in the simulation was 10^{-10}.

where: x_0 is some point near x. If x is the root, then:

$$f(x) = 0, \implies 0 \approx f(x_0) + (x - x_0)f'(x_0)$$
$$\implies x_0 - \frac{f(x_0)}{f'(x_0)} \approx x$$

Assuming that the local linear approximation improves the initial estimate, x_0, which is near a root $f(c) = 0$, we can iterate this function using Newton's iteration formula:

$$x_n \approx x_{n-1} - \frac{f(x_{n-1})}{f'(x_{n-1})} \tag{4.8}$$

$$\tag{4.9}$$

where: n is the n^{th} iteration of the formula and x_n is the estimated root on the nth iteration.

Whether or not Newton's iteration formula converges depends on the derivatives of f: f' and f". Practically speaking, Newton's method won't converge if f' is small, causing $\frac{f(x_0)}{f'(x_0)}$ to be large relative to $|x_n - x|$ because it will over-correct the subsequent iteration. The conditions for convergence are given in theorem 4.

Theorem 4 (Turner [Tur01])**.** ***Convergence Conditions for Newton's Method***
Let f have a root on the interval [a, b], be twice differentiable on the interval, and satisfy the conditions:

1. *f(a)f(b) < 0*
2. *f' has no roots on [a, b]*
3. *f" has no roots on [a, b], and*
4. $|\frac{f(a)}{f'(a)}| < |b - a|$ *and* $|\frac{f(b)}{f'(b)}| < |b - a|$.

Then Newton's method will converge to the root x such that f(x) = 0 from any starting point on [a,b].

The proof of theorem 4 is beyond the scope of this thesis.

Chapter 5

Analysis

5.1 Introduction

This chapter describes the steps taken in processing the raw experimental data into meaningful, logically consistent data. Specifically, this means: calibrating the instruments (section 5.3 on page 151), performing the necessary cuts to eliminate impertinent events (section 5.4 on page 193), and then extracting meaningful observables to compare with the theoretical calculations: the total cross section, σ (section 5.5 on page 211), and the differential cross section and analyzing power, both based on the parameterization of the associated Legendre polynomials (section 5.6 on page 216).

First, we discuss the necessary software for manipulating the data, then we move onto calibration, then cuts, and finally computing the final data (i.e. observables).

5.2 ROOT

"The development of ROOT is a continuous conversation between users and developers with the line between the two blurring at times and the users becoming co-developers." [ROO14]

ROOT [Ant09, ROO14, Bru97] is a data analysis framework capable of efficiently handling large volumes of data [Ant09] and performing a variety of data analysis features e.g. data acquisition, event reconstruction, detector simulation, event generation, and any type of rudimentary data analysis desired [Bru97]. ROOT is an object-orientated "framework" [Bru97] that is remarkably similar to the GEANT4 "toolkit" [Ago03] (section 4.2): "framework" and "toolkit" are synonyms in this context.

Like GEANT4, ROOT is based on object-orientated `C++` programming with a suite of built-in classes to enable: black-box programming, and modular updating by developers (both official and unofficial: users are empowered to be developers). ROOT has a number of other similarities to GEANT4, which should come as no surprise since they are both officially supported by CERN [Ago03, Ant09], and the concept developers from ROOT previously worked on GEANT3.[1]

The notable differences between ROOT and GEANT4 are: (1) ROOT is used primarily for data acquisition and analysis, while GEANT4 is used for simulations, and (2) ROOT strongly utilizes *hierarchical* object structure. The hierarchical object structure of ROOT enables inheritance of important class members, the notable example is the TObject class which the majority of classes in ROOT are descendants of. TObject controls basic object functions like: Write() (saves the object), GetName() (returns name of the object), and Delete() (deletes the object).

ROOT runs in three modes (just like GEANT4), via: a GUI (e.g. BFROOT section 5.2.1 on page 149), command line (i.e. the prompt shown in figure 5.1 on the next page), or batch code. We elected to utilize the first mode and, continuing the work of Wurtz [Wur10b]: we created all of the remaining GUI-accessible classes necessary to perform the entire data analysis from start to finish (discussed in section 5.2.1 on page 149).

[1] Rene Brun and Fons Rademakers developed the concept behind ROOT [Bru97].

```
 ****************************************
 *                                      *
 *       W E L C O M E to R O O T       *
 *                                      *
 *   Version  5.30/02 21 September 2011 *
 *                                      *
 *  You are welcome to visit our Web site *
 *         http://root.cern.ch          *
 *                                      *
 ****************************************

ROOT 5.30/02 (tags/v5-30-02@40973, Sep 22 2011, 10:55:04 on linux)

CINT/ROOT C/C++ Interpreter version 5.18.00, July 2, 2010
Type ? for help. Commands must be C++ statements.
Enclose multiple statements between { }.
root [0]
```

Figure 5.1: ROOT prompt.

ROOT has an impressive number of data analysis classes developed by the ROOT team and the rest of the ROOT community, to rigorously meet a plethora of data analysis demands. Class information is currently stored on the ROOT website,[2] but is most conveniently accessed by utilizing a non-scholarly search engine with the keyword "ROOT" accompanying the object class name. Each class has a website with a list of: class members, inherited class members, descendants, includes, and libraries. This makes it easy to find the correct syntax and available members of any ROOT class.

[2]The classes can be referenced at: `http://root.cern.ch/root/html/index.html`.

5.2.1 BFROOT

BFROOT is a ROOT GUI designed to handle data analysis for data produced specifically by the Blowfish detector array. BFROOT was initially designed by, and the base classes were built by Wurtz [Wur10b] to provide a more user-friendly and powerful option for data analysis. Advanced classes to fill in the necessary steps for a complete analysis of deuteron photodisintegration data using Blowfish were added during this work. The complete data analysis of this experiment can now be performed entirely using the GUI, without writing a single line of code.

BFROOT generates new ROOT classes, each with its own respective source and header file: the TGBF prefixed classes are designed to handle the GUI (g for graphic), while the TBF prefixed classes perform the actual operations; the T is for user defined Type; the BF is for Blowfish. The graphical classes (TGBF) instantiate the operational classes (TBF) via class pointers which are then used to perform operations based on the user's GUI commands; the graphical classes are instantiated by the main menu class (TGBFMainMenu) which is instantiated by a simple batch code (rootlogon.C) that also loads the necessary libraries. Thus the operation of BFROOT is performed entirely by the GUI interface, starting at the main menu (figure 5.2 on the next page).

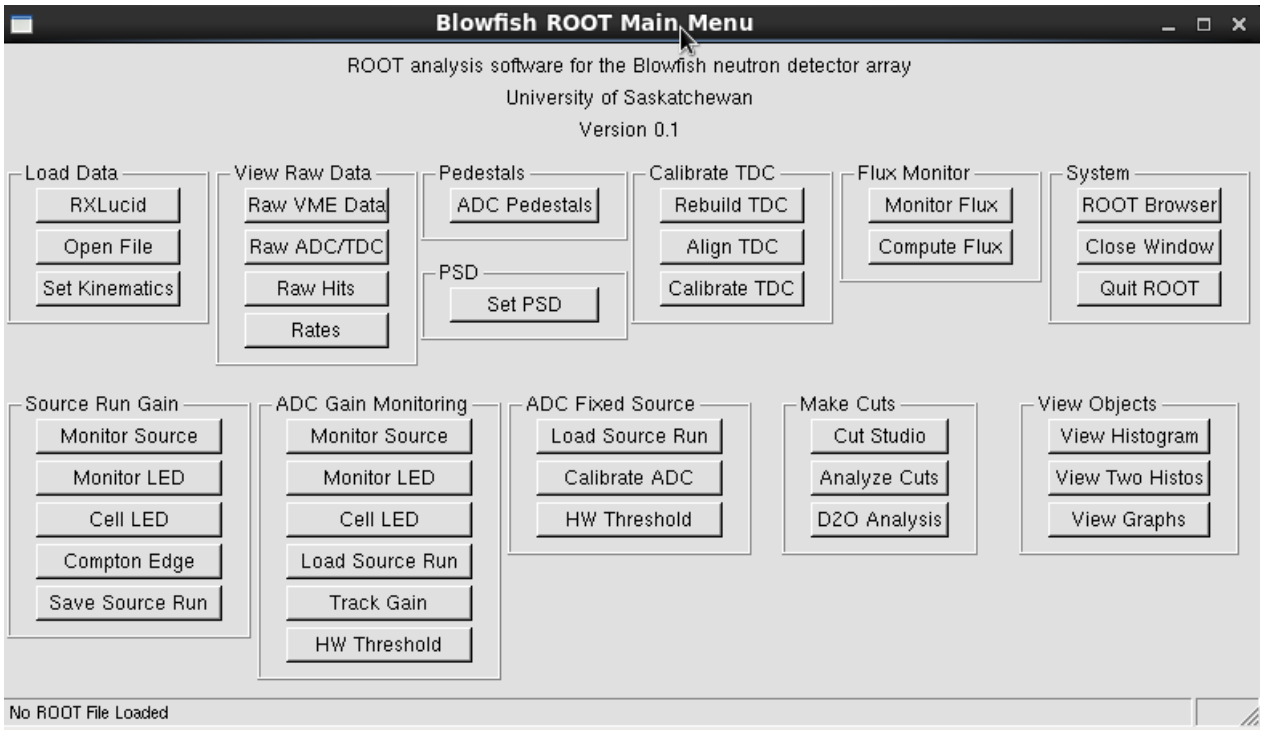

Figure 5.2: BFROOT Main Menu. This class is instantiated by rootlogon.C and is used to subsequently instantiate all other graphical classes via the buttons, which then instantiate necessary operational files.

The raw data and most of the processed data are stored in trees: a ROOT vertical data storage structure designed to optimize input/output and memory usage [Ant09]. Each tree contains branches; the data are stored in the leaves of the branches.[3]

The TBFFileObjectControl handles manipulation of data via trees and histograms filled by these trees. Utilizing the inheritance based structure of ROOT: all TBF classes are descendants of TBFFileObjectControl (which is itself a descendant of the ROOT class: TObject), thus enabling them to access the data stored by TBFFileObjectControl.

The graphical classes also utilize inheritance, but they are simply descendants of the ROOT window frame class: TGMainFrame.

In summary, future deuteron photodisintegration experiments using Blowfish may be

[3]The classes are appropriately named: TTree, TBranch and TLeaf (respectively).

performed entirely using BFROOT; with minimal updates necessary for similar experiments. It is the hope that subsequent upgrades will utilize the modular design of BFROOT and create optional packages specialized for a variety of experimental configurations.

The version of BFROOT created by Wurtz is available at: `http://nucleus.usask.ca/~ward/`.

RLucid

Although it is possible to use ROOT to handle data acquisition, we elected to use Lucid in this experiment because the Lucid code had already been written and optimized for other, similar experiments (e.g. Sawatzky [Saw05]). Therefore, in order to utilize BFROOT we had to first convert the Lucid format data files into ROOT format: this was performed by RLucid. RLucid was created by Wurtz [Wur07] specifically for converting Blowfish data from Lucid to ROOT format. The package runs harmoniously with BFROOT, and can be run either independently or via the BFROOT GUI. See Wurtz [Wur07] for more information.

The latest version of RLucid is available at: `http://nucleus.usask.ca/~ward/RLucid/index.html`.

5.3 Calibration

5.3.1 Beam Calibration

Verifying the Beam Polarization

The Optical Klystron-4 at HI$\vec{\gamma}$S forces electrons in the storage ring to oscillate in the horizontal plane, causing them to emit horizontally polarized ultraviolet (UV) synchrotron radiation (as described fully in section 3.3 on page 53); these UV photons may then backscatter off of the next bunch of electrons and produce MeV-energy polarized photons. Sawatzky [Saw05] noticed during his data runs that there was an unexpected asymmetry in the neutron yields with respect to the azimuthal angle (ϕ); this eventually led to the discovery that mirror degradation had caused the UV photons to change polarization when they reflected off of the optical cavity mirror (by $\approx 9^{\circ}$), and thus the high energy photons from backscatter-

ing showed this same change in the polarization. It is for this reason that we verify the ϕ symmetry following the procedure of Blackston [Bla07].

Based on the expansion of the differential cross section (eq. (2.20) on page 49 $\frac{d\sigma}{d\Omega} \propto \cos\phi, \sin\phi, \text{and} \cos 2\phi$), it should be clear that the reaction is symmetric about the azimuthal angle, ϕ. Therefore, if we observe an azimuthal asymmetry then we will know that Blowfish is not properly aligned, or the polarization axis is not horizontal (or some admixture of the two). The converse is also true because the ϕ distribution depends purely on the polarization: if we do not observe an azimuthal asymmetry then the detectors are properly aligned and the beam is polarized horizontally (or the two effects are perfectly canceling one another).

Excluding the parameters used to test target alignment (i.e. c and d in eq. (2.20) on page 49), the most general function we can fit to the differential cross section for average theta is:

$$Y(\phi) = A + B\cos(2\phi - 2\delta) \tag{5.1}$$

where: A and B are fit parameters for scale, δ is a fit parameter which measures the deviation of the polarization axis from horizontal, and ϕ is the azimuthal angle [Bla07].

Averaging the neutron yields for each arm then fitting eq. (5.1) yields a measure of the deviation of the polarization axis (δ).

Out-of-Time Photons

As discussed previously in section 3.3.1 on page 58: HI$\vec{\gamma}$S has 64 stable trajectories for electrons (each 5.6 ns apart), but only 2 of these are supposed to be used to run the FEL (free-electron laser) in gamma ray mode. In this experiment we saw evidence that the electrons in the storage ring were spreading into other stable trajectories (or *buckets*); this is a theory to explain the observed out-of-time photons produced by the beam, called the *Bucket-Spillover Theory*.

Using a peak finding algorithm [Mor00], the time-to-digital (TDC) spectra were analyzed for each run. A typical raw TDC spectrum looks something like figure 5.3 on the next page (left) in contrast to what a normal spectrum should look like: figure 5.3 on the next page

(right).

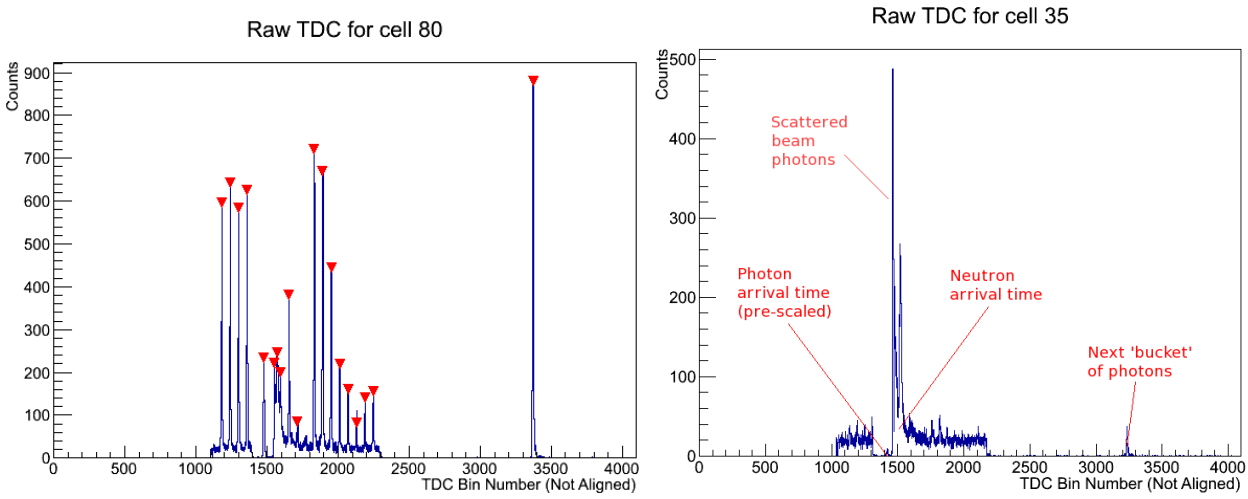

Figure 5.3: Out-of-Time Beam Photons in the TDC spectrum. Left image: a typical downstream TDC spectrum with out-of-time photons. The red carets are the peaks found by the peak finding algorithm[Mor00]. The downstream rings see the most photons due to the angular dependence of the scattering cross section: most upstream TDC spectra do not have visible peaks. Right image: what the TDC spectrum looks like when out-of-time photons of less prevalent.

In order to test the *Bucket-Spillover Theory*, we measured the spacing of the out-of-time photons in Run 154. Run 154 used a long, H_2O target (10.7 cm) and consequently contains only a few neutrons (i.e. much fewer than the D_2O runs): it was used in an attempt to see only the scattered photons. Analysis of the peaks found in the downstream ring of cells[4] using Morhavc *et al.*'s algorithm [Mor00] showed that the peaks found; on average, were 5.36 ± 0.49 ns apart: consistent with the Bucket-Spillover Theory, which would predict a 5.6 ns (1 'bucket') spacing.[5]

The number of out-of-time photons at each observed peak was estimated by utilizing a background computing algorithm [Mor97] to estimate the number of background events

[4]Cells 81-88 excluding 87, which was empty. These were selected for improved statistics: photons scatter at a rate inversely proportional to the angle.

[5]5.6 ns is the nominal electron spacing of HI$\vec{\gamma}$S, as is shown in appendix D on page 289 [Wel09].

in the TDC, then integrating the peaks above this background. This provided quantitative evidence of the out-of-time photons and was utilized to scale the total cross section to account for these out-of-time events.

Some of the noteworthy properties of these out-of-time photons:

1. The relative number of out-of-time photons changes from run to run, but the timing of their arrival remains constant. See figure 5.4 on the next page.

2. The relative number of out-of-time photons increased sharply when the short target was put in. See figure 5.5 on page 156. The total cross section data between the long and short targets agree after they are corrected for out-of-time photons: implying that the increase in out-of-time photons when the short target was put in is not an artifact of the analysis.

3. The relative number of out-of-time photons during a run appears to reach an equilibrium after which the length of time the beam has been running doesn't affect the ratio of out-of-time photons. See figure 5.5 on page 156.

4. There is no correlation between the beam flux and relative number of out-of-time photons. See figure 5.6 on page 157.

5. The number of out-of-time photons in the final data depends strongly on the lower light cut (section 5.4.3 on page 199) because they scatter primarily due to Compton scattering at relatively large angles ($> 22.5°$): increasing the lower light cut decreases their prevalence in the data.

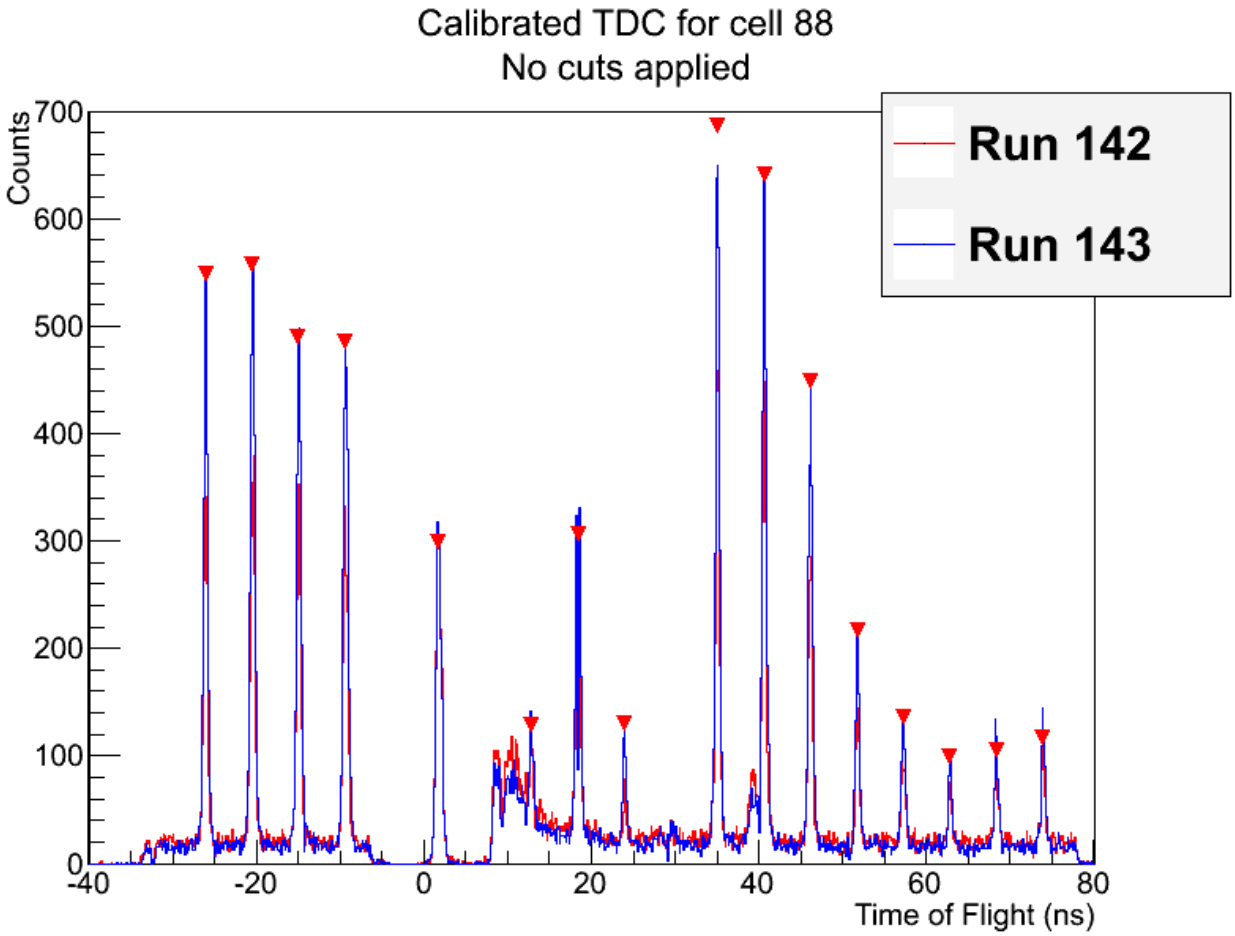

Figure 5.4: Out-of-Time Beam Photon Arrival Time Constancy. A comparison of the out-of-time photons observed in the TDC spectra for run 142 (red) vs run 143 (blue). The TDC has been calibrated and aligned such that the target-to-cell free path photon time-of-flight corresponds to the expected time of arrival of the photons ($\approx$ 1.5 ns). Notice that the peaks of the two runs clearly coincide in time but not in magnitude: this can be seen by observing that the blue spectrum has greater magnitude peaks, but the red spectrum has greater magnitude the rest of the time (i.e. a larger background). The time coincidence is consistent with the Bucket-Spillover Theory.

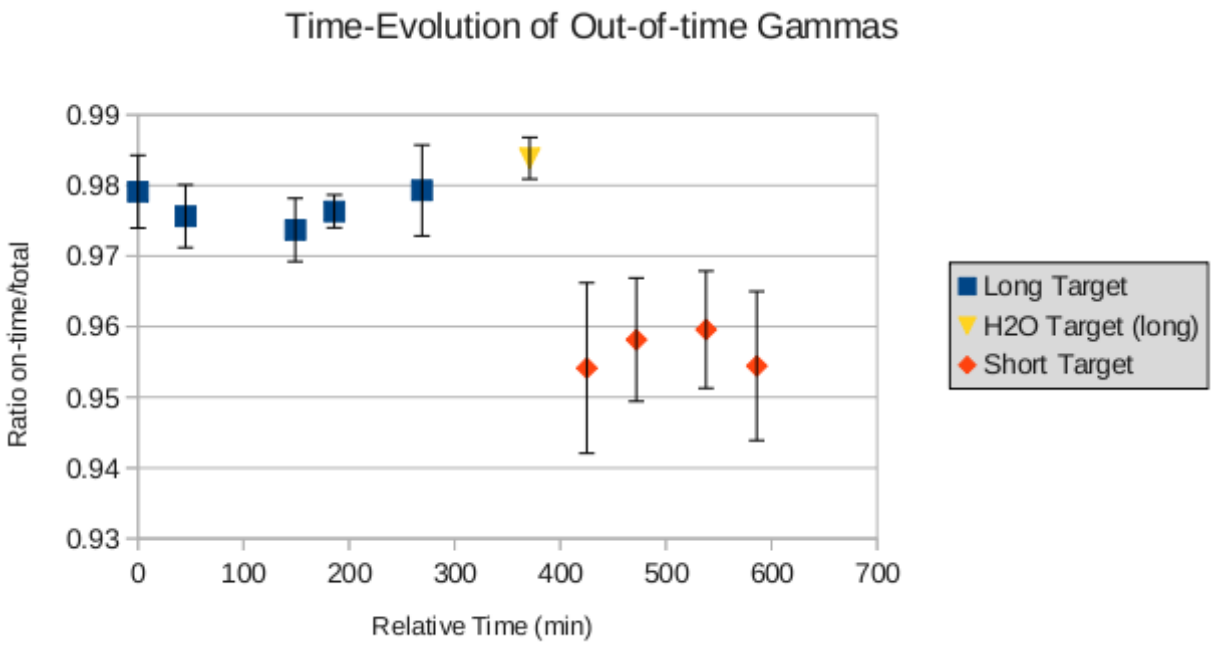

Figure 5.5: Out-of-Time Beam Photon Time Evolution during Experiment. The ratio of the number of photons that arrived at the expected time (within error) over the total number of photons estimated in each TDC spectrum for cells with statistically significant photon peaks (i.e. the downstream rings). Each data point represents a run, runs include: 142, 143, 149, 150, 152, 154, 155, 157, 158 and 159 (chronological order). The ratio was observed to change randomly over time for a given target length and systematically when the target length was changed (likely coincidental).

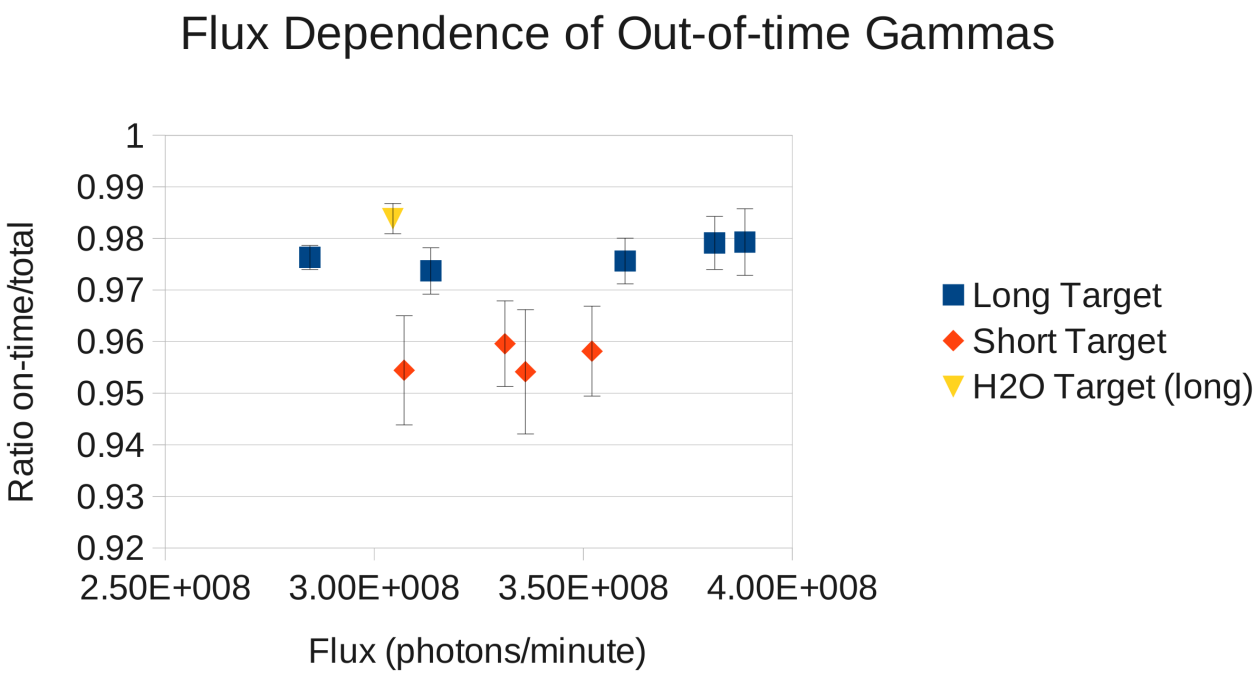

Figure 5.6: Out-of-Time Beam Photons as a Function of Beam Flux. The ratio of the number of photons that arrived at the expected time (within error) over the total number of photons estimated in each TDC spectrum for cells with statistically significant photon peaks (i.e. the downstream rings). Each data point represents a run, runs include: 142, 143, 149, 150, 152, 154, 155, 157, 158 and 159. There is no apparent correlation between the flux and the ratio.

The fact that there doesn't appear to be any correlation between the expected variables: time and flux, implies that there is a different variable controlling the presence of out-of-time photons. With this in mind, it is recommended that correlations be investigated for the other important variables, namely: the storage ring energy and the timing of electron injections from the booster ring. The out-of-time photon estimating algorithm should also be verified rigorously.

The lingering question is: what changed when we put the short target in (that could account for this systematic increase in out-of-time photons)?[6]

[6]Initial conjecture implicated higher flux rates were demanded for the short target, so more electrons were

5.3.2 ADC Calibration

Pedestals

As mentioned in section 3.10.4 on page 100, in order to improve ADC linearity: a constant DC current is drawn by the modules. The integrated value of this DC offset: called the pedestal, must be measured and subtracted from the ADC values before any other analyses are performed. This means measuring the amount of charge in the short and long gates; for each cell, when there is nothing in the cell. The P_trig trigger (see section 3.10.1 on page 88) acts when an event is measured by the discriminators while Lucid is demanding a pedestal read-out: gates are generated for each cell and the short and long ADC values are calculated. Normally, the integrated charge is compared to a reference pedestal, plus a fudge factor to account for electronic noise: if the charge is less than the reference charge then the cell is assumed to have been empty and the data are not stored. When Lucid demands pedestals, the comparison is not made and instead *all* ADC values are stored (as pedestal values). This methodology isn't perfect (it does allow true events into the pedestals) but it is able to account for dark current being produced by PMTs, and since the multiplicity is relatively low (typically 1-1.1 on average during this experiment) approximately 87 times out of 88 the pedestal readout will not include an event. During analysis, the P_trig triggered events are plotted on a histogram for each ADC channel (i.e. cell) and a peak finding function is fit to extract the median of the pedestal value, this looks like figure 5.7 on the next page.

injected into the storage ring and these electrons simply repelled each other via the Coulomb Force: causing the buckets to spread out more drastically than the long target runs. The problem with this hypothesis is that it is wrong: the photon flux wasn't any higher for the short target runs (figure 5.6 on page 157).

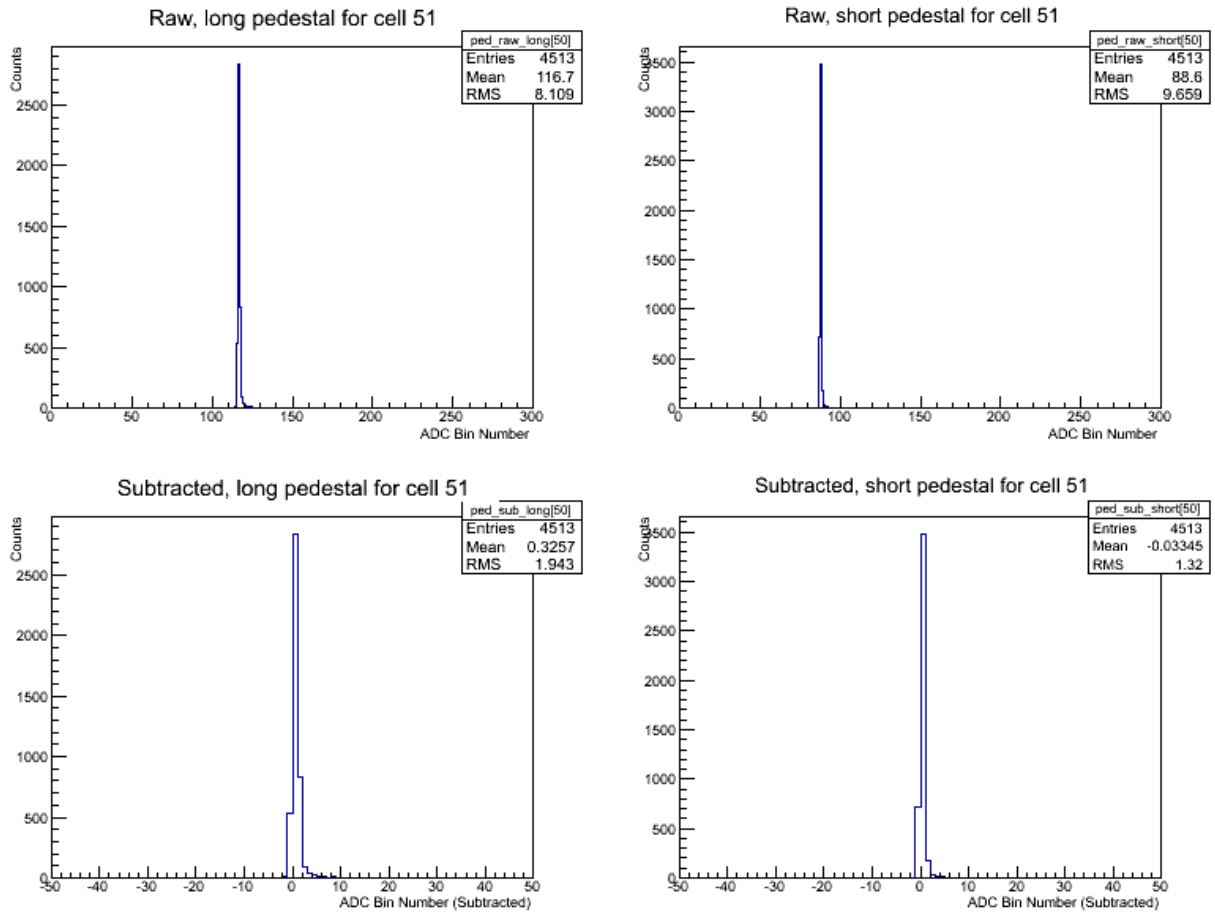

Figure 5.7: Pedestal Determination and Subtraction. The long (top left) and short (top right) gated ADC values for pedestal events of run 139, cell 51 are show, along with their values once the pedestals have been subtracted (bottom).

Once the pedestals have been determined, they are subtracted from the ADC values.

Determining the ADC Gains

The ADC gains need to be carefully adjusted in order to maximize the energy resolution ($\Delta E \propto \frac{1}{\#\text{bins used}}$) while preventing useful data (i.e. neutrons) from overflowing. In practical terms this means setting the gains such that the highest energy particles we want to detect are as close as possible to ADC bin 3500 (of 4096): any higher and the data become confounded (see section 3.10.4 on page 100), any lower and the binning will waste the energy resolution.

The ADC modules have their gains set internally, so we adjust the gains by means of the voltage applied to the PMTs.

In this experiment, a radioactive source with Compton edge[7] near the energy of the neutrons we intended to measure was placed in Blowfish and the voltages to each PMT cell were altered such that the Compton edge appeared near the middle of the ADCs.

During analysis, the radioactive source runs were used to determine the gains by fitting a detector response function to the energy spectrum. For the Blowfish cells this means finding the inflection point of the energy spectrum by fitting eq. (5.2):[8]

$$f(x) = p_0 + p_1 x + p_2 \text{erfc}(\frac{x - p_3}{p_4}) \tag{5.2}$$

where: f(x) is fit to the energy spectrum, p_i are the fitting parameters (p_3 is the inflection point), and erfc is the complimentary error function. The inflection point is mapped into a Compton edge location via a phenomenological scaling factor: figure 5.8 on the next page illustrates.

[7]Liquid organic scintillators are, as a rule, incapable of giving photopeaks with which to fit [Kno00]; BC-505 is no different. Our detectors are also incapable of giving a Compton edge, but we can estimate its location using the inflection point position.

[8]We use this same function to scale the light output (see section 5.3.2 on the next page).

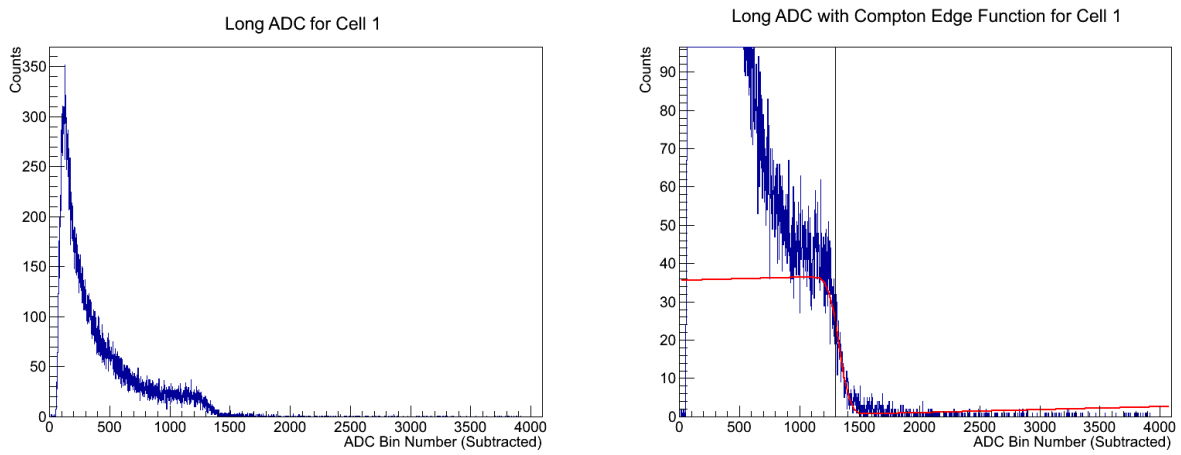

Figure 5.8: Determining the Gain of the Blowfish Cells. The spectrum on the left is a raw americium-beryllium ADC spectrum, the spectrum on the right is the same spectrum fitted with eq. (5.2) on page 160. The vertical black line indicates the computed Compton edge position: this is compared to the literature value in order to deduce the gain.

Gain runs were generally only taken at the start and end of the day, so we used the Gain Monitoring System to track the gain run-by-run.

A complication arrived in determining the gain for runs 149-157 because the gain monitoring system has been shown to drift when Blowfish is rotated [Pyw09b]; so the gain monitoring system was not used for these runs and instead the correct gains were assumed to lay somewhere between the values of the earliest and latest calibration runs.

Once determined, the gain data were used during data analysis to perform the light cuts (section 5.4.3 on page 199).

Scaling the Light Output

In order to extract the differential cross section (section 5.6 on page 216) we assume that *after all of the data analysis cuts are applied*, the simulation accurately replicates the detector efficiencies in order to extract the total cross section (section 5.5 on page 211). Pywell *et al.* [Pyw06] extracted the necessary light output parameters for BC-505 (discussed in section 3.8.2 on page 80), then demonstrated that the simulation accurately reproduces the

detector efficiency (figure 3.17 on page 82): using tagged neutrons at TRIUMF.

It therefore came as an unpleasant surprise when first Blackston [Bla07] and then Wurtz [Wur10c] discovered that many of the Blowfish cells are producing smaller ADC responses to neutrons than those predicted by the simulation, even after carefully calibrating the gains using multiple photon sources.[9] In the data from this experiment we observed the same problem: the calibrated ADC responses are smaller than we expect; and so we must compensate for it by enhancing the ADC gain for neutrons i.e. multiplying the cell light output by a corrective factor. These factors are extracted for each cell by scaling the calibrated ADC spectrum to match the simulation (each cell has a unique scaling factor); once the scaling factors are applied: the ADC spectra for the simulated and experimental data agree on the shape of the distribution (they don't before the factors are applied).

The physical reason behind this discrepancy was once believed to be an unknown aging process in the BC-505 cells; however, re-analyzing the 2008 data of Kucuker [Kuc10] revealed that the light scaling factors needed then were actually *larger* than those used for the 2010 data: if the cells are aging then the scaling factors should be *smaller* when the cells were younger. That doesn't mean the cells aren't aging, but it does mean that it can't be the only variable at play.

We have already found cells leaking BC-505, therefore it is possible that the cells are allowing oxygen to interact the BC-505. Less BC-505 may produce less light because there will be a lower probability of the primary particle interacting,[10] while the presence of oxygen will increase non-radiative energy transfer [Kno00] which will both decrease light output and reduce the quality of the pulse-shape discrimination [Sai].[11] Some cells show essentially unusable PSD, but there is no obvious correlation to the light scaling factors: this implies that there are at least two variables at play in these cells: the oxygen reducing the light output and some other confounding variable which is either increasing or decreasing the

[9] All comparisons of the photon ADC spectra from the simulated and experimental data demonstrate good agreement: only the neutrons disagree.

[10] The secondary particle (i.e. an electron or proton) will almost certainly deposit all of its energy in the BC-505 anyways (at our typical energies).

[11] The pulse-shape discrimination depends on the neutrons having much more non-radiative energy transfer than the photons, if the non-radiative energy transfer increases for both then photons will look more like neutrons.

ADC response.[12]

Previous investigators have failed to find a different culprit for the reduced ADC response to neutrons, the best current hypothesis (other than oxygen contamination); given the evidence currently available, is that the long gate for the ADC is being cutoff by ≈ 50 ns [Pyw09b], though this is widely considered improbable: but not impossible. It may be that the long gated ADC is being cutoff *and* some cells have some oxygen contamination: in this case the necessary loss of the long gate would be less than 50 ns (possibly much less).

At this time it seems most likely that there are two or more variables causing the problem, and it is the relationship between the two which is preventing elucidation. Using something simple like an α source to test the light output for each of Blowfish's cells may prove remunerative.

The actual values of the light scaling factors used are given in appendix H on page 297.

Gain Offset

We desire linear gains for the ADCs: with an intercept of 0, this way we can determine the gain using only a single energy feature on the ADCs; so that we only need to use a single radioactive source to calibrate. In this experiment, americium-beryllium (AmBe) sources were exclusively used to calibrate the data extracted so it was necessary to verify that the Blowfish gain was indeed linear with intercept 0; this can be achieved by plotting the feature position in the ADCs (i.e. ADC bin number) determined by several different sources at different energies and fitting the best function to describe the feature position as a function of energy. The resulting fit was linear with intercept 0: $\mathrm{ADC}(E) = gE$ where g is the correct gain: figure 5.9 on the next page shows the average gain for all cells, and figure 5.10 on page 165 shows the gains for four arbitrarily selected cells; both plots have excellent fits (linear regression, $R^2 > 0.99$) to functions of the form $\mathrm{ADC}(E) = gE + 0$.

[12] Dissolved oxygen can reduce the light output by $\approx 30\%$ [Sai].

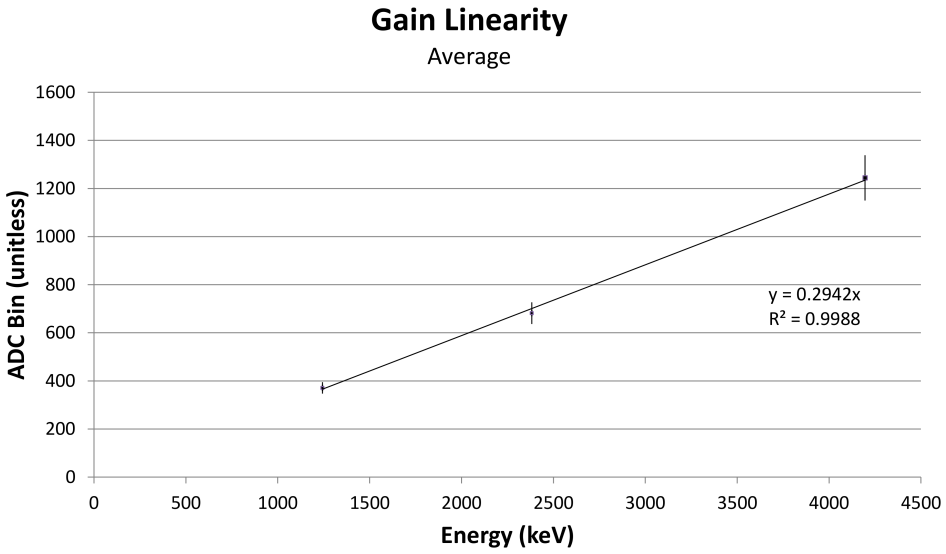

Figure 5.9: Gain Linearity of Cell Average. The ADC bin number versus literature energy value (uncertainty is negligible) for the Compton edges of three radioactive sources is plotted: ^{228}Th, ^{40}K and AmBe. The ^{228}Th and ^{40}K sources were performed simultaneously using background radiation (run 140), while the AmBe source was performed immediately prior (run 139) and the Gain Monitoring System was used to correct for drifting between. A linear function with no intercept ($y = 2.942x$) fits excellently.

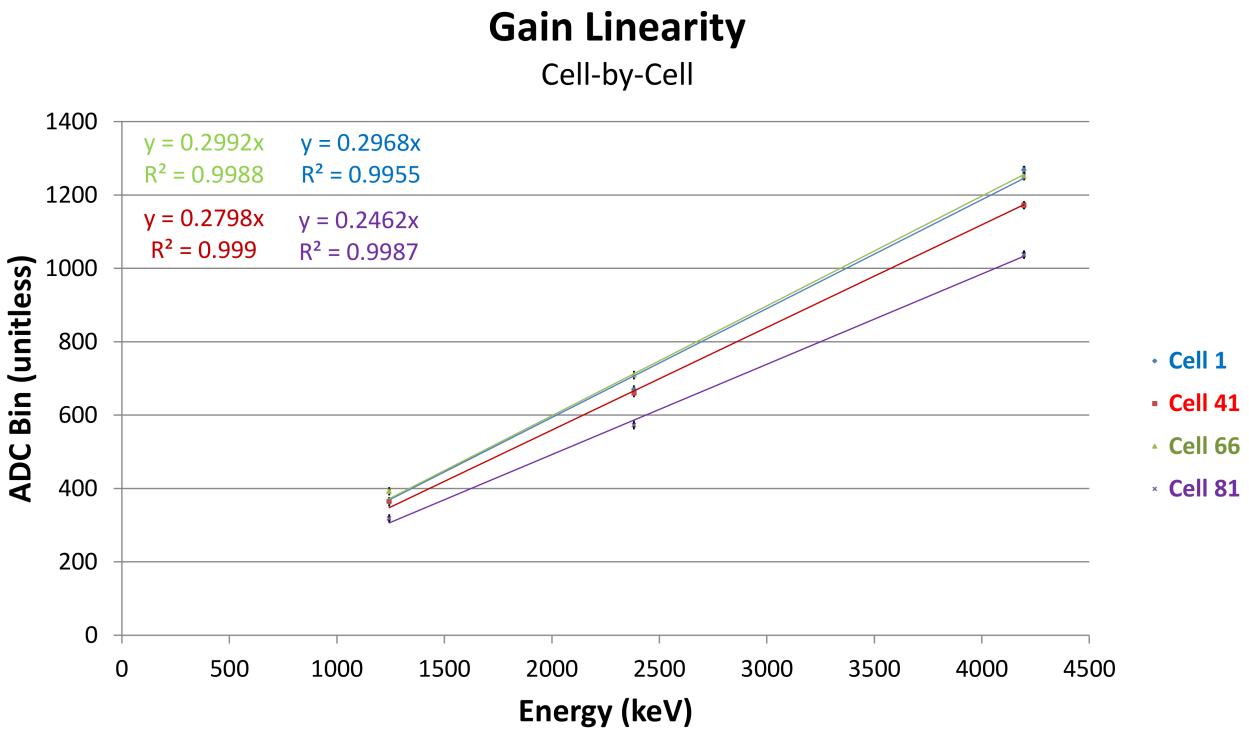

Figure 5.10: Gain Linearity of Arbitrary Cells. The ADC bin number versus literature energy value (uncertainty is negligible) for the Compton edges of three radioactive sources is plotted: ^{228}Th, ^{40}K, and AmBe. The ^{228}Th and ^{40}K sources were active simultaneously using background radiation (run 140), while the AmBe source was active immediately prior (run 139) and the Gain Monitoring System was used to correct for drifting. Four cells were arbitrarily selected and fit with a linear function with no intercept; all four show excellent fits (figure is colour coded with fit functions and linear regression values).

Thus we see that only one radioactive source was needed to determine the gain for these experimental runs: because the gain was linear with intercept 0.

5.3.3 Gain Tracking

The Gain Monitoring System (first described in section 3.10.3 on page 97) was used to continuously track changes in the ADC gains for all cells. The principle behind gain tracking

using the Gain Monitoring System is diagrammed in figure 5.11.

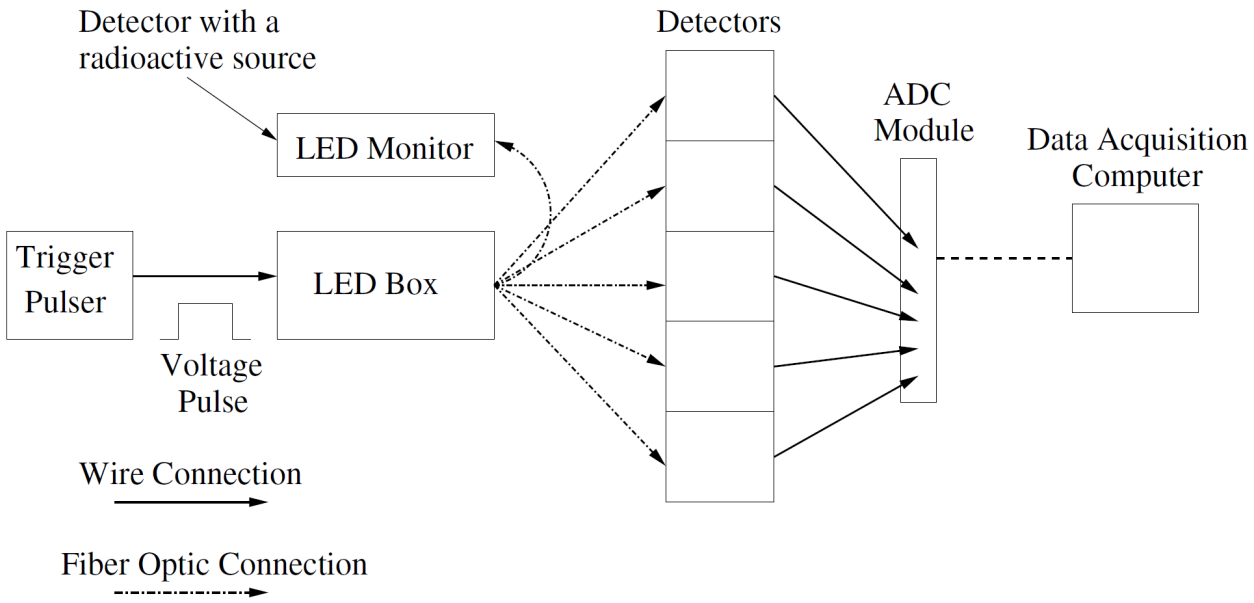

Figure 5.11: Gain Tracking Principle. The front-end computer turns the pulser on and off: when it is on it sends a periodic pulse to drive the four LEDs, which send a light pulse to all of the cells in Blowfish, as well as four pulses to the LED gain monitoring scintillators (one from each LED). The gain monitoring scintillators continuously monitor the LED light output. Image credit: Bewer [Bew05].

The quantitative principles of the Gain Monitoring System are outlined following the derivation in Subatomic Physics Internal Report-142 [Pyw09b] in appendix G on page 295. Tracking the gain relies on two key assumptions: that the ratio of light entering each strand of the fiber optic bundle remains constant, and that we can accurately determine the location of the LED feature on the cell and GSO ADCs.

We have no choice but to assume that the ratio of light remains constant; we can only verify that it is by taking additional source runs. It is believed that the ratio will remain constant so long as Blowfish is not moved, but if Blowfish is rotated then the ratios are likely to change; this is discussed in section 5.3.4 on page 170.

Accurately determining the location of the LED feature on the cell and GSO ADCs is readily achievable: in fact, the reason why LEDs were used is because they give a distinctive,

Gaussian, energy distribution. The data acquisition system is setup such that the LED flasher events are tagged and stored in a separate set of histograms. A typical ADC spectrum for flasher events is shown in figure 5.12 with a Gaussian fit.

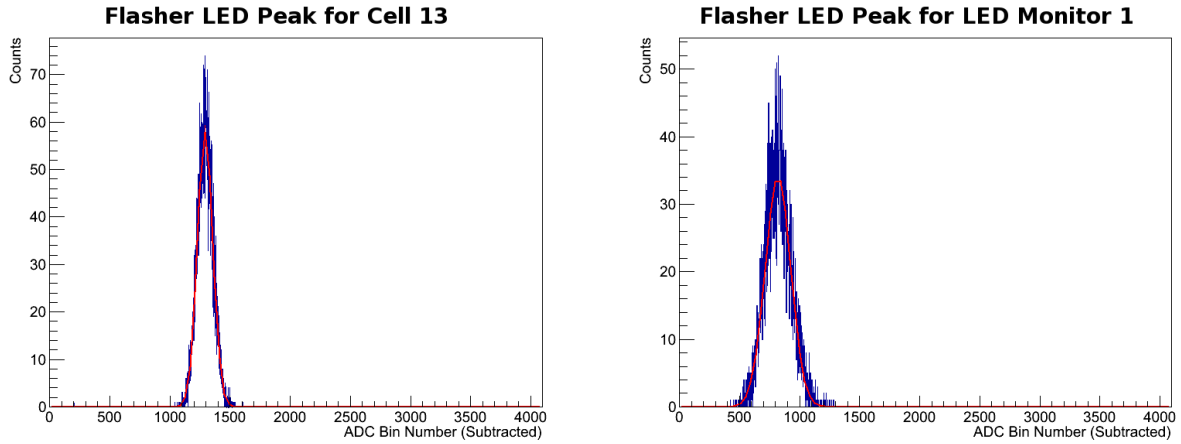

Figure 5.12: Detector Response to The LED Flash. Left: response of a Blowfish cell (cell 13). Right: response of the LED monitor (GSO detector). Both spectra are well fit by Gaussian distributions.

The GSO detectors are calibrated using a continuous gamma ray radioactive source, the GSO detectors are particularly good at measuring gamma rays (as opposed to the Blowfish cells) and are thus capable of distinguishing the photopeak. To determine the GSO detector gain we fit eq. (5.3) to the detector response:

$$f(x) = C + p_0 e^{-\frac{1}{2}\frac{(x-p_1)^2}{p_2^2}} + e^{p_3+p_4 x} \tag{5.3}$$

where: the p_i are fitting parameters. This function is complemented by an algorithm which estimates these parameters before the fit. Fitting this function to the detector's light output spectrum looks like figure 5.13 on the next page.

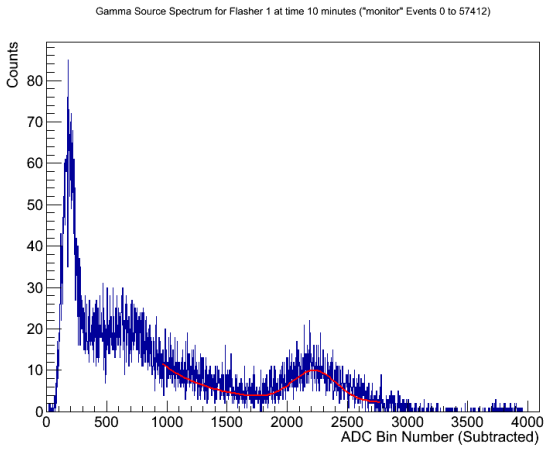

Figure 5.13: LED Monitor Spectrum (GSO detector). Eq. (5.3) on page 167 is used to find the location of the continuous radioactive source's photopeak.

This concludes the necessary background for a high-level understanding of the Gain Monitoring System; a description of the underlying electronics (figure 5.14 on the next page) follows.

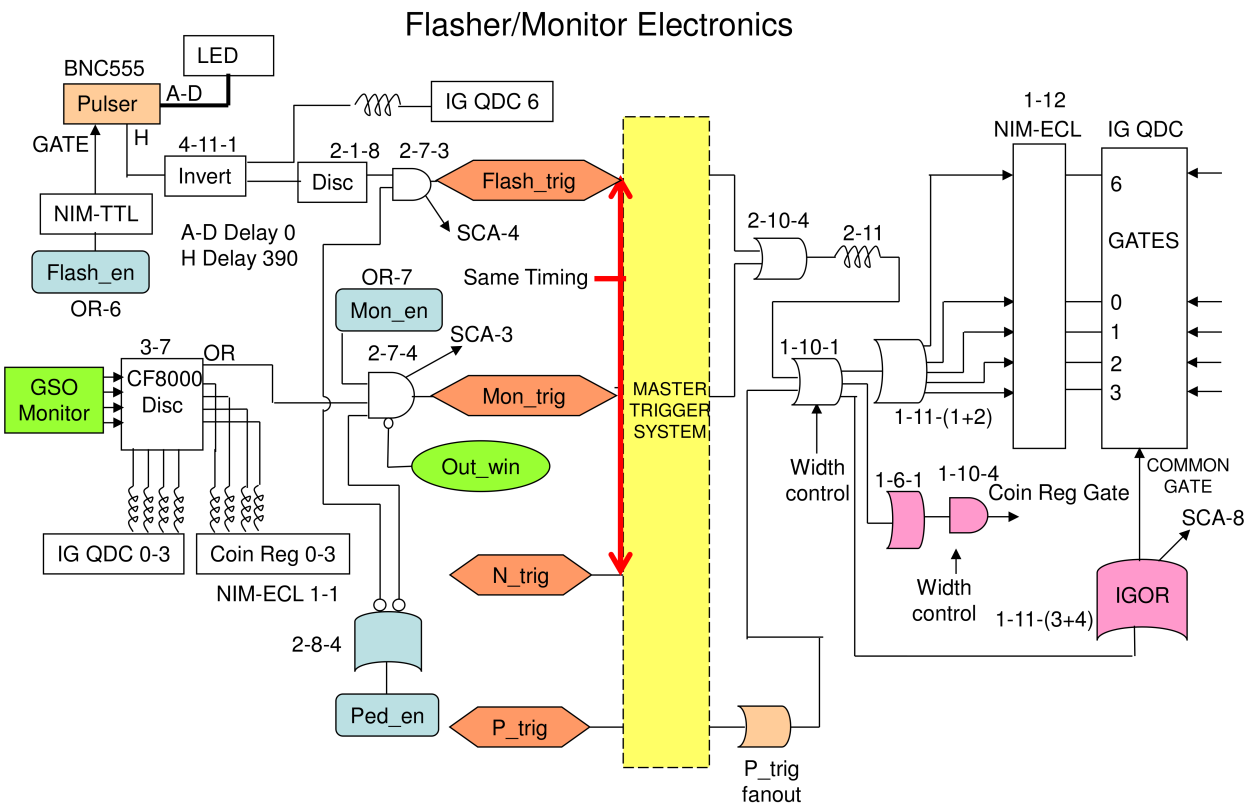

Figure 5.14: The Gain Monitoring System Electronics. Description in text. Definitions: LED: light-emitting diode, GSO: gadolinium-silicon-trioxide crystal (photon detector), IG: independent gate, QDG: charge-to-digital converter (ADC), NIM-TTL: NIM to TTL (transistor-transistor logic) logic converter, Coin Reg: coincidence register, NIM-ECL: NIM to ECL (emitter-coupled logic) logic converter, SCA: scaler, CF8000 Disc: CF8000 model constant fraction discriminator, BNC555 Pulser: model of the pulse generator used, Flash_en: enable flasher signal, Mon_en: enable monitor signal, Ped_en: enable pedestal signal, Flash_trig: LED flasher trigger, Mon_trig: LED gain monitoring trigger, N_trig: neutron trigger, P_trig: pedestal trigger, and Out_win: out window (see figure 3.22 on page 90).

The Gain Monitoring System is initiated by Lucid sending a Flash_en signal to the BNC555 pulse generator which turns it on. The BNC555 is set to some known frequency, once it is turned on it starts sending logical driving pulses to the four LED flashers (channels

A-D) which cause the LEDs to flash. A signal (channel H) is also sent into the electronics where it initiates a Flash_trig that subsequently enters the Master Trigger System (latching the system and preventing other triggers from obfuscating the flasher data). The signal from channel H is also sent to the independent gate ADC (IG ADC); this could; in theory, be used to monitor changes in the pulser gain, but instead it is only used to verify when the pulser is actually active.

The four GSO crystals monitoring the flasher system are continuously receiving signals from a nearby radioactive source. The CF8000 discriminator takes the GSO detector signals as input and outputs an 'or' signal that enables the Mon_trig trigger (toggled by the Mon_en signal), as well as outputting to a coincidence register that can be used to check that when the LED flashes: it sends a signal to all four GSO crystals (as it should). The Flash_trig and Mon_trig triggers gate the independent gate ADCs to ensure the signals are integrated at the proper time.

P_trig is initiated using Ped_en to determine the pedestals of the IG ADC.

This section should suffice for a functional understanding of the Gain Monitoring System, for a full account of the system please see Bewer [Bew05], the associated journal publication is Bewer *et al.* [Bew09]; for further functional information, please see Subatomic Physics Internal Report 142 [Pyw09b].

5.3.4 Gain Monitoring Problems

The Gain Monitoring System assumes that the ratio of light entering each strand of the fiber optic bunch; fed by the LED flasher, remains constant over time (see appendix G on page 295 for details). This assumption was tested by comparing the predictions of the Gain Monitoring System using the light ratio (via the gain) of two different calibration runs: run 136 and run 165. An example of the result is plotted in figure 5.15 on the next page.

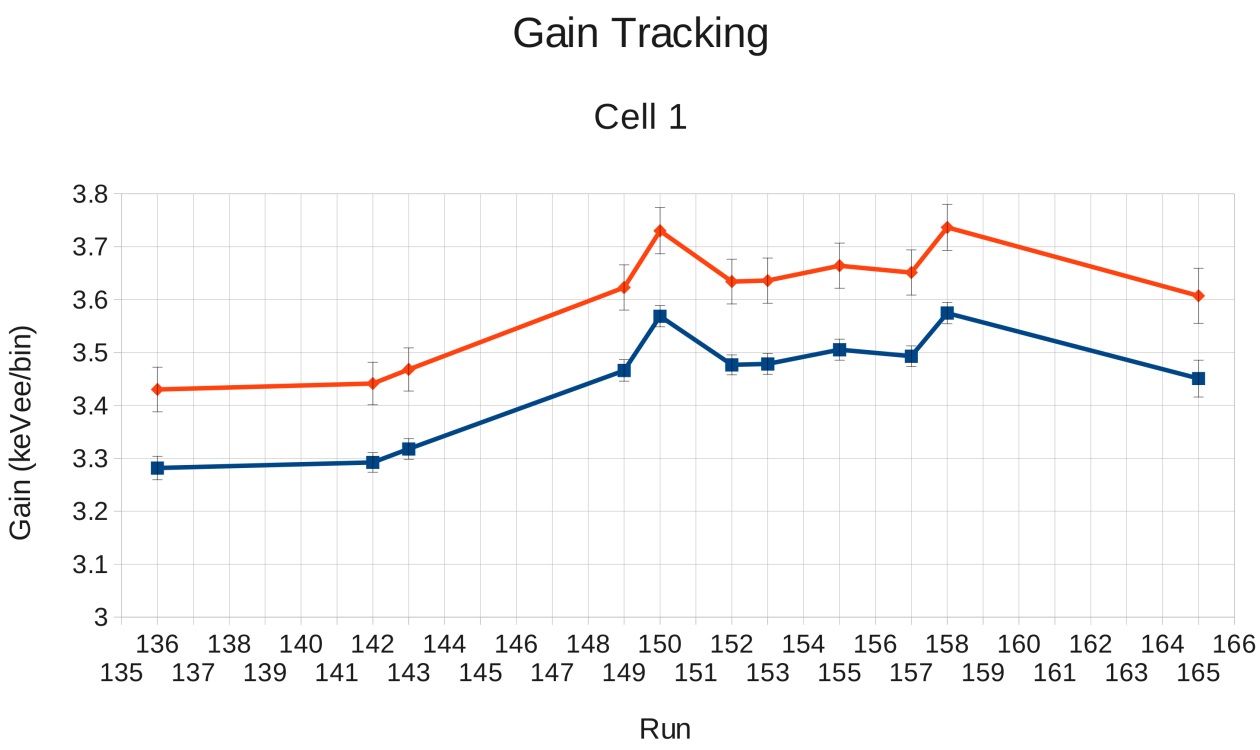

Figure 5.15: Discrepancy in the Gain Monitoring System. The two lines represent the gain at any point during the experiment, tracked with the Gain Monitoring System using two different calibration runs: run 165 (red) and run 136 (blue). If the light ratio remains constant over time then the two lines must agree perfectly: clearly the two do not agree on the correct gain, although they do agree on the systematic changes in the gain. Blowfish was rotated after run 143, after run 150 and after run 157. If this cell received less light after its rotations; or the GSO crystal received more light, then the blue line would underestimate the gain at run 165, as is observed.

As figure 5.15 illustrates: the gains predicted by the Gain Monitoring System are clearly in disagreement. This is believed to occur due to rotation of Blowfish: the rotation causes stress on the fiber optic bunches which changes the positioning of the strands and thus the relative ratio of light entering each strand [Pyw09b]. Our observed gains (e.g. figure 5.15) are consistent with this hypothesis.

5.3.5 TDC Calibration

Determining the TDC Gains

The gains of our TDCs are *nominally* 0.1 $\frac{ns}{bin}$: this is the best resolution they are capable of, and the scale is sufficiently large that we can measure everything we want within the 4096 bins of the modules. We measure the correct gain via the methodology outlined in section 3.10.2 on page 96.

Aligning the TDCs

During the experiment, we received a signal from the accelerator when electrons were in position to produce gamma rays (i.e. the *bunch* signal). We cannot use this signal to calibrate the TDCs because we don't know precisely how far the photons had to travel to hit the cells, furthermore, it would be inconvenient to have to consider any and all delays due to the wiring and electronics. Instead, we only use the accelerator signal to set the start time for the TDCs and then zero them based on the arrival time of the promptly scattered beam photons. We know the target-to-cell distance and the speed of the photons (c), so we can determine how long the photon time-of-flight was and therefore we know when the beam interacted with the target and can determine the neutron time-of-flight. With the neutron time-of-flight determined, we can cut those events that are energetically forbidden by kinematics: based on arrival time.

During data runs, the window of expected photon arrival (this is the G_win in section 3.10.1 on page 88) is pre-scaled to only be active once in every 1000 events in order to reduce detector dead-time. Unfortunately, this factor is too small to correctly calibrate the upstream cells: the photon scattering probability is highest at small angles,[13] meaning that the downstream cells get enough beam data but the upstream cells don't. Fortunately, runs were taken without pre-scaling for just such an eventuality. The nearest unscaled TDC calibration run was run 141: it was used to calibrate the TDCs for all of the data runs.

The TDC alignment algorithm searches a user defined TDC bin interval for the largest

[13] As per the Klein-Nishina Equation: appendix A on page 278 i.e. $\frac{d\sigma}{d\Omega} \propto \frac{1}{1+\frac{E_\gamma}{m_e c^2}(1-\cos\theta)}$.

peak using the Morhavc *et al.* algorithm [Mor00]. This peak is then fit with a Gaussian function and the mean is stored as the TDC offset. Since the TDC alignment only matters for the time-of-flight cut (section 5.4.4 on page 204) we didn't bother storing the uncertainty in the peak position for each cell:[14] instead electing to estimate the uncertainty of all cells as being the same. The process looks like figure 5.16.

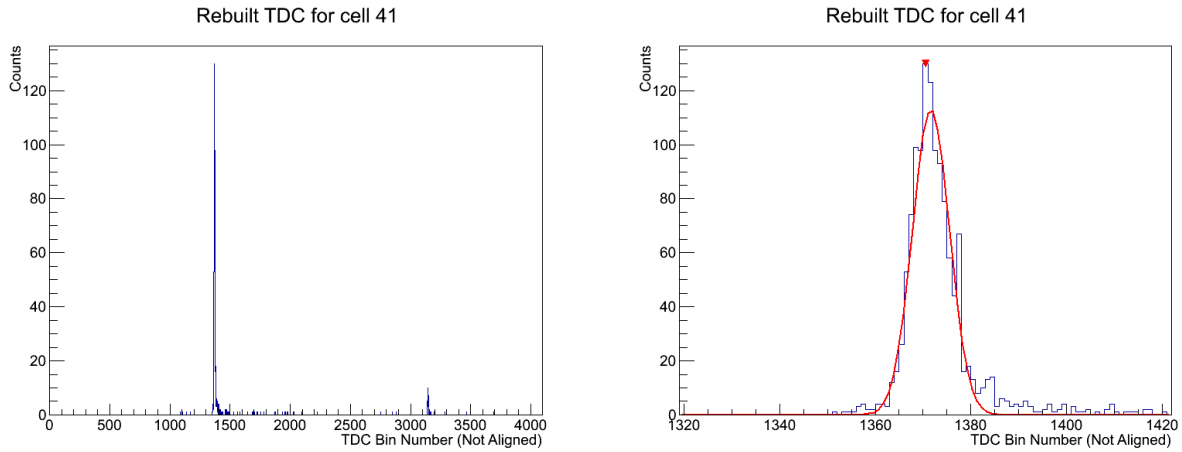

Figure 5.16: TDC Alignment. The left figure is the TDC spectrum from cell 41, run 141: as you can see the spectrum is dominated by the peak of promptly scattered photons (compare to figure 5.3 on page 153). The peak is fit with a simple Gaussian (shown right); the algorithm automatically zooms in on the peak so that the user can verify the fit quality. Note: "rebuilt" means that the bins have been correctly scaled in size to account for the variation from the nominal gain (i.e. the measured TDC gains divided by the nominal gain).

We estimated that the uncertainty in the peak finding algorithm was 1 bin (0.1 ns), though its contribution to the total TDC measurement uncertainty (see section 5.3.5 on the next page) is negligible.

[14] We also use the TDC to calculate the neutron energies, but we do not apply any cuts to the energy directly.

Time-of-Flight Uncertainty

The time-of-flight (TOF) spectrum is derived from the TDC spectrum by calibrating its gain (section 5.3.5 on page 172) and aligning it (section 5.3.5 on page 172). Each of these steps has an uncertainty associated with it: the gain is subject to differential (0.0015 ns[15]) and integral (0.41 ns[16]) non-linearity; and the alignment is subject to a small uncertainty in the peak-finding algorithm (0.1 ns) as well as a large random error (0.48 ns) including, but not limited to, the interaction point of the photons in the BC-505, and the discriminator trigger point. Combining all of these sources of error in quadrature yields an estimated uncertainty in the time-of-flight of 0.64 ns.

The random error was estimated by analyzing the variance of the photopeaks in the TDC spectra. The position of the photopeak is subject to two primary sources of error: the distance traveled by the photons detected, and the start/stop times determined by the electronics. The former is a function of where and how often the photons scatter and where they deposited their energy in the detector: both of these things we can estimate using known cross section data, and we can simulate the entire process. The start/stop times determined by the electronics cannot be simply simulated, so we elect to estimate this as a *trigger-point error* by contrasting the experimental and simulated spectra: see figure 5.17 on the next page.

[15]Nominally 1.5% of the bin width [CAE12].
[16]Nominally 0.1% of the full range scale (4095 bins) [CAE12].

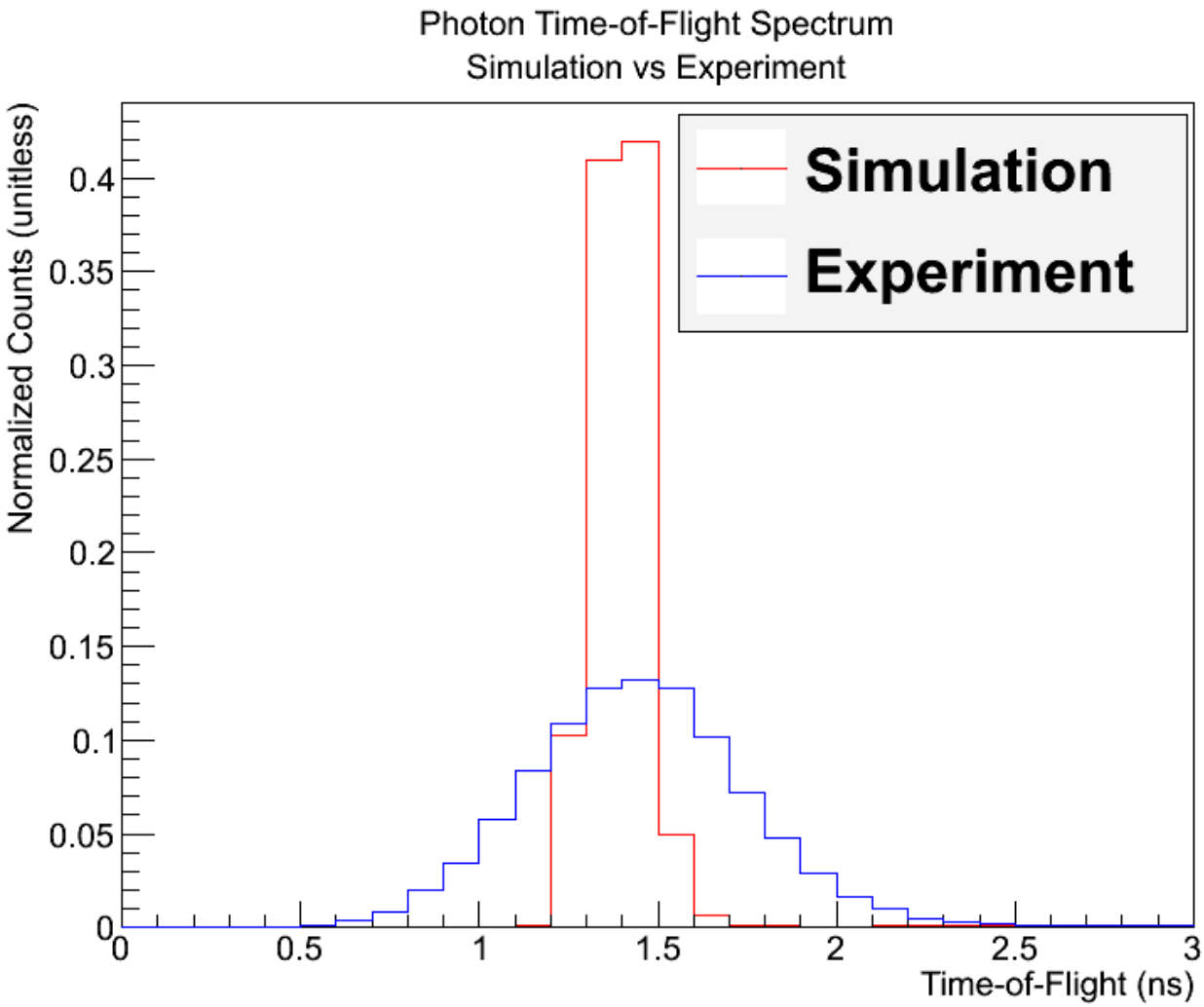

Figure 5.17: Time-of-Flight Uncertainty. Notice that the experimental spectrum is much broader than the simulated spectrum. Fitting a Gaussian function to each cell yields a mean variance of 0.48 ns for the experimental data and 0.13 ns for the simulated data. The photon peak is expected to have some variance to it naturally since the photon can scatter off of any part of the target and deposit its energy at any point in the detector. This implies that the experimental data has a total uncertainty of approximately 0.48 ns, of which 0.13 ns is due to photon distance traveled, and 0.35 ns is due to the discriminator trigger point changing (or any other random error).

Comparing the simulated and experimental time-of-flight spectra (figure 5.17), we can

estimate that the uncertainty due to the interaction point of the photons is 0.13 ns, and the uncertainty due to the trigger-point (and any miscellaneous random errors) is 0.35 ns, for a total of 0.48 ns. It is probable that the trigger-point error a convolution of the integral/differential non-linearity and the electronics, but we must accept that our estimated uncertainty (0.64 ns) may be up to 0.16 ns too large (i.e. if the uncertainty was entirely random): we consider this an acceptable loss of precision in order to compensate for the potential of a systematic error.

There is an additional systematic error due to the assumption that the photons travel, on average, from the center of the target to the center of the detector. Performing the necessary calculations, the photons arrive 0.007 ns early due to their interaction point in the BC-505, and they also arrive up to 0.006 ns early or late due to their interaction point in the target (depending on the cell's position); these are negligible relative to our estimated uncertainty and therefore were not included.

There is also another systematic error introduced by the peak-fitting algorithm we use, which may fit $\lesssim 0.06$ ns early (as is explained in section 5.3.6); this is small relative to our uncertainty and therefore we ignore it.

5.3.6 Decomposing the TDC Spectrum

Once the TDC has been properly calibrated both with the correct gain (see section 5.3.5 on page 172), and the correct alignment (see section 5.3.5 on page 172), we need not worry about the time-of-flight of the photons and can focus purely on the neutrons. We simulated the generation of neutrons under different conditions and discovered that the simulations predict an asymmetric time-of-flight distribution (see figure 5.18 on the next page and figure 5.19 on page 178) that peaks approximately 0.5 ns earlier than the *estimated time-of-flight*: the estimated time-of-flight is computed using the energy of the neutron from kinematics (see section 2.3 on page 23) and assuming a free path from the middle of the target to the middle of the detector (this is within 0.1 ns of the average time-of-flight). Evidently the neutrons should arrive earlier than our simple estimate by ≈ 0.5 ns due to processes which are accounted for in the simulation.

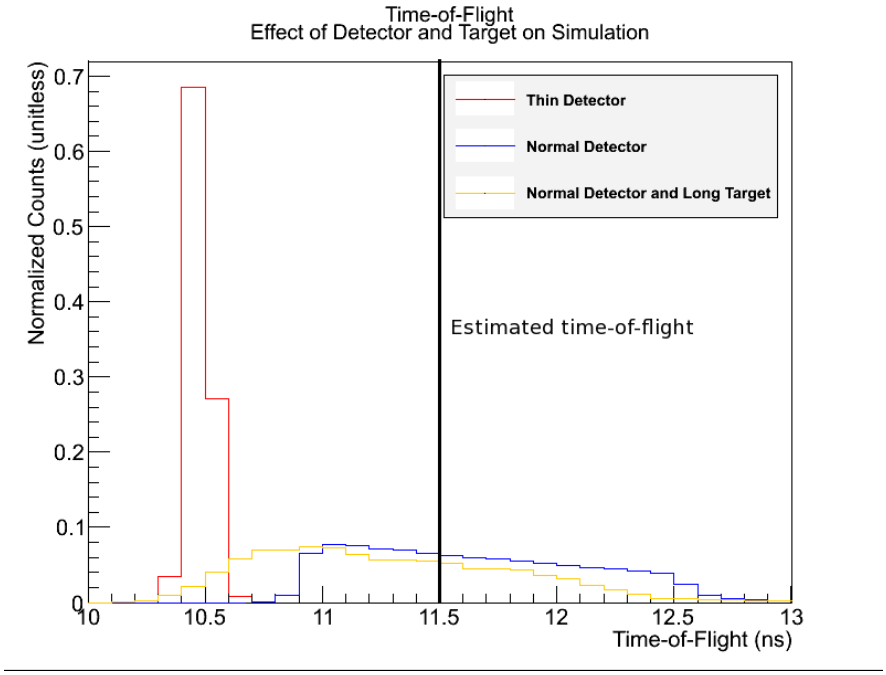

Figure 5.18: Simulated Effects in Neutron Time-of-Flight Spectrum. A single detector of variable width located perpendicular to the beam axis was simulated both with and without the target present via generating a neutron within the (possibly invisible) target. Red line: the thin detector has a width of a few mm; it can only detect neutrons within this few mm region. Blue line: a normal detector (6.4 cm) shows stretching out of linear slope topped peak: this corresponds to the neutrons interacting at different points in the detector (the slope is due to attenuation). Yellow line: a normal detector (6.4 cm) with the long D_2O target in place shows an asymmetric distribution with a peak at $\approx$ 0.5 ns earlier (at $\approx$ 11 ns) than the expected time-of-flight (black line). This means that we do not expect to see a symmetric distribution of neutrons. The estimated time-of-flight (black) assumes a free path from the middle of the target to the middle of the detector.

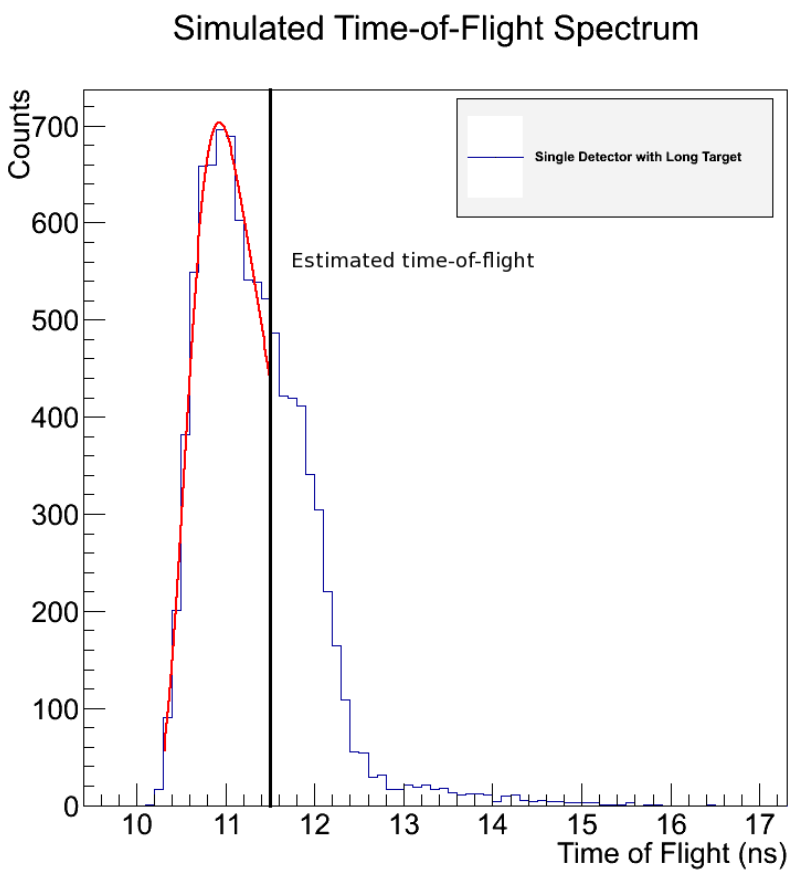

Figure 5.19: Asymmetric Neutron Time-of-Flight Spectrum in Simulation. A closer look at the yellow peak in figure 5.18 on page 177. The simulation consisted of a single detector of BC-505 and a long target of D_2O and nothing else. A Landau function (red) fits relatively well to the spurious peak (better than a Gaussian). The expected peak location is at 11.5 ns, the Landau function predicts the mean to be at 10.991±0.013 ns and a Gaussian function predicts the mean to be at 11.0325±0.0085 ns: both are early by approximately 0.5 ns. The estimated time-of-flight (black) assumes a free path from the middle of the target to the middle of the detector.

Figure 5.18 on page 177 demonstrates that due to simple scattering and interaction point processes (i.e. those processes at work in the simulation): the neutron time-of-flight peak should occur 0.5 ns sooner than the estimated time-of-flight.[17]

[17]The shift is not due to attenuation in the BC-505: the average neutron interaction point is 0.1 ns earlier than if they interacted at the middle of the detector (when detector attenuation is included); and the average

This means that if we fit a function; such as a Gaussian, to the peak of the neutron time-of-flight spectrum: we would be fitting to a peak 0.5 ns earlier than the mean neutron arrival time, and we'd see a spurious offset.

This result is of interest because when we fit a function to the time-of-flight peak we see that *the experimental data shows a similar systematic offset*: the neutrons in the experimental data arrive approximately 0.5 ns earlier than the estimated time-of-flight (see table 5.1). For the experimental data, the long target average (0.56 ± 0.22 ns) and short target average (0.28 ± 0.22 ns) may disagree on the value of this offset, but the difference is small relative to error ($\Delta t = 0.28 \pm 0.44$ ns) and therefore it was deemed of little merit investigating this phenomenon completely; as far as we can tell the simulated peak and experimental peak locations agree within error for both the long and short targets and therefore the neutrons are not arriving sooner than expected.

Run	Factor (ns)	
	Fit	Peak
Long Target Sim	0.403 ± 0.025	0.36 ± 0.18
Short Target Sim	0.373 ± 0.073	0.434 ± 0.051
Run 142 (long)	0.50 ± 0.39	0.71 ± 0.56
Run 150 (long)	0.51 ± 0.39	0.65 ± 0.51
Run 155 (short)	0.30 ± 0.39	0.28 ± 0.51
Run 158 (short)	0.29 ± 0.33	0.25 ± 0.56

Table 5.1: Neutron Time-of-Flight Offsets. The average peak location for the expected time-of-flight minus the measured time-of-flight. These numbers were derived by employing two methods: we fit the time-of-flight spectrum with a Gaussian (column 2), and we used a peak finding algorithm [Mor00] (column 3). We see that the neutrons arrive too early in the simulation and the experiment, and that the offsets are the same within error.

photon interaction point has a trivial effect on the neutron time-of-flight (≈ 0.0001 ns).

5.3.7 Upstream Scattering

The vacuum at the High Intensity Gamma Source (HI$\vec{\gamma}$S) extends some distance (approximately 50 m) from the free-electron laser before ending at a thin window in the collimator hutch. Photons are collimated, pass through the Five Paddle Flux Monitor then enter the upstream target room, and finally the downstream target room where we performed our experiment. This means that photons were able to: (1) scatter from the collimator, (2) scatter from the air inbetween the end of the vacuum and the target, and (3) scatter from any of the plethora of other objects inhabiting the target rooms.

In previous experiments (e.g. Blackston [Bla07]), some photons were observed to have arrived earlier than expected in the upstream rings of Blowfish resulting in a pair of peaks in the TDC spectrum. This experiment produced the same phenomenon (see figure 5.20 on the next page): the dominant peak in the TDC spectrum for the upstream ring (ring 1; $\theta = 157.5°$) arrives approximately 3.5 ns earlier than the photons which scatter off of the target.[18] This peak is markedly less significant in the neighbouring rings: decreasing in magnitude in rings: 2 ($\theta = 144.0°$) and 3 ($\theta = 130.5°$), until by ring 4 ($\theta = 117.0°$) it is no longer observed.

This phenomenon is consistent with upstream scattering of the beam: photons scatter upstream and then enter the detectors directly instead of hitting the target first; this explains both why they arrive earlier (they don't have to travel to the target and back), and why their presence is not detected in the downstream cells (Blowfish shields them with the upstream cells). Blackston [Bla07] tested this hypothesis by aligning the TDCs using the target, then he removed the target and measured the TDC spectra to see if the anomalous peak was still observed: it was, confirming that the anomalous photons were not scattering from the target.

We performed additional analysis in this experiment and determined the following:

1. The early photon-peak has a dirty energy spectrum (detector response: 0-10 MeVee), while the on-time photopeak is clean (0-1 MeVee): since Compton scattering is the

[18] Note: the out-of-time photons discussed in section 5.3.1 on page 152 are all spaced 5.36 ± 0.49 ns apart, thus excluding the possibility that these early photons are produced by that mechanism. Furthermore, the early photons discussed in this section were observed only in the upstream rings, rather than all cells.

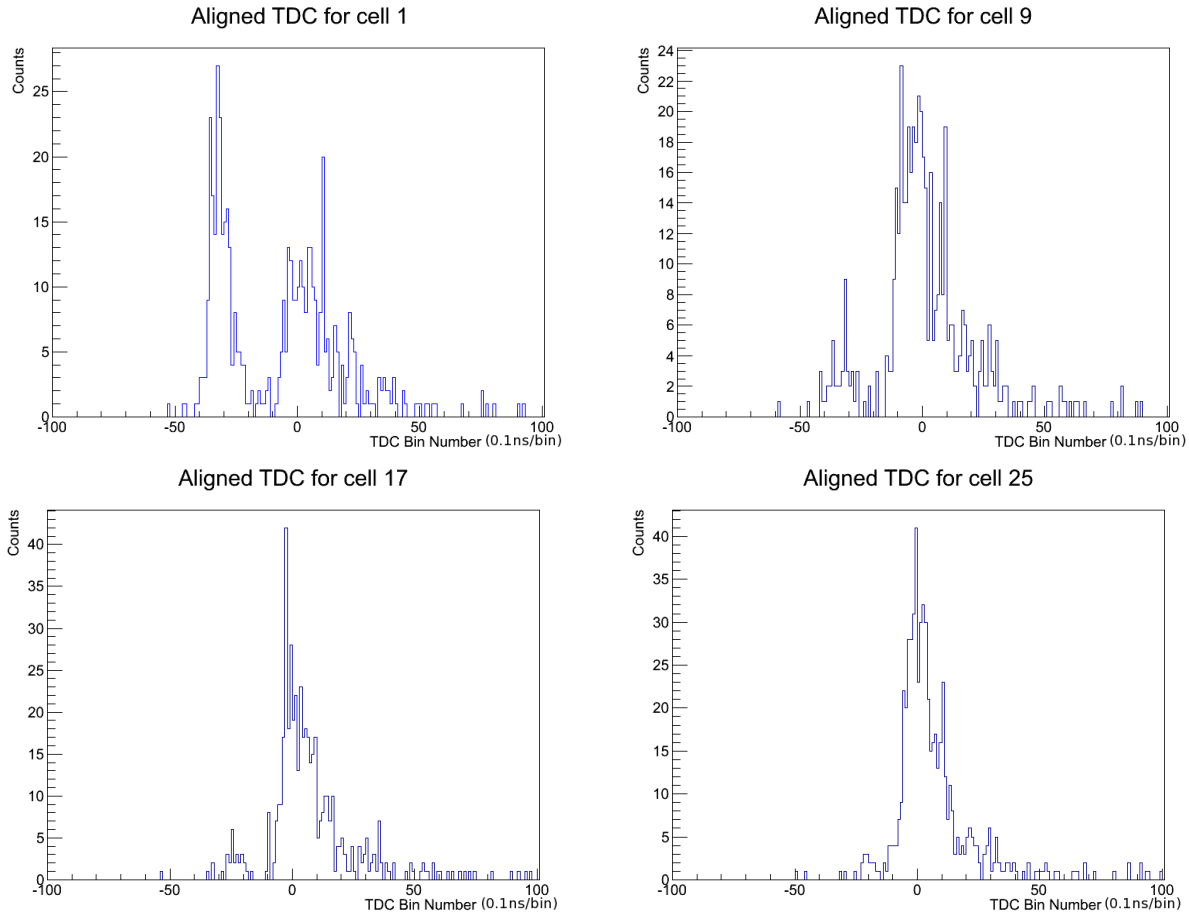

Figure 5.20: Upstream Scattering of Beam. Figures from left to right and top to bottom are the upstream aligned TDC spectra for: cell 1 ($\phi = 0°$, $\theta = 157.5°$), cell 9 ($\phi = 0°$, $\theta = 144.0°$), cell 17 ($\phi = 0°$, $\theta = 130.5°$), and cell 25 ($\phi = 0°$, $\theta = 117.0°$). Notice that the peak arriving before zero decreases in height as a function of θ, this is consistent with the early peak being due to upstream scattering.

dominant process, this is consistent with the early peak being composed of scattering at a variety of angles.

2. The simulation predicts that scattering in air will produce the spurious peak (no air: no peak), and it has a probability proportional to the distance the beam travels. With the beam placed 3 m upstream (of the target) the simulation predicts an early peak ≈ 0.2 ns later than the experimentally observed one.

All of these observations are consistent with the anomalous peak being due to upstream scattering. If the scattering is occurring in air, then the photons are probably scattering primarily $\gtrsim 3$ m upstream of the target.

5.3.8 Time-to-Digital Converter (TDC) Drift

The time-to-digital converter (TDC) offset values for the TDC calibration runs (i.e. those without pre-scaling of the beam photons) were compared to verify their accuracy. Several of the cells exhibited severe discrepancies between the valid TDC calibration runs (on the order of 1 ns), these cells were: cell 26, cell 30, cell 56, cell 82, and cell 84. These cells were immediately excluded from further data analysis (see section 5.4.7 on page 209), and an investigation was launched into analyzing the time-evolution of the offset position.

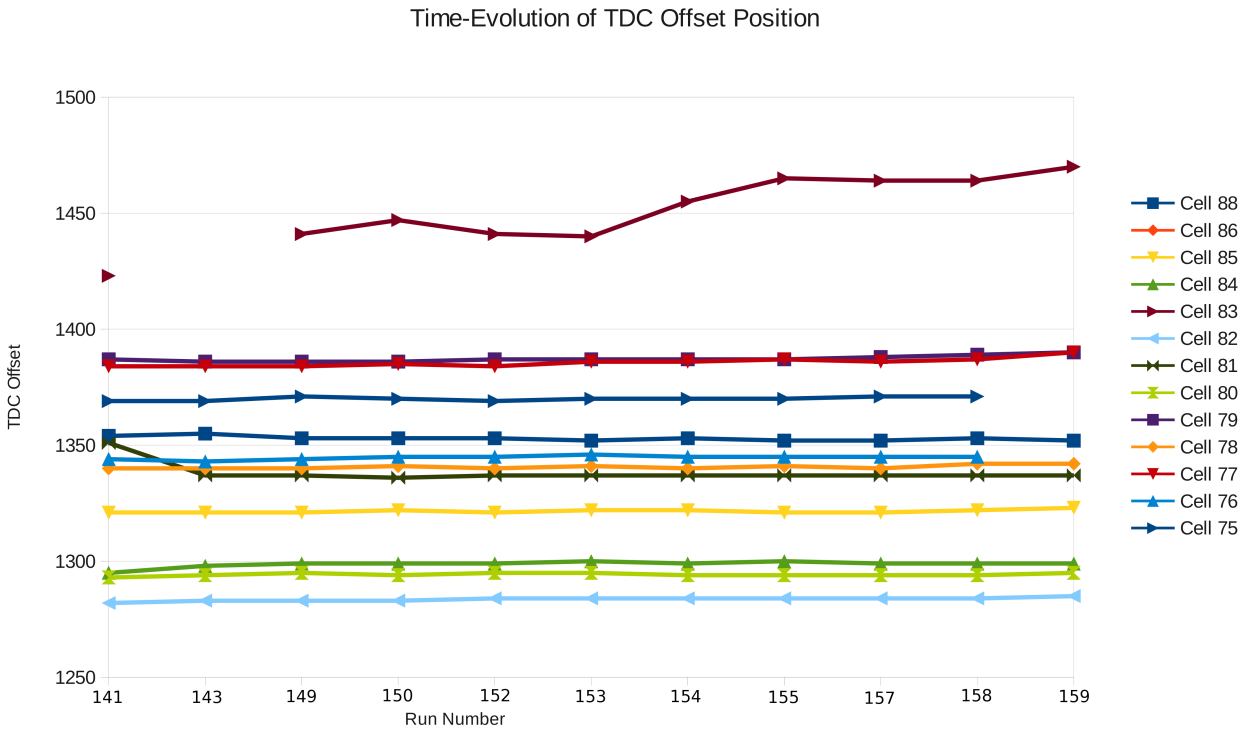

Figure 5.21: Time-to-Digital Converter Drift. Most cells exhibit stable peak positions, but some show a continuous drift such as cell 83; these cells must be omitted from analysis.[19]

Figure 5.21 was computed using data extracted from the downstream-most rings of the experimental runs where the prompt beam peak could be reliably resolved. Contrary to earlier observation via the TDC calibration runs: cells 82 and 84 did not appear to drift meaningfully, nor did any other cell except cell 83. In order to be conservative, cells 82 and 84 remained on the exclusion list, and cell 83 was also added. Cells 11 and 14 were later added to the exclusion list due to the suspicious shape of their TDC spectra in later runs, which appeared to show the neutrons arriving far too early (causing part of the neutron region of the TDC spectrum to be cutoff by the pre-scaling gamma window).

The final excludes due to inferred or observed TDC drift were cells: 9, 11, 14, 15, 22, 26,

[19]Note: run 142 was not included in figure 5.21 by mistake; it shows almost identical offset values as run 143.

30, 56, 82, and 84.

5.3.9 Pulse-Shape Discrimination

Blowfish's cells are sensitive to photons as well as neutrons, and so we had no choice but to measure unwanted photons. Furthermore, there are a sundry of sources with enough photons to produce more photons than neutrons in our detectors: background photons are omnipresent, the beam spits out photons at the wrong time (see section 5.3.1 on page 152), photons can be readily produced by delayed emission processes, and photons can spend many nanoseconds bouncing off of stuff in the target room before being attenuated. If it weren't for the arrival of photons at unexpected times from the beam, we could eliminate: the beam photons using a time-of-flight cut (see section 5.4.4 on page 204), the scattered and delayed photons using a GEANT4 simulation (see section 4.2 on page 105), and the background photons by simply assuming they're relatively constant in time. Unfortunately, out-of-time photons are a fact and so we had to find another way of eliminating photons from our data so that we were left with only neutrons: this method was pulse-shape discrimination.

Pulse-shape discrimination takes advantage of the fact that organic scintillators; like BC-505, are able to preserve differences in how photons and neutrons deposit their energy in them.[20] i.e. neutrons produce relatively more delayed fluorescence (see figure 3.14 on page 78).

The data we read from the v792 ADCs are simply numbers proportional to the charge they integrate, so we integrate each detector signal twice: once over a short interval (the short gate) which only integrates the first part of the pulse and once over a long interval (the long gate) which integrates the entire pulse (figure 5.22 on the next page illustrates).

[20]This is discussed in section 3.8.1 on page 74 See appendix A on page 278 and appendix B on page 282 for more information on photon and neutron interactions with matter (respectively).

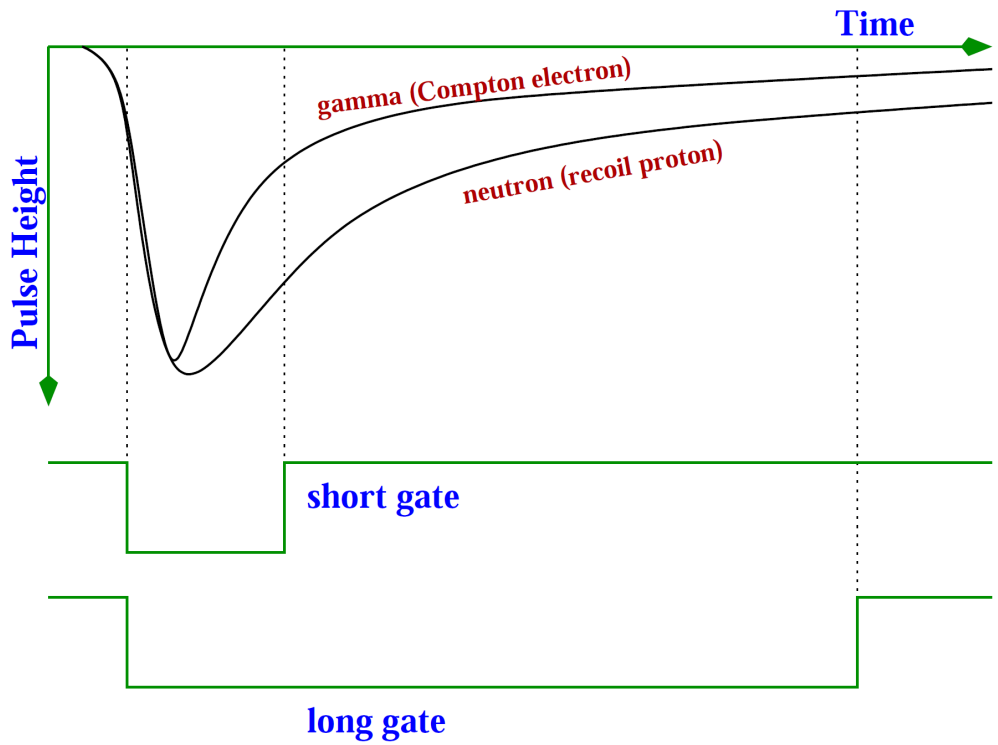

Figure 5.22: An Idealized View of How PSD is Performed. The pulses have been normalized for comparison. The short and long gate represent the integration periods used by the ADCs. A gamma ray (i.e. photon) deposits its energy faster than a neutron does (see section 3.8.1 on page 74): hence the photon short gate receives a larger portion of the total charge than does the neutron short gate. Image credit: Sawatzky [Saw05]

Plotting the values of the normalized difference between the gates ($\frac{\text{short - long}}{\text{long}}$) versus the long gate integral should then produce two lines: one representing the neutrons and one representing the photons; this is seen in figure 5.23 on the next page.

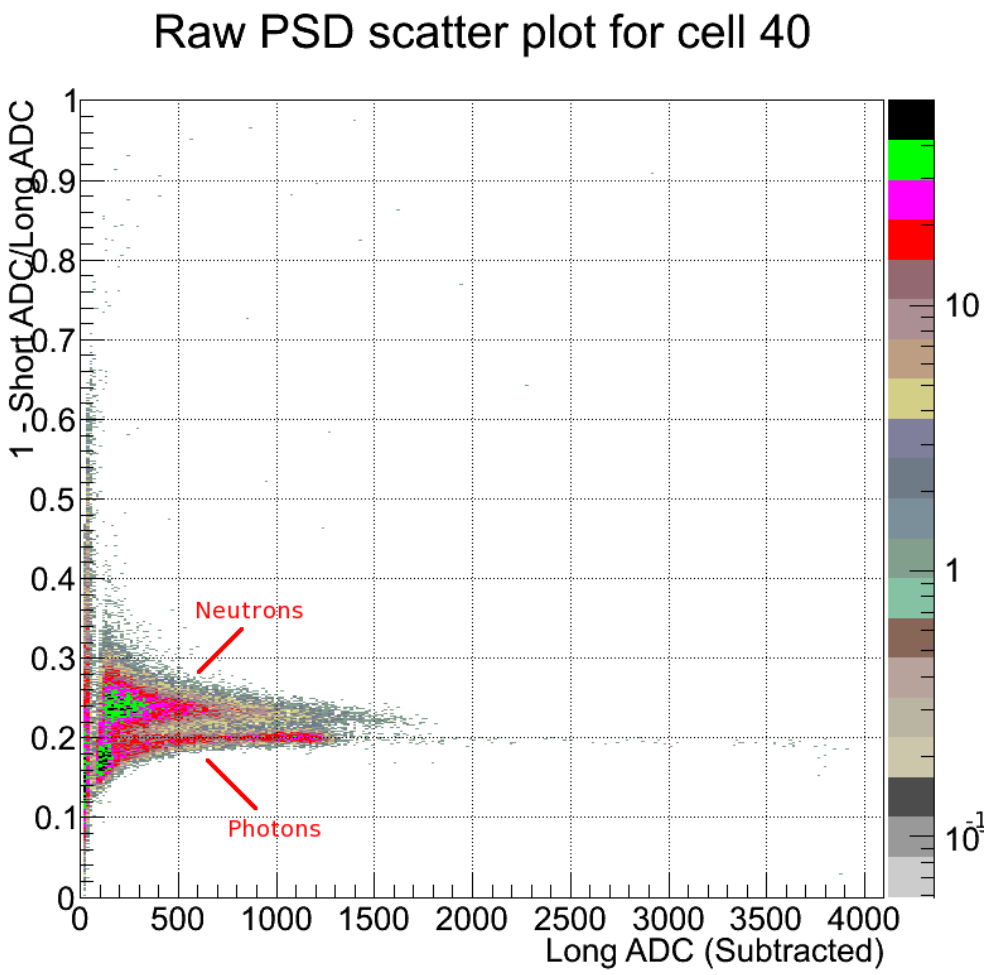

Figure 5.23: Raw PSD Plot. The short gated ADC integral and long gated ADC integral are plotted (both pedestal subtracted). The photons deposit a relatively larger portion of their energy in the short gate than the neutrons do, resulting in two distinct lines: the top line is produced by the neutrons and the bottom line is produced by the photons. The very low energy information ($x < 100$) is confounded by particles that deposit only a small fraction of their energy in the detector (e.g. by scattering off the edge of the detector).

In previous works (e.g. Sawatzky [Saw05], Blackston [Bla07], Kucuker [Kuc10], and Wurtz [Wur10c]) a simple formula; eq. (5.4) on the next page, was used to separate these lines by

altering two of its parameters:

$$PSD = L - S + \Phi - R \cdot L \tag{5.4}$$

where: PSD is the PSD parameter (neutrons have $PSD > 0$, ideally gammas have $PSD < 0$ too), L is the long gated ADC value, S is the short gated ADC value, Φ is a parameter called the offset, and R is a parameter called the rotation.

Optimization of the parameters in eq. (5.4) manually would require plotting each event for a given cell using eq. (5.4) and then altering the parameters until the neutron bunch all have $PSD > 0$ and as many photons as possible have $PSD \leq 0$; a PSD cut could then be applied to exclude all events with $PSD \leq 0$. Performing the PSD manually is time-consuming, subjective, and incapable of accurately estimating the uncertainty in the PSD.

In the current work, a new algorithm was employed to separate the neutrons and photons to an automatically estimated degree of certainty. The new algorithm is based on the observation that the y-axis variance in the neutron and photon lines of figure 5.23 on page 186 are very well described by Gaussian distributions: the pair are thus well described with respect to the y-axis by a double Gaussian distribution (the x dependence is well described by an exponential decay on top of a soft-edged step function pedestal). We take regular projections of the raw PSD scatterplot (e.g. figure 5.23 on page 186) at intervals along the x-axis: collapsing the x-axis and causing the 3-dimensional plot in x, y and z to become a 2-dimensional plot in y and z; then we fit a double Gaussian function to each slice (figure 5.24 on the next page) and record all of this information.

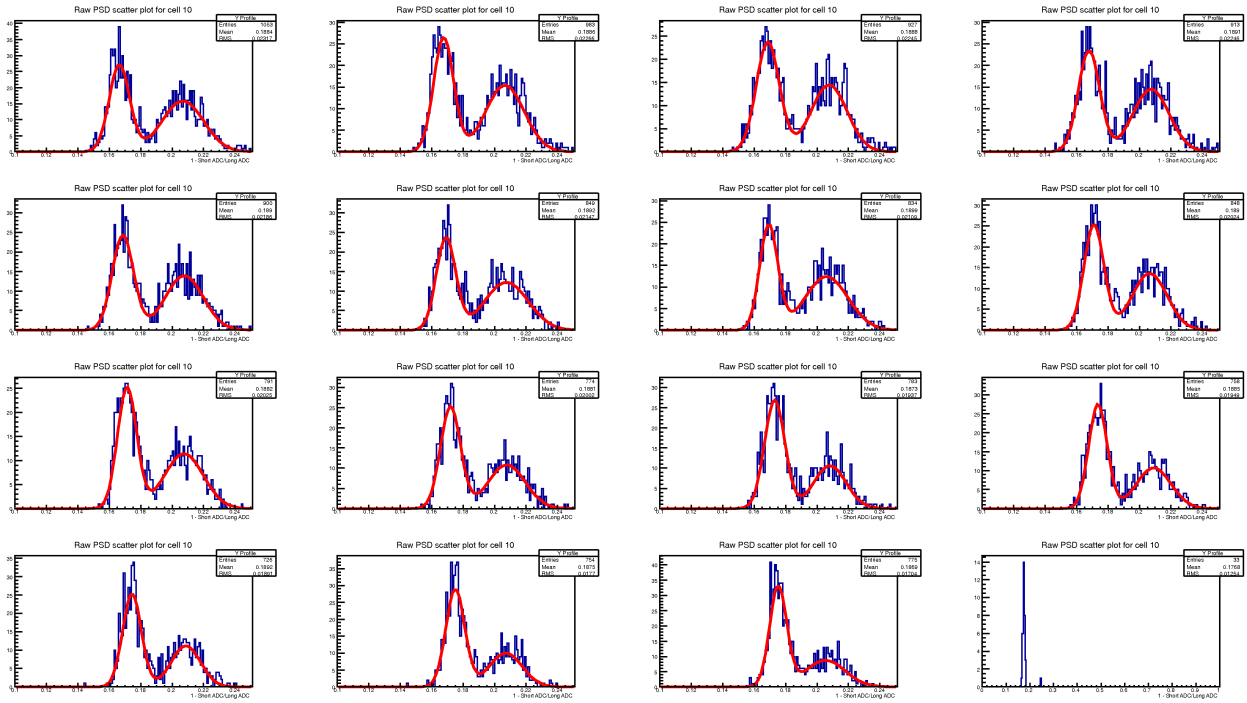

Figure 5.24: PSD Slice Plot Example. The 3-dimensional raw PSD scatter plot (e.g. figure 5.23 on page 186) is sliced along the x-axis then projected into 2-dimensions, yielding a series of 2-dimensional plots, or *slices*, such as this figure. Each slice is fit very well by a double Gaussian distribution (red lines); fits with reduced χ^2 values of less than 2 were automatically excluded (e.g. the bottom right plot) and all other fits were visual verified by the user.

After we have sliced and fit the PSD scatterplot, and have all of the pertinent information regarding the double Gaussian function fits: we place a point with y-value 2 standard deviations[21] away from the neutron mean (towards the photon mean) and x-value equal to the middle of the slice position along the x-axis on a new plot (e.g. figure 5.25 on the next page).

[21]This value is arbitrarily selected by the user. We also tried 0 standard deviations, but it gave insufficient precision to proceed (see section 7.1 on page 246 for details as to why).

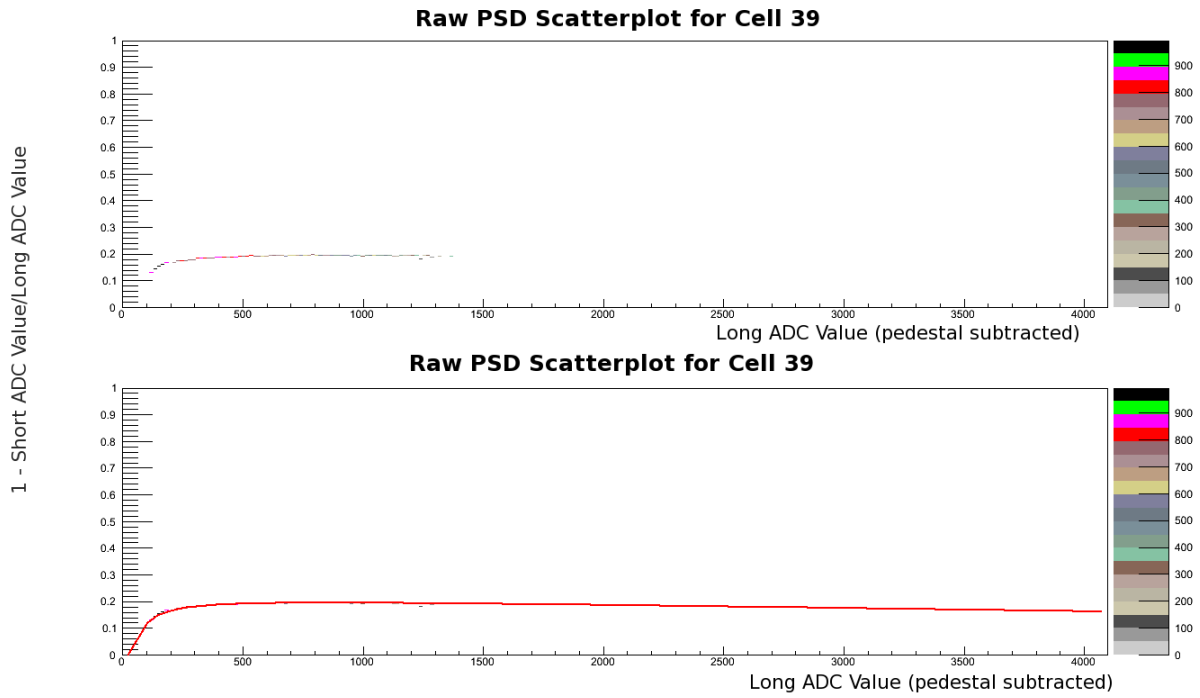

Figure 5.25: PSD Fit Plot. The fitting data from figure 5.24 on page 188 are used to fill this plot with appropriate weighting (darker colours are more strongly weighted), then a function of the form eq. (5.5) is fit (red line; lower plot) and appropriate parameters are extracted. These parameters are then used to plot a final PSD graph (e.g. figure 5.26 on the next page) which is used to determine the PSD cut.

Figure 5.25 is fit with the current PSD formula:

$$PSD = 1000(1 - \frac{S}{L} + \frac{\phi}{L} - R + Se^{-\lambda L} + J \cdot L) \tag{5.5}$$

where: PSD is the PSD parameter, L is the long gated ADC value, S is the short gated ADC value, ϕ is a parameter called the offset, and R is a parameter called the rotation, S is a parameter called the sheer, λ is a parameter called the decay, and J is a parameter called the jerk. The change from eq. (5.4) on page 187 is to divide by L in order to prevent inflated confidence in the PSD cut: the PSD is scaled by a constant instead (1000). Three additional parameters were also added (the last two terms), though the $Se^{-\lambda L}$ term is rarely used. The parameters are extracted by a fitting algorithm used on the PSD fit plot e.g. figure 5.25 on

page 189.

Once the necessary parameters have been extracted from figure 5.25 on page 189, a final PSD graph is plotted using eq. (5.5) on page 189 with the extracted parameters (e.g. figure 5.26). The parameters have been automatically adjusted such that the neutrons all appear with $PSD > 0$.

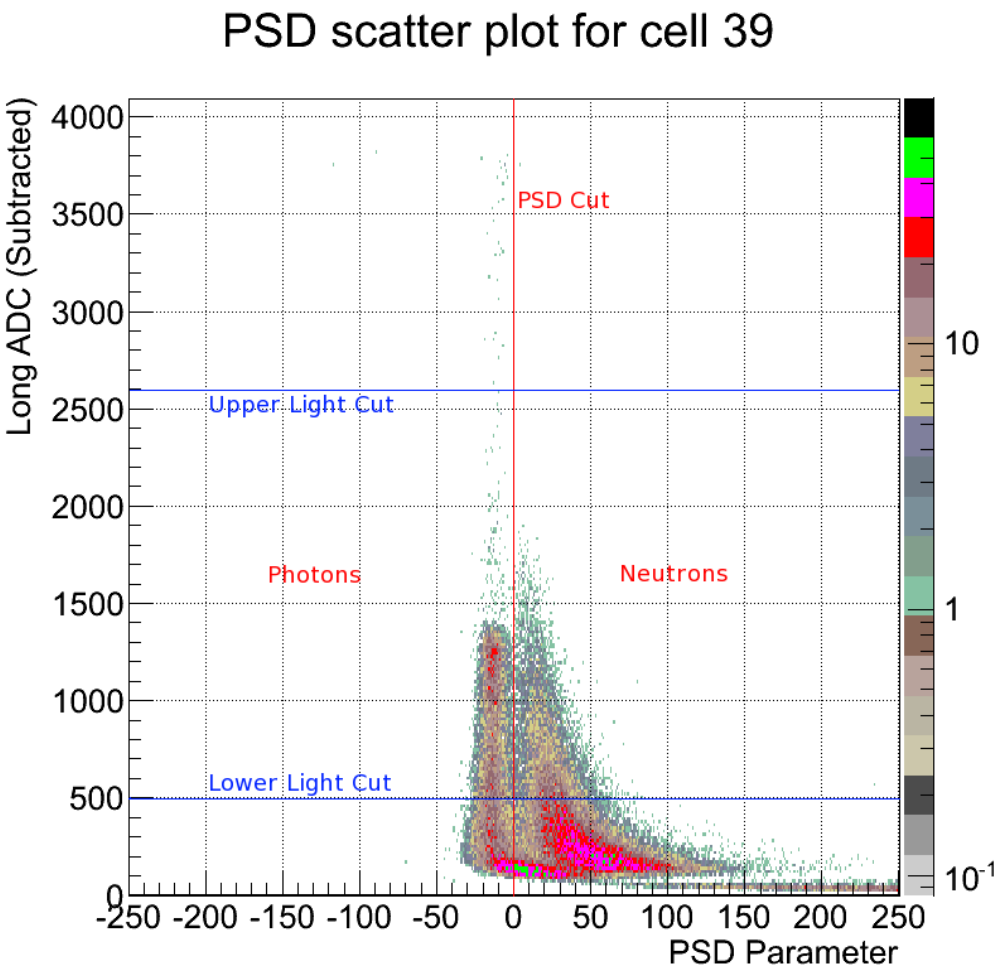

Figure 5.26: Final PSD Plot. An example of the final PSD plot from a source run (run 139). Everything below x = 0 is cut, and above x = 0 is kept. The light cuts (see section 5.4.3 on page 199) are placed at 1750 keVee and 9000 keVee in order to exclude the regions of overlap (notice that the photons curve past 0 at approximately long ADC bin 200).

One important point about this methodology is that it requires good statistics: lots of

neutrons and photons at high enough energies to fill the upper long gated ADC values. In this experiment AmBe source runs were used (run 139 and run 165) to determine the PSD, but they did not have good enough neutron statistics at high energies and consequently the PSD is the single largest contributor to the uncertainties in this experiment (see section 7.1 on page 246).[22] Future experiments producing neutrons above the AmBe spectrum[23] would benefit from using a source that provides high energy photons and neutrons, such as simply placing a lead block in Blowfish with the beam incident.

Once the PSD parameters had been computed for an AmBe source run, they were used in the subsequent data runs with the assumption that the PSD properties of the cells shouldn't have changed unless the ADC integration times (i.e short and long gates) or the gains changed significantly, because these are the only variables upon which the PSD depends.

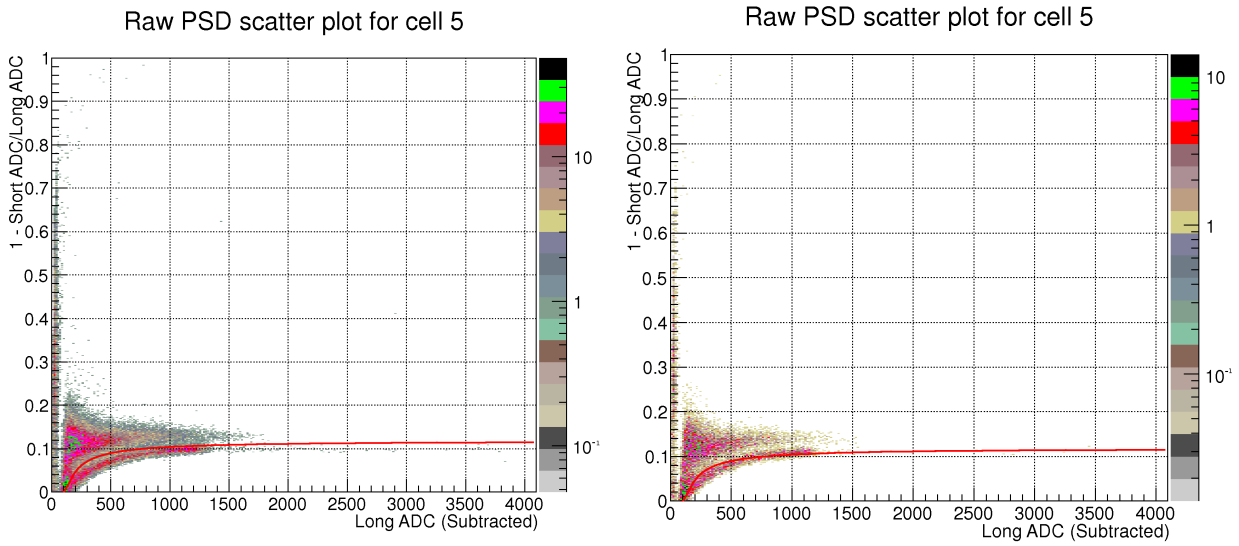

Figure 5.27: PSD Parameters Change During the Experiment. The PSD parameterization (red) clearly does not agree for both runs, likely due the systematic change in the gains of $33 \pm 11\%$ between runs 139 (left) and 165 (right). A similar change is observed between run 143 and run 149, but runs 139-143 agree as do runs 149-165.

[22] The solution to this appears to be either taking longer AmBe runs, or using a source with higher energy neutrons.

[23] AmBe producing neutrons of energies 0-10.9 MeV [Leb07].

Figure 5.27 on page 191 demonstrates that the best set of PSD parameters changed sometime between run 143 and run 149 (the intermediate runs have no usable data). This was likely due to a systematic shift in the gain because: the average gain for run 165 was $33 \pm 11\%$ larger than run 139, and no significant change in the pedestals was observed for any of the runs (which would indicate a change in the gate widths).

In order to compensate for the systematic change in the gain, the PSD had to be done twice: once before the change (run 139) and once after (run 165). Unfortunately, run 165 was a particularly short run and is the only AmBe source run available after run 139; consequently the uncertainties in the PSD for runs 149-159 are relatively high.

The new PSD methodology has been shown to give equivalent or better results than the traditional PSD methodology and has the advantages of: being substantially faster, being objective, and outputting an uncertainty estimate automatically [Pri14]. It is important that a higher order term be included in the PSD, rather than just the rotation (i.e. the jerk term in eq. (5.5) on page 189), otherwise the separation will be energy-dependent for cells showing this behaviour (because one will have to estimate the jerk term using the offset, rotation and a light cut) [Pri14].

A final note on PSD: several of the cells show exceptionally poor separation of the photons and neutrons (e.g. figure 5.28 on the next page: right), one hypothesis for this is that these cells have air in them. The presence of oxygen in the BC-505 cells increases non-radiative energy transfer [Kno00] which, as discuss in section 3.8.1 on page 74, leads to more triplet states which in turn leads to more delayed fluorescence: longer pulses. This confounds the photons and neutrons as photons produce more delayed fluorescence and hence longer pulses.

In September 2013, two ostensibly undamaged Blowfish cells were removed for inspection and it was discovered that they were both leaking substantially: it is therefore quite possible that some of the cells have been exposed to air (recall that the ADC neutron spectra are lower than expected and had to be scaled: discussed in section 5.3.2 on page 161). Figure 5.28 on the next page may have been contaminated with air sometime between 2008 and 2010.

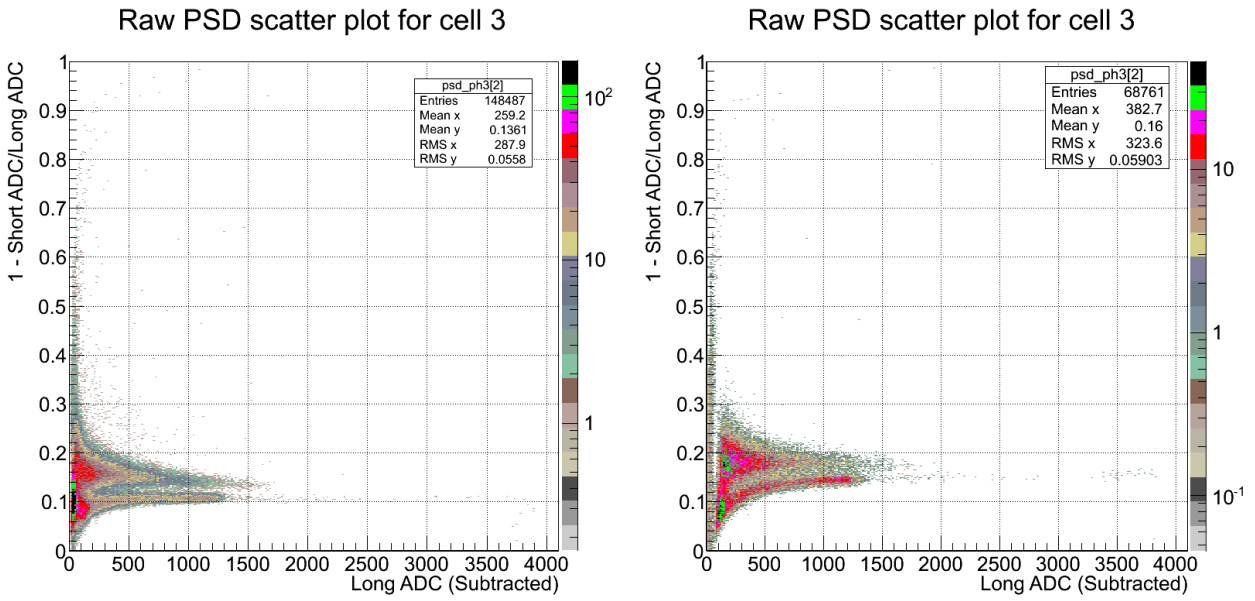

Figure 5.28: Aging Cell PSD. Left image: the raw PSD for an AmBe run taken in 2008. Right image: an AmBe run taken in 2010 with the same cell. Clearly the lower arm (the photons) has a different slope, and the separation between the two arms has been dramatically reduced. The photon arm *should* be horizontal, the fact that it curves in the right image is consistent with oxygen contamination which has increased quenching.

5.4 Analysis Cuts

Not surprisingly, raw data is not conducive to scientific discussion: the data must be processed in order to eliminate noise and confounding variables, and then extract meaningful observables. In this experiment we desired the total cross section, σ, and its angular dependence $\frac{d\sigma}{d\Omega}$:[24] this means we needed to accurately determine how many photons hit the target, how many neutrons were produced by the photodisintegration of deuterons in the target, and where the neutrons ended up going.

We used the Five Paddle Flux Monitor (described in section 3.9 on page 85) to measure the beam intensity, then used these data to calculate the number of photons that were incident

[24] We can calculate the analyzing power using the cross section data.

on the target; no cuts were required for these data, as they utilize corrective factors instead (as discussed in section 5.5.1 on page 211).

The neutron yields for each cell required that the neutron events measured from the photodisintegration of the deuteron be separated from all other measured events. The photons were removed by performing the pulse-shape discrimination cut (section 5.4.2 on page 196), complimented by the light cut (section 5.4.3 on page 199); followed by a background radiation cut (section 5.4.5 on page 206). The background radiation cut also removed the cosmic ray background of heavy charged particles entering the detectors. Most of the neutrons formed from other sources (primarily photodisintegration of oxygen via $^{16}O(\gamma,n)^{15}O$) were removed by the time-of-flight cut (section 5.4.4 on page 204) or the light cut (section 5.4.3 on page 199), and the remaining neutrons (as well as anything else that made it through all of the cuts) were removed using the H_2O target correction (section 5.4.6 on page 208). Known artifacts produced by the data acquisition and analysis systems were also removed by the light cut, and the multiplicity cut (section 5.4.1 on the next page). Finally, cells which demonstrated evidence of photons in the yield data after all of the cuts were applied; such as out-of-time photons (section 5.4.8 on page 209, were excluded (section 5.4.7 on page 209); along with cells which could not be properly calibrated for technical reasons.

Every cut has an uncertainty associated with it, in general the procedure for propagating the uncertainty in the neutron yields depended on first finding a way to estimate the maximum and minimum values each cut can take within their estimated uncertainties, then using these values to produce a neutron yield: changing only one cut value at a time, then proceeding with the rest of the cuts as normal. This resulted in a perturbed final neutron yield: the difference between this perturbed value and the normal value was deemed the uncertainty in the neutron yield due to the respective cut.

We applied the same cuts to the simulated data as the experimental data in order to assume the simulation accurately reproduces the experimental efficiency.

Note that the upper and lower cuts form an *inclusive* interval in all cases.

5.4.1 Multiplicity Cut

Table 5.2: Multiplicity Cut Summary

Purpose	Eliminate and compensate for incomplete signals in detectors.
Upper Cut	1
Lower Cut	1
Uncertainty	Assumed to be 0.

The *multiplicity* is the number of cells which recorded concurrent events (i.e. within the ADC integration intervals): e.g. a multiplicity of 2 means 2 cells recorded events above the detection threshold. The multiplicity cut is necessary because if more than one cell recorded an event (i.e. multiplicity > 1) then there may be partial signals which arrived in the ADCs while they were already busy processing an earlier signal.[25] The Blowfish array has 88 detectors in it; when any one cell records an event (i.e. when the discriminator for that cell fires): all cells are read (see section 3.10.1 on page 88 for details). If an event occurred in a second cell while the cells were being read then it would appear as a partial event which may or may not be fully integrated by the ADCs. Since we do not know if the ADC properly integrated the second pulse, we cannot use it (its PSD wouldn't be accurate), and so we elected to exclude all events if more than one cell fired in Blowfish during a single readout.

The multiplicity cut must be applied before the PSD cut (section 5.4.2 on the next page) and the lower light cut (section 5.4.3 on page 199) because short and long ADC gates may not have been properly aligned and therefore their relative values would be meaningless for the PSD and the value of the long gated ADC might be too small (causing the signal to fall below the lower light cut).

The multiplicity was computed during data analysis by simply counting the number of cells that fired at each readout. The number of excluded events due to the multiplicity cut: called the *multiplicity factor*, was also recorded for each cell so that the data could be scaled

[25] It is also possible that the earliest signal is a partial signal: if the first signal arrives outside of the neutron window. The key is the signal which generated the gates is complete, but any other signal could be incomplete.

up to compensate for the multiplicity cut. Once the multiplicity cut was performed, we applied the rest of the cuts and afterwards compensated for the multiplicity cut by scaling the total neutron yield in each cell by its unique multiplicity factor.

We assume that the cut was perfectly compensated for by the factor and hence do not include an uncertainty calculation.

5.4.2 Pulse-Shape Discrimination (PSD) Cut

Table 5.3: PSD Cut Summary

Purpose	Eliminate photon events from detectors.
Upper Cut	None.
Lower Cut	Mean minus 2 standard deviations.
Uncertainty	Estimated using fitting algorithm.

The purpose of the pulse-shape discrimination (PSD) cut was to exclude as many photons as possible from the data without introducing any new, unwanted error e.g. by excluding an unknown number of neutrons. The location of the cut was based on the statistical fit explained in section 5.3.9 on page 184: a double Gaussian function was fit to the neutrons and photons (one Gaussian for each) and then the cut was placed at some point on the neutron Gaussian. Two locations for the cut were tried: at the neutron mean and two standard deviations towards the photons from the neutron mean, the latter cut was used on the final data.

When the cut was applied at the mean of the neutron distribution: all of the photons were eliminated; unfortunately this came at a price: the uncertainty in the fitting algorithm was amplified causing large uncertainties in the neutron yields which prevented a reasonable parameterization of the differential cross section: ostensibly because the parameterizing algorithm couldn't handle the large errors. This is a simple matter of the shape of the neutron distribution (which is described by a Gaussian): the integral of the Gaussian function has most of its area near the mean, so a small error in the position at the mean translates into a

large total error; a large error in the position far from the mean translates into a relatively small error.

The large errors generated by performing the PSD cut at the mean motivated instead the use of a cut placed two standard deviations from the mean (i.e. encompassing 97.72% of the neutrons). The price for this smaller uncertainty is that some photons survive the PSD cut and become false positives. The background photons (i.e. not from the beam) surviving the PSD cut were easily subtracted (see section 5.4.5 on page 206), but cells which demonstrated out-of-time photons after the PSD cut was applied had to be excluded (see section 5.4.7 on page 209 for details).

The fitting process which calculated the PSD parameter outputs up to 5 parameters, each with an uncertainty generated using the Minos technique by the TMinuit class of ROOT [Jam81, Ead06]. We used this to estimate the maximum error in the PSD using eq. (5.6) on the next page.

Recall eq. (5.5) on page 189:

$$PSD = 1000(1 - \frac{S}{L} + \frac{\phi}{L} - R + Se^{-\lambda L} + J \cdot L)$$

where: PSD is the PSD parameter, $L \pm dL$ is the long gated ADC value, $S \pm dS$ is the short gated ADC value, $\phi \pm d\phi$ is a parameter called the offset, and $R \pm dR$ is a parameter called the rotation, $S \pm dS$ is a parameter called the sheer, $\lambda \pm d\lambda$ is a parameter called the decay, and $J \pm dJ$ is a parameter called the jerk.

We estimate the error by computing the maximum and minimum values of PSD given a set of uncertainties in its parameters:

$$PSD_{\frac{max}{min}} = 1000(1 - \frac{S}{L} + \frac{\phi \pm d\phi}{L} - (R \mp dR) + (S \pm dS)e^{-(\lambda \mp d\lambda)L} + (J \pm dJ) \cdot L) \quad (5.6)$$

where one reads the upper symbol in a $\pm$ sign for maximum PSD value (PSD_{max}) and the lower symbol for the minimum PSD value (PSD_{min}). There are covariances between the parameters, hence why we chose to propagate the error using the above equation, rather than a standard error propagation technique. We do not include an $\frac{S \mp dS}{L}$ term because we any variation in the short gate value is perfectly compensated for by a similar variation in the long gate value.

The maximum and minimum values for the PSD were computed using eq. (5.6), then the PSD cut was applied using these values along with the rest of the cuts performed normally. This resulted in a neutron yield for each detector which differed from the correct yield only due to the position of the PSD cut. Computing the difference in neutrons measured in each detector when the PSD cut was normal, at a maximum, and at a minimum provided an estimate for the upper and lower errors associated with the PSD cut. Figure 5.29 on the next page illustrates the process.

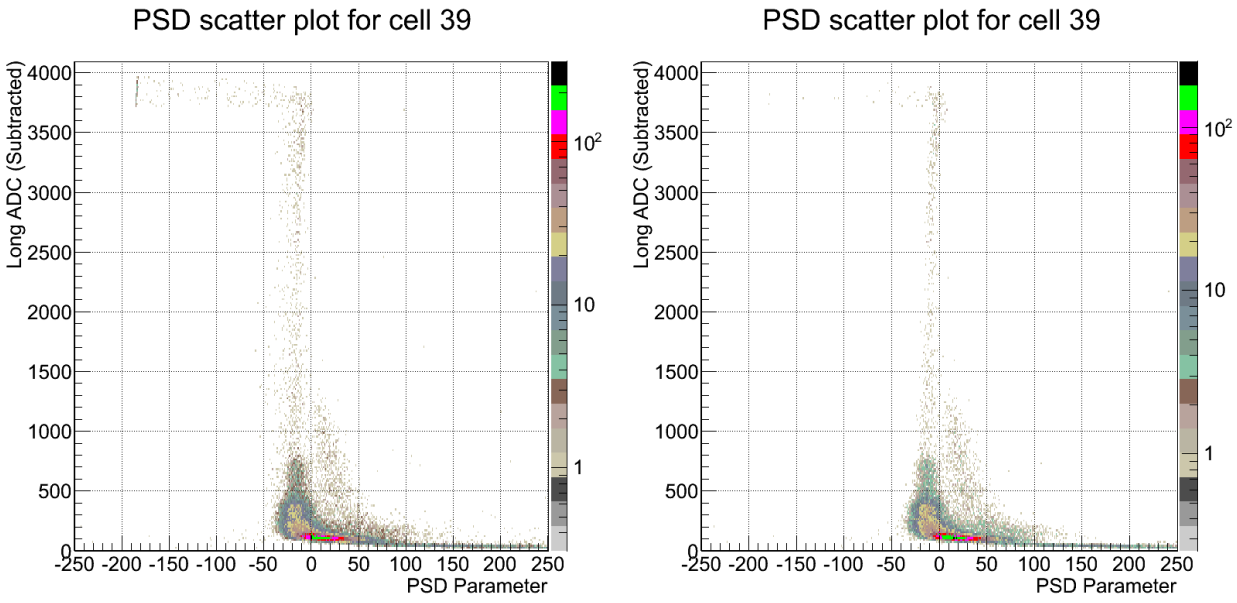

Figure 5.29: Estimating the Uncertainty in the PSD Cut. The left plot is a normal PSD plot from run 142, the right plot is the maximum PSD plot from the same run (calculated using eq. (5.6) on page 198). The data from both plots are completely processed, culminating in two neutron yields for each Blowfish cell. The PSD cut accepts all values above 0, so the neutron yield of the right plot will be larger than the left plot: the difference is considered the upper error for the PSD cut. The lower error is computed in the same way, except that the minimum PSD value is used instead of the maximum PSD value.

5.4.3 Light Cuts

Table 5.4: Light Cut Summary

Purpose	Eliminate photon events from detectors.
Upper Cut	9000 keVee
Lower Cut	1750 keVee
Uncertainty	Calculated from uncertainty in ADC gain and linearity.

The detector response of a scintillator (i.e. the light output) is commonly measured in electron-equivalent electronvolts (eVee): the kinetic energy of an electron which would produce that much light (i.e. a 1 eV electron; by definition, causes a light output of 1 eVee in a scintillator). Therefore, when we calibrate our detectors they are calibrated in terms of eVee: i.e. in terms of light intensity; hence, we refer to the energy cuts applied to the detectors as *light cuts*.

Recall figure 5.30 on the next page (the same as figure 5.26 on page 190): the light cut was applied to eliminate false positives due to the photon PSD spectrum overflowing onto the positive x-axis.

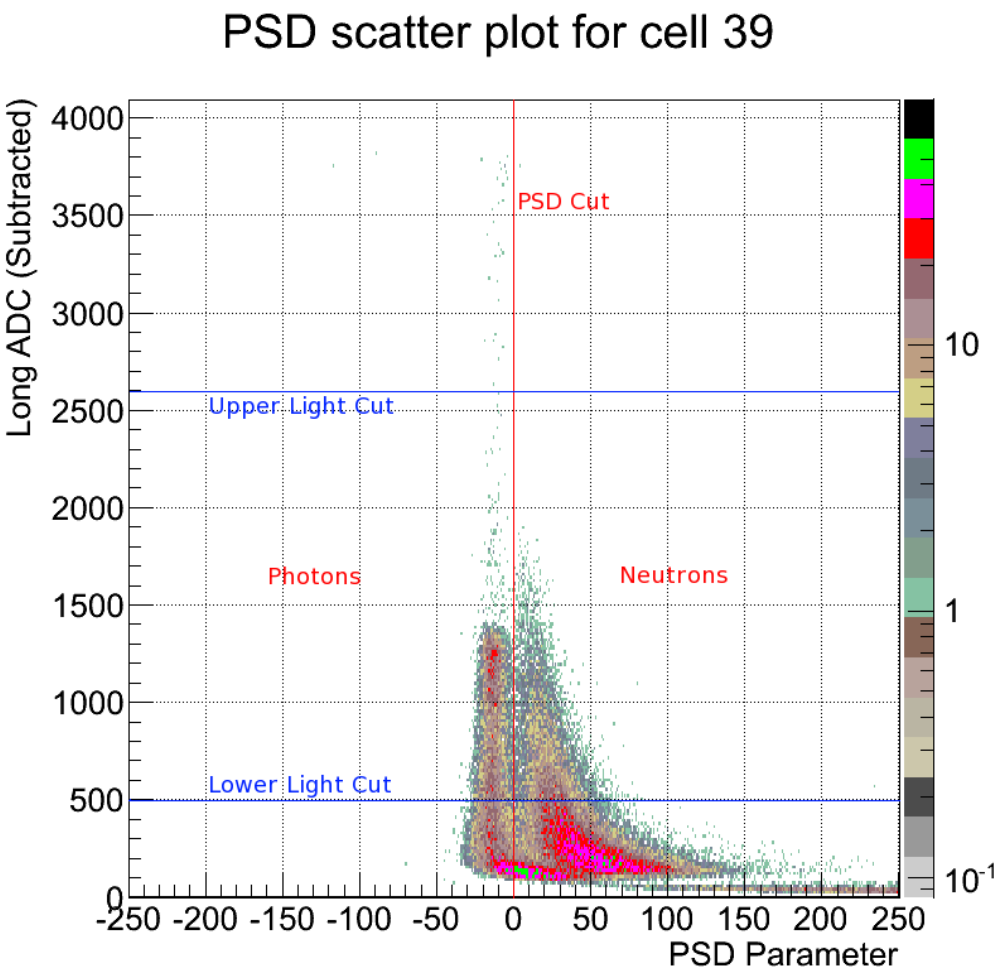

Figure 5.30: Final PSD Plot. An example of the final PSD plot from a source run (run 139). Everything below 0 is cut, and above 0 is kept. The light cuts are placed at 1750 keVee and 9000 keVee in order to exclude the regions of overlap (notice that the photons curve past 0 at approximately long ADC bin 200). Notice that there are a few events above the upper light cut with $PSD > 0$: these must be photons since the neutrons are kinematically restrained to fall below the upper light cut.

The lower light cut must be applied because PSD requires a difference between the short and long gated ADC values:[26] if a particle of any kind interacts within a small enough window then the short and long gated ADC values will be the same and the particles will have identical PSD parameters. Therefore, the lower light cut was placed at the highest

[26]Recall that the short and long gates refer to the time period over which the ADC integrates charge.

estimated location of photon and neutron overlap for the majority of cells. An additional benefit to this cut is that it was placed above the hardware threshold (which is $\approx$ 300 keVee) thus eliminating the need to compensate for it.

The purpose of the upper light cut is to reject ADC artifacts at no cost: the neutrons are energetically forbidden by kinematics to show up above 9 MeV, and even if some exotic process was producing higher energy neutrons: the detector response of a 9 MeV neutrons is $\leq$6 MeVee [Pyw06], meaning neutrons with energies up to $\approx$ 13.5 MeV would still be included after the cut was applied. The ADC artifacts are known to occur as a consequence of the sliding-scale technique (discussed in section 3.10.4 on page 100) [CAE10]: hence why we must apply the upper light cut (we choose it such that all ADC bins $\geq$ 3500 are excluded from analysis).

The light cut is illustrated using the calibrated long gate ADC spectrum in figure 5.31.

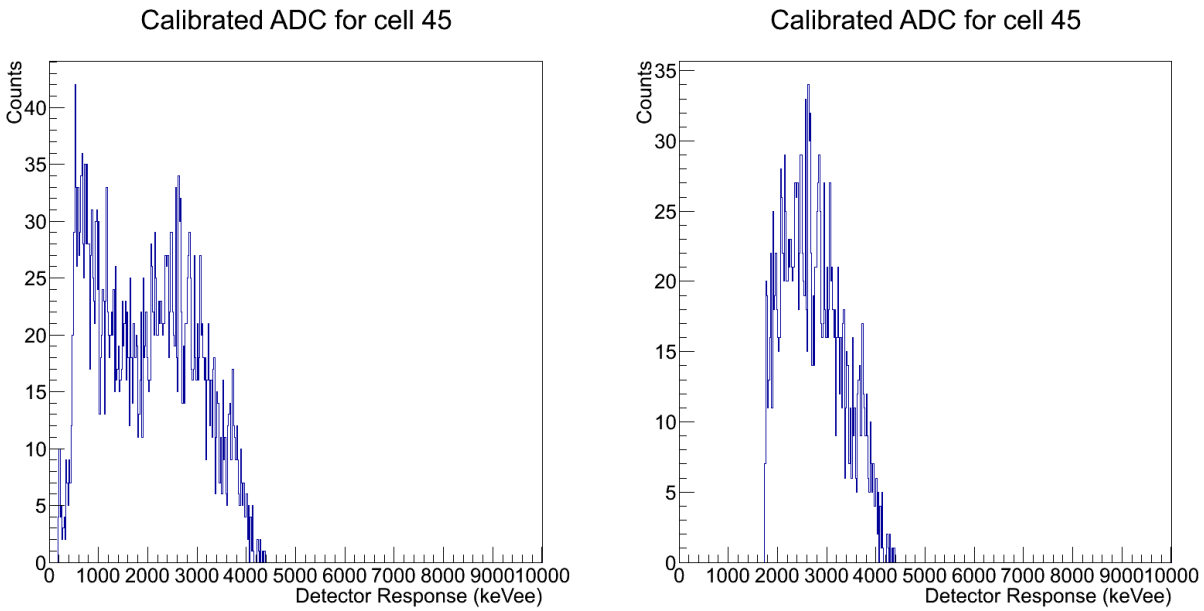

Figure 5.31: Effect of the Light Cuts. The left plot shows a typical uncut, long gated calibrated ADC spectrum (from run143) and the right plot shows the same spectrum after the light cuts have been applied.

We assumed that the light cuts would not affect the data in any way that the simulation would not account for by applying the same light cuts to the simulated data. We later altered

the position of the light cuts to ensure that this assumption is valid: the final data do not depend on the positions of the light cuts (see appendix J on page 302 for details).

We estimated the light cut uncertainty using standard error propagation techniques: the nominal ADC uncertainties, the uncertainty in the pedestal, and the uncertainty in the gain were appropriately scaled and added in quadrature.

The uncertainty in the neutron yield was propagated by raising and lowering the upper and lower light cuts by the uncertainties calculated, then applying all other cuts normally. This resulted in four sets of cell yields with varied light cuts, the difference between each set of yields and the normal set was computed, resulting in an upper and lower error for both the upper and lower light cuts.

5.4.4 Time-of-Flight Cut

Table 5.5: Time-of-Flight Cut Summary

Purpose	Eliminate beam photons and neutrons for other sources.
Window (long target)	Cells 1-8 cut from 7.12 to 17.31 ns (expected TOF: 12.33 ns)
	Cells 9-16 cut from 7.02 to 17.19 ns (expected TOF: 12.23 ns)
	Cells 17-25 cut from 6.90 to 17.01 ns (expected TOF: 12.09 ns)
	Cells 26-33 cut from 6.76 to 16.78 ns (expected TOF: 11.92 ns)
	Cells 33-40 cut from 6.61 to 16.51 ns (expected TOF: 11.73 ns)
	Cells 41-48 cut from 6.45 to 16.23 ns (expected TOF: 11.53 ns)
	Cells 49-56 cut from 6.30 to 15.95 ns (expected TOF: 11.33 ns)
	Cells 57-64 cut from 6.16 to 15.68 ns (expected TOF: 11.15 ns)
	Cells 65-72 cut from 6.05 to 15.44 ns (expected TOF: 11.00 ns)
	Cells 73-80 cut from 5.96 to 15.23 ns (expected TOF: 10.87 ns)
	Cells 81-88 cut from 5.90 to 15.08 ns (expected TOF: 10.78 ns)
Window (short target)	Cells 1-8 cut from 8.47 to 15.93 ns (expected TOF: 12.33 ns)
	Cells 9-16 cut from 8.37 to 15.82 ns (expected TOF: 12.23 ns)
	Cells 17-25 cut from 8.23 to 15.65 ns (expected TOF: 12.09 ns)
	Cells 26-33 cut from 8.07 to 15.43 ns (expected TOF: 11.92 ns)
	Cells 33-40 cut from 7.90 to 15.19 ns (expected TOF: 11.73 ns)
	Cells 41-48 cut from 7.72 to 14.93 ns (expected TOF: 11.53 ns)
	Cells 49-56 cut from 7.55 to 14.66 ns (expected TOF: 11.33 ns)
	Cells 57-64 cut from 7.40 to 14.41 ns (expected TOF: 11.15 ns)
	Cells 65-72 cut from 7.27 to 14.19 ns (expected TOF: 11.00 ns)
	Cells 73-80 cut from 7.17 to 14.00 ns (expected TOF: 10.87 ns)
	Cells 81-88 cut from 7.10 to 13.86 ns (expected TOF: 10.78 ns)
Uncertainty	0.64 ns (included in intervals)

As discussed in section 2.3 on page 23: we assume that the photodisintegration of the deuteron occurs elastically and compute the kinetic energy of the outgoing neutron as a function of its emission angle. We used the computed kinetic energy, along with a conservative estimate of the range of free paths that a neutron could take to predict the time-of-flight,[27] then cut all events which do not fall within this interval. This eliminates most of the confounding neutrons produced by photodisintegration reactions of other nuclei.

The time-of-flight (TOF) interval includes all possible undeviated paths that a $d(\vec{\gamma},n)p$ neutron can take from the target to a detector; we account for neutrons which scatter before being detected by applying the same cut to the simulation. The intervals used are given in table 5.5 on page 204. The cut is illustrated in figure 5.32.

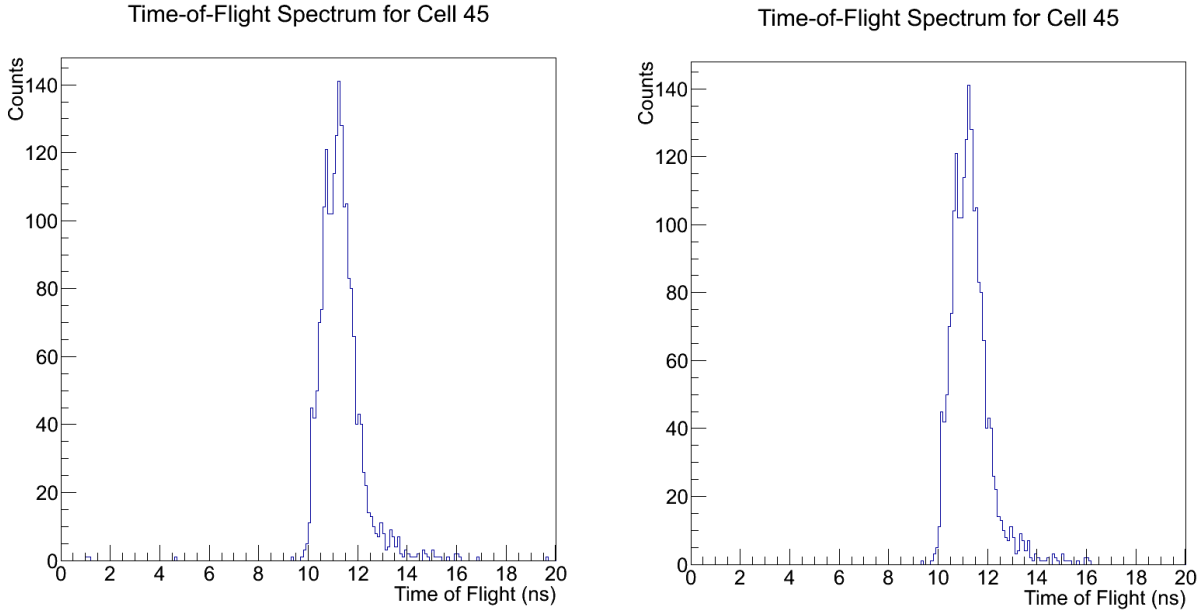

Figure 5.32: Effect of the Time-of-Flight Cut. The left plot shows a typical time-of-flight spectrum (from run 143) and the right plot shows the same spectrum after the cut has been applied. The difference for this cell before and after the cut is not dramatic because the PSD cut has already been applied.

The vast majority of the target is composed of ^{1}H, ^{16}O, ^{12}C, and D: H has no neutrons, ^{12}C has a neutron separation energy greater than the beam energy (18.7 MeV [Son13]), and the

[27] Considering: the possible interaction points with respect to the geometry, the energy distribution observed by each cell due to its angular size, and all pertinent uncertainties.

neutrons from $^{16}O(\gamma,n)^{15}O$ have a minimum expected time-of-flight of 15 ns (the maximum; without scattering, is 26 ns);[28] meaning that after the time-of-flight cut almost all of the neutrons left will have been produced by $d(\vec{\gamma},n)p$. The time-of-flight cut also excludes the vast majority of photons that make it past the PSD cut (section 5.4.2 on page 196) because the prompt scattered photons from the beam are excluded (they arrive at ≈ 1.5 ns).

5.4.5 Background Cut

Table 5.6: Background Cut Summary

Purpose	Subtract background radiation from detectors.
Background Interval	[-30 ns, -10 ns]
Uncertainty	$\sqrt{\text{Counts}}$

The background cut compensates for any background radiation that made it past the rest of the cuts and into the neutron yield. We integrate the number of events that occurred before the beam arrived (from -30 ns to -15 ns); which should include only background radiation, then assume the background rate is the same in the part of the time-of-flight spectrum used.

We can safely assume that the background rate is uniform so long as there is no correlation between the background rate and the beam; unfortunately, the out-of-time photons from the beam (described in section 5.3.1 on page 152) arrive periodically every 5.36 ± 0.49 ns relative to the on-time beam. We therefore had no choice but to exclude cells with out-of-time photons present.

A typical background cut for an included cell looks something like figure 5.33 on the next page.

[28] This was calculated for the long target assuming that the neutron is generated at the closest point of the target to the detector, then interacts at the closest edge of the detector using the separation energy from the National Nuclear Data Center [Son13].

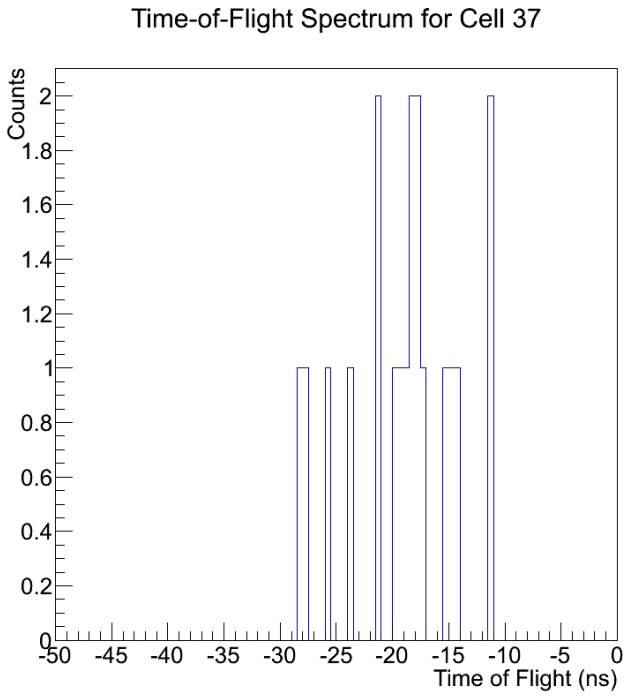

Figure 5.33: Typical Background Spectrum (run 142). A background spectrum consists of the recorded events between -30 and -15 ns (i.e. when the beam photons hit the target), this should contain only background radiation and out-of-time photons from the beam. Using eq. (5.7a), the spectrum corrects the neutron yields for background radiation.

The average background count value is taken and then scaled up to the time-of-flight interval and subtracted from the neutron yield:

$$N' = N - \frac{I}{15\ ns}B = N - I \cdot \frac{\int_{-30\ ns}^{-15\ ns} T(t)dt}{15\ ns} \tag{5.7a}$$

where: N' is the background corrected neutron yield, N is the neutron yield before correction, B is the background yield, $T(t)$ is the time-of-flight spectrum (in hits/ns), and I is the time-of-flight cut interval.

We propagate the error using the normal technique but neglecting the error in the time interval, then the error in the background counts is given by $\sqrt{B}$:

$$dN' = \sqrt{dN^2 + (\frac{I}{15\ ns} dB)^2} = \sqrt{dN^2 + (\frac{I}{15\ ns})^2 B} \tag{5.7b}$$

5.4.6 Water (H_2O) Target Correction

Table 5.7: Water Target Correction Summary

Purpose	Compensate for false-positives and neutrons from other sources.
Cut	^1H_2O data were fully analyzed then subtracted from other runs.
Uncertainty	Full estimate: treated like D_2O data.

Even after all of the cuts were performed, we still had a few false positives (photons and other non-neutron radioactive particles) and neutrons from reactions other than $d(\vec{\gamma},n)p$. As mentioned earlier, $^{16}O(\gamma,n)^{15}O$, is the primary culprit for other neutrons since it is in abundance in the target and not energetically prohibited; $^{13}C(\gamma,n)^{12}C$ is another example. Regardless of where the neutrons are from, so long as we utilize the experimental run with a light water target (run 154): we will have nearly identical conditions except that there are now almost no neutrons in the hydrogen nuclei (only those due to naturally occurring deuterium); therefore, the neutron yield of run 154 will give the best estimate of the number of false positives and neutrons from other reactions in our data.

In order to compensate for excluded cells (the H_2O run has a different cell exclusion table than the other runs), we elected to parameterize the differential cross section for neutron production by the water target and extract an effective total cross section.

The parameters are reported in section 6.3 on page 224.

The total cross section was computed following the same methodology as the D_2O data, and is reported in section 6.2 on page 218.

5.4.7 Cell Exclusions

The possible reasons for cell exclusion are: unable to calculate the gain (section 5.3.2 on page 159), unable to produce meaningful PSD separation (section 5.3.9 on page 184), TDC drift (section 5.3.8 on page 182), the cell recorded no events, or out-of-time (OOT) photons were present after all cuts were made (section 5.4.8). These phenomena are described in their respective sections.

The exclusions for all of the experimental runs analyzed are listed in appendix I on page 298, along with the reasons for their exclusion.

5.4.8 Out-of-Time Photon Exclusions

Not all cells will have a significant contribution from out-of-time photons: they are much more likely to scatter at low angles into the downstream cells (as per the Klein-Nishina equation: eq. (A.1) on page 280), and the PSD cut may or may not exclude them. A peak finding algorithm [Mor00] was applied to the background time-of-flight spectrum (i.e. $t \in [-50\text{ ns}, 0\text{ ns}]$) to look for anomalies, then it was subjected to a validation algorithm which verified the periodicity was consistent with the out-of-time photons (i.e. arriving every 5.36 ± 0.49 ns), and finally the cell was recorded and the user was asked to verify the presence of out-of-time photons in the spectrum.[29] For example, a cell which was detected as having out-of-time photons is shown in figure 5.34 on the next page.

[29] Future iterations of this algorithm could readily be made more robust and fully automated, but currently it is insufficiently accurate for full automation.

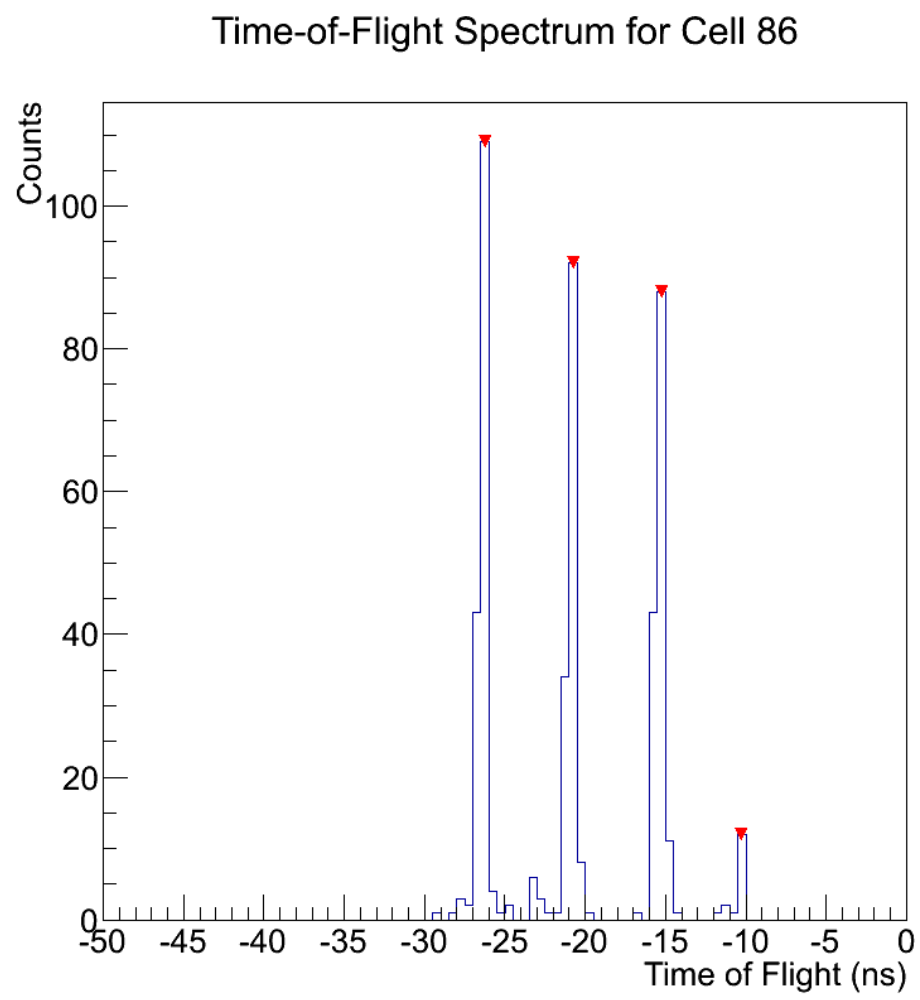

Figure 5.34: Typical Background Time-of-Flight Spectrum with Out-of-Time Photons Present (run142). This cell was excluded based on the presence of the peaks (red markers), which are believed to be out-of-time photons due to their periodicity.

Cells which were verified by the user as having out-of-time photons in them were added to the cell exclusion table and were not included in the final analysis (see section 5.4.7 on page 209 for details). If they were not excluded then it is possible that they could bypass the time-of-flight cut: by arriving at 5.6 ns or 11.2 ns (they have already bypassed the PSD cut if they are found in the background spectrum).

5.5 Total Cross Section

The total cross section is a probabilistically weighted area which represents how likely a specific interaction is to occur. We therefore need to know: the number of nuclear targets (i.e. the atomic density and target length), the number of photons available (i.e. the flux at and in the target), and the number of neutrons produced via the reaction. We had to measure: the target length, the photon flux (section 5.5.1), and the neutron yield; everything else can be taken from literature to calculate the total cross section.

5.5.1 Computing the Beam Flux

We computed the beam flux using the Five Paddle Flux Monitoring System (described in section 3.9 on page 85). The Five Paddle detector was placed into the beam-line; upstream of the target, where it 'sampled' the beam: it detects a small portion of the photons in the beam ($\approx 2\%$) and allows the rest to pass unimpeded. The accelerator keeps track of the number of electron bunches, and so we counted the number of times an electron was in position to produce a photon in the FEL (free-electron laser). Knowing how often the beam *could* produce a photon, we need only know the relative probability of it being detected in order to appropriately scale up the number of photons detected by the Five Paddle detector: this essentially comes down to accurately (and hopefully precisely) determining the efficiency of the Five Paddle detector.

By taking a few beam measurements with both the Five Paddle detector and the sodium iodide detector (both are described in section 3.9 on page 85) with varying beam intensities, we determined the relative efficiencies of the detectors, and then using a GEANT4 simulation to account for photon scattering and attenuation, we can determined the absolute efficiency of the Five Paddle detector. The GEANT4 simulation is also capable of accurately predicting the Five Paddle detector efficiency directly, however we only use it as a consistency check. Runs 145-148 were performed with varying beam intensities and the sodium iodide detector in place. The measured count rates of the sodium iodide detector and the Five Paddle detector were then plotted against each other to determine the raw calibration factor (f_m' in eq. (5.8) on the next page), this is illustrated in figure 5.35 on the next page.

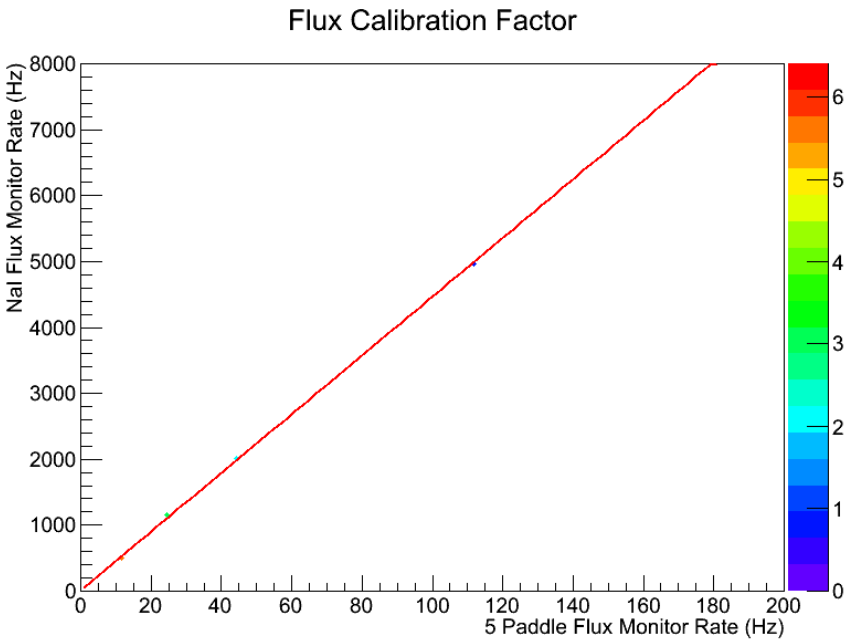

Figure 5.35: Calibrating the Five Paddle Flux Monitor. The sodium iodide detector rate is plotted versus the Five Paddle rate in order to determine the relative efficiencies.

With the raw calibration factor derived graphically using figure 5.35, simulations were run to derive two calibration factors (C_A and C_B in eq. (5.8)). The remaining variables were all measured in the lab: the live time of the experiment, and the Five Paddle measurements: the total number of events (N_m in eq. (5.8)), the total number of veto events (N_ν in eq. (5.8)), and the background event rate (B_m in eq. (5.8)). With all of these data, we can compute the beam flux at the target, N_t:

$$\begin{aligned} N_\gamma &= C_A f'_m B \ln\left(\frac{B - N_\nu}{B - N_\nu - N_m}\right) \\ \frac{N_i}{T_{live}} &= f'_m\left(\frac{N'_m}{T_{live}} - B_m\right) \\ N_t &= \frac{N_\gamma}{C_B} \end{aligned} \tag{5.8}$$

where: N_t is the number of photons at the start of the target (this is what we want), f'_m is a calibration factor extracted from figure 5.35, C_A and C_B are calibration factors extracted

via the simulation, N_i is the integrated number of counts in the sodium iodide detector, N_m is the flux monitor counts read by scaler 9, T_{live} is the live-time of the experiment, B is the number of bunches of electrons in the accelerator during the live time, B_m is the background rate of Five Paddle, and N_ν is the number of veto events measured by Five Paddle [Pyw11].

Eq. (5.8) on page 212 gives us an estimate for the number of photons incident on the target, with an uncertainty (using standard techniques). Due to the presence of out-of-time photons in the beam (section 5.3.1 on page 152), we must scale down the estimated number of photons incident on the target, because the out-of-time photons will produce neutrons that are eliminated by the time-of-flight cut. For example, if a photon arrives two periods later than expected from the beam (i.e. at 11.2 ns) then the neutrons it produces will not start to arrive until well after the time-of-flight cut (i.e. at $\approx$ 20 ns), even though they have the appropriate energy and may have not scattered: if we do not correct for this then we will have an artificially low total cross section due to rejection of valid data.

In section 5.3.1 on page 152, the technique used for estimating the ratio of out-of-time photons from the beam was described. For simplicity sake, we assume that *all* out-of-time photons which produce neutrons were excluded by the time-of-flight cut, then the out-of-time corrected beam flux is given by:

$$N_t' = R \cdot N_t \tag{5.9}$$

where the number of photons incident on the target (N_t) is corrected by the out-of-time factor ($R = \frac{\text{Number of photons on time}}{\text{Number of photons}}$), giving the corrected number of photons incident (N_t').

We use N_t' from eq. (5.9) to calculate the total cross section, following the methodology set forth in section 5.5.2 on the next page. We take the extreme conservative estimate for the error in N_t' and take it as $\delta N_t' = (1 - R)N_t$.

5.5.2 Computing the Total Cross Section

The empirical definition of the cross section is derived in section 2.4 on page 25, we rearrange eq. (2.4) on page 27 to get eq. (5.10):

$$\sigma = \frac{N_D \mu}{\rho n N_0 (1 - e^{-\mu x})} \tag{5.10}$$

where: N_D is the number of daughter particles produced by an interaction in a target of length x, N_0 is the number of incident particles, σ is the reaction cross section as defined by this equation (cm^2/atom), ρ is mass density (g/cm^3), n is the number density (atoms/g), and μ is the linear mass attenuation coefficient (cm^{-1}).

Using eq. (5.10), we calculated the cross section from the number of neutrons that we measured using eq. (5.11) on the next page: derived as follows.

The number of neutrons we measure depends on the efficiency:

$$N_d \equiv \epsilon_d N_D$$

where: N_D is the number of neutrons incident on a detector, d, ϵ_d is the detector's efficiency defined by this equation, and N_d is the number of neutrons measured by detector d. Similarly, the simulation of the detector has relation:

$$N_d^{sim} \equiv \epsilon_d^{sim} N^{sim}$$

where: N^{sim} is the number of neutrons simulated, ϵ_d^{sim} is the efficiency of the simulated detector defined by this equation, d, and N_d^{sim} is the number of neutrons measured by detector d.

We then make the key assumption that the detector and simulation efficiencies are the same. This enables us to solve eq. (5.10) on page 214 with available data:

$$\sigma = \frac{N^{sim}}{N_d^{sim}} \frac{N_d \mu}{\rho n N_0 (1 - e^{-\mu x})} \tag{5.11}$$

Note that Wurtz [Wur10c] derived a similar result, but assumed that the target was infinitesimally thin (i.e. $1 - e^{-\mu x} = \mu x$)

Note that μ in eq. (5.11) is close but not equal to the linear mass attenuation coefficient recorded in table A.2 on page 281. This is because we have different geometry than what is used to measure the mass attenuation coefficients; using the simulation, we estimated that the *effective* beam attenuation was $0.01604 \pm 0.00015\ \mathrm{cm}^{-1}$ for the long target and $0.015844 \pm 0.000096\ \mathrm{cm}^{-1}$ for the short target, this scales as an approximately 1% smaller cross section than would be estimated using the linear mass attenuation coefficient from literature.

Eq. (5.11) assumes that the experimental and simulated detector efficiencies are the same. Although this is a source of error (discussed in section 7.1 on page 246), there is a compelling argument for why it should be true. The factors involved in the efficiency are: geometry, interaction probability with the detector, light output, dead-time, and electronic efficiency. The geometry and interaction probability have been shown to be consistent in the past (see section 4.2.4 on page 110), as has the light output [Pyw06]; furthermore, our raw data spectra are perfectly consistent with the simulation (see appendix J on page 302). This leaves only the dead-time and electronic efficiency, we assert here that these are both very close to 100% efficient: the former because we simply turn off the DAQ when the detector is busy

(so the dead-time doesn't matter), and the latter because the lower light cut (described in section 5.4.3 on page 199) is well above the hardware threshold.

Thus, using eq. (5.11) on page 215 we can calculate the total cross section; the error is estimated using standard error propagation (i.e. take the differential then add errors in quadrature).

5.6 Differential Cross Section

The total cross section defines the magnitude of the deuteron photodisintegration interaction, we wish to enhance our knowledge by including the spatial distribution of the interaction: the differential cross section $\frac{d\sigma}{d\Omega}$. In section 4.4.2 on page 119 we showed that the Legendre Expansion of the differential cross section (eq. (2.20) on page 49); can be written in terms of the neutron yields $N_{d,lk}^{sim}$ from the simulation of probability density functions ρ_{lk}:

$$\begin{aligned} N_d \approx & A[(1 - \sum_{k=1}^{4} a_k - 3e_2 - 6e_3 - 10e_4 - c_1 - \frac{3}{2}c_2 - d_1 - \frac{3}{2}d_2)N_{d,00}^{sim} \\ & + \sum_{k=1}^{4} a_k N_{d,0k}^{sim} + 3e_2 N_{d,22}^{sim} + 6e_3 N_{d,23}^{sim} + 10e_4 N_{d,24}^{sim} \\ & + c_1 N_{d,11}^{sim} + \frac{3}{2}c_2 N_{d,12}^{sim} + d_1 N_{d,11'}^{sim} + \frac{3}{2}d_2 N_{d,12'}^{sim}] \end{aligned} \tag{5.12}$$

where: N_d is the neutron yield in a detector, d, and $N_{d,lk}^{sim}$ is the simulated neutron yield for the probability density function ρ_{lk}.

We simulated each probability density function, then processed the data from each simulated run in the same manner as the experimental data: with all of the same cuts; this gave us a neutron yield associated with each probability density function i.e. $N_{d,lk}^{sim}$ in eq. (5.12) for each of the 88 detectors on Blowfish (N_d, $\{d|d \in \mathbb{Z} \wedge d \in [1, 88]\}$).

With the neutron yields from the experimental and simulated data, we used the χ^2 reducing implementation of the TMinuit class in ROOT (including the Minos error estimation technique [Jam75] and a robust correlation estimator for the parameters [Rou99]) to extract

the parameters of best fit for eq. (5.12) on page 216.[30] With the Legendre polynomial coefficients extracted, and the total cross section data following the procedure in section 5.5 on page 211 we can calculate the differential cross section using eq. (2.20) on page 49.

5.6.1 Analyzing Power

Using the Legendre expansion of the differential cross section; and the parameters extracted as delineated in section 5.6 on page 216, we can compute the analyzing power:[31] an observable which depends only on the polar angle (θ), but is sensitive to variations in the polarization (i.e. the e parameters). Recall that the analyzing power is:

$$\Sigma(\theta) \equiv \frac{1}{\Sigma^l} \frac{\frac{d\sigma}{d\Omega}(\theta, \phi = 0^\circ) - \frac{d\sigma}{d\Omega}(\theta, \phi = 90^\circ)}{\frac{d\sigma}{d\Omega}(\theta, \phi = 0^\circ) + \frac{d\sigma}{d\Omega}(\theta, \phi = 90^\circ)} \tag{5.13a}$$

$$= \frac{1}{\Sigma^l} \frac{\sum_{k=2} e_k P_k^2(\cos\theta)}{\sum_{k=1} a_k P_k^0(\cos\theta)} \tag{5.13b}$$

where: $\frac{d\sigma}{d\Omega}$ is the differential cross section, Σ^l is probability of an incident photon being horizontal polarized, the a_k and e_k are the extracted parameters from the Legendre expansion, and P_k^i are the associated Legendre polynomials. Note: the polarization would normally cancel in the second expression, but recall that we defined the e parameters such that they incorporated the polarization.

[30] We also used the log-likelihood reducing algorithm: it produced the same result.

[31] The analyzing power is also known as the photon asymmetry.

Chapter 6

Results and Discussion

6.1 Introduction

In this chapter we present and discuss the fully processed data: the total cross section (section 6.2), the values for the parameters of the Legendre expansion of the differential cross section (section 6.3 on page 224) and the subsequently calculated observables (section 6.3.1 on page 235).

We used our results to perform several consistency checks on the simulation, these are described in appendix J on page 302.

6.2 Total Cross Section

Using the procedure in section 5.5 on page 211, we computed the total cross section for each run using the total neutron yield from Blowfish and the number of incident photons from the Five Paddle Flux Monitor (section 3.9); the results are given in: table 6.1 on the next page, table 6.2 on page 220, and figure 6.1 on page 221.

Run	Target	Cross Section (μbarns)
142	10.7 cm	661 ± 51
143	10.7 cm	670^{+59}_{-60}
149	10.7 cm	644^{+51}_{-54}
150	10.7 cm	644 ± 48
152	10.7 cm	649^{+55}_{-57}
153	10.7 cm	667^{+62}_{-64}
154	10.7 cm (H_2O)	11^{+10}_{-9}
155	2.0 cm	636^{+87}_{-85}
157	2.0 cm	650^{+57}_{-58}
158	2.0 cm	657^{+62}_{-58}
159	2.0 cm	646^{+77}_{-72}

Table 6.1: Run-by-Run Total Cross Section Data. These data have not had the water target correction applied (i.e. the values include the contribution by the H_2O target: 11^{+10}_{-9} μbarns).

Average	Cross Section (μbarns)
Long Target	$643 \pm 55(25)$
Short Target	$638 \pm 71(36)$
Total	$643 \pm 62(21)$
Theory	685.14
Skopik *et al.* [Sko74]	640 ± 31
Ahrens *et al.* [Ahr74]	672 ± 61 (interpolated)
Bernabei *et al.* [Ber86]	689 ± 69 (interpolated)
Michel *et al.* [Mic89]	693 ± 32 (interpolated)
DeGraeve *et al.* [DGr91]	716 ± 22
Weighted Average*	690 ± 15

Table 6.2: Averaged Total Cross Section Data. The experimental averages are reported for the long target, short target, and both; after the water target correction has been applied. Our data are reported with uncertainties, $\Delta\sigma$ estimated by assuming the error for each run are entirely systematic ($\Delta\bar{\sigma} = \frac{1}{N}\sum_{i=1}^{N}\Delta\sigma_i$); parenthesis: uncertainty if the run errors are entirely random ($\Delta\bar{\sigma} = \frac{1}{\sqrt{\sum_{i=1}^{N}\Delta\sigma_i^{-2}}}$). *Weighted Average: weighted average of Skopik *et al.*, Ahrens *et al.*, Bernabei *et al.*, Michel *et al.*, and Degraeve *et al.*

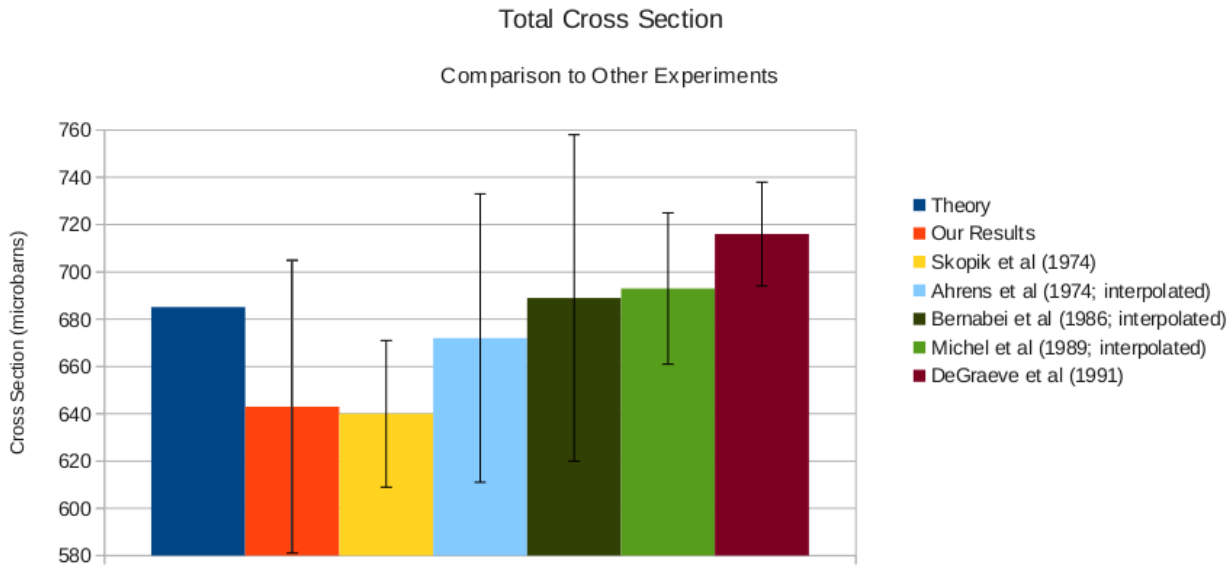

Figure 6.1: Total Cross Section. Our experimental results compared to the theoretical prediction, and the results of previous experiments. Our results agree with theory and previous experiments: within error.

Our results agree with theory and previous experimental values if we take a conservative estimate of our systematic error, and they agree with *most* experiments with a cavalier estimate of our systematic error; but the cross section is lower than expected by $\approx 7\%$. This implies that we may have had a systematic error present in all of the experimental runs, for example: the radius of Blowfish (40.64 ± 0.30 cm) was set once, and it is highly unlikely that it changed: if it was set to be too large by the uncertainty value then our cross section would be lower by a factor of the surface area ratios (0.985[1]); the possible sources of such a systematic error are discussed in detail in section 7.1 on page 246.

As a consistency check on our values, we also computed the cross sections by: assuming that Blowfish acts as one large detector, and by using the overall scaling parameter from the Legendre expansion of the neutron yield (eq. (6.2) on page 224). All methodologies agree on the reported values.

[1]This propagates into a cross section which is $\frac{S_r}{S_{r+dr}} = (\frac{r}{r+dr})^2 = 0.985$ smaller than reality i.e. our cross section would really be 653 μbarns.

In order to determine the total cross section, we had to assume that the simulated efficiencies are equal to the experimental efficiencies for Blowfish. In section 5.3.2 on page 161 we discussed how we forced the ADC spectra to agree between the simulation and experiment by scaling the calibrated ADC values. There was a lingering question of the agreement between simulated and experimental TDC spectra, though, (discussed in detail in section 5.3.6 on page 176) and if they do not agree then the time-of-flight cut will cause the simulated and experimental efficiencies to differ. Therefore we verified that the time-of-flight cut was not changing the outcome of the experimental cross section data by drastically altering it: it doesn't, it only improves the precision (figure 6.2 and accompanying table 6.3 on the next page).

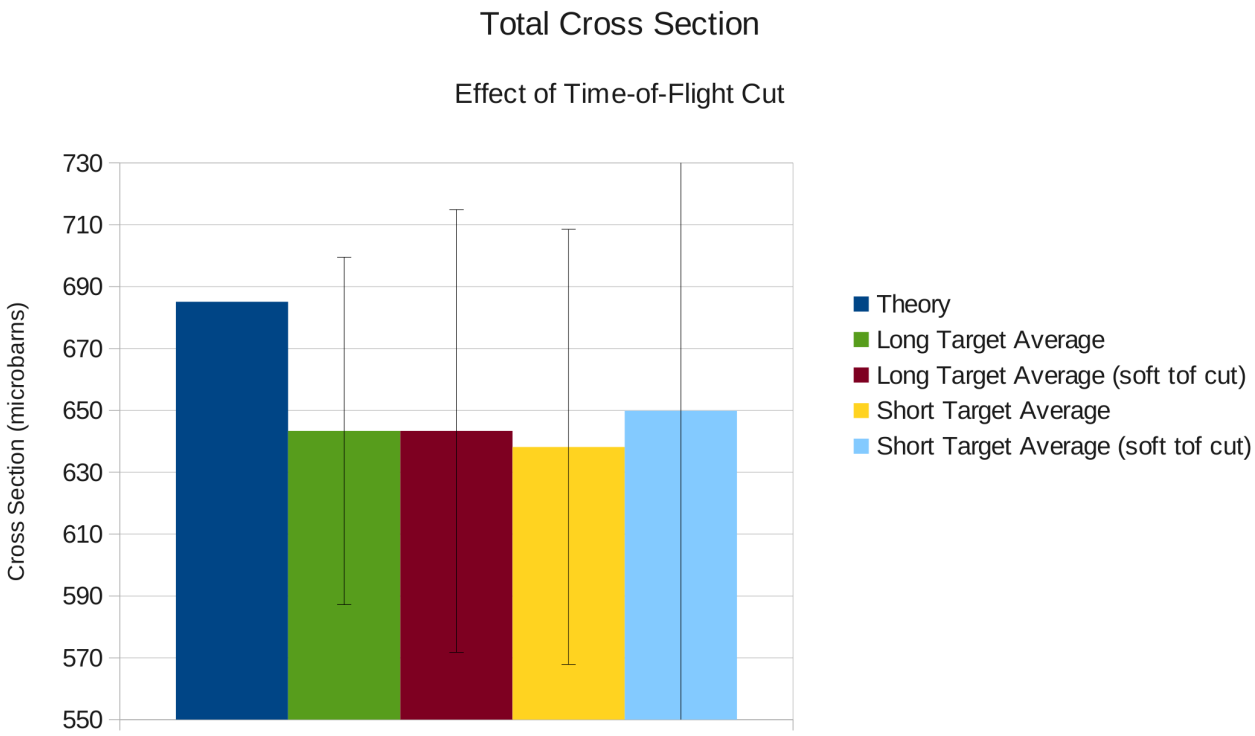

Figure 6.2: Total Cross Section with Varied Time-of-Flight Cut. Notice that all data agree very well with each other, and the theory. The time-of-flight cut is working perfectly: it doesn't change the cross section meaningfully, but it does reduce the uncertainty. Soft TOF cut: 5-50 ns.

Average	Cross Section (μbarns)
Theory	685.14
Long Target	643 ± 55
Long Target (soft)	643 ± 72
Short Target	638 ± 71
Short Target (soft)	650 ± 150

Table 6.3: Total Cross Section with Varied Time-of-Flight Cut. Soft TOF cut: 5-50 ns.

6.2.1 Discussion of Cross Section Data

Our results agree with other researchers and theory, within error, although our results are systematically lower than the weighted average of other researchers by approximately 7% (47 μbarns).

Our results agree especially well with Skopik *et al.* [Sko74], but their results depended on a model-derived photon flux, and the subsequent model-independent results of Ahrens *et al.* [Ahr74] showed that Skopik *et al.*'s results were systematically high at 20 and 25 MeV, implying there may have been problems with Skopik *et al.*'s photon flux model, and we therefore must infer that the similarity between our results and Skopik *et al.*'s could be merely a coincidence.

Our total cross sections agree after all reasonable consistency checks are made: changing the time-of-flight cut, comparing the short and long targets, and changing the methodology for computing the cross section. Our results are self consistent.

We conclude that our results are consistent with theory and other researchers, and that our experiment may have had an appropriately quantified systematic uncertainty during all of the runs which caused our results to be lower than expected. This is supported by the observed 'over-fit' of the experimental parameterization: $\langle \chi^2_{red} \rangle = 1$ [Tay97], yet our fit yields $\chi^2_{red} = 0.31$; consistent with the presence of significant systematic error in our data. Two possible systematic uncertainties which contributed are the beam energy and the radius of Blowfish, together these could contribute to the cross section being an estimated 25 μbarns

lower than expected (see section 7.1 on page 246 for details).

6.3 Legendre Parameterization of the Differential Cross Section

Recall from section 2.5.4 on page 44 that the differential cross section can be expanded in terms of the associated Legendre polynomials [Cam82, Kuc10]:

$$\begin{aligned}\frac{d\sigma}{d\Omega} \approx & \frac{\sigma}{4\pi}\left[1+\sum_{k=1}^{4} a_k P_k^0(\cos\theta)+\sum_{k=2}^{4} e_k P_k^2(\cos\theta)\cos 2\phi\right. \\ & \left.+\sum_{k=1}^{2} c_k P_k^1(\cos\theta)\cos\phi+\sum_{k=1}^{2} d_k P_k^1(\cos\theta)\sin\phi\right] \end{aligned} \tag{6.1}$$

where: P_k^i are the associated Legendre polynomials, the a_k, and the e_k are theoretical parameters, and the c_k and the d_k are parameters used to verify the target alignment, and σ is the total cross section.

The theoretical parameterization was extracted directly from the theoretical calculations using eq. (6.1), while the experimental parameterization was extracted by mapping the Legendre expansion into a simulated neutron yield (described in section 4.4.2 on page 119):

$$\begin{aligned} N_d \approx & A[(1-\sum_{k=1}^{4} a_k - 3e_2 - 6e_3 - 10e_4 - c_1 - \frac{3}{2}c_2 - d_1 - \frac{3}{2}d_2)N_{d,00}^{sim} \\ & + \sum_{k=1}^{4} a_k N_{d,0k}^{sim} + 3e_2 N_{d,22}^{sim} + 6e_3 N_{d,23}^{sim} + 10e_4 N_{d,24}^{sim} \\ & + c_1 N_{d,11}^{sim} + \frac{3}{2}c_2 N_{d,12}^{sim} + d_1 N_{d,11'}^{sim} + \frac{3}{2}d_2 N_{d,12'}^{sim}] \end{aligned} \tag{6.2}$$

where: N_d is the neutron yield in a detector, d, of Blowfish, N_{ik}^{sim} are the simulated neutron yields associated with the P_k^i associated Legendre polynomial, the a_k, e_k, c_k and d_k parameters are the same as in eq. (6.1), and A is a fit parameter proportional to the efficiencies and the total cross section.

Following the procedure in section 5.6 on page 216, we extracted parameters for each

of the experimental runs; including the H_2O target run, using eq. (6.2) on page 224. We verified the fit results from ROOT with a simple χ^2 reducing algorithm, as well as via the log-likelihood minimization implementation of TMinuit (ROOT), and found that they all agreed on the parameter values within error. The runs were scaled by their respective value of A in eq. (6.2) on page 224, and then averaged together giving two average neutron yields: one for the long target, and one for the short target.[2] The scaled average neutron yield is given in figure 6.3 on the next page along with: its parameterization using the simulated Legendre probability density functions (PDFs), and the theoretical parameters expressed using the simulated Legendre PDFs. We see good agreement between the neutron yields and both the extracted parameterization ($\chi^2_{red} = 0.31$) and the theoretical parameterization ($\chi^2_{red} = 0.74$).

[2]The long and short target have different geometries and therefore required different simulations, thus it would be frivolous to average their yields together: only their parameters are worth comparing.

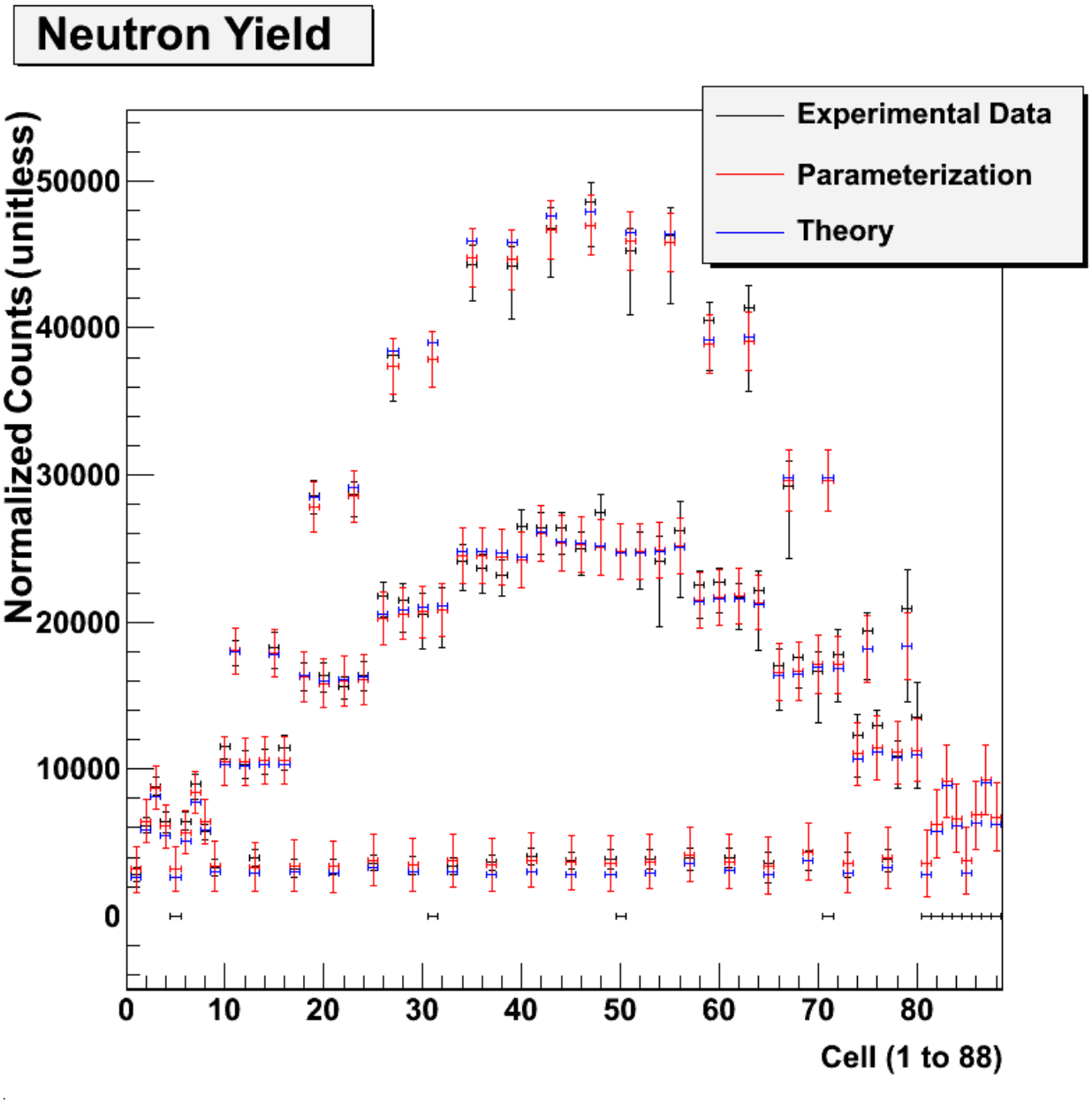

Figure 6.3: Parameterized Neutron Yield for Long Target Average. We see good agreement between the neutron yields and both: the extracted parameterization ($\chi^2_{red} = 0.31$), and the theoretical parameterization ($\chi^2_{red} = 0.74$). The agreement between the theoretical and extracted parameterizations is excellent: every theoretical prediction is within the error interval of the respective parameterized prediction, and is typically very close to the median value. Note: Excluded cells are set to -1. 76 of the 88 cells were used.

The long target runs provided the largest yields, and so they gave the most precise set of parameters; while the short target parameters serve as a test for target length dependence. The parameters for the long and short target averages are given in table 6.4 along with the theoretical parameters from Schwamb and Arenhövel [Sch01c, Sch01a, Sch01b].

Parameter	Long Target Value	Short Target Value	Theory
a_1	-0.149 ± 0.020	-0.123 ± 0.043	-0.157
a_2	-0.861 ± 0.030	-0.840 ± 0.070	-0.897
a_3	0.120 ± 0.038	0.129 ± 0.071	0.146
a_4	0.010 ± 0.033	-0.032 ± 0.055	-0.015
e_2	0.4296 ± 0.0043	0.4224 ± 0.0081	0.45
e_3	-0.0226 ± 0.0029	-0.0184 ± 0.0047	-0.024
e_4	-0.0005 ± 0.0024	-0.0027 ± 0.0033	0.0014

Table 6.4: Legendre Expansion Parameters. The theoretical parameterization is accurate to $<$ 1%. Note: we assume the horizontal polarization is perfect, otherwise our e parameters must be divided by the linear polarization ratio. We report the first column (long target) parameters as our best parameters. Note: we report the symmetric error, as the non-parabolic error is very close (table 6.6 on page 232).

The theoretical calculations for the photon asymmetry (i.e. analyzing power) and differential cross section performed by Schwamb and Arenhövel (discussed in section 2.5.3 on page 34) were used to extract the theoretical parameters in table 6.4 via a simple χ^2 reducing algorithm. The theoretical parameterization agrees with the theoretical calculations to well within 1% at all data points for the analyzing power and differential cross section; figure 6.4 on the next page shows the quality of the theoretical parameterization.

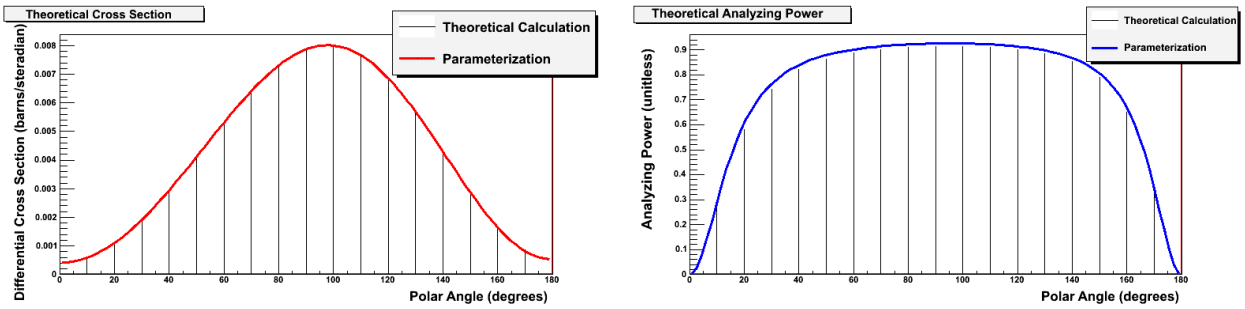

Figure 6.4: Parameterized Theoretical Predictions of the full Schwamb and Arenhövel calculation. Left: the differential cross section averaged over ϕ. Right: the analyzing power (a.k.a the photon asymmetry). All data points agree with the parameterization to $< 1\%$.

The individual contributions to the theoretical calculation from: meson exchange currents, Δ baryon degrees of freedom, and relativistic corrections, showed too small of a difference in their predictions to resolve any meaningful discrepancies given the level of precision of our experimental data. Therefore, only the full calculation from Schwamb and Arenhövel has been included here.

Neglecting the parameter errors in the theoretical values, we see that the short and long targets agree with each other's parameterizations but not with the theoretical one: figure 6.5 on the next page and figure 6.6 on page 230. Our best parameters (the long target ones) agree with the theoretical parameters within 2σ 86% of the time, and agree within 1σ 57% of the time: therefore, a case can be made that the discrepancy we see between theory and experiment *could* be purely statistical.

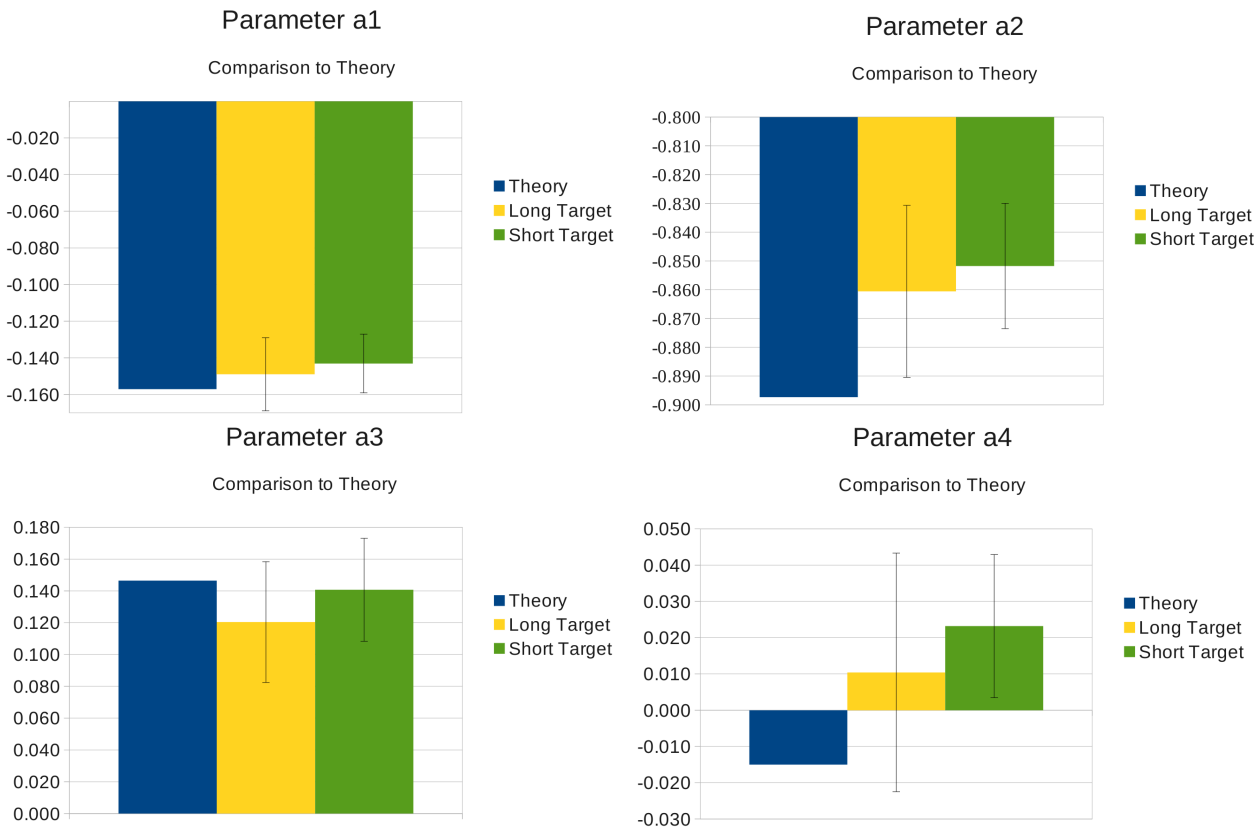

Figure 6.5: Comparison of the Extracted a_k Parameters. The long and short target parameters agree very well, but the agreement with theory is dubious (at least for a_2 and a_4). Note that the a_2 plot has a suppressed zero.

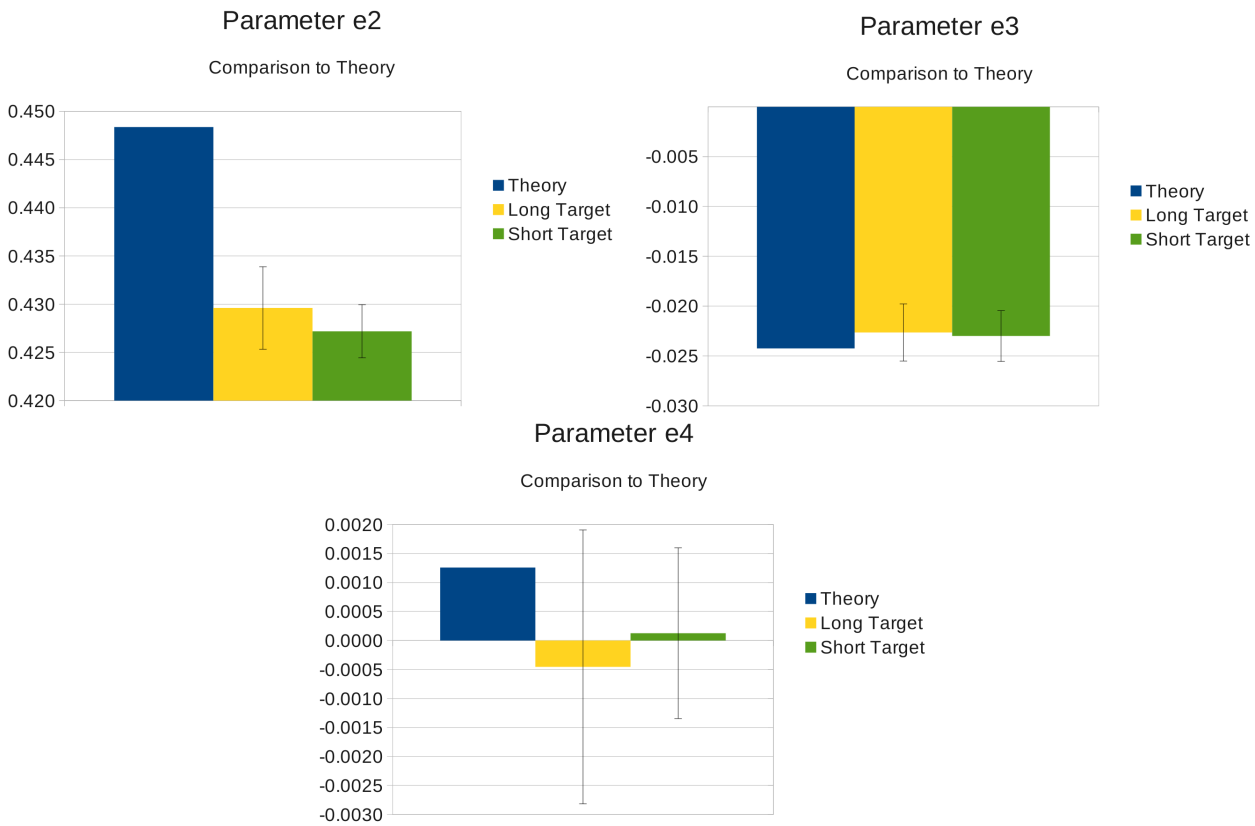

Figure 6.6: Comparison of the Extracted e_k Parameters. The long target parameters agree very well with the short target parameters, but not with the theoretical parameters (except e_3). Note that the e_2 plot has a suppressed zero.

Although the associated Legendre polynomials are orthonormal, the simulated neutron yields for the respective probability density functions clearly are not: there are strong correlations between many of the parameters, allowing them to compensate for one-another. This is most likely due to finite sampling of the Legendre polynomials, rather than an artifact of the mapping into a neutron yield because we verified that the simulated neutron yields preserve the parameterization when simulated (appendix J on page 302).

Some of these correlations may have a physical origin (see eq. (2.19) on page 48 for the theoretically predicted correlations), namely the even parameters with each other and the odd parameters with each other: for example the a_1 and a_3 parameters are approximately equal in magnitude (opposite in sign) given a basic assumption about the photodisintegration process (i.e. no splitting [Bla07]); others are unlikely to be, namely the even parameters are

unlikely to be strongly correlated to the odd parameters. It is unclear whether the fitting procedure was able to find these physical correlations in the data or if the correlations are purely due to a poor fit. The robust correlation matrix is given in table 6.5: where outliers have been automatically excluded via Rousseeuw *et al.*'s [Rou99] algorithm.

Parameter	a_1	a_2	a_3	a_4	e_2	e_3	e_4
a_1	1	0.65	0.30	0.40	−0.36	0.41	0.19
a_2	0.65	1	0.72	0.60	−0.61	−0.12	0.38
a_3	0.30	0.72	1	0.67	−0.46	−0.52	0.59
a_4	0.40	0.60	0.67	1	−0.40	−0.19	0.39
e_2	−0.36	−0.61	−0.46	−0.40	1	0.18	−0.24
e_3	0.41	−0.12	−0.52	−0.19	0.18	1	−0.23
e_4	0.19	0.38	0.59	0.39	−0.24	−0.23	1

Table 6.5: Correlation of Fit Parameters (long target average). After fitting the neutron yields to eq. (6.2) on page 224, the correlation matrix was calculated for the extracted parameters. Noteworthy correlations: the a parameters are all correlated strongly to one another, and a_2 and e_2 are strongly correlated (they're the dominant parameters in the expansion). Theory predicts correlations between even/even and odd/odd but not even/odd parameter pairs.

Given the correlations in table 6.5 it was necessary to use the Minos error estimation technique: which includes the contribution of parameter correlations to the uncertainty in each parameter [Jam94]. The full parameter errors are given in table 6.6 on the next page: clearly the symmetric uncertainties are very good approximations for the asymmetric ones.

Parameter	Experimental Value	Symmetric Uncertainty	Upper Uncertainty	Lower Uncertainty
a_1	-0.149	± 0.020	$+0.020$	-0.020
a_2	-0.861	± 0.030	$+0.030$	-0.031
a_3	0.120	± 0.038	$+0.039$	-0.038
a_4	0.010	± 0.033	$+0.033$	-0.033
e_2	0.4296	± 0.0043	$+0.0043$	-0.0043
e_3	-0.0226	± 0.0029	$+0.0029$	-0.0029
e_4	-0.0005	± 0.0024	$+0.0024$	-0.0023

Table 6.6: Full Errors for Parameterization (long target average). The parabolic (symmetric) uncertainties are an excellent approximation for the asymmetric uncertainties (lower and upper uncertainties).

The additional c and d parameters included in the Legendre expansion in order to verify target alignment were found to be less than their respective errors, and we therefore conclude that there was no problem with the target alignment (table 6.7); these parameters were excluded from the final fit (i.e. table 6.4 on page 227).

Parameter	Value
c_1	0.01468 ± 0.02166
c_2	0.00086 ± 0.01340
d_1	-0.00091 ± 0.00936
d_2	-0.00618 ± 0.00694

Table 6.7: Additional Parameters from fit to average (long target). All values are 0 within error.

All of the reported parameters include a neutron background subtraction (i.e. water target correction) to remove neutrons from other sources, as described in section 5.4.6 on page 208. The result of the light water target parameterization is given in table 6.8 on the next page.

Parameter	Value
$A(4\pi) = \sigma_{eff}$	$11 \pm 10\mu$barns
a_1	0.17 ± 0.48
a_2	-0.07 ± 0.63
a_3	0.19 ± 0.60
a_4	0.04 ± 0.48
e_2	0.18 ± 0.065
e_3	-0.007 ± 0.034
e_4	-0.016 ± 0.022

Table 6.8: Light Water Target Parameters (long target).

The fit to the light water target (run 154) neutron yield is shown in figure 6.7 on the next page. The parameterization was performed instead of subtracting the light water target yield directly because there was only one H_2O target run and most of the cells in that run had to be excluded.

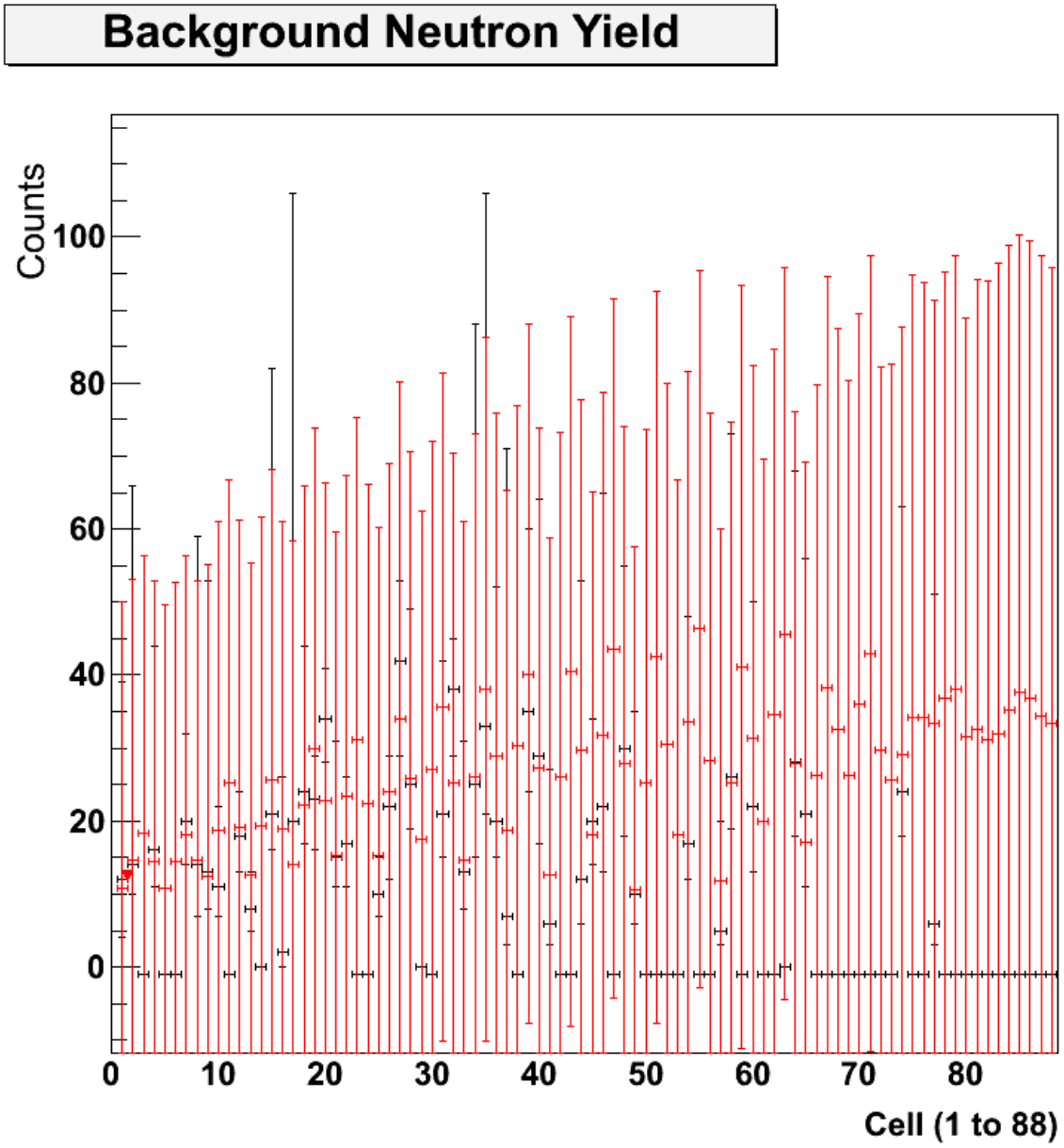

Figure 6.7: Light Water Target Neutron Yield. The H_2O target neutron yield (black) was parameterized (red) so that it could be subtracted from the D_2O data. The fit is poor because there are many missing cells and the yield is small.

6.3.1 Observables

Using the Legendre parameterizations from section 6.3 on page 224 we calculated the experimental observables: the cross section and the analyzing power, for both the experimental and theoretical parameterizations. All of the experimental observables in this section use the long target parameters from table 6.4 on page 227; the theoretical observables were calculated using the theoretical parameters from table 6.4 on page 227 and were scaled, where appropriate, by the experimental cross section from section 6.2 on page 218.

We start by considering the differential cross section projected into one dimension by averaging over the azimuthal angle (ϕ): figure 6.8; this is equivalent to the unpolarized cross section and depends only on the a_k parameters.

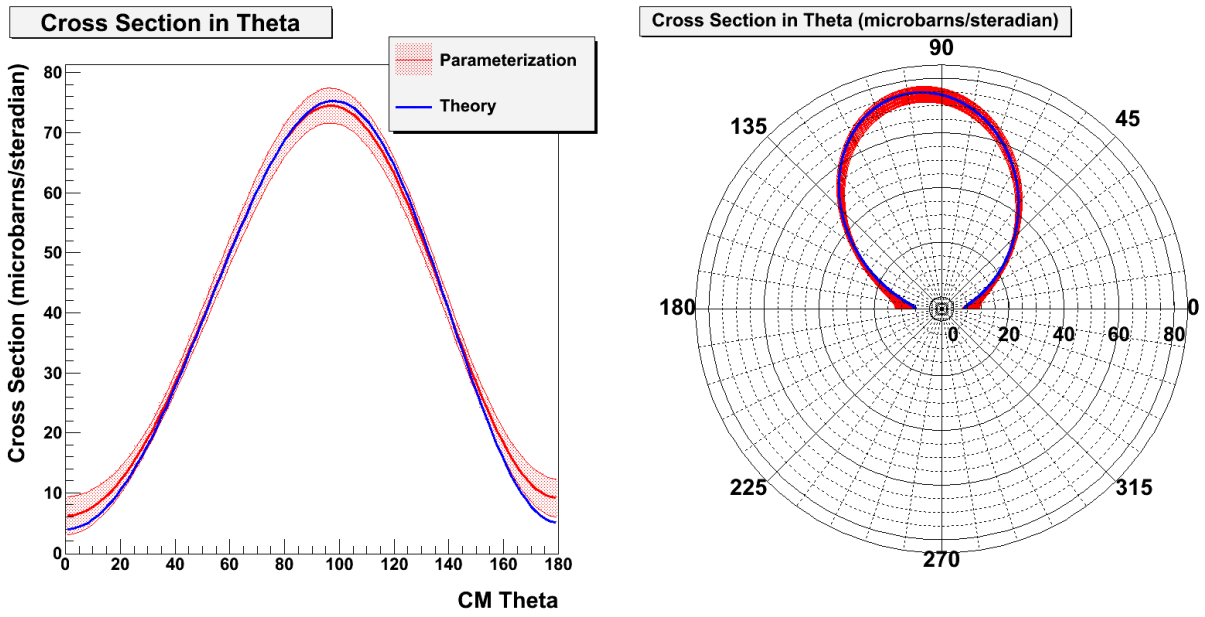

Figure 6.8: Differential Cross Section vs θ in the CM Frame. The differential cross section has been averaged over ϕ. The theoretical (blue) and experimental (red) results agree, except for possibly near the backwards most angle (near $\theta = 180°$). Theory has been scaled to the experimental results. Left image: Cartesian coordinates. Right image: polar coordinates: angle is theta (in degrees), and the radius is cross section (in microbarns). The legend is the same for both images.

We see excellent agreement between our results and the theoretical calculation for the

unpolarized cross section in figure 6.8 on page 235, except at the backwards-most angles where we find the theory is slightly lower than our measurement.

We have also computed some ratios shown to be of interest at lower energies (i.e. $E_\gamma <$ 10 MeV) by previous researchers [Bir88, Ste87, Saw05], the unpolarized (i.e. ϕ-averaged) cross section ratios at: 45°/90°, 135°/90°, and 155°/90° are given in table 6.9, and compared to previous researcher's results in figure 6.9 on the next page.[3]

Ratio	Our Results	Theory
$\frac{\sigma(45^\circ)}{\sigma(90^\circ)}$	0.470 ± 0.029	0.460
$\frac{\sigma(135^\circ)}{\sigma(90^\circ)}$	0.631 ± 0.037	0.639
$\frac{\sigma(155^\circ)}{\sigma(90^\circ)}$	0.304 ± 0.030	0.281

Table 6.9: Ratio of Cross Section at Select Lab Polar Angles (θ). Our results agree with the theoretical predictions, as expected from figure 6.8 on page 235.

[3]We cannot directly compare these ratios using the neutron yields because of Blowfish's geometry, and so we had to use the parameterization to calculate these ratios.

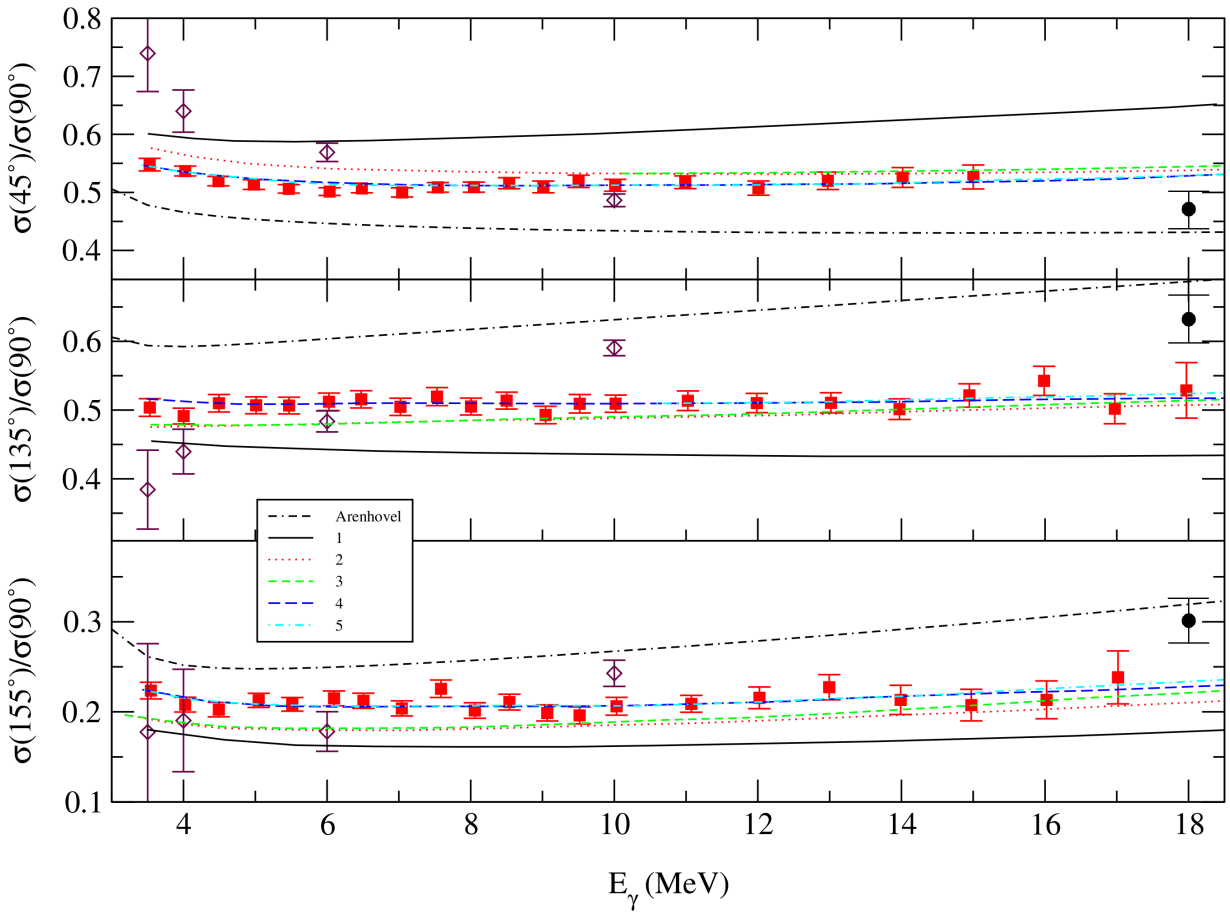

Figure 6.9: Ratio of Cross Section at Selected Neutron Lab Angles for Energy in Range 3-18 MeV. Closed circles: present work, open diamonds: Sawatzky [Saw05], solid squares: Stephenson *et al.* [Ste87], the numbered lines are calculations performed by Hadjimichael *et al.* [Had87], and the dotted line labeled Arenhövel is an old calculation by Arenhövel *et al.* [Are00]. Our results clearly disagree with the predictions of Hadjimichael, and agree reasonably well with Arenhövel's old calculation. The discrepancy between our data and Stephenson *et al.*'s is likely due to their unaccounted for beam polarization.

The next observable we consider is the differential cross section averaged over the polar angle (θ): figure 6.10 on the next page. The θ-averaged cross section depends on the even parameters: a_2, a_4, e_2, and e_4.

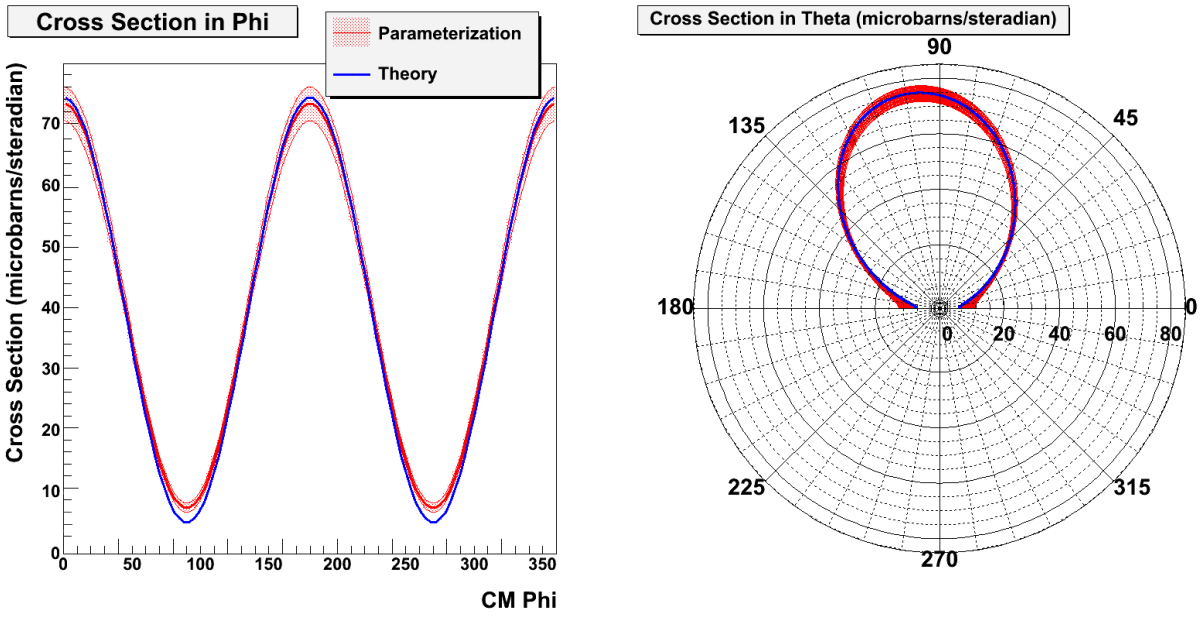

Figure 6.10: Differential Cross Section vs ϕ in the CM Frame. The differential cross section has been averaged over θ (polar angle). We see agreement between theory (blue) and our results (red) except near $\phi = 90°$ and 270°, where the theory underestimates the cross section. Theory has been scaled to the experimental results. Left image: Cartesian coordinates. Right images: polar coordinates: angle is ϕ in degrees, and the radius is cross section in microbarns. The legend is the same in both images.

Figure 6.10 shows that our results agree well with theory, except near 90° and 270° (i.e. in the vertical plane) where the theory is lower than our measurement.

Next we provide a visual representation of the experimental cross section in the center-of-momentum/mass frame: figure 6.11 on the next page (theory is not included in these plots).

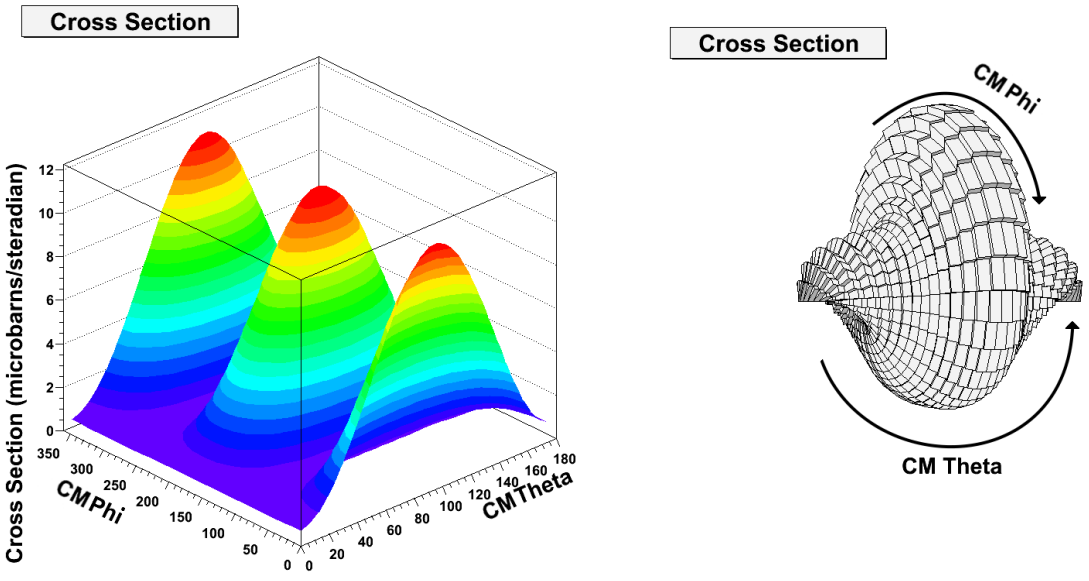

Figure 6.11: Cross Section in 3 Dimensional Plot. Left image: Cartesian coordinates. Right image: polar coordinates: θ (polar angle) starts at the left end ($\theta \in [0, \pi]$) and ϕ (azimuthal angle) starts at the horizontal position directly into the page ($\phi \in [0, 2\pi)$).

Finally, we compare the analyzing power in figure 6.12 on the next page (defined by eq. (5.13) on page 217), where we see the largest discrepancy between our results and theory.

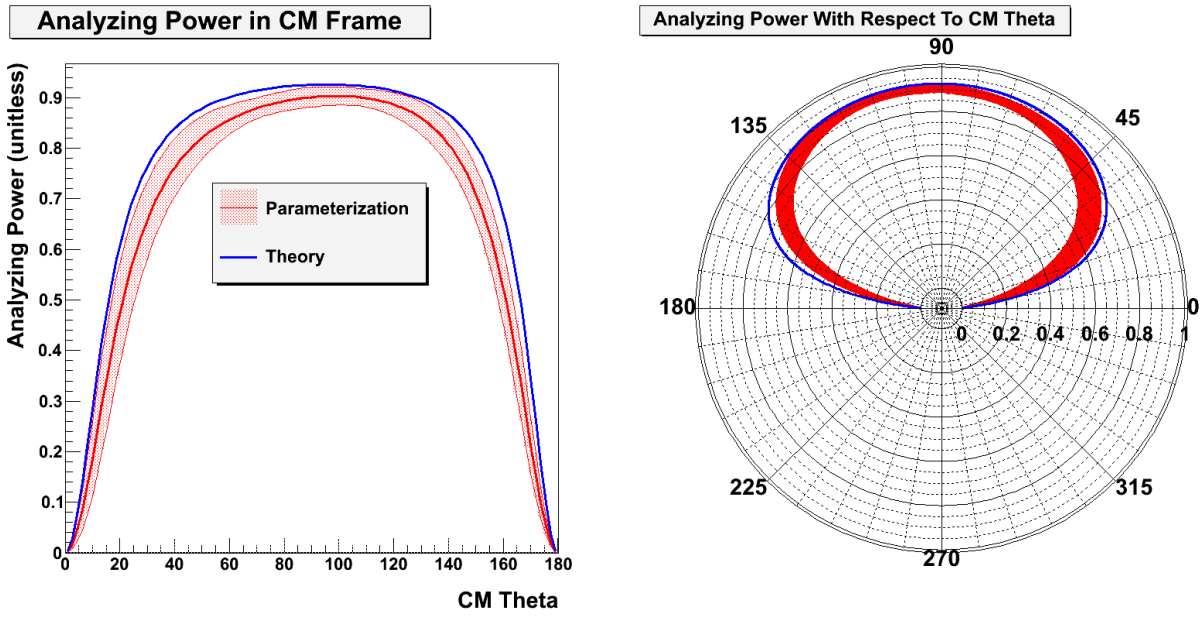

Figure 6.12: Analyzing Power. We see that our results (red) are systematically lower than the theoretical prediction (blue). Left image: Cartesian coordinates. Right image: polar coordinates: the angle is θ in degrees, and the radius is analyzing power (unitless). The legend is the same in both images.

The analyzing power is highly sensitive to correlations in the a and e parameters because it is proportional to the ratio of the sum of the e parameters over the sum of the a parameters. The fact that theory over-estimates the analyzing power relative to our results is a manifestation of the disagreement between the theoretical and experimental parameters seen in section 6.3 on page 224.

6.3.2 Discussion of Parameterization and Descendant Observables

It is clear from section 6.3 on page 224 that we must make a distinction between our experimental *data* i.e. the neutron yields for each detector, and our *parameterized* results i.e. the Legendre parameterization and the subsequent observables calculated using it (i.e. all of the ones in section 6.3.1). The predicted neutron yield in our detectors by both the experimental parameterization ($\chi^2_{red} = 0.31$) and the theoretical one ($\chi^2_{red} = 0.74$) agree with the actual neutron yield, and; perplexingly, the parameterized neutron yield agrees *perfectly* with the

theoretically predicted neutron yield (see figure 6.3 on page 226): despite the fact that the actual parameters themselves don't agree perfectly. If our *data* agree with the theoretical prediction but our *interpolation* does not then our interpolation may be inaccurate; any discrepancies between theoretical and parameterized observables would then be solely due to the limitations of the fit.

The discrepancy with the theoretical parameterization can be rectified by considering the correlation between the a_2 and e_2 parameters: e_2 is smaller than theory and a_2 is larger than theory, and the two are correlated by a factor of -0.61; which explains why the theoretical parameterization and analyzing power do not agree: a_2 and e_2 are compensating for each other (a_2 and e_2 are the dominant parameters). Blackston [Bla07] performed a full transition matrix element analysis and showed that the calculation by Schwamb and Arenhövel [Sch01c, Sch01a, Sch01b] greatly over-estimates the M1 contribution at 14 and 16 MeV, assuming that splitting of the partial waves occured. Using eq. (2.19) on page 48 we can see that theoretically:

$$|a_2| \propto |\mathcal{E}1|^2 + |\mathcal{M}1|^2 + \text{higher order terms}$$
$$|e_2| \propto |\mathcal{E}1|^2 - |\mathcal{M}1|^2 + \text{higher order terms}$$

thus the E1 amplitude is the dominant contribution to the correlation between the a_2 and e_2 parameters, with the M1 amplitude being the dominant contribution to any differences between the two (Blackston shows that the next term, E2, is $\approx \frac{1}{10}^{\text{th}}$ the magnitude of M1 at 18 MeV). If the theoretical E1 amplitude was too large then both the a_2 and e_2 parameters predicted would be too large: this is what we observed in our data. Blackston, however, demonstrated that Schwamb and Arenhövel's E1 transition amplitude agreed well with their results at 14 and 16 MeV, contrary to this interpretation. There is another major problem with this interpretation: there is no explanation for why some parameters which are not expected to be physically correlated (i.e. even/odd pairs) are strongly correlated according to the fitting algorithm (e.g. a_1 and a_2).

Due to the seemingly ubiquitous correlations in the parameters (every single parameter is correlated to a different parameter to a correlation of > 0.5) we cannot fairly pairwise

compare how one parameter could compensate for another and thus rectify the discrepancy with theory. Instead we can use the correlation matrix as evidence that the parameters *could* be compensating for one another sufficiently to cause the discrepancy. Since the Minos error technique includes an estimate of the parameter correlations in the errors it reports [Jam94], we can use a statistical argument that the theory could agree with the parameterization within error.

Our best parameters (the long target ones in table 6.4 on page 227) agree with the theoretical parameters within 2σ 86% of the time, and agree within 1σ 57% of the time: if the estimated parameter uncertainties were exactly 1 standard deviation then we would expect agreement within 1σ 68.3% of the time and agreement within 2σ 95.5% of the time: this is close to the observed agreement frequency. It is possible, then, that our parameterization of the experimental data only disagrees with theory because the minimization procedure found a different minimum than the theoretical parameters due to parameter correlations, then the fitter correctly estimated that the extracted parameters could be equivalent to the theoretical ones. It is unclear why an incorrect parameterization gave the better minimum (fit: $\chi^2_{red} = 0.31$; theory: $\chi^2_{red} = 0.74$), but it seems reasonable that *this could be a consequence of a systematic error in the neutron yields* (consistent with what was observed with the total cross section).

Correlations between the Legendre parameters should not exist mathematically because the terms in the Legendre expansion are orthogonal; however, we could not fit our experimental data directly to the Legendre expansion: we mapped it into a finite data set (of neutron yields) via the GEANT4 simulation. This process is the only reasonable source of a non-physical correlation. The χ^2 value of the parameterization we extract depends only on: the number of data points, the expected neutron yields, observed neutron yields, and the uncertainties in each of these: therefore, we can reduce the correlations between parameters by: (1) increasing the number of cells on Blowfish (increasing the polar; θ, coverage at the same time would help reduce spatial bias, such as by making the downstream-most cells usable), or (2) improving our uncertainty estimates i.e. decrease the error estimates of accurate cells and increase the error estimates of inaccurate cells.

Increasing the number of cells in Blowfish would require a major overhaul,[4] but improving the error estimates in future experiments is readily achievable and desirable on its own merit. The pulse-shape discrimination (PSD) methodology is by far the largest source of error (see section 7.1 on page 246), and its uncertainties are larger than possible due to poor statistics: we can improve the accuracy of this in future experiments by taking longer PSD source runs (e.g. americium-beryllium). Reducing the PSD uncertainty may: increase the relative uncertainty in inaccurate cells as other sources of error contribute a larger portion to the uncertainty, and decrease the relative uncertainty in the accurate cells via the converse; this will allow the accurate cells to weigh more heavily on the χ^2 value, which should make the absolute minimum χ^2 value more distinct, which will reduce parameter cross correlations.

In spite of the issues with the Legendre expansion, we can always compare the expected theoretical neutron yields directly to the measured neutron yields: this is the most rigorous method of comparing our results to theory (because it is immune to issues with the experimental parameterization).

The data do hint that there may be a discrepancy with the theoretically predicted cross section at small polar angles, θ: this can be seen by the systematic underestimated neutron yield prediction for the last ring in figure 6.3 on page 226. This discrepancy is, however, significantly smaller than our error bars and therefore nothing can be concluded from our observation.

This leaves the awkward task of weighing the two possible explanations: either the theoretical calculation for the multipole amplitudes is incorrect (most likely the E1 amplitude), or there are non-physical correlations in the parameters due to the sampling methodology. Since Blackston demonstrated the former was false at 14 and 16 MeV for the same reaction and we observed inexplicable correlations between even/odd parameter pairs (e.g. a_1 and a_2) we must conclude that the a_2/e_2 correlation we observed is most likely *not* due to a discrepancy with theory. We conclude that no significant discrepancy exists with theory: any apparent discrepancy with theory can be explained by a poor parameterization.

Finally, we note that no discrepancy exists in the parameterization due to the target

[4] Alternatively, we can make the last ring of Blowfish usable with a sufficiently strong PSD cut, such as one placed at 0σ from the neutron mean. Altering the short gate width may also improve the PSD.

length: the short and long target parameters agree well within their error intervals.

6.4 Beam

We verified the beam polarization following the procedure in section 5.3.1 on page 151: assuming a ϕ symmetry, the shift is $0.95 \pm 0.51^\circ$ from horizontal. The beam polarization was, therefore, most likely 98.5-99% horizontal. We incorporated the polarization into the e parameters, and so it would be reasonable to divide our e parameters by 0.9905 ± 0.0051 (though we do not).

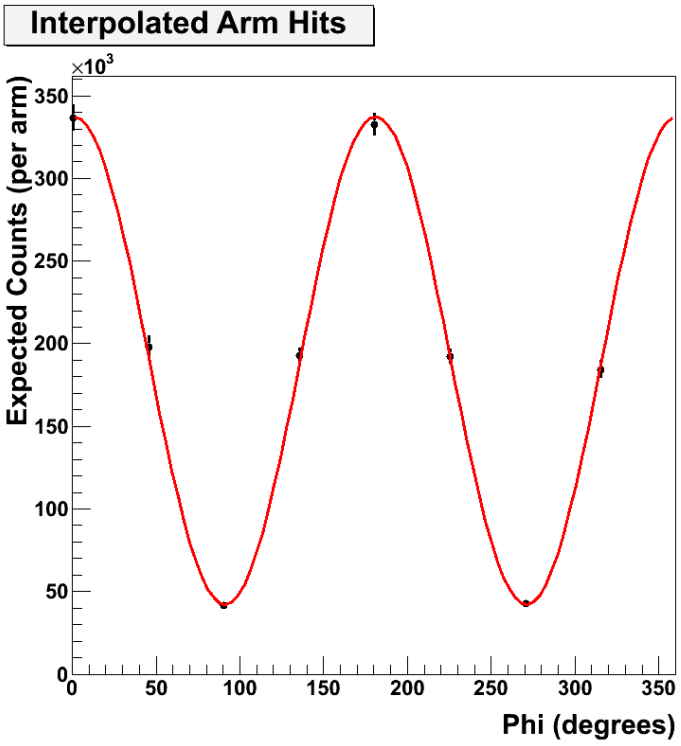

Figure 6.13: Beam Asymmetry. The interpolated arm yield was parameterized (red) by $c_0 + c_1 \cos(2(\phi - c_2))$ (ϕ in degrees). The shift from perfect ϕ symmetry is $c_2 = 0.95 \pm 0.51^\circ$: this is fairly trivial.

We also checked to see if the experimental analyzing power in section 1.5 on page 4 could be made to agree better with theory if it the polarization was not completely horizontal. We found that the best agreement came at a horizontal polarization of 97.5%.

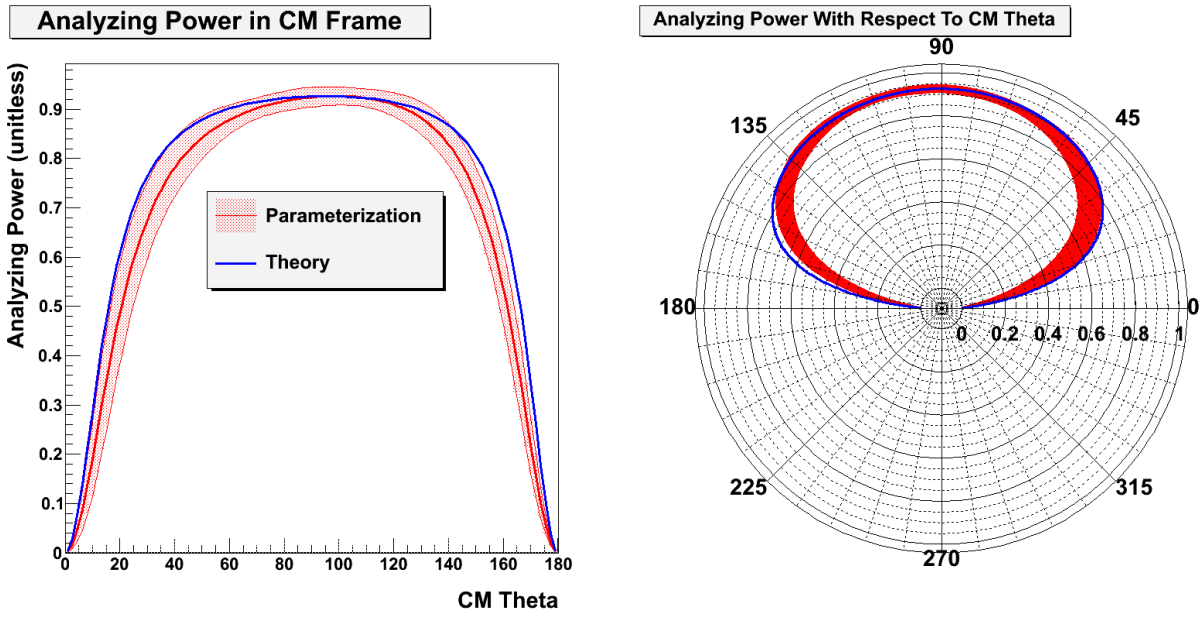

Figure 6.14: Analyzing Power with Imperfect Beam Polarization. The experimental parameterization (red) has been scaled by 0.975, this corresponds to a beam which is 97.5% horizontally polarized. We see a better agreement with theory than if we assume perfect horizontal polarization (figure 6.12 on page 240). Left image: Cartesian coordinates. Right image: polar coordinates: angle is theta (in degrees), and the radius is analyzing power (unitless). The legend is the same in both plots.

We conclude that the experimentally determined analyzing power would agree better with theory if we considered that the beam was not completely polarized.

These data imply that the beam at HI$\vec{\gamma}$S was not perfectly polarized (but close), or it is also possible that imperfect detector alignment has caused the observed ϕ asymmetry.

Chapter 7

Conclusion

In this chapter we discuss sources of error (section 7.1), we provide insight for future experiments (section 7.2 on page 259), and we present our final data and conclusion (section 7.3 on page 261).

7.1 Sources of Error

In discussing the sources of error, we place specific focus on our best run: run 142 (long D_2O target). The largest source of error in our results is the PSD (pulse-shape discrimination) cut, which in the case of the upper error in the neutron yield, accounts for over 90% of the reported uncertainty (section 7.1.2 on page 248). Since we add our errors in quadrature, this means that few other sources of error contribute significantly to the total reported uncertainties, and we can therefore neglect the negligible contribution which a number of sources of error would have (section 7.1.3 on page 255).

7.1.1 Estimating the Sources of Error

As was described in section 5.4 on page 193, we estimate the uncertainty associated with each measurement and each data analysis cut using a combination of statistics, calculations, simulations, and compensating factors. The latter-most comes into play only when scaling the total flux to compensate for: out-of-time photons,[1] and the multiplicity. In general, the uncertainties were always estimated by: (1) standard error propagation using differentials

[1]The flux monitor measures the presence of out-of-time beam photons, but we do not measure the subsequent neutrons produced by them; therefore we simply scale the flux so that it includes only the on-time photons.

and then the individual contributions were added in quadrature,[2] (2) analyzing the results of taking the minimum and maximum possible values, or (3) by altering a value in the simulation then using (2). All error estimates in measurements include both the nominal device uncertainty, and the propagated uncertainties (including any observed additional uncertainties).

The standard methodology for estimating the uncertainty in the neutron yield was to compute the uncertainty in a particular cut using standard techniques, then perturb the cut by that value and record the change in the total neutron yield after all other cuts were performed (each cut has its error described in its respective subsection of section 5.4 on page 193). Where measurement errors could be propagated, they were, and where they couldn't be (or were difficult to) we simulated the effect.

The simulated uncertainties were estimated by using an early parameterization of the differential cross section to simulate the expected neutron distribution, then sources of uncertainty were simulated by altering the simulation setup (e.g. the longitudinal target alignment was estimated by shifting the target forward by 1 mm in the simulation). The simulated data and uncertainties were analyzed the same way as the experimental data (i.e. by perturbing cut placement), then they were scaled linearly to the experimental neutron yield and included in the experimental neutron yield uncertainty.

The quantified sources of error, and the method used to estimate its affect are summarized in table 7.1 on the next page. A full discussion of the methods used will be found in each source of error's respective section.

[2]If the errors were clearly dependent, then they were simply added linearly.

Table 7.1: Summary of Error Methodologies.

Source of Error	Methodology
Target Alignment	Simulation.
Detector Alignment	Simulation.
Beam Alignment	Simulation.
Beam Attenuation	Simulation, and literature [Ber11].
Blowfish Radius	Simulation.
Out-of-Time Photons	Estimated fraction was added to error.
Beam Energy	Beam specifications and experimental geometry.
Parameterization	Minos technique [Jam75].
Light Output	Nominal ADC non-linearity [CAE10], and gain uncertainty.
Time-of-Flight	Nominal TDC non-linearity [CAE12], and statistical estimate of random error.
Counting Uncertainty	$\sqrt{\text{Counts}}$ [Kno00]
Pulse-Shape Discrimination	Minos error in statistical fit [Jam75].
Target Length	Inferred [Kuc10].
Target Density	Literature [Wea79].

The effects of these sources of error are given in section 7.1.2.

7.1.2 Breakdown of Quantified Sources of Error

The original purpose of this experiment was to test a few potential sources of error in Blowfish and the data acquisition system in order to prepare for future high precision experiments; consequently, the uncertainties in this experiment were not rigorously minimized. If longer radioactive source runs had been taken, then it is certain that the uncertainties in the light cuts (via the gain) and the PSD cut could be smaller; the latter is of significant importance since it is the largest source of error in the neutron yield, which in turn is the largest source of error in the total cross section, and PSD is the only reliable way to remove photon events

when out-of-time beam photons are present (therefore we had to exclude many cells due to an imperfect PSD cut).

Here we breakdown the sources of error in our most precise run: run 142 (long D_2O target), along with a typical cell: cell 27 to provide perspective on errors in terms of neutron yields. Relative to other runs, run 142 has a smaller uncertainty associated with the PSD than runs 149-159 (run 143 has roughly the same uncertainties as run 142), and a smaller uncertainty associated with the light cuts than the intermediate runs: runs 149-157.

Table 7.2 on the next page quantifies the uncertainties in cell 27 (with accompanying figure 7.2 on page 251) and the total cell averages for run 142 as a whole (with accompanying figure 7.1 on page 251).

Error Summary of Neutron Yield for Cell 27 and Run 142.

Source	Uncertainty in Cell Yield	% Total Cell Yield	Run Average
Counting Uncertainty and Background	±72	1.4	2.6 ± 1.2
Lower Light Cut (low)	−61	1.2	1.0 ± 0.4
Lower Light Cut (high)	+45	0.9	1.0 ± 0.4
Upper Light Cut (low)	0	0	0 ± 0
Upper Light Cut (high)	0	0	0 ± 0
PSD (low)	−732	14.0	13.9 ± 6.2
PSD (high)	+81	1.5	5.8 ± 4.0
Beam Alignment	±57	1.1	2.5 ± 1.6
Detector Alignment	±57	1.1	1.3 ± 1.4
Blowfish Radius	±112	2.1	1.8 ± 1.3
Target Alignment: Longitudinal	±26	0.5	1.1 ± 1.1
Target Alignment: Transverse	±71	1.4	1.1 ± 0.9
Upper Total	+196	3.7	8.0 ± 4.0
Lower Total	−754	14.4	15.2 ± 5.7
Total Yield	5234	100	100

Table 7.2: A breakdown of the errors in the neutron yield for cell 27 and the run 142 average. The second column from the left gives the value (in number of neutrons) of each source of error in the yield; values preceded by + are errors which can only increase the yield, those preceded by − can only decrease the yield, and those preceded by ± are equally able to increase or decrease the yield. Right-most column: run average ± standard deviation.

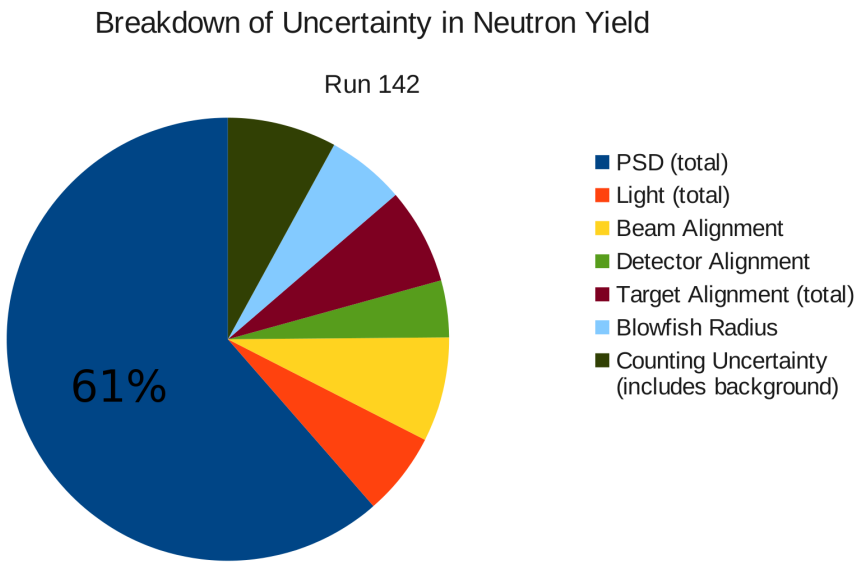

Figure 7.1: We compare the relative errors for each source of error in the cell average of run 142. Note: these are *not* relative contributions to the total error because we add the total error in quadrature.

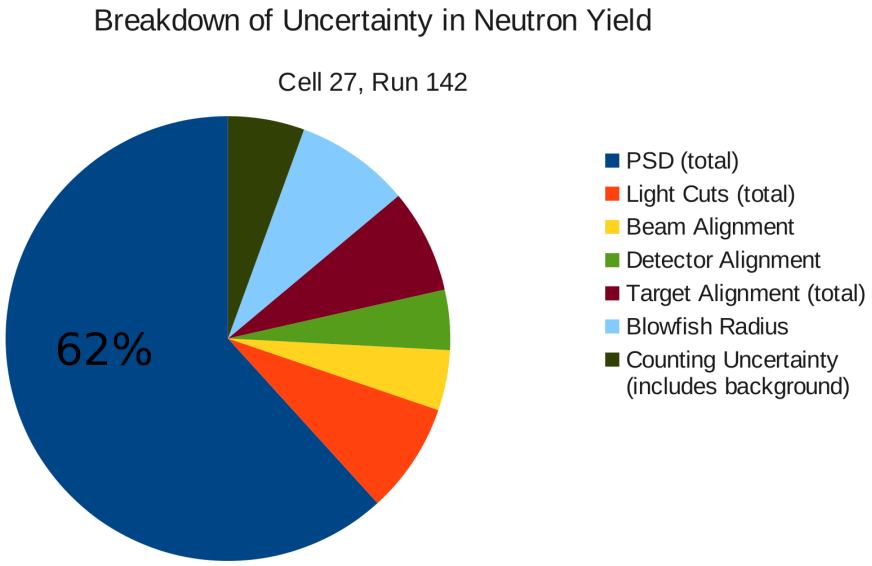

Figure 7.2: We compare the relative errors for each source of error in cell 27 during run 142. Note: these are *not* relative contributions to the total error because we add the total error in quadrature.

In table 7.2 on page 250 we see a great deal of variance from cell-to-cell in some of the uncertainties: this may have caused problems with the fit minimization when we parameterized the neutron yields: if the uncertainty estimates aren't accurate; in fact, it could be the source of the discrepancy in the parameterization observed in section 6.3 on page 224.

Reducing the total uncertainty in the neutron yield depends heavily on the PSD: for cell 27 (run 142), the uncertainty in the low PSD cut accounts for 97% of the total upper uncertainty, and the high PSD cut accounts for 41% of the total lower uncertainty. The reason that the PSD uncertainty is so large may be that the americium-beryllium source runs necessary to compute the PSD did not have enough events to get a good fit at energies past $\approx$ 3500 keVee; future experiments must therefore ensure that there are many events available to perform PSD, *especially at higher energies* (i.e. all the way up to the upper light cut).

The PSD cut has an asymmetric error for two reasons: (1) the statistical distribution of the neutrons, and (2) the fact that the lower light cut has some redundancy with the high PSD cut. The neutrons closely follow a Gaussian distribution, and therefore since the uncertainty in the position of the PSD cut is symmetric (i.e. the uncertainty in the mean and standard deviation): the resulting change in the yield *due to* the PSD cut will be asymmetric.

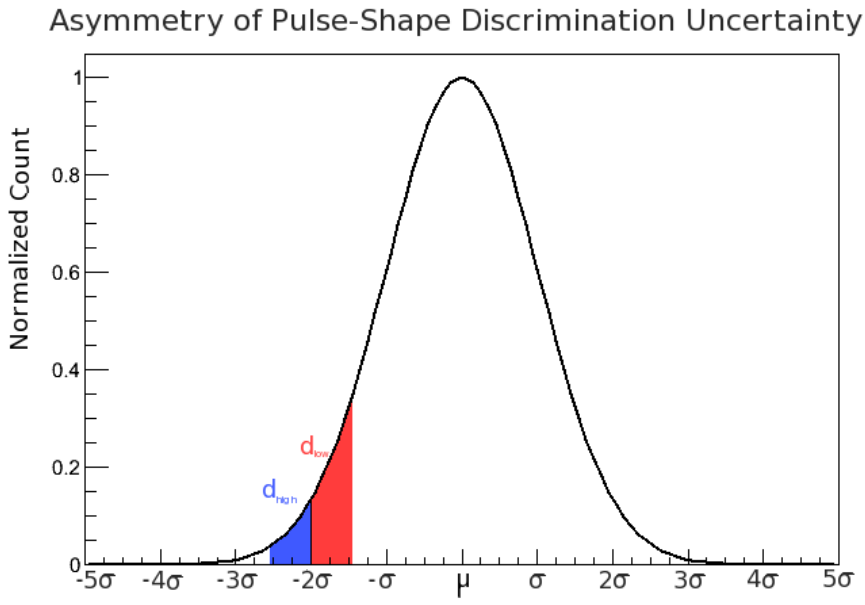

Figure 7.3: If the neutrons satisfy a Gaussian distribution, and the PSD cut is applied at -2σ from the mean, $\mu \pm d$, then the 'high' error propagation (blue) will always be smaller then the 'low' one (red).

Figure 7.3 illustrates that if the PSD cut is placed away from the neutron mean, then the uncertainty is asymmetric. Since we placed the cut at 2σ, this will cause our total neutron yields to be systematically low because the errors are asymmetric in favour of less neutrons (but the errors we compute are symmetric).

We used the neutron yield to extract the parameters. The only remaining source of error for the parameterization (that we've accounted for) is cross correlation between the parameters, we discussed this in section 6.3 on page 224 and the robust correlation matrix is given in table 6.5 on page 231.

The total cross section has several additional sources of error including the neutron yield. Table 7.3 on the next page (and accompanying figure 7.4 on the next page) summarizes the quantified sources of error for the total neutron production. We assume symmetric errors because after the totals have been computed and averaged over all of the cells (error averaged in quadrature) the difference between the lower and upper uncertainty becomes trivial e.g. run 142 has a total cross section (including neutrons from other sources) of

$\sigma = 661(+51)(-51)\ \mu$barns.

Table 7.3: Error Summary of Total Cross Section for Run 142. Right column: average value for all cells $\pm$ one standard deviation.

Source	% Total Cross Section
Beam Attenuation	$2.5386 \pm 0.0045\%$
Target Density	$7.2558 \pm 0.0043\%$
Target Length	$1.7126 \pm 0.0048\%$
Flux	$10.7748 \pm 0.0046\%$
Neutron Yield	$23.2 \pm 7.8\%$
Simulated Neutron Yield	$1.93 \pm 0.46\%$
Total	$27.6 \pm 6.8\%$

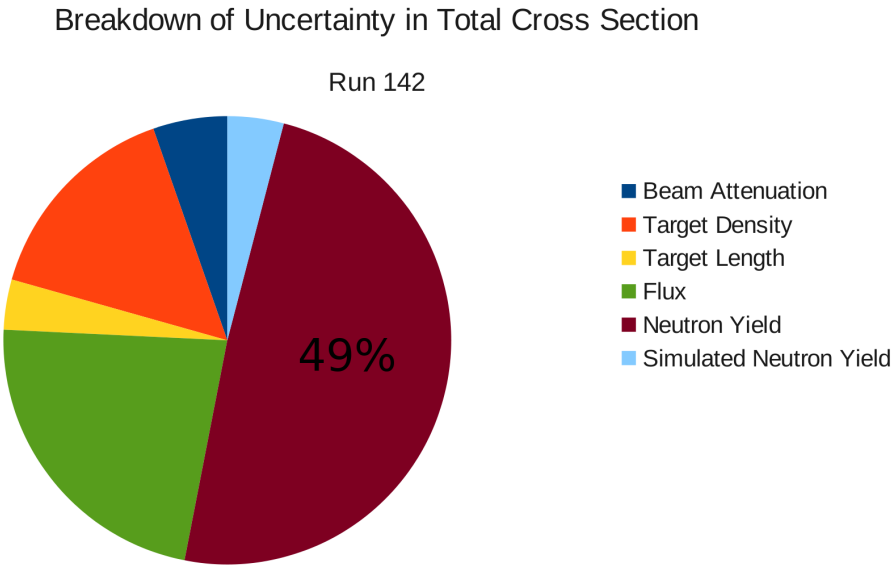

Figure 7.4: We compare the relative errors for each source of error in run 142. Note: these are *not* relative contributions to the total error because we add the total error in quadrature.

Section 6.2 on page 218 unveiled that our measured cross section is lower than typical experimental results (and theory) by $\approx 7\%$ ($\approx 45\ \mu$barns); however, our results do agree

within the quantified error interval. This implies that a systematic error; which we accounted for, pervaded all of the runs. The radius of Blowfish is an obvious suspect since the cell radius was set once then never changed, but this could only account for a change in the total cross section of $\approx 1.5\%$ (≈ 10 μbarns). The beam energy could have been systematically wrong as well, based on interpolated data from several sources [Ahr74, Ber86, Mic89] a change in energy from 18 MeV to 18.27 MeV would reduce the cross section by $\approx 2.3\%$ (≈ 15 μbarns); we wouldn't observe the neutrons arriving later than kinematics predicts in the time-of-flight spectrum because such a small change in energy would only appear as a 0.05 ns change in time-of-flight: well below our TDC precision. If these two uncertainties systematically varied from their expected values by their maximum uncertainties, there would still be another $\approx 3.1\%$ (≈ 20 μbarns) unaccounted for in the cross section discrepancy between our data and previous experiments.

The PSD uncertainty could cause a systematic underestimate in the neutron yield due to the asymmetric error in the cut location: because the simulation has exceptional PSD, it would not fully account for this effect. An underestimate in the neutron yield could easily account for the missing events, as it contributes; on average, 23.2% (≈ 150 μbarns) to the total uncertainty, and the dominant contribution to the neutron yield uncertainty is the PSD cut.

We therefore conclude that one or more source of error in table 7.3 on page 254 was systematic, or, we over-estimated the errors and the source of the discrepancy is an unaccounted for source of error.

7.1.3 Unaccounted Sources of Error

In this section we discuss unaccounted sources of error, the effect they would produce in the data, and some estimate of their relative importance: based on a simulation or simple calculation.

Incorrect Light Output

We found a substantial disagreement between the simulated and experimental calibrated ADC spectra for neutrons i.e. their light output spectra. Since the light outputs for neutrons

(when calibrating with photons) agreed previously in 2006 [Pyw06], we assumed that some unknown process had caused the experimental light outputs for neutrons to drop and consequently scaled up the experimental light output to compensate. This rectified the shape of the experimental ADC spectrum with the simulation, but the uncertainty in the value of the scaling factor was observed to be small, and therefore assumed to be negligible; which may not be true.

In order to extract the scaling factors, we used the same fitting algorithm for the simulated and experimental ADC spectra, and therefore we expect that an uncertainty in the scaling factors is purely random: any systematic error would tend to cancel out when we took the ratio of the simulated and experimental ADC inflection points (recall: scaling factor for cell i = $\frac{\text{simulated inflection point}}{\text{experimental inflection point}}$). A random error would tend to cancel out over the 88 cells (recall each cell has a unique scaling factor) and therefore we do not expect a significant effect on either the differential cross section or the total cross section.

It is also worth noting that if the light outputs are not correctly compensated for by a simple multiplicative factor to the ADC neutron gain (e.g. if they need a constant added to them), then the light cut will cause a bias in the data: we observed that the light cut doesn't change the results significantly, and therefore conclude that the multiplicative factor is correctly compensating for the reduced neutron gain during this experiment, at least to first-order.

Efficiencies

In order to extract the total cross section, we assumed that the simulated and experimental efficiencies are the same. If the simulation does not accurately reproduce the actual efficiencies then our cross section, σ will be incorrect and is proportional to the ratio of efficiencies: $\sigma \propto \frac{\text{simulation efficiency}}{\text{efficiency}}$. This would also prevent us from reliably extract the differential cross section from the neutron yield because the different simulation efficiency may produce a spatial bias.

Effect of Beam Attenuation in Neutron Yield

In our simulations we generated neutrons in the target in order to emulate photodisintegration reactions without a knowledge of the cross section for the reaction. This means that we had to compensate for beam photons which would scatter out of the target, or fall below the threshold energy for the reaction, and thus reduce the number of photons available in the downstream part of the target i.e. the effective beam attenuation coefficient, μ.[3]

The beam attenuation coefficient depends on our geometry and the threshold energy for the reaction, this means that we need to consider both the specific geometry of our reaction (including target length) and the photon energy at which the reaction will no longer be measured (8 MeV[4]).

Using the simulation, we divided the target into numerous longitudinal slices and counted the number of photons which entered each slice, and left each slice or scattered so that they fell below the energy threshold. The simulations were run a few million times and then the attenuation coefficients were extracted from the data: the long target attenuation coefficient was $\mu_{L,eff.} = 0.01604 \pm 0.00015$ cm^{-1} and the short target attenuation coefficient was $\mu_{S,eff.} = 0.015844 \pm 0.000096$ cm^{-1}. These differ substantial from the literature value of the linear mass attenuation coefficient, which is: $\mu_{lit.} = 0.01842 \pm 0.00001$ cm^{-1} [Ber11].

When simulating the Legendre probability density functions we used the literature value, $\mu_{lit.}$, instead of the effective values, $\mu_{L,eff.}$ and $\mu_{S,eff.}$ (this was a matter of lack of foresight). The discrepancy in the attenuation coefficient was discovered late in data analysis, and so the new attenuation coefficients were not used when simulating the neutron yields (though they were used for calculating the total cross section). We then verified this would not have a substantial effect in the neutron yield by comparing the simulated neutron yield with different attenuation coefficients and found no significant variation within the counting uncertainty (figure 7.5 on the next page): meaning that relative to the experimental uncertainty this effect is trivial.

[3]Probability of attenuation $= e^{-\mu x}$.

[4]The minimum value for this threshold is 2.2 MeV (the threshold for deuteron photodisintegration), but we also had to consider that the lower light cut was eliminating all neutrons below an energy of ≈ 3.5 MeVee; performing the kinematic calculation this means that the incident photon must be above ≈ 8 MeV for it to be capable of producing a measurable neutron.

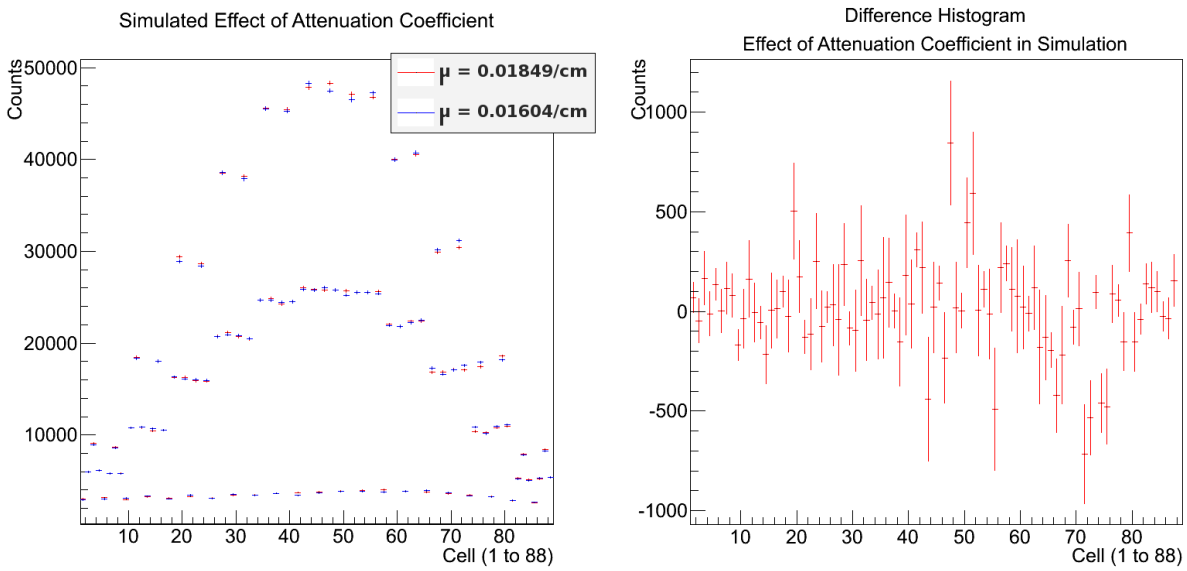

Figure 7.5: Effect of Beam Attenuation in Simulated Neutron Yield. Left image: the literature value for the attenuation coefficient of the beam [Ber11] (red) compared to the attenuation coefficient for our geometry, estimated using the simulation (blue). Right Image: we take the data from the left image and subtract the red histogram from the blue histogram; the result is randomly scattered around 0: implying that the two results are the same, within error.

The effect of this error in the data would be to decrease the neutron yield in the downstream cells in the simulated data relative to the experimental results (because the attenuation coefficient used in the simulation was too large), and therefore would cause a θ bias in the parameters in favour of forward scattering (θ near 0°).

Imperfect Beam Polarization

Sawatzky [Saw05] measured an $\approx 9°$ deviation in the horizontal polarization of the beam at HI$\vec{\gamma}$S during an experimental run, purportedly due to degradation of the UV mirrors. When we parameterize the neutron yields per arm and fit a generalized expression to check the azimuthal (ϕ) symmetry, we see a deviation of $0.95 \pm 0.51°$, and conclude that the horizontal polarization could vary by up to that much. The value of the e parameters we report in section 6.3 on page 224 include the horizontal beam polarization in them, which we assume

to be perfect (i.e. 1), this means that our e parameters are too small by a factor of 0.9905 $\pm$ 0.0051.

The deviation from horizontal is small and has a large uncertainty in it, implying that it is of minor importance. If the beam was not entirely horizontally polarized, then our e parameters are too small and should be scaled by dividing by the correct horizontal polarization ratio (because they are multiplied by the polarization relative to e.g. Cambi *et al.* [Cam82]).

Miscellaneous Sources of Error

Blackston [Bla07] includes several more sources of error than reported here: the variation in the solid angle coverage of each detector, the beam intensity profile, collimator size, depolarization of the beam due to scattering, and the parameterization of the light output response function. These were all reported to be small relative to the time-of-flight and PSD uncertainties [Bla07], and since we expect our PSD uncertainties to be much higher than Blackston's (because our error bars are larger), we conclude that these effects must be trivial relative to our estimated uncertainties.

7.2 Future Considerations

This experiment required extensive data analysis, and a few novel techniques to deal with old problems; future experiments will benefit from these techniques during data analysis, and can improve precision with a few additional considerations: we elucidate these considerations here.

First, future researchers will benefit from the new PSD algorithm which is faster and better at estimating the uncertainty. Use of the offset parameter, ϕ, should be used cautiously: some cells are much better fit by using the jerk parameter, J: fitting these cells to ϕ may result in pathological separation.

By far the largest source of uncertainty in this experiment was the novel pulse-shape discrimination (PSD) technique (described in section 5.3.9 on page 184), but we were forced to use it because of the presence of out-of-time photons in the data. The key to minimizing

the PSD uncertainty during analysis is good statistics in the source run used to calibrate the PSD, and ensuring that the neutrons and photons span the entire energy range of the ADCs.

Future experiments in the 0-10 MeV neutron energy range ($\approx$ 0-20 MeV beam energy) should use a hot AmBe source to take a long source run[5] after the long and short gates have been set (and after anytime the long or short gates change); experiments at higher energies should use a different source which has appropriately high energy neutrons and photons e.g. using a lead target should work for arbitrary energies. It is also possible that the gate optimization needs to be performed again: the PSD separation in 2010 was inferior to the separation in 2008, despite using the same nominal gate timing. Furthermore, some cells may have been contaminated with oxygen (e.g. cell 1 and cell 3): these cells should be thoroughly tested (and potentially replaced).

The presence of out-of-time photons was the most common reason for cells to be excluded in this experiment (see appendix I on page 298), but given it is unclear why they are forming and so there is no obvious way to prevent their production. One *could* watch the TDC spectra for the downstream cells carefully when taking data and stop the beam (dumping the electrons in the synchrotron) when out-of-time photons become prevalent in the data. This will seriously impact the data acquisition rate, and so an alternative is to insert a sensitive photon detector (e.g. an inorganic crystal) into Blowfish to better characterize the out-of-time photons present. During data analysis the distribution of out-of-time photons can then be inferred assuming Compton scattering and/or using a GEANT4 simulation: once the arrival times of the out-of-time photons are accurately known, the events arriving at those times can simply be rejected (neutron yields at those times can then be interpolated).[6]

Another source of error was the time-of-flight due; in large part, to our inability to align the TDCs for each run. Most of the cells have stable TDCs which only need to be aligned once per day of running, but as was shown in figure 5.21 on page 183: $\approx \frac{2}{13} = 15\%$ of cells had significant ($\gtrsim$ 1 ns) drifts in their alignment over the course of this experiment. We can align the TDCs during each run by setting the Gamma window activity rate at $\approx 1\%$ of events, it isn't possible to calibrate the upstream TDCs if the Gamma window activity is set

[5]I.e. a Lucid data file $>$ 300 MB, preferably close to the maximum: 2 GB.

[6]Such detectors would give additional freedom during analysis and could potentially be used to verify the beam flux and energy.

at 0.1% (such as it was during this experiment).

We should also test the calibration of our detectors: the decreased light output observed in this work, in the work of Blackston [Bla07] and Wurtz [Wur10c] is sufficient evidence that the BC-505 light outputs may have changed since they were last recorded in 2006 [Pyw06]. This may be indicative of an aging property of the BC-505 cells, and if so then it may prove remunerative to start replacing the cells. If the light output parameters appear to have changed, then they need to be recorded again so that the simulation accurately reproduces the actual cells. The light outputs must be the same as the simulation in order to extract the total cross section and the parameters for the differential cross section; furthermore, if the light outputs have dropped over time then it is probable that the PSD does not provide as much separation between neutrons and protons as it once did. With this said, we still don't know why the light output is lower in the experimental data than the simulated data: the light output parameters are only one possible contributor to the problem.

Finally, when it came to extracting the associated Legendre polynomial parameters during data analysis, we found strong correlations between the parameters. Adding more detectors should decrease this correlation; however, it is more practical to simply take the steps outlined in this section to reduce the uncertainties: the correlation may derive from a systematic error in the neutron yields.

7.3 Conclusion

Our results (chapter 6 on page 218) are summarized as follows: the theoretical predictions, our experimental results, and other researcher's experimental results all agree within error.

The total cross section agrees within error with theory and other experiments, though the reported value is $\approx 7\%$ (47 μbarns) lower than expected (figure 7.6 on the next page). We found that the total cross section was 643 ± 62 μbarns, compared to the weighted average of other researchers which is: 690 ± 15 μbarns; the theoretical calculation predicted 685.14 μbarns.

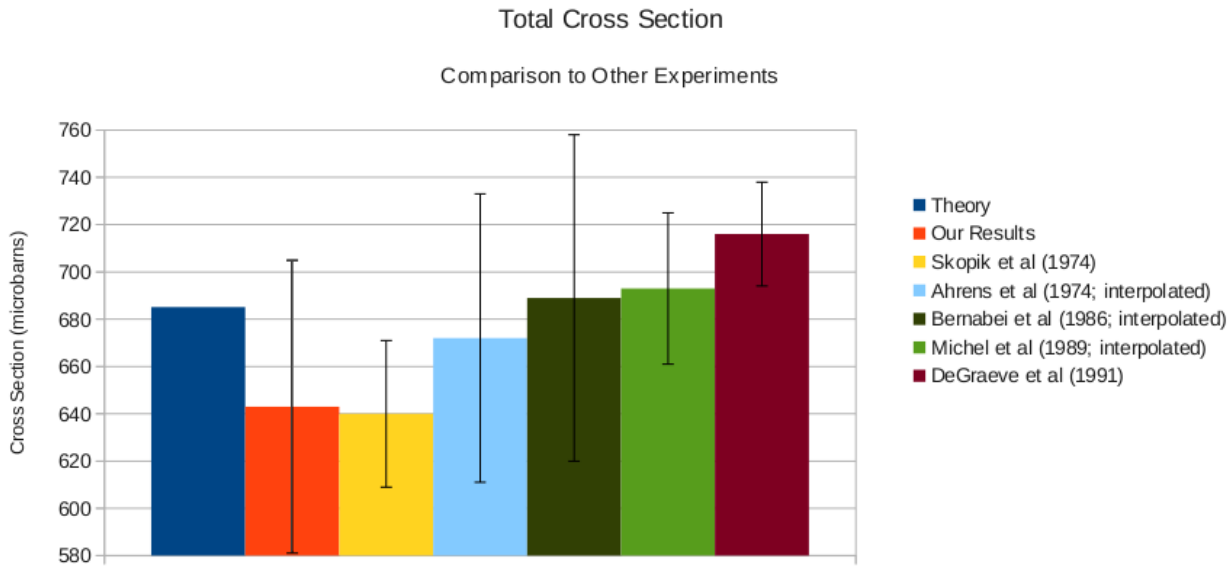

Figure 7.6: Total Cross Section. Our total cross section agrees with other researchers and the theoretical prediction (blue).

We parameterized our neutron yields using the associated Legendre polynomials:

$$\frac{d\sigma}{d\Omega} \approx \frac{\sigma}{4\pi}\left[1 + \sum_{k=1}^{4} a_k P_k^0(\cos\theta) + \sum_{k=2}^{4} e_k P_k^2(\cos\theta)\cos 2\phi\right] \tag{7.1}$$

where: P_k^i are the associated Legendre polynomials, the a_k, and the e_k are fit parameters, and σ is the total cross section.

Our neutron yields (figure 7.7 on the next page) are consistent with the theoretical parameterization ($\chi^2_{red} = 0.74$), but we also found a better set of parameters to fit our data ($\chi^2_{red} = 0.31$).

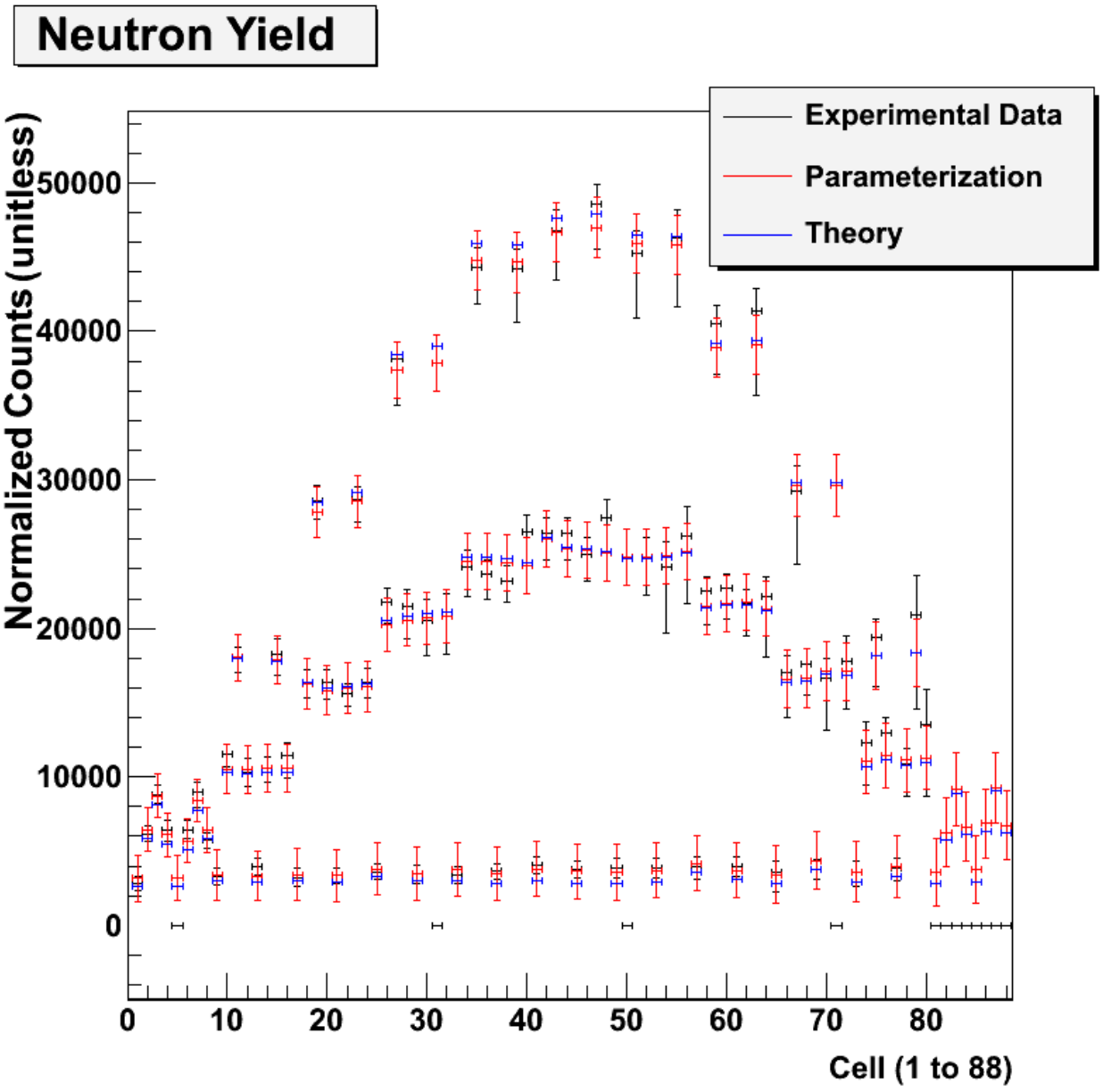

Figure 7.7: Parameterized Neutron Yield for Long Target Average. We see good agreement between the neutron yields and both: the extracted parameterization ($\chi^2_{red} = 0.31$), and the theoretical parameterization ($\chi^2_{red} = 0.74$). The agreement between the theoretical and extracted parameterizations is excellent: every theoretical prediction is within the error interval of the respective parameterized prediction, and is typically very close to the median value. Note: Excluded cells are set to -1. 76 of the 88 cells were used.

Our parameters were prone to strong cross correlations; we estimated the errors in them using the Minos technique [Jam75], and found that although the parameterization we extract from our data agrees with the theoretical parameterization within expectations (assuming the errors represent 1 standard deviation): the experimental parameters agree with the theoretical parameters within 2σ 86% of the time, and agree within 1σ approximately 57% of the time. This may imply that we fit to a χ^2 minimum which existed purely as an artifact of the analysis, or it may alternatively be due to a discrepancy with the theoretical E1 transition amplitude contrary to what was observed by Blackston [Bla07]. Our parameterization of the experimental data and the calculation performed by Schwamb and Arenhövel [Sch01c, Sch01a, Sch01b] are given in table 7.4.

Parameter	Long Target	Short Target	Theory
a_1	-0.149 $\pm$ 0.020	-0.123 $\pm$ 0.043	-0.157
a_2	-0.861 $\pm$ 0.030	-0.840 $\pm$ 0.070	-0.897
a_3	0.120 $\pm$ 0.038	0.129 $\pm$ 0.071	0.146
a_4	0.010 $\pm$ 0.033	-0.032 $\pm$ 0.055	-0.015
e_2	0.4296 $\pm$ 0.0043	0.4224 $\pm$ 0.0081	0.45
e_3	-0.0226 $\pm$ 0.0029	-0.0184 $\pm$ 0.0047	
e_4	-0.0005 $\pm$ 0.0024	-0.0027 $\pm$ 0.0033	

Table 7.4: Legendre Expansion Parameters. The theoretical parameterization is good to $<$ 1%. Note: we assume the horizontal polarization is perfect, therefore our e parameters should be divided by the linear polarization ratio (0.9905 $\pm$ 0.0051). We report the first column (long target) parameters as our best parameters. Note: we report the symmetric error, as the non-parabolic error is very close.

We calculated a few observables: the differential cross section and the analyzing power, using the Legendre parameterization. These observables demonstrate the ability for some parameters to compensate for each other: in the neutron yield (figure 7.7 on page 263) the parameterizations agree exceptionally, in the ϕ-averaged cross section (figure 7.8 on the next page) and the θ-averaged cross section (figure 7.9 on page 266) we see the parameterizations

disagree at extreme angles, and finally in the analyzing power (figure 7.10 on page 267) the different parameterizations show substantial disagreement.

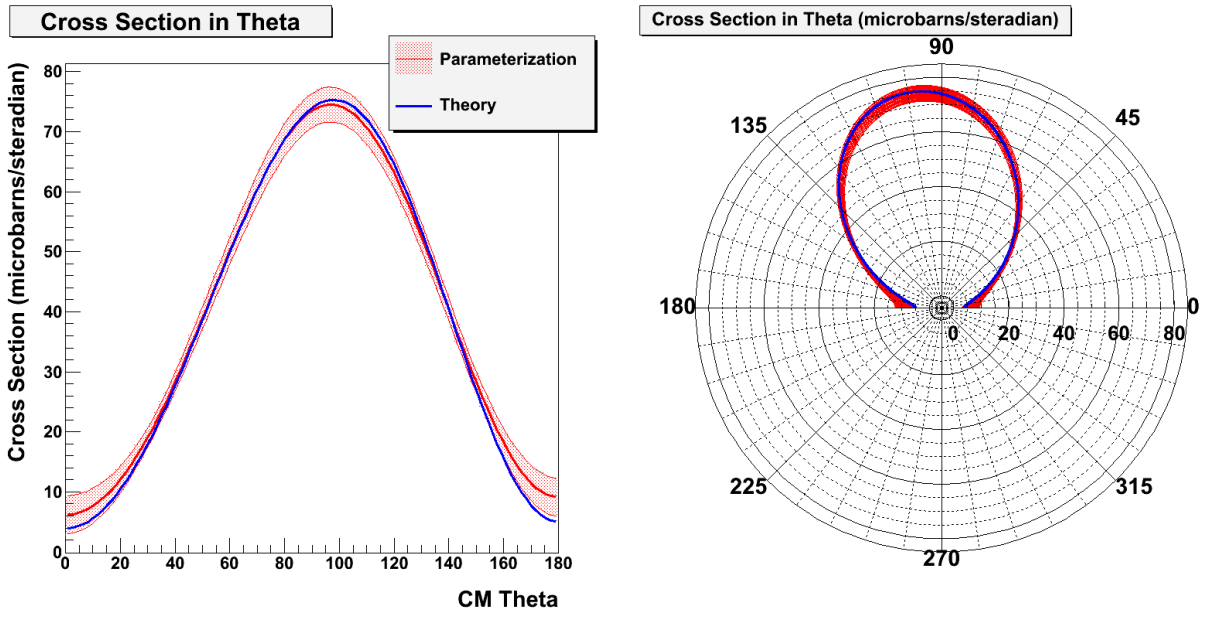

Figure 7.8: Differential Cross Section vs θ in the CM Frame. The differential cross section has been averaged over ϕ. The theoretical (blue) and experimental (red) results agree, except near the backwards most angle (near $\theta = 180°$). Theory has been scaled to the experimental results. Left image: Cartesian coordinates. Right image: polar coordinates: angle is theta (in degrees), and the radius is cross section (in microbarns). The legend is the same for both images.

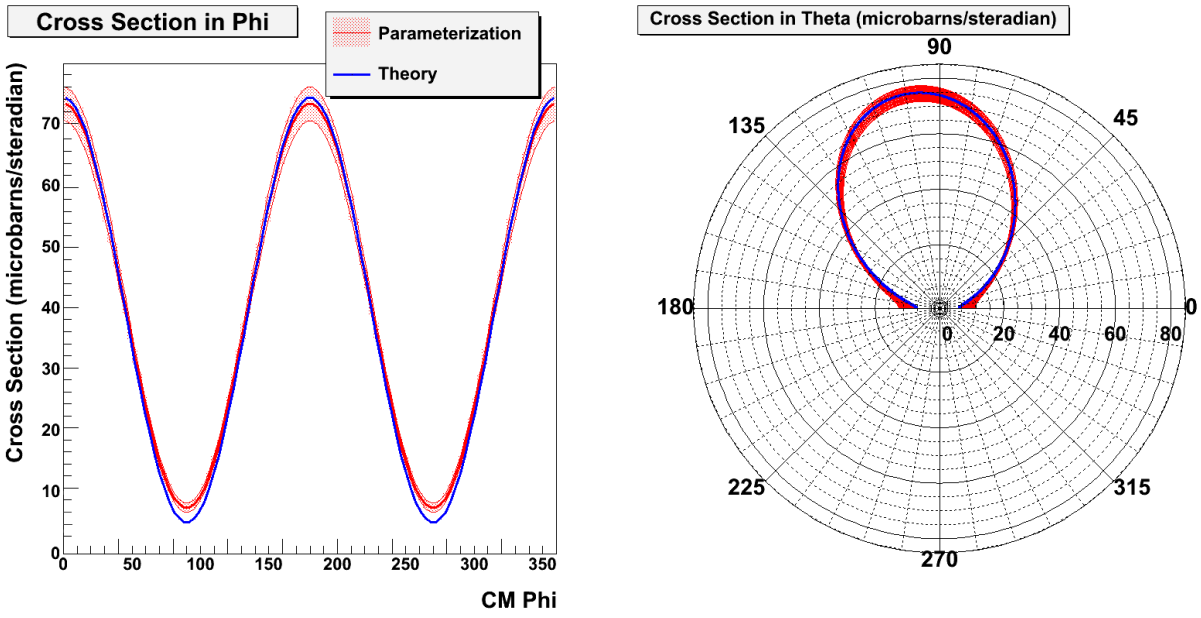

Figure 7.9: Differential Cross Section vs ϕ in the CM Frame. The differential cross section has been averaged over θ (polar angle). We see agreement between theory (blue) and our results (red) except near $\phi = 90°$ and $270°$, where the theory underestimates the cross section. Theory has been scaled to the experimental results. Left image: Cartesian coordinates. Right images: polar coordinates: angle is ϕ (in degrees), and the radius is cross section (in microbarns). The legend is the same in both images.

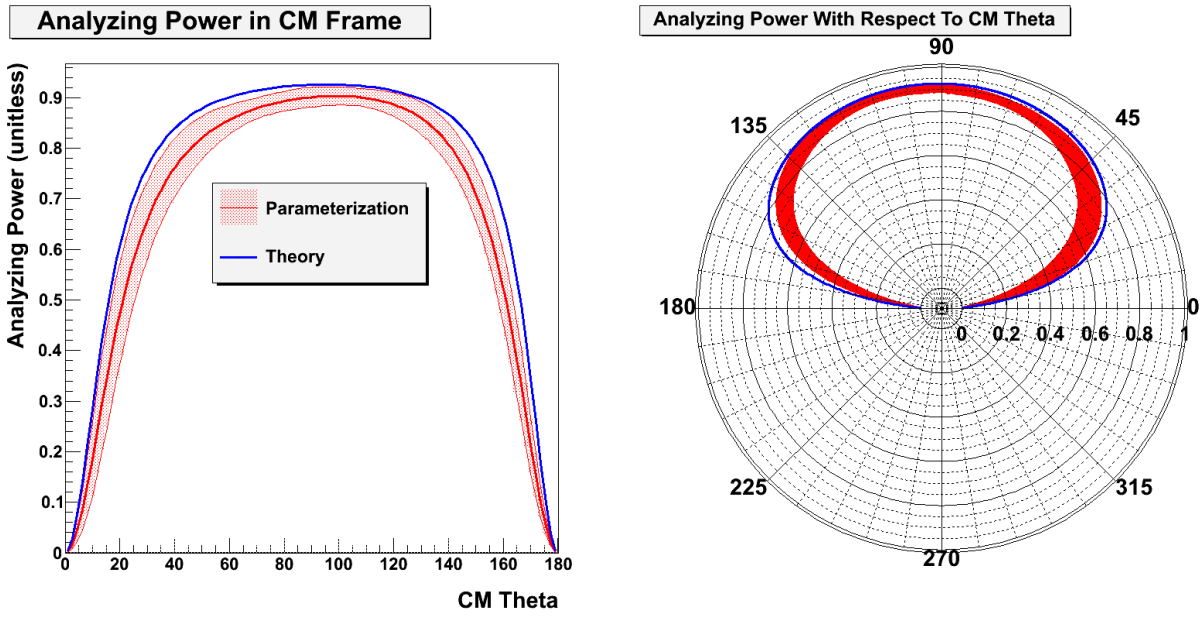

Figure 7.10: Analyzing Power. We see that our results (red) are systematically lower than the theoretical prediction (blue). Left image: Cartesian coordinates. Right image: polar coordinates: the angle is theta (in degrees), and the radius is analyzing power (unitless). The legend is the same in both images.

Continuing the investigation preformed by Sawatzky [Saw05], we computed the $\sigma(\theta = 90°)$ normalized ϕ-averaged cross section at lab polar angles: $\theta = 45°, 135°$, and $155°$, and compared to the theoretical calculation by Schwamb and Arenhövel [Sch01c, Sch01a, Sch01b] (table 7.5), as well as continuing the comparison performed by Sawatzky (figure 7.11 on the next page)

Ratio	Our Results	Theory
$\frac{\sigma(45°)}{\sigma(90°)}$	0.470 ± 0.029	0.460
$\frac{\sigma(135°)}{\sigma(90°)}$	0.631 ± 0.037	0.639
$\frac{\sigma(155°)}{\sigma(90°)}$	0.304 ± 0.030	0.281

Table 7.5: Ratio of Cross Section at Select Lab Polar Angles (θ). Our results agree with the theoretical predictions, as expected from figure 6.8 on page 235.

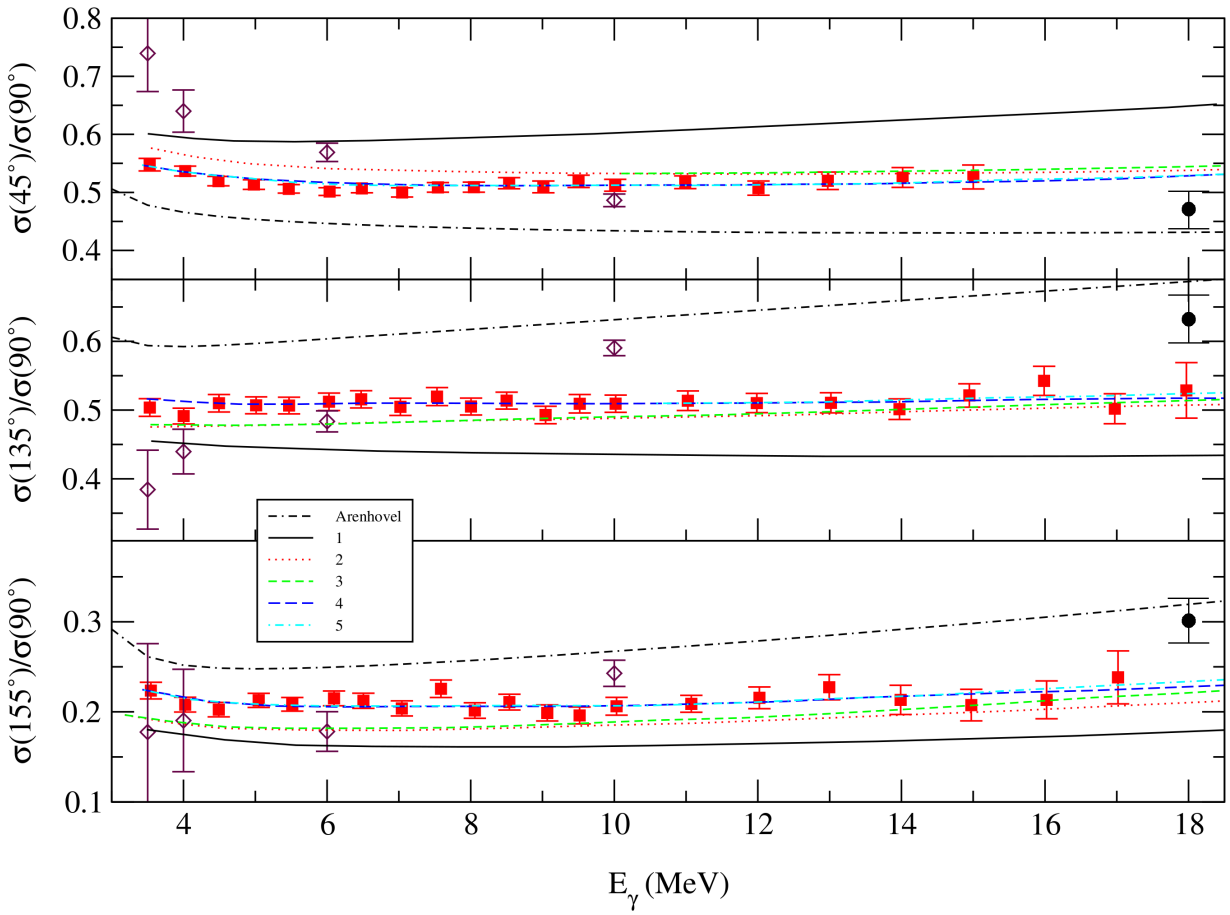

Figure 7.11: Ratio of Cross Section at Selected Neutron Lab Angles for Energy in Range 3-18 MeV. Closed circles: present work, open diamonds: Sawatzky [Saw05], solid squares: Stephenson *et al.* [Ste87], the numbered lines are calculations performed by Hadjimichael *et al.* [Had87], and the dotted line labeled Arenhövel is an old calculation by Arenhövel *et al.* [Are00]. Our results clearly disagree with those of Stephenson's, and agree reasonably well with Arenhövel's old calculation.

We see excellent agreement between our results and the calculation performed by Schwamb and Arenhövel in table 7.5 on page 267 and we are close to the older calculations performed by Arenhövel [Are00] as seen in figure 7.11. We also see a strong disagreement with the calculations performed by Hadjimichael *et al.* [Had87], and the experimental results of Stephenson *et al.* [Ste87]. The latter is consistent with the purported confounding variable in Stephen-

son *et al.*'s work because their detector calibration was affected by the partial polarization [Kuc10].

Finally, we see no discrepancy in any of our results between the short and long target runs,[7] contrary to the results of Kucuker [Kuc10]. This implies that spin-dependent scattering in our experimental setup is not significant relative to our uncertainties.

In conclusion, we see that our results are consistent with the calculation performed by Schwamb and Arenhövel and our total cross section is consistent with previous experiments. Our results do, however, suggest that the E1 transition amplitude calculated by Schwamb and Arenhövel may be too large, but our uncertainties are too large to conclude anything about it.

[7] There is no point comparing the observables for the short and long target because they are calculated using the parameterization, and the parameters agree excellently between the short and long target runs.

References

[Ago03] S. Agostinelli, J. Allison, K. Amako, J. Apostolakis, H. Araujo, P. Arce, M. Asai, D. Axen, S. Banerjee, G. Barrand, *et al.* (Geant4 collaboration), Nucl. Instrum. Methods **A506**, 250 (2003).

[Ahr74] J. Ahrens, H. Eppler, H. Gimm, M. Krning, P. Riehn, H. Wffler, A. Zieger, and B. Ziegler, Phys. Lett. B52, 49 (1974).

[Ant09] I. Antcheva, M. Ballintijn, B. Bellenot, M. Biskup, R. Brun, N. Buncic, Ph. Canal, D. Casadei, O. Couet, V. Fine, *et al.*, Comput. Phys. Commun. **180**, 2499 (2009).

[Apo08] J. Apostolakis, G. Folger, V. Grichine, A. Howard, V. Ivanchenko, M. Kosov, A. Ribon, V. Uzhinsky, and D. Wright, in *Proceedings of the Nuclear Science Symposium Conference, Dresden, 2008*, published by IEEE, p. 833.

[Are00] H. Arenhövel, W. Leidemann, and E. Tomusiak, Few–Body Systems, **28**, 147 (2000). Sections:

[Are91] H. Arenhövel and M. Sanzone, *Photodisintegration of the Deuteron: a Review of Theory and Experiment* (Springer, 1991), Vol. 3.

[Ari01] J. Arias and M. Lozanos (editors), *An Advanced Course in Modern Nuclear Physics* (Springer, Berlin, 2001), 1st ed.

[Bag73] J. Baglin, R. Carr, E. Bentz Jr., and C–P. Wu. Nucl. Phys. **A201**, 593 (1973).

[Bei52] A. Beiser, Rev. Mod. Phys., **24**, 273 (1952).

[Ber86] R. Bernabei, A. Incicchitti, M. Mattioli, P. Picozza, D. Prosperi, L. Casano, S. d'Angelo, M. De Pascale, C. Schaerf, G. Giordano, G. Matone, S. Frullani, and B. Girolami, Phys. Rev. Lett., 57, 1542 (1986).

[Ber11] M. Berger, J. Hubbell, S. Seltzer, J. Chang, J. Coursey, R. Sukumar, D. Zucker, and K. Olsen, Xcom: photon cross sections database, `http://www.nist.gov/pml/data/xcom/`, created: 2009, last updated: 2011.

[Ber12] J. Beringer, J. Arguin, R. Barnett, K. Copic, O. Dahl, D. Groom, C. Lin, J. Lys, H. Murayama, C. Wohl, *et al.* (Particle Data Group), Phys. Rev. D, 86, 1 (2012).

[Bet34] H. Bethe and W. Heitler, in *Proceedings of the Royal Society of London A, 1934*, **146**, p. 83.

[Bet35] H. Bethe and R. Peierls, in *Proceedings of the Royal Society of London A, 1935*, **148**, p. 146.

[Bet54] H. Bethe and L. Maximon, Phys. Rev., **93**, 768 (1954).

[Bew05] B. Bewer, *Development of a Gain Monitoring System for a Neutron Detector Array*, M.Sc. thesis, University of Saskatchewan, 2005.

[Bew09] B. Bewer, R. Pywell, R. Igarashi, and W. Wurtz, Nucl. Instrum. Methods, **A608**, 417 (2009). Cited in section(s):

[Bir88] Y. Birenbaum, Z. Berant, A. Wolf, S. Kahane, and R. Moreh, Phys. Rev. Lett., **61**, 810 (1988).

[Bla07] M. Blackston, *Precision Measurements of Deuteron Photodisintegration Using Linearly Polarized Photons of 14 and 16 MeV*, Ph.D. thesis, Duke University, 2007.

[Bla08] M. Blackston, M. Ahmed, B. Perdue, H. Weller, B. Bewer, R. Pywell, W. Wurtz, R. Igarashi, S. Kucuker, B. Norum, K. Wang, J. Li, S. Mikhailov, V. Popov, Y. Wu, and B. Sawatzky, Phys. Rev. C, **78**, 034003 (2008).

[Bol61] L. Bollinger and G. Thomas. Rev. Sci. Instrum., **32**, 1044 (1961).

[Boo94] G. Booch, *Object Oriented Analysis & Design with Application* (The Benjamin/Cummings Publishing Co. Inc, 1994), 2nd ed.

[Bor70] M. Bormann, R. Kühl, K. Schäfer, and U. Seebeck, Nucl. Instrum. Methods, **88**, 245 (1970).

[Bru97] R. Brun and F. Rademakers, Nucl. Instrum. Methods **A389**, 81 (1997).

[Bry72] R. Bryan and A. Gersten, Pys. Rev. D **6**, 341 (1972).

[Bur04] H. Burkhardt, V. Grichine, P. Gumplinger, V. Ivanchenko, R. Kokoulin, M. Maire, and L. Urban, in *Proceedings of the Nuclear Science Symposium Conference, Rome, 2004*, published by IEEE **3**, p. 1907.

[CAE10] CAEN, *Technical Information Manual: Mod. V792 Series; Mod. V792 N Series* (CAEN, New York, 2010), 18th ed.

[CAE12] CAEN, *Technical Information Manual: Mod. V775 Series; Mod. V775 N Series* (CAEN, New York, 2012), 14th ed.

[Cam82] A. Cambi, B. Mosconi, and P. Ricci, Phys. Rev. C, **26**, 2358 (1982).

[Car11] B. Carlson and D. Hirata, Few–Body Systems, **49**, 85–89 (2011).

[Che97] Chen and Kortlarchyk, *Interactions of Photons and Neutrons with Matter* (World Scientific, Singapore, 1997), 1st ed.

[Cho52] C. Chou, Phys. Rev., **87**, 904 (1952).

[Dav54] H. Davies, H. Bethe, and L. Maximon, Phys. Rev., **93**, 788 (1954).

[Dev94] L. Devroye, *Non–Uniform Random Variate Generation* (Springer–Verlag, New York, 1994), 1st ed.

[DFE10] DFELL/TUNL, HIGS Flux Performance Table for High–Flux Quasi–CW Operation (2010), `http://www.tunl.duke.edu/documents/public/HIGSBeamParameters.pdf`.

[DGr91] A. De Graeve, A. Zieger, R. Van De Vyver, C. Van Den Abeele, H. Ferdinande, L. Van Hoorebeke, D. Ryckbosch, F. De Smet, and B. Ziegler, Nucl. Phys. **A530**, 420 (1991).

[DGr92] A. De Graeve, R. Van de Vyver, A. Zieger, C. Van Den Abeele, L. Van Hoorebeke, D. Ryckbosch, H. Ferdinande, F. De Smet, B. Ziegler, P. Wilhelm, *et al*, Phys. Rev. C, **45**, 860 (1992).

[Dic12] R. Dick, *Advanced Quantum Mechanics: Materials and Photons* (Springer, New York, 2012), 1st ed.

[Ead06] W. Eadie and F. James, *Statistical methods in experimental physics* (World Scientific, 2006), 2nd ed.

[Ebr12] J–P. Ebran, E. Khan, T. Nikšić, and D. Vretenar, Nature **487**, 341 (2012).

[Els88a] C. Elster, W. Ferchländer, K. Holinde, D. Schütte, and R. Machleidt, Phys. Rev. C **37**, 1647 (1988).

[Els88b] C. Elster, K. Holinde, D. Schütte, and R. Machleidt, Phys. Rev. C, **38**, 1828 (1988).

[Els89] C. Elster and P. Tandy, Phys. Rev. C, **40**, 881 (1989).

[Fey] R. Feynman, as recorded on YouTube at `http://www.youtube.com/watch?v=lytxafTXg6c`.

[Gad09] T. Gaddis, *Starting Out With C++: From Control Structures Through objects* (Pearson, Boston, 2009), 6th ed.

[Gea] S. Agostinelli *et al* (2003)[Ago03] has 8478 citations according to Google Scholar as of Oct 28$^{\text{th}}$, 2013, `http://scholar.google.ca/scholar?hl=en&q=GEANT4%E2%80%94a+simulation+toolkit&btnG=&as_sdt=1%2C5&as_sdtp=`.

[Ger71] A. Gersten, R. Thompson, and A. Green, Phys. Rev. D **3**, 2076 (1971).

[Gha96] S. Ghahramani, *Fundamentals of probability* (Prentice Hall, 1996), 1st ed.

[Gri87] D. Griffiths, *Introduction to Elementary Particles* (Harper and Row Publishers, New York, 1987), 1st ed.

[Had87] E. Hadjimichael, M. Rustgi, and L. Pandey, Phys. Rev. C **36**, 44 (1987).

[Han11] H. Hans, *Nuclear Physics: Experimental and Theoretical* (New Academic Science Limited, Kent, 2011), 2nd ed.

[Ive03] J. Ives, *Simulation and Measurement of the Response of the Blowfish Detector to Low-Energy Neutrons*, M.Sc. thesis, University of Saskatchewan, 2003.

[Jam75] F. James and M. Roos, Comput. Phys. Commun. **10**, 343 (1975).

[Jam81] F. James, in *Proceedings of the 6^{th} CERN School of Computing, Vraona-Attiki, 1980*, p. 182.

[Jam94] F. James, *MINUIT, Function Minimization and Error Analysis; Reference Manual* (CERN Computing and Networks Division, 1994), `http://hep.fi.infn.it/minuit.pdf`.

[Kno00] G. Knoll, *Radiation Detection and Measurement* (John Wiley and Sons, Hoboken, 2000), 3rd ed.

[Kor99] E. Korkmaz, G. O'Rielly, D. Hutcheon, G. Feldman, D. Jordan, N. Kolb, R. Pywell, G. Retzlaff, B. Sawatzky, D. Skopik, *et al.*, Nucl. Instrum. Methods **A431**, 446 (1999).

[Kuc10] S. Kucuker, *Photodisintegration of the Deuteron at 20 MeV*, Ph.D. thesis, University of Virginia, 2010.

[Kuk01] V. Kukulin, I. Obukhovsky, V. Pomerantsev, and A. Faessler, Physics of Atomic Nuclei **64**, 1667 (2001).

[Lac81] M. Lacombe, B. Loiseau, R. Vinh Mau, J. Cote, P. Pires, and R. De Tourreil, Phys. Lett. **B101**, 139 (1981).

[Leb07] L. Lebreton, A. Zimbal, and D. Thomas, Radiation Protection Dosimetry **126**, 3 (2007).

[Lei87] W. Leidemann and H. Arenhövel, Nucl. Phys. **A465**, 573 (1987).

[Leo87] W. Leo, *Techniques for Nuclear and Particle Physics Experiments: A How–to Approach* (Springer–Verlag, Berlin/Heidelberg, 1987), 1st ed.

[Lit97] V. Litvinenko, B. Burnham, M. Emamian, N. Hower, J. Madey, P. Morcombe, P. O'Shea, S. Park, R. Sachtschale, K. Straub, *et al.*, Phys. Rev. Lett. **78**, 4569 (1997).

[Mac87] R. Machleidt, K. Holinde, and C. Elster, Physics Reports **149**, 1 (1987).

[Mac11] R. Machleidt and D. Entem, Physics Reports **503**, 1 (2011).

[Mar00] R. Martin, J. Knauer, and P. Balo, Applied Radiation and Isotopes **53**, 785 (2000).

[Mav10] O. Mavrichi, *Photon Flux Monitor for a Mono-energetic Gamma Ray Source*, M.Sc. thesis, University of Saskatchewan, 2010.

[Met49] N. Metropolis and S. Ulam, Journal of the American Statistical Association **44**, 335 (1949).

[Mic89] P. Michel, K. Moeller, J. Moesner, and G. Schmidt, J. Phys. G. **15**, 1025 (1989).

[Mik07] S. Mikhailov, M. Busch, M. Emamian, S. Hartman, Y. Kim, J. Li, V. Popov, G. Swift, P. Wallace, P. Wang, *et al.*, in *Proceedings of the Particle Accelerator Conference, 2007*, published by IEEE, p. 1209.

[Mor97] M. Morháč, J. Kliman, V. Matoušek, M. Veselskỳ, and I. Turzo, Nucl. Instrum. Methods **A401**, 113 (1997).

[Mor00] M. Morháč, J. Kliman, V. Matoušek, M. Veselskỳ, and I. Turzo, Nucl. Instrum. Methods **A443**, 108 (2000).

[Mur95] D. Murray and the Saskatchewan Accelerator Laboratory, *LUCID User's Guide* (University of Saskatchewan, 1995), `http://nucleus.usask.ca/technical_reports/report_index.html`.

[Nag75] M. Nagels, T. Rijken, and J. De Swart, Phys. Rev. D **12**, 744 (1975).

[OSh95] P. O'Shea, F. Carter, C. Dickey, N. Hower, V. Litvinenko, R. Sachtschale, G. Swift, P. Wang, Y. Wu, and J. Madey, in *Proceedings of the Particle Accelerator Conference, 1995*, published by IEEE, Vol. 2, p.1090.

[Par64] F. Partovi, Ann.Phys. **27**, 79 (1964).

[Pat11] S. Patel, *Nuclear Physics: An Introduction* (Anshan, Kent, 2011), 2nd ed.

[Pes95] M. Peskin and D. Schroeder, *An Introduction to Quantum Field Theory* (Addison–Wesley, U.S.A, 1995), 1st ed.

[Pia99] M. Pia, *The Geant4 Object Oriented Simulation Tookit* (CERN, 1999), `http://geant4.web.cern.ch/geant4/results/papers/tampere99-overview.pdf`.

[Pri14] G. Pridham (unpublished), *Subatomic Physics Internal Report 148: Analyzing the New Pulse–Shape Discrimination Algorithm* (2014).

[Pyw] R. Pywell (private communcation).

[Pyw06] R. Pywell, B. Sawatzky, J. Ives, N. Kolb, R. Igarashi, and W. Wurtz, Nucl. Instrum. Methods **A565**, 725, 2006.

[Pyw09a] R. Pywell, O. Mavrichi, W. Wurtz, and R. Wilson, Nucl. Instrum. Methods **A606**, 517 (2009).

[Pyw09b] R. Pywell and W. Wurtz. *Subatomic Physics Internal Report 142: Blowfish Gain Analysis for 2008 Runs* (2009), `http://nucleus.usask.ca/technical_reports/report_index.html`.

[Pyw09c] R. Pywell, *Subatomic Physics Internal Report 140: Calibration of The 5–Paddle Flux Monitor* (2009), `http://nucleus.usask.ca/technical_reports/report_index.html`.

[Pyw11] R. Pywell, *Subatomic Physics Internal Report 146: Calibration and Use of the 5–Paddle Flux Monitor* (2011), `http://nucleus.usask.ca/technical_reports/report_index.html`.

[QGS] `http://geant4.cern.ch/support/proc_mod_catalog/physics_lists/hadronic/QGSP_BERT.html`.

[ROO14] The ROOT Team, *Root User's Guide* (2014), `http://root.cern.ch/drupal/content/users--guide#UG`.

[Ros89] P. Rossi, E. De Sanctis, P. Sandri, N. Bianchi, C. Guaraldo, V. Lucherini, V. Muccifora, E. Polli, A. Reolon, and G. Urciuoli, Phys. Rev. C **40**, 2412 (1989).

[Rou99] P. Rousseeuw and K. Van Driessen, Technometrics **41**, 212 (1999).

[Rud04] M. Rudd, M. Ali, P. Stone, J. Coursey, R. Dragoset, A. Kishore, K. Olsen, A. Sansonetti, G. Wiersma, D. Zucker, Y. Kim, K. Irikura, and M. Zucker, electron–impact cross sections for ionization and excitation, `http://www.nist.gov/pml/data/ionization/`, created: 1997, last updated: 2004.

[Sai] Saint–Gobain Crystals, *Safety and Handling Liquid Scintillators*, `http://www.crystals.saint-gobain.com/uploadedFiles/SG-Crystals/Documents/Operation_Handling/Safety%20and%20Handling%20Liquid%20Scintillators.pdf`.

[Sai08] Saint–Gobain Crystals, *BC–505 Liquid Scintillator* (2008), `http://www.crystals.saint-gobain.com/uploadedFiles/SG-Crystals/Documents/SGC%20Organics%20Brochure.pdf`.

[Sai09] Saint–Gobain Crystals, *BC–501/BC–501A/BC–519 Liquid Scintillator* (2009), `http://www.crystals.saint-gobain.com/uploadedFiles/SG-Crystals/Documents/SGC%20BC501_501A_519%20Data%20Sheet.pdf`.

[Sai11] Saint–Gobain Crystals, *Scintillation Products* (2011), http://www.crystals.saint-gobain.com/uploadedFiles/SG-Crystals/Documents/SGC%20BC505%20Data%20Sheet.pdf.

[Saw05] B. Sawatzky, *A Measurement of the Neutron Asymmetry in $d(\vec{\gamma}, n)p$ Near Threshold*, Ph.D. thesis, University of Virginia, 2005.

[Sch89] K. Schmitt and H. Arenhövel, Few–Body Systems **7**, 95 (1989).

[Sch91] K. Schmitt, P. Wilhelm, and H. Arenhövel, Few–Body Systems **10**, 105 (1991).

[Sch01a] M. Schwamb and H. Arenhövel, Nucl. Phys. **A696**, 556 (2001).

[Sch01b] M. Schwamb and H. Arenhövel, Nucl. Phys. **A690**, 682 (2001).

[Sch01c] M. Schwamb and H. Arenhövel, Nucl. Phys. **A690**, 647 (2001).

[Sko74] D. Skopik, Y. Shin, M. Phenneger, and J. Murphy, Phys. Rev. C **9**, 531 (1974).

[Son13] A. Sonzogni, the National Nuclear Data Center Chart of Nuclides at http://www.nndc.bnl.gov/chart/, retrieved: 2013.

[Ste87] K. Stephenson, R. Holt, R. McKeown, and J. Specht, Phys. Rev. C**35**, 2023 (1987).

[Ste88] N. Stepanov, ITEP Preprint **55**, (1988).

[Tay97] J. Taylor, *An Introduction to Error Analysis: The Study of Uncertainties in Physical Measurements*, (University Science Books, Sausalito, 1997), 2nd ed.

[Tor96] N. Törnqvist and M. Roos, Phys. Rev. Lett. **76**, 1575 (1996).

[Tur01] P. Turner, *Guide to Scientific Computing* (CRC Press, Boca Raton, 2001), 2nd ed.

[Wal69] R. Walker, Phys. Rev. **182**, 1729 (1969).

[Wal04] J. Walecka, *Theoretical nuclear and subnuclear physics* (World Scientific, 2004).

[Wea79] R. Weast (editor), *CRC Handbook of Chemistry and Physics* (CRC Press, Boca Raton, 1979), Vol. 60.

[Wei79] S. Weinberg, Physica A **96**, 327 (1979).

[Wel02] J. Wellisch, QGSP_BERT_HP physics list for Geant4 (2002).

[Wel09] H. Weller, M. Ahmed, H. Gao, W. Tornow, Y. Wu, M. Gai, and R. Miskimen, Progress in Particle and Nuclear Physics **62**, 257 (2009).

[Whe58] A. Whetstone and J. Halpern, Phys. Rev. **109**, 2072 (1958).

[Wir84] R. Wiringa, R. Smith, and T. Ainsworth, Phys. Rev. C **29**, 1207 (1984).

[Won94] C. Wong, International Journal of Modern Physics E **3**, 821 (1994).

[Wur07] W. Wurtz, *RLucid Version 0.4* (2007), `http://nucleus.usask.ca/~ward/RLucid/doc/RLucid--0.4.pdf`.

[Wur10a] W. Wurtz, BlowfishX simulation package for Geant4, `http://nucleus.usask.ca/~ward/`.

[Wur10b] W. Wurtz, *Blowfish–ROOT analysis package version 0.0* (2010), `http://nucleus.usask.ca/~ward/src/bfroot.pdf`.

[Wur10c] W. Wurtz, *Photodisintegration of Lithium Isotopes*, Ph.D. thesis, University of Saskatchewan, 2010.

[XP06] XP2262 Photomultiplier, `http://www.et-enterprises.com/photomultipliers/photonis-photomultipliers`.

[Zuc11] M. Zucker, M. Berger, J. Coursey, and J. Chang, Estar: stopping powers and ranges for electrons, `http://physics.nist.gov/PhysRefData/Star/Text/ESTAR.html`, created: 2009, last updated: 2011.

Appendix A

Photon Interactions with Matter

The photons involved in this experiment are almost entirely in the MeV energy range: lower energy photons ($\lesssim$ 500 keV) are drowned in a sea of noise in our detectors (because the gain is calibrated to the MeV-scale), while higher energy photons ($\gtrsim$ 20 MeV) overflow in our detectors and are thus meaningless; therefore the discussion present here will focus on photons with energies between 500 keV and 18 MeV.

The important photon interaction mechanisms in nuclear physics are: *The Photoelectric Effect*, *Compton Scattering* (off electrons), and *Pair Production* [Kno00].[1] The photons incident on the Five Paddle Beam Flux Monitor are at beam energy (18 MeV), while the photons scattered into Blowfish cells are on the scale of 0.5-2 MeV (by kinematics). The dominant process in this energy regime (0.5-18 MeV) is Compton scattering, followed by pair production (when $E_\gamma \geq 1.022$ MeV); for example, see figure A.1 on the next page.

[1]These processes are well understood and are not worth describing here. They can be found in any introductory nuclear physics text; for example, Knoll [Kno00] has a full description of these processes

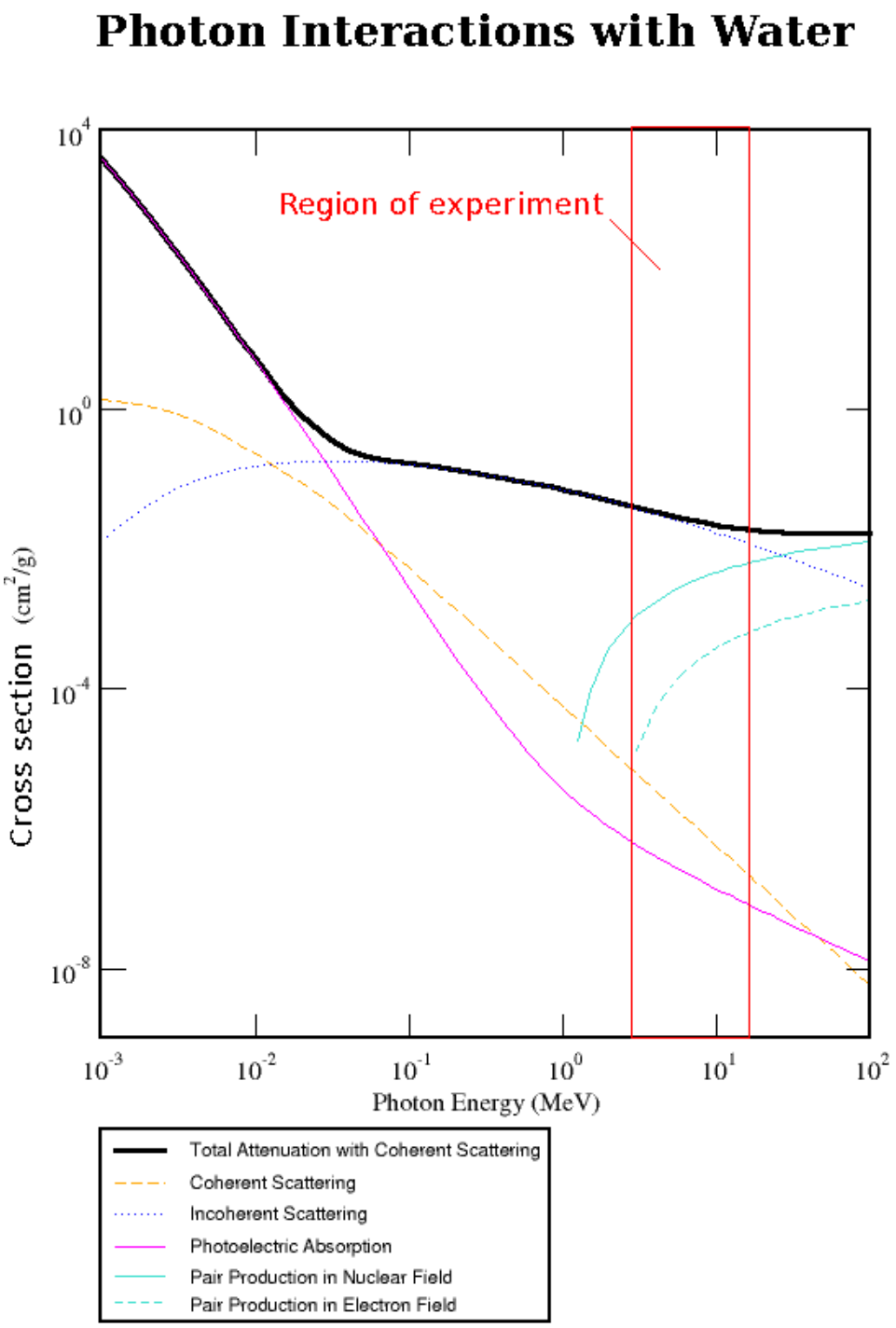

Figure A.1: The cross sections for photon interactions with water (H_2O) as a function of energy are provided for example: the other materials involved in this experiment show similar trends in the relative contribution of photo-processes. We expect Compton scattering to dominate in Blowfish ($\approx$ 1 MeV) and the Five Paddle Flux Monitor (18 MeV); with pair production relevant in the latter and a minor effect in the former (when possible).

We can further characterize the relative probability of an event occurring using the Klein-Nishina Equation for Compton Scattering:

$$\frac{d\sigma}{d\Omega} = Zr_0^2 \left(\frac{1}{1+\alpha(1-cos\theta)} \right)^2 \left(\frac{1+cos^2\theta}{2} \right) \left(1 + \frac{\alpha^2(1-cos\theta)^2}{(1+cos^2\theta)[1+\alpha(1-cos\theta)]} \right) \quad \text{(A.1)}$$

where: Z is the number of protons in the scattering target nucleus, r_0 is the classical Bohr radius, $\alpha = \frac{h\nu}{m_e c^2}$, ν is the incident photon's frequency, m_e is the electron's mass, θ is the scattering angle, and $\frac{d\sigma}{d\Omega}$ is the differential cross section [Kno00].

The energy deposited in a material due to Compton Scattering is described by eq. (A.2):

$$E_{final} = \frac{E_{initial}}{1 + \frac{E_{initial}}{m_e c^2}(1-cos\theta)} \quad \text{(A.2)}$$

where: E is the photon's energy, m_e is the mass of an electron, and θ is the scattering angle [Kno00].

The relative probability of pair production requires a more involved treatment: it was performed by Bethe and Heitler [Bet34, Bet54, Dav54], first in 1934 and subsequently improved upon in 1954. The energy deposited in a material due to pair production depends on the penetrating power of the electron/positron pair in the material and the material's volume.

The probability of an interaction can alternatively be described empirically using models based on available cross section data; data relevant to this experiment can be found in table A.1 (elements) and table A.2 on the next page (materials).

Target Element	Energy (MeV)	Scattering (barns)	Photoelectric (barns)	Pair Production Production (barns)	Total Attenuation (cm^{-1})
^{1}H	18	$3.296 \cdot 10^{-2}$	$4.531 \cdot 10^{-11}$	$5.276 \cdot 10^{-3}$	-
^{1}H	1	$2.114 \cdot 10^{-1}$	0.000	0.000	-
^{16}O	18	$2.636 \cdot 10^{-1}$	$2.193 \cdot 10^{-6}$	$2.146 \cdot 10^{-1}$	-
^{16}O	1	1.691	$1.101 \cdot 10^{-4}$	1.693	-
^{27}Al	18	$4.284 \cdot 10^{-1}$	$2.279 \cdot 10^{-5}$	$5.450 \cdot 10^{-1}$	0.0587
^{27}Al	1	$1.184 \cdot 10^{-3}$	0.000	0.000	0.166
^{12}C	18	$1.977 \cdot 10^{-1}$	$5.345 \cdot 10^{-7}$	$1.244 \cdot 10^{-1}$	-
^{12}C	1	$2.659 \cdot 10^{-5}$	0.000	0.000	-

Table A.1: Photon Attenuation Coefficients for Elements in This Experiment.

Target Material	Energy (MeV)	Scattering (barns)	Photoelectric (barns)	Pair Production (barns)	Total Attenuation (cm^{-1})
Aluminum	18	$4.284 \cdot 10^{-1}$	$2.279 \cdot 10^{-5}$	$5.450 \cdot 10^{-1}$	0.0587
Aluminum	1	$1.184 \cdot 10^{-3}$	0.000	0.000	0.166
Water	18	$3.295 \cdot 10^{-1}$	$2.193 \cdot 10^{-6}$	$2.252 \cdot 10^{-1}$	0.01849
Water	1	2.115	$1.101 \cdot 10^{-4}$	0.000	0.07052
Heavy Water (D_2O)	18	$3.295 \cdot 10^{-1}$	$2.193 \cdot 10^{-6}$	$2.252 \cdot 10^{-1}$	0.01842
Heavy Water (D_2O)	1	2.115	$1.101 \cdot 10^{-4}$	0.000	0.07026
1,2,4-trimethylbenzene	18	2.175	$4.811 \cdot 10^{-6}$	$1.801 \cdot 10^{-1}$	0.01475
1,2,4-trimethylbenzene	1	$1.396 \cdot 10^{1}$	$2.393 \cdot 10^{-4}$	0.000	0.06129
Lucite	18	1.779	$7.059 \cdot 10^{-6}$	$5.363 \cdot 10^{-1}$	0.02040
Lucite	1	$1.142 \cdot 10^{1}$	$3.532 \cdot 10^{-4}$	0.000	0.08112

Table A.2: Photon Attenuation Coefficients for Materials in This Experiment. The materials in this table were present in this experiment as follows. Aluminum: the frame of the Blowfish detector array is made of aluminum, and the Five Paddle Flux Monitor has a aluminum radiator in it. Water and heavy water are both used as targets. 1,2,4-trimethylbenzene is the primary component of the scintillator used (BC-505). Lucite: the target and cell support structures are made out of Lucite.

These data are applied to calculations using eq. (2.3) on page 27. Note that the total attenuation has been measured under detector geometry which is sensitive to low angle scattering (i.e. it ignores low angle scattering as well as high angle scattering), whereas typical detector geometries are not sensitive to this. For example, the target attenuation (D_2O at 18 MeV) in this experiment was estimated using a GEANT4 simulation (section 4.2 on page 105) to be: 0.01604 $\pm$ 0.00015 cm^{-1} for the long target, and 0.015844 $\pm$ 0.000096 cm^{-1} for the short target.

Appendix B

Neutron Interactions with Matter

Neutrons preferentially interact via the strong or weak force: the electromagnetic and gravitational properties of neutrons are simply insufficiently strong to compete with the other two fundamental forces. Our detectors utilize the nuclear force for neutron detection,[1] so we discuss it here.

A neutron in matter can interact via the nuclear force by: scattering, or being absorbed; either of these interactions will lead to an excited nucleus.[2] The energy transfer due to elastic scattering is described kinematically by:

$$E_{recoil} = \frac{4A}{(1+A)^2}\cos^2\theta E_{neutron} \tag{B.1}$$

where: E_{recoil} is the kinetic energy of the recoiling nucleus hit, θ is the angle between the incident neutron and the recoiling nucleus, $E_{neutron}$ is the incident neutron kinetic energy, and $A = \frac{\text{mass of recoil}}{\text{mass of neutron}}$, which is approximately the atomic number of the recoiling nucleus. This equation is only valid non-relativistically [Kno00].

The A^2 term in the denominator of eq. (B.1) means that lighter nuclei are able to absorb more of the incident neutron's energy; this is the main reason why hydrogenous materials are sought-after in neutron detectors (such as the detectors we use). In general, neutron interaction cross sections are proportional to $\frac{1}{v}$ (where v is the speed of the neutron), so materials composed of small A nuclei will not only absorb more energy from a scattering neutron (and hence have a better detector response), but they will also enhance the probability of further scattering.

The energy transfer due to neutron absorption for inelastic scattering must be treated case-by-case by imposing conservation of momentum and energy, and the relevant nuclear energy levels.

Computing the relative probability of a neutron interaction depends on the nucleus involved, and the model used to approximate the nuclear force. Consequently there is no simple formula to predict a scattering or absorption event: thus day-to-day calculations rely on empirical data and eq. (2.3) on page 27 to compute neutron interactions (see table B.1 on the next page for relevant cross section data). We discuss the theoretical predictions for the neutron production cross section in this experiment in section 2.5 on page 28.

[1] The strong force is considered to be equivalent to the nuclear force here as the energies in this experiment are well below quark excitation threshold i.e. pion-production threshold.

[2] I will judiciously assume that we are not dealing with free nucleon scattering. It should also be noted that 'nucleus' includes a proton i.e. the nucleus of hydrogen.

Element/ Compound	Energy (MeV)	Density (g/cm^3)	Atomic Weight (g/mol)	Total Cross Section (barns)	Attenuation Coefficient (cm^{-1})
^{1}H	8	-	1	1.11707	-
^{2}H	8	-	2	1.22053	-
^{16}O	8	-	16	0.865396	-
^{27}Al	8	2.70	27	1.84204	0.111
^{12}C	8		12.00	1.85292	-
H_2O	8	1.008	18	3.1	0.1042
D_2O	8	1.10534	20	3.306	0.1099
$(CH_3)_3C_6H_3$	8	0.8758	120	30.	0.1328(0.05963*)
Lucite $(C_5O_2H_8)_n$	8	1.18	100	20.	0.14

Table B.1: Neutron Cross Sections for Materials in Experiment. 1,2,4-trimethylbenzene: $(CH_3)_3C_6H_3$, is the primary component of BC-505: the scintillator we use in Blowfish. *This is the attenuation coefficient for just hydrogen scattering: the detectors are much less likely to respond to ^{12}C scattering because the recoiling ^{12}C nucleus typically carries less energy than the hardware threshold (depending on the scattering angle).

Appendix C

Full Kinematics Calculation

We perform the kinematic calculations for 18 MeV elastic deuteron photodisintegration.

Steps:

1. Assume the initial state is in the deuteron's lab frame, then transform it into CM frame.
2. Compute $\beta = \frac{v_{frame}}{c}$.
3. Deduce the neutron's CM frame momentum using conservation of energy and momentum. Find an expression for the momentum in terms of the known experimental variables: photon energy/momentum, deuteron rest energy, and CM emission angle, θ (we can later transform the lab frame θ into the CM frame θ i.e. step 5).
4. Transform the neutron's CM frame momentum into the lab frame.
5. Deduce relation between CM frame θ and lab frame θ using trigonometry and expressions from steps 4 and 5.

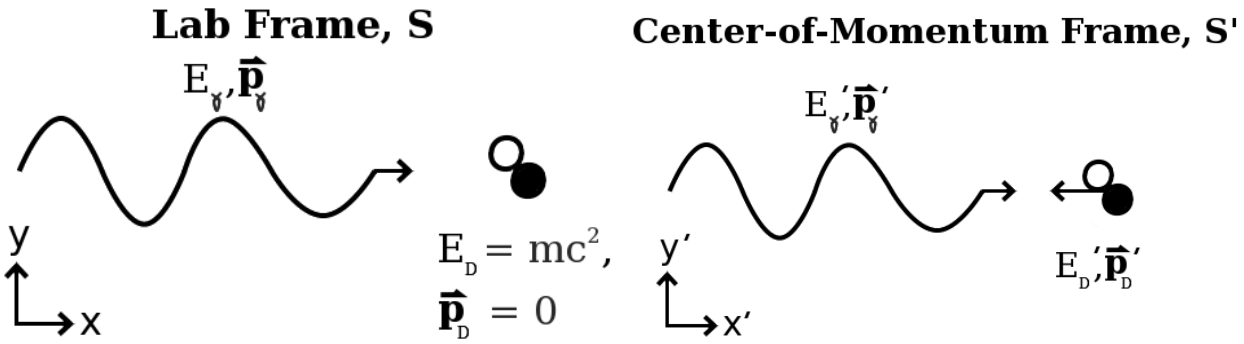

Figure C.1: Deuteron Photodisintegration Kinematics. We take the origin to be at the collision point.

1. We start in the lab frame with:

$$\mathbf{p}_\gamma = p_\gamma \begin{bmatrix} 1 \\ 1 \\ 0 \\ 0 \end{bmatrix}; \quad \mathbf{p}_D = \begin{bmatrix} m_D c \\ 0 \\ 0 \\ 0 \end{bmatrix}$$

then we Lorentz transform using the contravariant boost matrix, L [Wur10c], into the CM frame:

$$\mathbf{p}' = L\mathbf{p}$$
$$L = \begin{bmatrix} \gamma & -\beta\gamma & 0 & 0 \\ -\beta\gamma & \gamma & 0 & 0 \\ 0 & 0 & 1 & 0 \\ 0 & 0 & 0 & 1 \end{bmatrix}; \quad \mathbf{p}'_\gamma = \gamma p_\gamma \begin{bmatrix} 1-\beta \\ 1-\beta \\ 0 \\ 0 \end{bmatrix}; \quad \mathbf{p}'_D = \begin{bmatrix} \gamma m_D c \\ -\gamma\beta m_D c \\ 0 \\ 0 \end{bmatrix}$$

2. We compute β by applying the CM condition:

$$\begin{aligned} p_{\gamma,x}\hat{x} &= -p_{D,x}\hat{x} \\ \implies \gamma p_\gamma(1-\beta) &= \gamma\beta m_D c \\ \implies \beta &= \frac{E_\gamma}{E_\gamma + m_D c^2} \end{aligned} \tag{C.1}$$

where I have substituted in $p_\gamma c = E_\gamma$.

Eq. (C.1) gives $\beta = \frac{0.0095}{\text{c}}$ for this experiment i.e. the CM frame is moving at 0.95% c. As discussed in section 2.5.3 on page 34, the theoretical model we compare to assumes that the deuteron is moving non-relativistically, which we can see is true to the order of $\gamma - 1 = 4.5 \cdot 10^{-5}$.

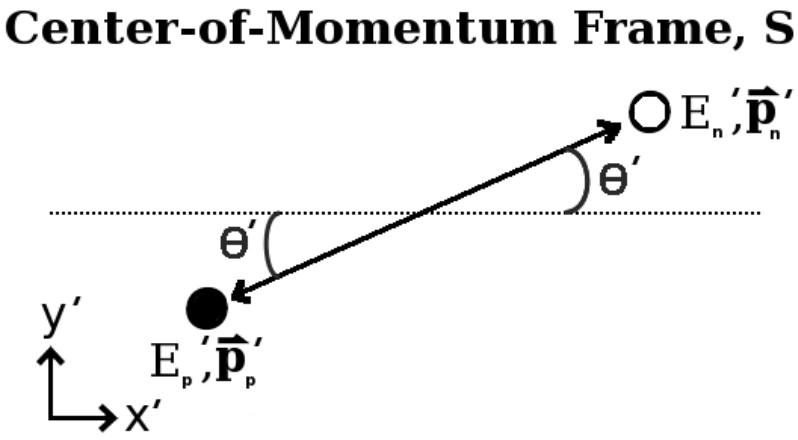

Figure C.2: Center-of-Momentum Frame after Photodisintegration. We take the origin to be the collision point. Proton (black fill), and neutron (white fill).

3. We apply conservation of energy and momentum to deduce the neutron's momentum and energy (assuming an elastic collision):

$$\begin{aligned}
&E' \equiv E'_\gamma + E'_D = E'_n + E'_p, \text{ and } \vec{p}'_\gamma + \vec{p}'_D = 0 = \vec{p}'_n + \vec{p}'_p \\
&\implies (E'_n)^2 = (E' - E'_p)^2 \\
&\implies m_n^2 c^4 = m_p^2 c^4 + E'^2 - 2E'\sqrt{p'^2_n c^2 + m_p^2 c^4} \\
&\implies p'_n = \frac{1}{c}\sqrt{(\frac{E'^2 + (m_p^2 - m_n^2)c^4}{2E'})^2 - m_p^2 c^4}
\end{aligned}$$

from which we can get the energy using $E^2 = p^2c^2 + m^2c^4$.

4. We transform the neutron's 4-momentum back into the lab frame by using the inverse Lorentz Transformation (computed using $L^{-1}L = I$):

$$\begin{aligned}
&\mathbf{p} = L^{-1}\mathbf{p}' \\
&\mathrm{p}_n = \begin{bmatrix} \frac{\gamma}{c}E'_n + \beta\gamma p'_n \cos\theta' \\ \frac{\gamma}{c}\beta E'_n + \gamma p'_n \cos\theta' \\ p'_n \sin\theta' \\ 0 \end{bmatrix}; \quad L^{-1} = \begin{bmatrix} \gamma & \beta\gamma & 0 & 0 \\ \beta\gamma & \gamma & 0 & 0 \\ 0 & 0 & 1 & 0 \\ 0 & 0 & 0 & 1 \end{bmatrix}
\end{aligned} \tag{C.2}$$

5. We use trigonometry to find an expression for θ in terms of CM variables:

$$\begin{aligned}
&p_{n,x} = p_n \cos\theta \\
&p_{n,y} = p_n \sin\theta \\
&\implies \tan\theta = \frac{p_{n,y}}{p_{n,x}}
\end{aligned}$$

we can sub in using eq. (C.2) on page 286 to get θ as a function of CM variables:

$$\tan\theta = \frac{p'_n \sin\theta'}{\frac{\gamma}{c}\beta E'_n + \gamma p'_n \cos\theta'}$$

Kinematics summary:

$$\begin{aligned}
\beta &= \frac{E_\gamma}{E_\gamma + m_D c^2} \approx 0.0095 \text{ (for } E_\gamma = 18 \text{ MeV)} \\
E'_\gamma &= \gamma E_\gamma (1-\beta) \\
E'_D &= \gamma m_D c^2 \\
E' &= E'_\gamma + E'_D \\
p'_n &= \frac{1}{c}\sqrt{(\frac{E'^2 + (m_p^2 - m_n^2)c^4}{2E'})^2 - m_p^2 c^4} \\
\mathbf{p}_n &= \begin{bmatrix} \frac{\gamma}{c}E'_n + \beta\gamma p'_n \cos\theta' \\ \frac{\gamma}{c}\beta E'_n + \gamma p'_n \cos\theta' \\ p'_n \sin\theta' \\ 0 \end{bmatrix} = \begin{bmatrix} \frac{E_n}{c} \\ p_{n,x} \\ p_{n,y} \\ 0 \end{bmatrix} \\
\theta &= \arctan\left(\frac{p_{n,y}}{p_{n,x}}\right) \\
E_n &= \sqrt{p_n^2 c^2 + m_n^2 c^4}
\end{aligned} \tag{C.3}$$

C.1 Lorentz Transformation between Frames

We used kinematics to derive a transformation between the CM and lab frames for the angles θ and ϕ.

ϕ is perpendicular to the motion of the frame, so:

$$\phi_{lab} = \phi_{CM}$$

Using kinematics:

$$\cos\theta_{lab} = \frac{\beta\gamma E^n_{CM} + \gamma p^n_{CM}\cos\theta_{CM}}{p^n_{lab}(\theta_{CM})} \tag{C.4}$$

where: E^n is the neutron's energy, p^n is the neutron's momentum, $\gamma = \frac{1}{\sqrt{1-\beta^2}}$, and $\beta = \frac{v}{c}$.

A rigorous treatment of the transformation of a probability density function from the CM to Lab Frame is achieved through the use of the Jacobian:

$$\rho_{CM} = \rho_{lab} \cdot |\frac{d\Omega_{lab}}{d\Omega_{CM}}| \tag{C.5}$$

which is given by differentiating eq. (C.4).

Proof.

$$\begin{aligned}
\rho_{CM} &\equiv \frac{dn}{dS} \\
&= \frac{dn}{d\Omega_{CM}} \\
&= \frac{dn}{d\Omega_{lab}} \cdot |\frac{d\Omega_{lab}}{d\Omega_{CM}}| \\
&= \rho_{lab} \cdot |\frac{d\Omega_{lab}}{d\Omega_{CM}}|
\end{aligned}$$

where: ρ is a PDF, S is the surface area, $d\Omega$ is a solid angle surface area element, and n is the number of particles. □

Appendix D

The High Intensity Gamma Source (HI$\vec{\gamma}$S) Metrics

We summarize the primary components of the HI$\vec{\gamma}$S facility here, including the: linear accelerator, booster ring, storage ring, and FEL.

Linear Accelerator [OSh95]

Max Energy	0.295 GeV
Energy Spread	0.2%
Energy Jitter	<0.1%
RF Frequency	2856.76 MHz
Electron Gun	Thermionic RF with α-magnet
Pulse Current	40 mA

Booster Ring [Mik07]

Max Beam Energy	1.2 GeV
Energy Spread at Max $\frac{\Delta E}{E}$	$6.8{\cdot}10^{-4}$
Circumference	31.902 m
RF Frequency	178.55 MHz
Number of Buckets	19

Storage Ring [Wel09]

Energy Range	0.24-1.2 GeV
Circumference	107.46 m
RF Frequency	178.547 MHz
Number of Buckets	64
Trajectory Spacing	5.6 ns
Max Current (one bunch)	95 mA
Max Current (two bunches)	> 80 mA

Table D.1: HI$\vec{\gamma}$S Metrics. Definitions: RF: Radio-frequency, used to describe the oscillation of the applied electric potential. Buckets: the number of nodes in the oscillating potential (i.e. potential energy minimums, see section 3.3.1 on page 58 for details).

Free-electron Laser [Wel09]	
Gamma Ray Energy	
Operational Range	1-158 MeV
Used (this experiment)	18.00 ± 0.27 MeV
Polarization	>95%
Gamma Ray Burst Frequency	5.58 MHz
Number of Wigglers	4 (2 of each polarity)
Max Magnetic Field of Wigglers	0.286 T (at 3 kA)
Resonant Cavity Length	53.73 m
Resonant Wavelengths	1064-190 nm
Optical Beam Size (σ)	
At 1064 nm	0.61-0.68 mm
At 190 nm	0.26-0.29 mm
Electron Beam Size (σ)	
Horizontal	0.14-0.40 mm
Vertical	0.02-0.07 mm

Table D.2: HI$\vec{\gamma}$S FEL Metrics. There are two available polarities: horizontal and circular. The FEL gamma ray energy refers to the energy of the Compton backscattered photons that leave the optical cavity.

Appendix E

GEANT4 Example

Using the BlowfishX implementation, a neutron was simulated starting inside a D_2O target with 8.49 MeV of kinetic energy moving in some direction. GEANT4 computes the trajectory of the instantiated particle (in this case the 8.49 MeV neutron) using discrete steps in space through the materials specified in the toolkit implementation, until it finally leaves the world volume in one way or another. The verbatim output from GEANT4 is provided in table E.1 on the next page, and example GUI output is provided in figure E.1.

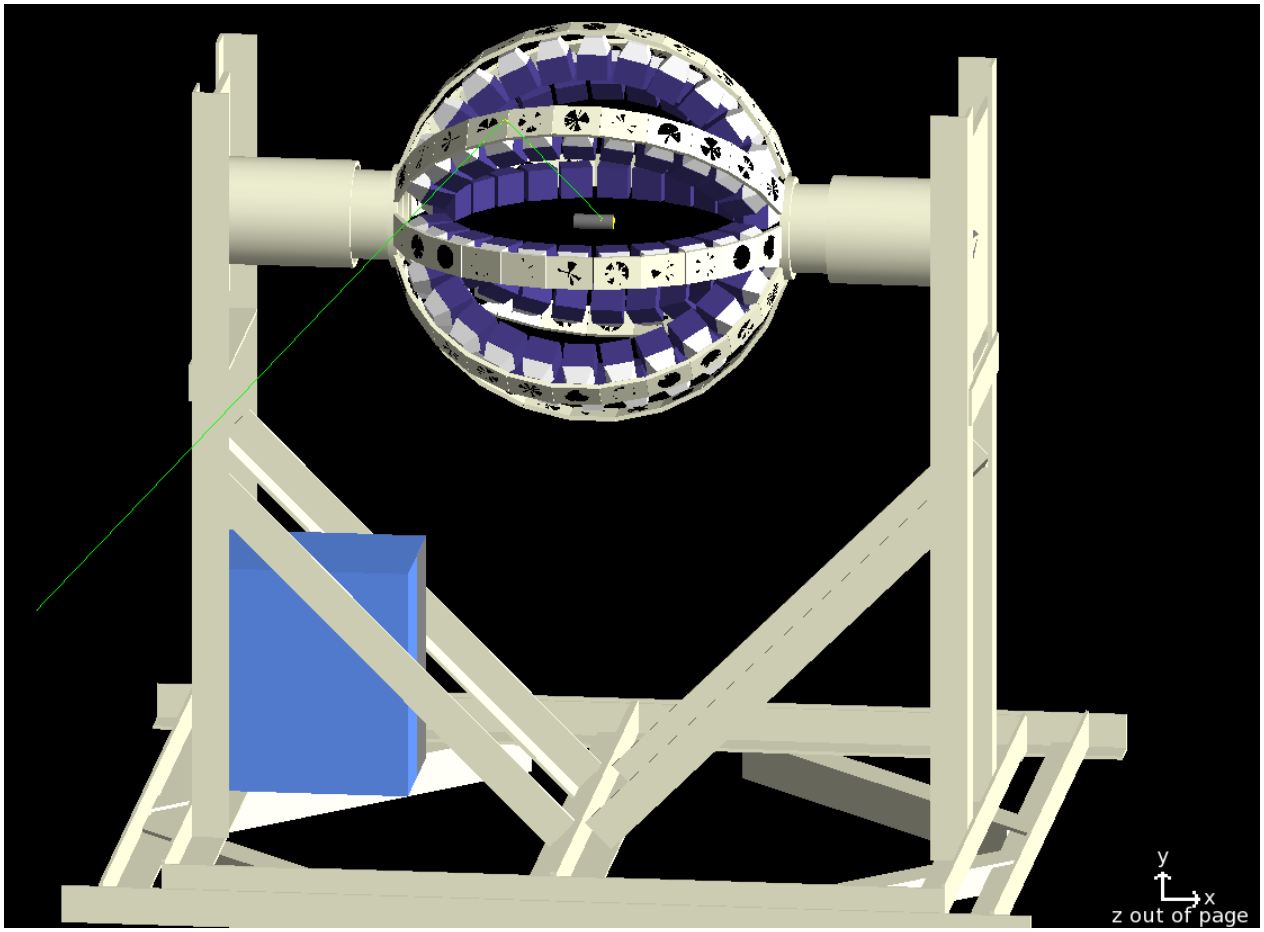

Figure E.1: GEANT4 Output Example. A neutron (green line) is simulated as leaving the target with some definite position and momentum, striking the aluminum frame and then scattering out of the world volume. This graphic was taken from a different; though similar, simulation than the output table (table E.1 on the next page).

Table E.1: GEANT4 Output Example. The initial particle (an 8.49 MeV neutron) proceeded step-by-step through the world volume, interacting with materials as it went. Notice that at step 17 there was an event named `hadElastic`, this was an elastic scattering event between the incident particle (the neutron) and another hadron. In this case, a proton was separated from whatever material the neutron interacted with. When a separation event occurs, a new particle is created with energy and momentum determined from the event, then it too is tracked just as the neutron was; thus cascading into a series of particles. When the proton was separated at step 17, a proton was generated at the same point in space (x = -339 mm, y = 247 mm and z = 259 mm) with kinetic energy and momentum determined by kinematics. This proton was then tracked, as you can see.

* G4Track Information: Particle = neutron, Track ID = 1, Parent ID = 0

Step	X(mm)	Y(mm)	Z(mm)	KinE(MeV)	dE(MeV)	StepLeng	TrackLeng	NextVolume	ProcName
0	32.6	-8.9	2.45	8.49	0	0	0	Target	initStep
1	36	-12	6.21	7	0	5.95	5.95	Target	hadElastic
2	-2.13	4.58	19	7	0	43.5	49.5	TargetWall	Transportation
3	-2.58	4.77	19.1	7	0	0.512	50	ExpHallPhys	Transportation
4	-340	152	132	7	0	385	435	ArrayContainerPhys	Transportation
5	-350	155	135	7	0	10.3	446	CellContainerPhys	Transportation
6	-352	156	136	7	0	2.35	448	CellWrapPhys	Transportation
7	-352	157	136	7	0	1.01	449	CellLucitePhys	Transportation
8	-363	161	140	6.04	0	12	461	CellLucitePhys	hadElastic
9	-361	163	141	6.04	0	2.5	464	CellActivePhys	Transportation
10	-354	173	144	2.82	0	12.6	476	CellActivePhys	hadElastic
11	-347	215	207	2.82	0	76.5	553	CellLucitePhys	Transportation
12	-347	217	210	2.82	0	3.77	556	CellWrapPhys	Transportation
13	-347	218	211	2.82	0	1.19	558	CellContainerPhys	Transportation
14	-344	237	239	2.82	0	34	592	NeutronCellPhys	Transportation
15	-343	239	243	2.82	0	4.2	596	CellLightGuidePhys	Transportation
16	-342	248	255	1.17	0	14.8	611	CellLightGuidePhys	hadElastic
17	-339	247	259	1.09	0	5.43	616	CellLightGuidePhys	hadElastic
18	-318	251	298	1.09	0	44	660	NeutronCellPhys	Transportation
19	-310	253	314	1.09	0	18.2	678	CellContainerPhys	Transportation
20	-310	253	314	1.09	0	0.453	679	ArmAssContainerPhys	Transportation
21	-307	254	319	1.09	0	5.3	684	ArrayContainerPhys	Transportation
22	-213	274	496	1.09	0	202	886	ExpHallPhys	Transportation
23	849	500	2.5e+03	1.09	0	2.28e+03	3.16e+03	OutOfWorld	Transportation

* G4Track Information: Particle = proton, Track ID = 6, Parent ID = 1

Step	X(mm)	Y(mm)	Z(mm)	KinE(MeV)	dE(MeV)	StepLeng	TrackLeng	NextVolume	ProcName
0	-339	247	259	0.0816	0	0	0	CellLightGuidePhys	initStep
1	-339	247	259	0	0.0816	0.00104	0.00104	CellLightGuidePhys	hIoni

Appendix F

Target Attenuation Probability Density Functions

In order to simulate the beam attenuation due to atomic scattering, we used inverse transform sampling (section 4.4.3 on page 141): this requires the correct attenuation probability density function (PDF), its corresponding cumulative distribution function (CDF), and the subsequent inverse of the CDF (CDF^{-1}).

We simulated neutrons, so it was necessary to determine the PDF for neutron emission from an attenuated beam of photons. Starting from the definition of cross section:

$$\sigma \equiv \frac{A \cdot P}{\Gamma} \tag{F.1}$$

where: A is the total target area, P is the probability of an interaction and Γ is the number of target nuclei within the target. The cross section, σ is the effective target size that the projectile encounters.

Now consider N photons at position x, the next infinitesimal step (dx) produces a change in photons (dN) via a cross section σ:

$$\begin{aligned} \frac{dN}{N} &= -\frac{\sigma\Gamma}{A} \\ &= -\frac{\sigma\rho n A dx}{A} \\ &= -\sigma\rho n dx \end{aligned} \tag{F.2}$$

where: A is the total target area, $\Gamma = \rho n$ is the number of target nuclei within the encountered volume, ρ is the mass density, n is the number density, and σ is the target cross section.

Let σ be the total cross section for neutron production via photodisintegration, then the change in the number of total neutrons produced (dN_n) with respect to the step (dx) is:

$$\frac{dN_n}{dx} = -\frac{dN}{N \cdot dx} = \sigma\rho n \tag{F.3}$$

where: dN_n is the number of neutrons produced during the step, N is the number of incident photons at position x, σ is the respective cross section for the process and ρn is the target density.

Since the number of neutrons is an integer, eq. (F.3) is valid only if we interpret $\frac{dN_n}{dx}$ as a probability density function (PDF), thus allowing dN_n to take on any real value. In order for $\frac{dN_n}{dx}$ to satisfy the neutron production PDF, it must first be normalizing by the neutron production for the entire target length. Before this can be achieved, though, we first needed to determine $N(x)$: the number of gammas at position x. If one considers all

possible processes for photon absorption (σ_{total}), then eq. (F.2) on page 293 can be solved via integration, giving:

$$N = N_0 e^{-\mu x} \tag{F.4}$$

where: N_0 is the number of incident particles, N is the number of particles at position x and $\mu \equiv \sigma_{total}\rho n$ [Pat11].

Note that the 18 MeV photon attenuation coefficient under good geometry [Ber11] is a good approximation for the attenuation under our experimental geometry, but the correct coefficient is $\approx 10\%$ smaller (see section 5.5 on page 211 for details).

Now all of the pieces of the puzzle are available and the neutron production PDF can be defined using:

$$\begin{aligned} f(x) &= \frac{\frac{dN_n}{dx}}{\int_0^l \frac{dN_n}{dx} dx} \\ \mu &\approx 0.02 cm^{-1}, \sigma\rho n \approx 3 \cdot 10^{-6} cm^{-1} \implies \mu >> \sigma\rho n \\ &\implies f(x) = \frac{\sigma\rho e^{-\mu x}}{1 - e^{-\mu l}} \end{aligned} \tag{F.5}$$

where we have assumed that the attenuation due to nuclear effects (σ) is negligible. Noting that the PDF criteria (theorem 1 on page 116) are met: $f : \mathbb{R} \mapsto [0, \infty)$, and $\int_{-\infty}^{\infty} f(x)dx = 1$.

The simulation is implemented using Inverse Transform Sampling (section 4.4.3 on page 141), which requires the inverse cumulative distribution function (CDF):

$$\begin{aligned} C(x) &\equiv \int_{-\infty}^{x} f(x')dx' \\ &\implies C(x) = \frac{1 - e^{-\mu x}}{1 - e^{-\mu l}} \end{aligned} \tag{F.6}$$

Eq. (F.6) has an analytical inverse:

$$\begin{aligned} C^{-1}(x) &= -\frac{1}{\mu}\ln(1 - x + xe^{-\mu l}) \\ &\implies C^{-1}(u) = -\frac{1}{\mu}\ln(1 - u + ue^{-\mu l}) \text{ is the correct sampling function.} \end{aligned} \tag{F.7}$$

Using a pseudo-random number generator provided by the GEANT4 toolkit, target attenuation was implemented using eq. (F.7).

Appendix G

Gain Tracking Principle

We demonstrate why the Gain Monitoring System has to assume a constant ratio of light in order to track cell gains by presenting a derivation given in SPIR-142 [Pyw09b]. A full description of the Gain Monitoring System hardware is given in section 3.10.3 on page 97, and its operation is described in section 5.3.3 on page 165.

The pulser drives each flasher, causing them to output pulses of light from the LED, through the fiber optics and into the Blowfish cells and GSO crystals. The LED intensity may drift over time. Consider only one of the four LEDs and suppose that it outputs some amount of light, L, and a fraction of that light x_i reaches cell i which has gain g_i; then the LED peak will appear in ADC bin A_{Fi}:

$$A_{Fi} = \frac{x_i L}{g_i}$$

Meanwhile, we continuously determine the gain of the GSO crystal using a radioactive source: suppose that the feature we fit to has energy E and appears in ADC bin A of the GSO detector, then; by definition, the gain of the GSO detector is g:

$$g = \frac{E}{A}$$

Some fraction of the light, L, is also sent from the LED into the GSO detector; let that fraction be x, let A_F be the bin it appears in:

$$A_F = \frac{xL}{g}$$

We can determine g using the flash monitor radioactive source, and we can determine the gain of the Blowfish cells g_i by taking a radioactive source run. Using source run data we define R_i as the ratio of light received by cell i over the ratio received by the GSO detector:

$$R_i \equiv \frac{x_i}{x} = \frac{g_i A_{Fi}}{g A_F}$$

Now we wish to determine the gain during a data run with no radioactive source to calibrate the cells and determine g_i. Consider a data run some time after the source run. Let L' be the light produced by an LED, let g'_i be the new cell gain, and let g' be the new GSO gain. We can determine g' as above using:

$$g' = \frac{E}{A'}$$

Where E is the feature from the radioactive source in continuous use and A' is the ADC bin where that feature appeared.

The flasher produces a peak in cell i at ADC bin A'_{Fi} that is proportional to the light: L', the gain: g'_i and the new ratio of sent down the fiber optic: x'_i:

$$A'_{Fi} = \frac{x'_i L'}{g'_i}$$

Similarly, the flasher produces a peak in the GSO detector at channel A'_F:

$$A'_F = \frac{x' L'}{g'}$$

Solving for the cell gain: g'_i yields:

$$g'_i = g' \frac{A'_F}{A'_{Fi}} \frac{x'_i}{x'} = g' \frac{A'_F}{A'_{Fi}} R'_i$$

We can go no further: we know g', A'_F and A'_{Fi}, but we don't know R'_i. In order to determine the new cell gain, we must assume that the ratio of light reaching the GSO detector and cell i: R_i remains constant i.e. $R_i = R'_i$. With this assumption we have:

$$g'_i = g' R_i \frac{A'_F}{A'_{Fi}} \tag{G.1}$$

Thus after we take a source run to determine R_i, we can determine the cell gains at any subsequent time *so long as R_i remains constant*

.

Appendix H

Light Scaling Factors

The light scaling factors used in this experiment are given in this section. The calibrated ADC value for each measured event was scaled by the appropriate cell-dependent factor in table H.1 (depending on which cell the event was measured by) before any cuts were applied. A full description of what light scaling factors are and why they were used can be found in section 5.3.2 on page 161.

Cell:	Factor	Cell:	Factor	Cell:	Factor	Cell:	Factor
1:	1.093	23:	1.106	45:	1.065	67:	1.143
2:	1.075	24:	1.090	46:	1.063	68:	1.049
3:	1.092	25:	1.040	47:	1.125	69:	1.052
4:	1.074	26:	1.070	48:	1.076	70:	1.019
5:	1.085	27:	1.076	49:	1.031	71:	1.090
6:	1.067	28:	1.078	50:	1.000	72:	1.039
7:	1.181	29:	1.058	51:	1.065	73:	1.014
8:	1.116	30:	1.089	52:	1.056	74:	1.039
9:	1.000	31:	1.086	53:	1.034	75:	1.158
10:	1.061	32:	1.100	54:	1.036	76:	1.035
11:	1.143	33:	1.192	55:	1.027	77:	1.194
12:	1.095	34:	1.055	56:	1.061	78:	1.016
13:	1.074	35:	1.111	57:	1.022	79:	1.423
14:	1.089	36:	1.083	58:	1.159	80:	1.017
15:	1.033	37:	1.069	59:	1.047	81:	1.082
16:	1.095	38:	1.064	60:	1.213	82:	1.118
17:	1.048	39:	1.041	61:	1.060	83:	1.000
18:	1.053	40:	1.070	62:	1.044	84:	1.000
19:	1.061	41:	1.042	63:	1.077	85:	1.054
20:	1.051	42:	1.058	64:	1.066	86:	1.040
21:	1.074	43:	1.074	65:	1.009	87:	1.000
22:	1.054	44:	1.059	66:	1.000	88:	1.184

Table H.1: Cell-by-Cell Light Scaling Factors.

Appendix I

Cell Exclusions

The actual cell exclusion tables for this experiment are given in this section. A full description of the reasons for cell exclusions can be found in section 5.4.7 on page 209

Table I.1: Cell Exclusions for Runs 142-149 (Long Target)

Run	Reason for Exclusion	Cell(s) Excluded
142	Any (total)	1, 6, 7, 8, 9, 11, 14, 15, 19, 22, 25, 26, 30, 32, 50, 56, 58 65, 67, 69, 73, 74, 76, 78, 81, 82, 83, 84, 85, 86, 87, 88
	PSD	7, 9, 25
	TDC	9, 11, 14, 15, 22, 26, 30, 56, 58, 82, 84
	Gain	9, 32, 58
	Empty	87
	OOT Photons	1, 6, 8, 19, 25, 50, 56, 65, 67, 69, 73, 74, 76, 78, 81, 82, 83, 84, 85, 86, 88
143	Any (total)	1, 6, 7, 9, 11, 14, 15, 18, 19, 22, 25, 26, 30, 32, 50, 51, 52, 56, 58, 59, 62, 65, 66, 67, 69, 72, 73, 74, 76, 78, 81, 82, 83, 84, 85, 86, 87, 88
	PSD	7, 9, 25
	TDC	9, 11, 14, 15, 22, 26, 30, 56, 58, 82, 84
	Gain	9, 32, 58
	Empty	87
	OOT Photons	1, 6, 14, 18, 19, 22, 50, 51, 52, 56, 59, 62, 65, 66, 67, 69, 72, 73, 74, 76, 78, 81, 82, 83, 84, 85, 86, 88
149	Any (total)	1, 5, 6, 8, 9, 11, 14, 15, 18, 19, 20, 22, 25, 26, 30, 32, 40, 50, 51, 53, 54, 55, 56, 58, 62, 65, 66, 67, 69, 71, 72, 73, 74, 75, 76, 78, 79, 80, 81, 82, 83, 84, 85, 86, 87, 88
	PSD	6, 8, 9, 19, 25, 56
	TDC	9, 11, 14, 15, 22, 26, 30, 56, 58, 82, 84
	Gain	9, 32, 58
	Empty	87
	OOT Photons	1, 5, 6, 8, 18, 19, 20, 22, 25, 40, 50, 51, 53, 54, 55, 56, 62, 65, 66, 67, 69, 71, 72, 73, 74, 75, 76, 78, 79, 80, 81, 82, 83, 84, 85, 86, 88

Table I.2: Cell Exclusions for Runs 150-153 (Long Target)

Run	Reason for Exclusion	Cell(s) Excluded
150	Any (total)	1, 5, 6, 8, 9, 11, 14, 15, 18, 19, 22, 25, 26, 30, 32, 40, 47, 49, 50, 51, 53, 54, 55, 56, 58, 62, 65, 66, 67, 69, 71, 72, 73, 74, 75, 76, 78, 79, 81, 82, 83, 84, 85, 86, 87, 88
	PSD	6, 8, 9, 19, 25, 56
	TDC	9, 11, 14, 15, 22, 26, 30, 56, 58, 82, 84
	Gain	9, 32, 58
	Empty	87
	OOT Photons	1, 5, 6, 8, 14, 18, 19, 25, 40, 47, 49, 50, 51, 53, 54, 55, 56, 62, 65, 66, 67, 69, 71, 72, 73, 74, 75, 76, 78, 79, 81, 82, 83, 84, 85, 86, 88
152	Any (total)	1, 6, 8, 9, 11, 14, 15, 18, 19, 22, 25, 26, 30, 32, 50, 53, 55, 56, 58, 64, 65, 66, 67, 69, 72, 73, 74, 75, 78, 81, 82, 83, 84, 85, 86, 87, 88
	PSD	6, 8, 9, 19, 25, 56
	TDC	9, 11, 14, 15, 22, 26, 30, 56, 58, 82, 84
	Gain	9, 32, 58
	Empty	87
	OOT Photons	1, 6, 8, 14, 18, 19, 22, 25, 50, 53, 55, 56, 64, 65, 66, 67, 69, 72, 73, 74, 75, 78, 81, 82, 83, 84, 85, 86, 88
153	Any (total)	1, 6, 8, 9, 11, 14, 15, 18, 19, 22, 25, 26, 30, 32, 50, 51, 53, 56, 58, 62, 65, 66, 67, 69, 71, 73, 74, 76, 78, 81, 82, 83, 84, 85, 86, 87, 88
	PSD	6, 8, 9, 19, 25, 56
	TDC	9, 11, 14, 15, 22, 26, 30, 56, 58, 82, 84
	Gain	9, 32, 58
	Empty	87
	OOT Photons	1, 6, 14, 18, 19, 25, 50, 51, 53, 56, 62, 65, 66, 67, 69, 71, 73, 74, 76, 78, 81, 82, 83, 84, 85, 86, 88

Table I.3: Cell Exclusions for Run 154 (Long H_2O Target)

154	Any (total)	1, 6, 8, 14, 18, 19, 25, 33, 42, 45, 46, 50, 51, 53, 54, 55, 56, 57, 62, 64, 65, 66, 67, 69, 70, 71, 72, 73, 74, 75, 76, 78, 79, 81, 82, 83, 84, 85, 86, 88
	PSD	6, 8, 9, 19, 25, 56
	TDC	9, 11, 14, 15, 22, 26, 30, 56, 58, 82, 84
	Gain	9, 32, 58
	Empty	87
	OOT Photons	1, 6, 8, 14, 18, 19, 25, 33, 42, 45, 46, 50, 51, 53, 54, 55, 56, 57, 62, 64, 65, 66, 67, 69, 70, 71, 72, 73, 74, 75, 76, 78, 79, 81, 82, 83, 84, 85, 86, 88

Table I.4: Cell Exclusions for Runs 155-157 (Short Target)

Run	Reason for Exclusion	Cell(s) Excluded
155	Any (total)	1, 6, 8, 9, 11, 14, 15, 18, 19, 20, 22, 25, 26, 30, 32, 50, 54, 56, 58, 62, 65, 67, 69, 71, 73, 74, 75, 78, 80, 81, 82, 83, 84, 85, 86, 87, 88
	PSD	6, 8, 9, 19, 25, 56
	TDC	9, 11, 14, 15, 22, 26, 30, 56, 58, 82, 84
	Gain	9, 32, 58
	Empty	87
	OOT Photons	1, 6, 8, 14, 18, 19, 20, 25, 50, 54, 56, 62, 65, 67, 69, 71, 73, 74, 75, 78, 80, 81, 82, 83, 84, 85, 86, 88
157	Any (total)	1, 3, 4, 5, 6, 7, 8, 9, 11, 14, 15, 18, 19, 20, 21, 22, 25, 26, 30, 32, 40, 42, 50, 53, 55, 56, 58, 62, 65, 66, 67, 69, 71, 72, 73, 74, 75, 76, 78, 79, 80, 81, 82, 83, 84, 85, 86, 87, 88
	PSD	6, 8, 9, 19, 25, 56
	TDC	9, 11, 14, 15, 22, 26, 30, 56, 58, 82, 84
	Gain	9, 32, 58
	Empty	87
	OOT Photons	1, 3, 4, 5, 6, 7, 8, 14, 18, 19, 20, 21, 25, 40, 42, 50, 53, 55, 56, 62, 65, 66, 67, 69, 71, 72, 73, 74, 75, 76, 78, 79, 80, 81, 82, 83, 84, 85, 86, 88

Table I.5: Cell Exclusions for Runs 158-159 (Short Target)

Run	Reason for Exclusion	Cell(s) Excluded
158	Any (total)	1, 3, 4, 5, 6, 7, 8, 9, 10, 11, 14, 15, 18, 19, 20, 22, 25, 26, 30, 32, 37, 45, 50, 51, 53, 56, 58, 62, 65, 66, 67, 69, 71, 72, 73, 74, 75, 76, 77, 78, 79, 80, 81, 82, 83, 84, 85, 86, 87, 88
	PSD	6, 8, 9, 19, 25, 56
	TDC	9, 11, 14, 15, 22, 26, 30, 56, 58, 82, 84
	Gain	9, 32, 58
	Empty	87
	OOT Photons	1, 3, 4, 5, 6, 7, 8, 9, 10, 14, 18, 19, 20, 25, 37, 45, 50, 51, 53, 56, 62, 65, 66, 67, 69, 71, 72, 73, 74, 75, 76, 77, 78, 79, 80, 81, 82, 83, 84, 85, 86, 87, 88
159	Any (total)	1, 3, 5, 6, 7, 8, 9, 11, 14, 15, 18, 19, 20, 22, 25, 26, 30, 32, 50, 53, 56, 58, 65, 66, 67, 69, 72, 73, 74, 75, 78, 79, 80, 81, 82, 83, 84, 85, 86, 87, 88
	PSD	6, 8, 9, 19, 25, 56
	TDC	9, 11, 14, 15, 22, 26, 30, 56, 58, 82, 84
	Gain	9, 32, 58
	Empty	87
	OOT Photons	1, 3, 5, 6, 7, 8, 14, 18, 19, 20, 25, 50, 53, 56, 65, 66, 67, 69, 72, 73, 74, 75, 78, 79, 80, 81, 82, 83, 84, 85, 86, 87, 88

Appendix J

Simulation Consistency Checks

Previous researchers have performed consistency checks on the simulation of Blowfish (see section 4.2.4 on page 110). We have performed additional consistency checks in order to both provide additional evidence for future researchers, and to verify the internal consistency of this experiment. For the first time, we have verified the probability density function implementation method (i.e. primary generator action) in GEANT4 by comparing the results of two different particle generating classes, and we've also performed numerous internal consistency checks between the simulated and experimental data to ensure that they match.

The probability density function implementation (see section 4.3 on page 114 for details) was tested for consistency by performing the same implementation using two different methods that utilized two different classes (G4ParticleGun and G4GeneralizedParticleSource; discussed in section 4.3 on page 114). The Legendre PDFs (probability density functions; see section 4.4.2 on page 119 for details) were simulated via both implementations and they were found to agree within statistical error *so long as target attenuation of the beam was not included*.[1] For example, the yield of a relatively complex Legendre PDF (ρ_{22}) is shown in figure J.1 on the next page.

[1]The reason for this discrepancy is: a linear approximation for target attenuation was used in the G4GeneralizedParticleSource implementation; it was eventually abandoned for this reason

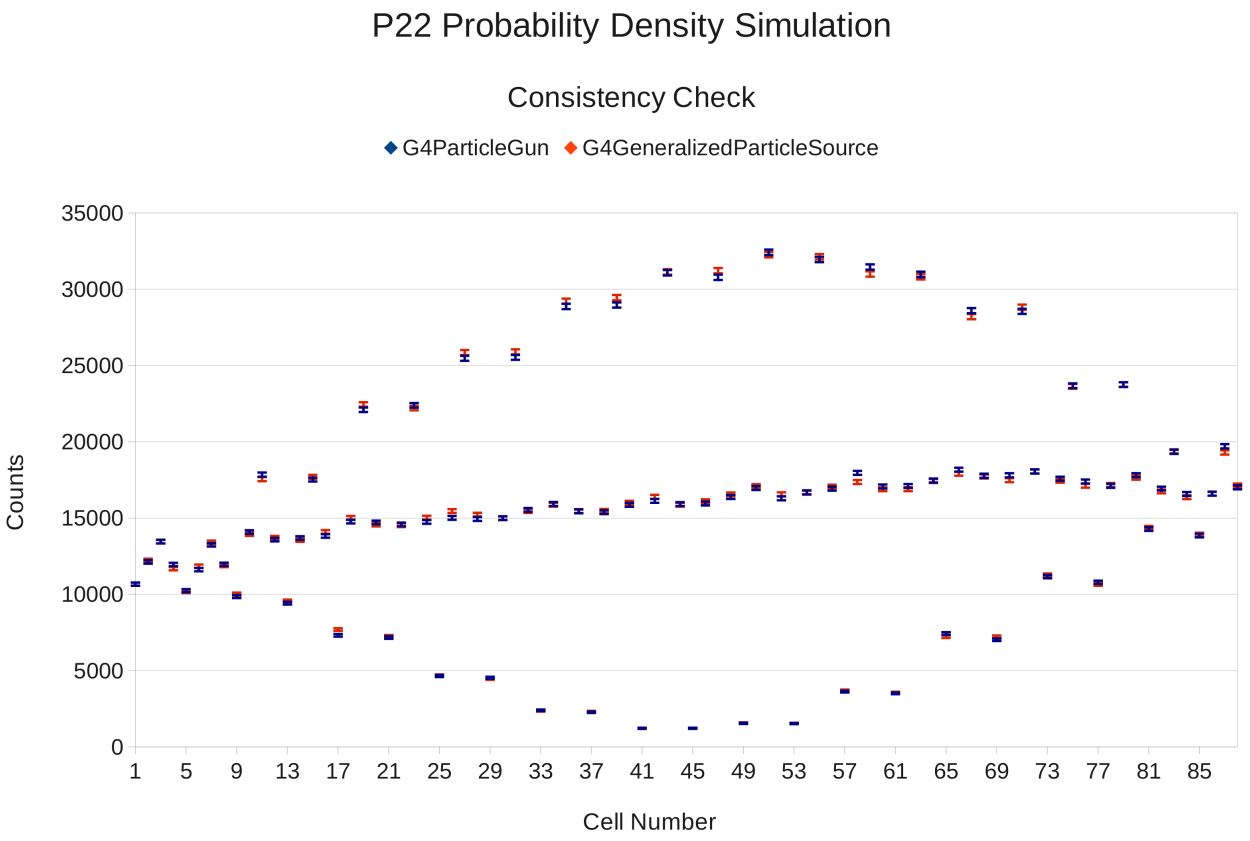

Figure J.1: Particle Generation Consistency Check. A comparison between the output of two different simulation implementations of the Legendre PDFs: one using the G4ParticleGun class of GEANT4, and the other using the G4GeneralizedParticleSource class.

The quantitative comparison between the two implementations is provided in table J.1.

Error Interval	Cells in Agreement (of 88)	Expected Cells in Agreement (of 88)
1σ	64	60 (68.2%)
1.5σ	85	76 (86.6%)
2σ	86	84 (95.4%)
3σ	88	88 (99.8%)

Table J.1: Particle Generation Consistency Check. The output of two different simulation implementations of the ρ_{22} Legendre PDF: one using the G4ParticleGun class of GEANT4, and the other using the G4GeneralizedParticleSource class were compared to see if their error intervals (in standard deviations, σ) overlapped. This was compared to the expected agreement achieved by assuming a normal distribution. As you can see: the two methods agree to better than the expected level of agreement.

The observed agreement in the simulated Legendre Probability Density Functions provides

confidence in the particle generation method used (G4ParticleGun).

Next we compared the final yield data extracted from the experiment to a simulation based on the parameterization of the same experimental data. The experimental runs were parameterized using the Legendre expansion, then simulated using the same parameters. The final results; after all cuts have been applied, for the experimental data from run 142 and the simulated data from that same run are plotted in figure J.2 on the next page. It must be stressed that the comparison in figure J.2 on the next page is a convolution of the fit quality of the parameterization and the accuracy of the simulation (because the simulated yield can only agree as well as the parameterization of the yield does).

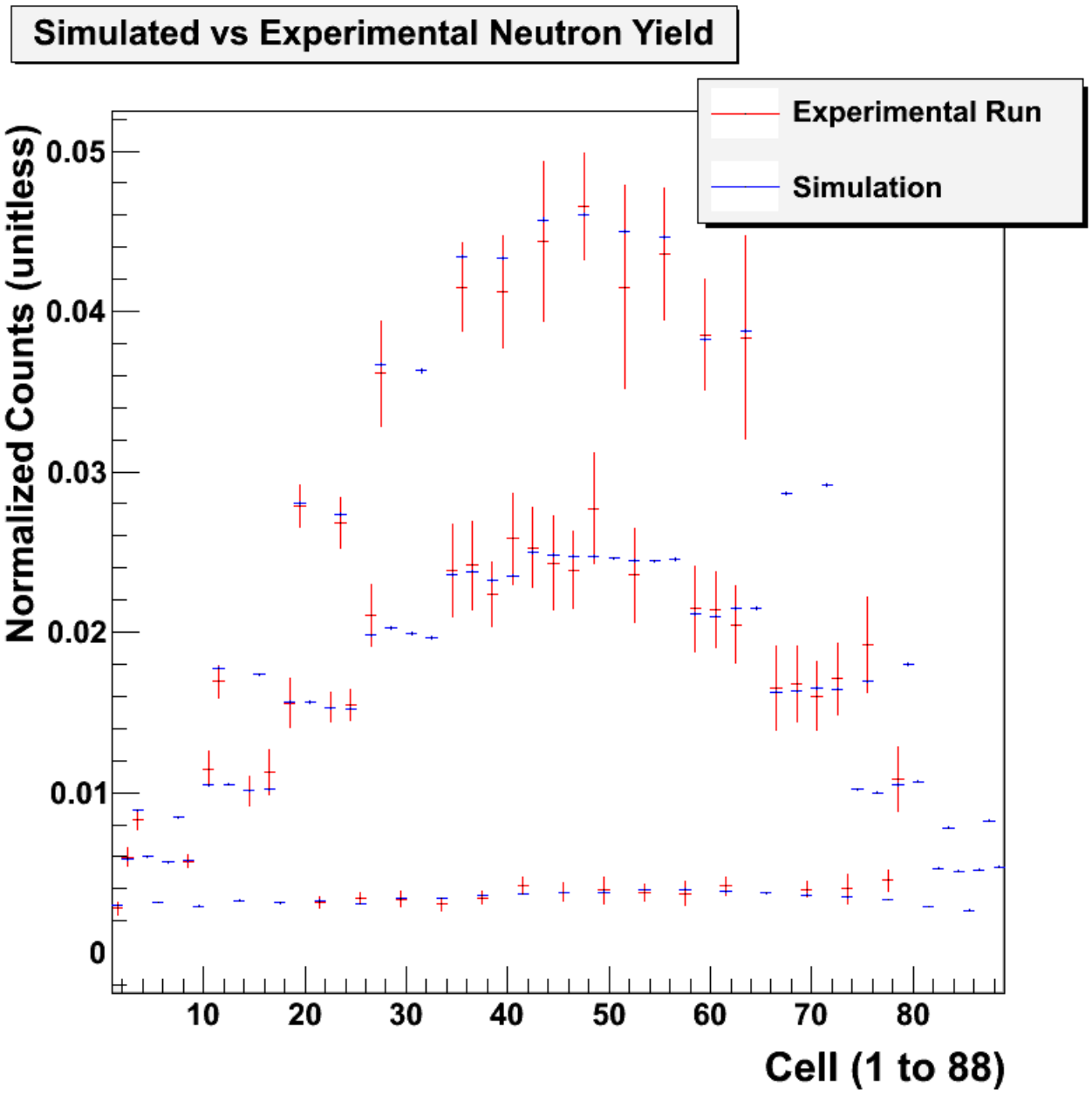

Figure J.2: Simulation Consistency Check for Neutron Distribution and Parameterization. The simulation was tested for consistency by comparing the experimental run (red) to a simulation run (blue) which used the parameters extracted from the experimental run. These two data sets should agree perfectly if: the parameterization of the run was perfect, and the simulation accurately reproduced the experimental conditions. We see that nearly all of the data points agree within error. Note: missing data are excluded cells.

Figure J.2 demonstrates that the simulation is able to reproduce the experimental neutron yields via the parameterization, this provides evidence that both our simulation and fitting

procedure are working properly. In order to test purely the quality of the simulation, the simulation was parameterized in the normal fashion and then the parameterizations of run 142 and its simulation were compared in figure J.3.

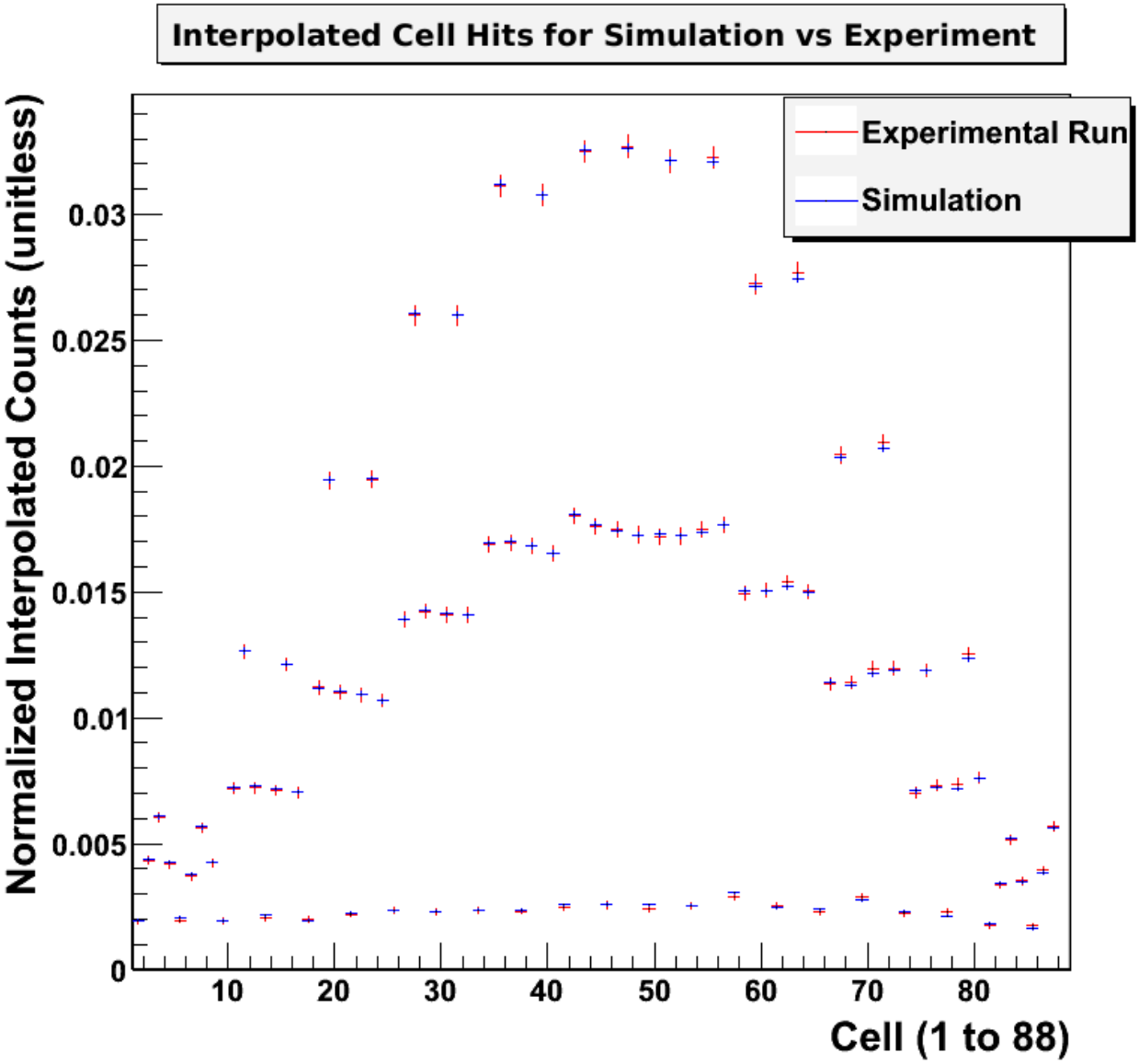

Figure J.3: Simulation Consistency Check for Neutron Distribution. The interpolated data from run 142 (i.e. the parameterization; red) is compared to the simulated yield (blue) which used the same parameterization. The two agree almost perfectly, demonstrating that the simulation is accurately replicating the spatial distribution of the neutron yield.

The excellent agreement in figure J.3 demonstrates that the simulation is not producing any pathologies in the probability density function approach outlined in chapter 4 on page 104

i.e. the simulation is working perfectly, any discrepancy in figure J.2 on page 305 *must be due to the parameterization*.

The final consistency check we can make is to compare the raw data between the simulation and an experimental run (run 142). The only raw data we use are: the TDC spectra and the ADC spectra.

Comparing the ADC spectra, we initially saw that the simulation expects larger light yields than the experiment for most cells (though some cells agree very well e.g. figure J.4: left plot); this is starkly demonstrated by moving the light cut up: figure J.4: right plot.

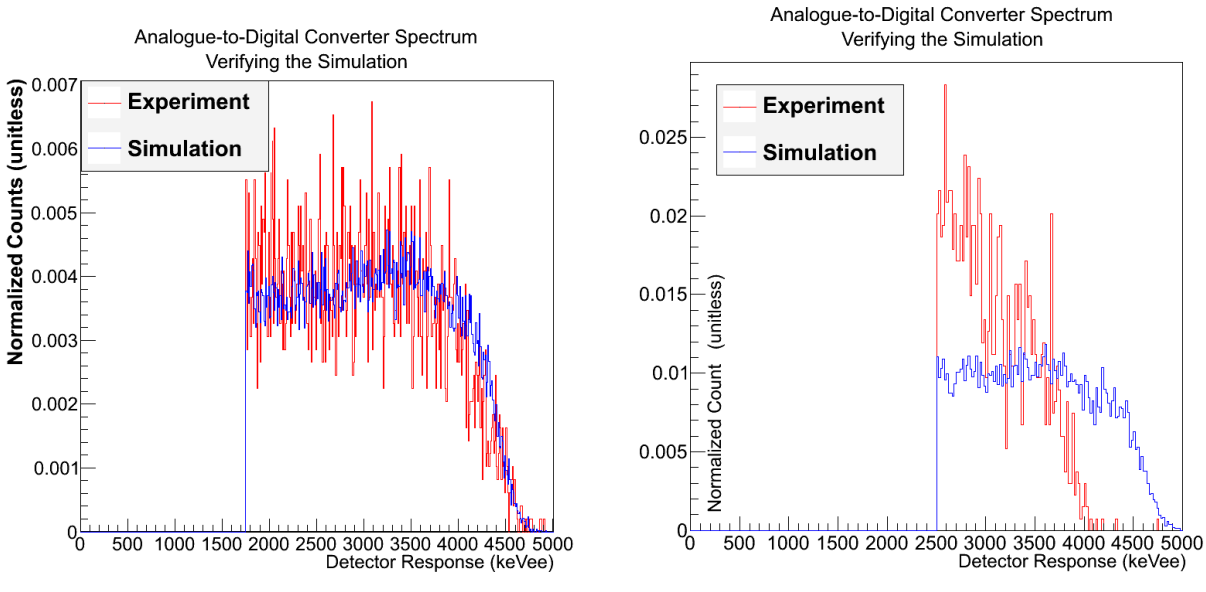

Figure J.4: Simulated vs Experimental Light Output. The analogue-to-digital converter spectrum for an experimental run (red) versus its simulation (blue) after all of the cuts have been applied to both data sets. Left image: we see good agreement between the spectra, with some random (symmetric) variation; this was a particularly good cell (cell 53). Right image (cell 60): moving the light cut up to 2500 keVee, we see that the experimental data greatly underestimates the light output compared to the simulation.

Since we have good reason to believe that the simulation had an accurate light output in the past [Pyw06, Ive03], we assume that the simulation is still correct and there is some unknown affect reducing the ADC values given by neutrons. We scaled the light output as outlined in section 5.3.2 on page 161, and then found that the results did not change depending on the light cut position: figure J.5 on the next page.

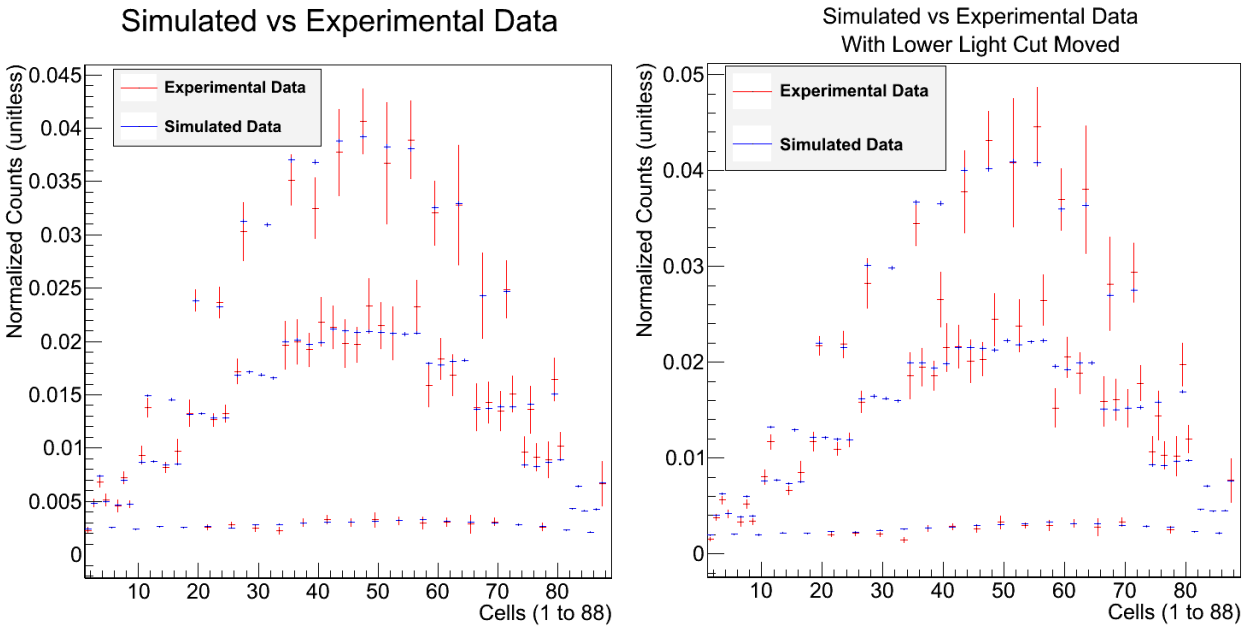

Figure J.5: The Simulation Correctly Reacts to the Light Cut. The simulated and experimental data agree, even when the lower light cut is moved from 1750 keVee (left) to 2500 keVee (right). The simulation thus is properly compensating for the lower light cut. Note: missing data are excluded cells.

Scaling the experimental light output by heuristic factors rectified all lingering discrepancies, and therefore allows us to assume that our simulation accurately replicates the detector response.

The TDC spectra agree in shape, but there appears to be an offset of unknown origin, this is discussed in detail in section 5.3.6 on page 176, and therefore not included here. The TDC spectra are only pertinent to the data in determining the placement of the time-of-flight cut. Given that there may exist an offset between the simulated and experimental TDC spectra, we performed full data analyses for the data with a 'hard' time-of-flight cut (determined by kinematics, usually $\approx$ 5-15 ns) and a 'soft' time-of-flight cut (5-50 ns): where the soft time-of-flight cut was chosen such that a negligible number of late events would be excluded from the data, and the only early data excluded would be photons. The final results were found to be independent of the time-of-flight cut selected (though the 'hard' cut gives better precision, as expected; see section 6.2 on page 218 and section 6.3 on page 224 for comparisons), demonstrating that the apparent discrepancy between the simulated and experimental TDC spectra is negligible, or entirely subjective.

J.1 Discussion of Simulation Consistency

We failed to uncover any discrepancy between the simulated and experimental data which would change our results. The detector efficiency and geometry is being well replicated by the simulation, thus justifying our assumption that they were the same when we computed the cross section (section 5.5.1 on page 211) and when we derived the Legendre expansion of

the differential cross section in terms of simulated neutron yields (section 4.4.2 on page 119). Furthermore, we see that the methodology for simulating the Legendre probability density functions (section 4.4.2) is consistent with an entirely different approach.

We did; however, notice that the simulation is not replicating the ADC data for neutrons anymore: we assume this is a problem with the experimental conditions, and not the simulation. We can justify this assumption because the simulation is still correctly replicating the photon ADC data, and there has been no significant change to the code since the neutron light output was verified in 2006: it still uses the same light tables that it did then.